

**SOLID STATE SUPERCAPACITORS BASED ON
MANGANESE DIOXIDE THIN FILM**

**A THESIS SUBMITTED TO
D. Y. PATIL EDUCATION SOCIETY (DEEMED TO BE
UNIVERSITY), KOLHAPUR**



**FOR THE DEGREE OF
DOCTOR OF PHILOSOPHY
IN
PHYSICS
UNDER THE FACULTY OF
INTERDISCIPLINARY STUDIES
BY**

Mr. VIKAS JAYAWANT MANE

M. Sc.

UNDER THE GUIDANCE OF

PROF. C. D. LOKHANDE

M. Sc., Ph. D.

**DEAN AND RESEARCH DIRECTOR,
CENTRE FOR INTERDISCIPLINARY RESEARCH,
D. Y. PATIL EDUCATION SOCIETY,
(DEEMED TO BE UNIVERSITY),
KOLHAPUR- 416 006.**

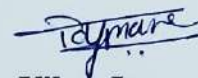
September (2021)

DECLARATION

I hereby declare that the thesis entitled **“SOLID STATE SUPERCAPACITORS BASED ON MANGANESE DIOXIDE THIN FILM”** submitted for the degree of **Doctor of Philosophy (Ph.D.) in Physics** the **Centre for Interdisciplinary Research** faculty of the **D. Y. Patil Education Society (Deemed to be University), Kolhapur** is completed and written by me, has not before made the basis for the award of any degree/diploma/other related heading of this or any other university in India/any other country/examining body to the best of my knowledge. Further, I assert that, I have not dishonoured any of the requirements under copyright and piracy/cyber/IPR act amended by UGC from time to time.

Place: Kolhapur

Date: 09/09/2021



~Mr. Vikas Jayawant Mane

(Research Student)

**D. Y. Patil Education Society (Deemed to be
University), Kolhapur**

Centre for Interdisciplinary Research



Certificate

This is to certify that the thesis entitled "SOLID STATE SUPERCAPACITORS BASED ON MANGANESE DIOXIDE THIN FILM" which is being submitted herewith for the award of the Degree of Doctor of Philosophy (Ph.D.) in Physics of D. Y. Patil Education Society (Deemed to be University), Kolhapur, is the result of the original research work completed by **Mr. Vikas Jayawant Mane** under my supervision and guidance and to the best of my knowledge and belief the work embodied in this thesis has not formed earlier the basis for the award of any Degree or similar title of this or any other University or examining body.

Place: Kolhapur

Date: 09/09 /2021

Research Guide

Prof. C. D. Lokhande

**Forwarded through,
Prof. C. D. Lokhande
Head and Research Director,
Centre for Interdisciplinary Research**

ACKNOWLEDGEMENT

This was a beautiful journey, a journey of expanding the boundaries of knowledge, a journey of finding your strength weakness, a journey of becoming mentally and emotionally strong. It become more beautiful and interesting because of the people I met way along the way. I would like to take this opportunity to acknowledge those fascinating people.

I would like to express my profound appreciation and respect towards my cherished guide **Prof. C. D. Lokhande (Research Director, Centre for Interdisciplinary Research, D. Y. Patil University, Kolhapur)** for his valuable guidance, keen awareness, strong inspiration and constant encouragement during my Ph.D. work. This work would not have been possible without his guidance, discussion and support. Under his guidance, I successfully overcame many difficulties and learned a lot. He is not only a helpful advisor, but like a family member. His genuine caring, concern, and faith in me enabled me to attend to life while also earning my Ph.D. I am very much thankful to him for selecting me as his PhD student and I feel very fortunate to be part of CDL group.

I would like to express my sincere thanks to Vice-Chancellor **Prof. R. K. Mudgal**, Pro-Vice Chancellor **Dr. Shimpa Sharma** and Registrar **Dr. V. V. Bhosale** for the inspiration and support. I also thank **Dr. U. M. Patil, Dr. J. L. Gunjekar, Dr. Vishwajeet Khot and Dr. Arvind Gulbake** who helped me to analyze the results with all their empathy and cooperative mind. All of you and other CDL group members always inspire me to hard work.

I would also like to express my sincere thanks to, **Dr. A. C. Lokhande, Dr. R. N. Bulakhe, Dr. V. C. Lokhande** for providing me very important sample characterization data, during entire research work. A special thanks to **Dr. D. S. Dhawale and Dr. S. P. Mane** for the leisurely chats we had related to research as well as different topics.

I am very much thankful to **Prof. C. D. Lokhande Endowment Charitable Trust, Pune** has a financial support for their kind co-operation during my research work.

I would also like to express my sincere thanks to my seniors Dr. R. B. Pujari, Dr. A. M. Patil, Dr. P. K. katkar, Dr. S. B. Kale, Dr. T. T. Ghogare, Dr. S. J. Marje, for insightful guideline and valuable suggestion during my Ph. D. work. I also have a thank to my all present laboratory colleagues **Navnath Padalkar, Shivaji Ubale, Priti Bagwade, Sachin Pujari, Shrikant Sadavar, Ranjit Nikam, Sambhaji Kumbhar, Vinod Patil, Navaj Shaikh, Rohini Shinde, Satish Jadhav, Suraj Khalate, Dhanaji Malavekar, Sambhaji Khot, Vikas Magdum, Akash Patil, and Satish Phalke.**

I hereby express my deepest appreciation and regards to my beloved parents Father **Jayawant** (Nana), Mother **Mangal** (Aai), and my lovely Brother **Ramdas** (Bhau) for their continuously support with encouragement me to complete my research.

I would like to acknowledge that even though I tried my best, it is not possible to acknowledge all those known and unknown faces individually for their direct and indirect contribution for the successful completion of my work. I am thankful to all of you for your kind cooperation.

Place: Kolhapur

Date: 09/09/2021

~Vikas

SUMMARY OF RESEARCH WORK

A) Published (Indian) Patents (03):

- [1] Chandrakant D. Lokhande, **Vikas J. Mane**, Vaibh C. Lokhande, Shivaji B. Ubale, Vishwanath V. Bhosale, “Asymmetric solid state supercapacitor for energy storage”, (2020), Application No.- **202021011232**.
- [2] Chandrakant D. Lokhande, Dhanaji B. Malavekar, **Vikas J. Mane**, Vishwanath V. Bhosale, Vaibh C. Lokhande, “A method for coating of cerium sulfide-carbon based composite”, (2020), Application No.- **202021002802**.
- [3] Chandrakant D. Lokhande, Trupti T. Ghogare, Priti P. Bagawade, **Vikas J. Mane**, Vishwanath V. Bhosale, “A method for synthesis of dysprosium sulfide (Dy_2S_3) thin film and supercapacitive application thereof”, (2020), Application No.- **201921046414**.

B) Papers Published (10)/Submitted at International Journals (02):

- [1] **Vikas J. Mane**, Dhanaji B. Malavekar, Shivaji B. Ubale, Ravi N. Bulakhe, Insik In, Chandrakant D. Lokhande, “Binder free lanthanum doped manganese oxide @ graphene oxide composite as high energy density electrode material for flexible symmetric solid state supercapacitors”, *Electrochem. Acta*, 335, (2020), 135613-135625, (I.F.- **6.90**).
- [2] **Vikas J. Mane**, Dhanaji B. Malavekar, Shivaji B. Ubale, Vaibh C. Lokhande, Chandrakant D. Lokhande, “Manganese dioxide thin films deposited by chemical bath and successive ionic layer adsorption and reaction deposition methods and their supercapacitive performance”, *Inorg. Chem. Commun.*, 115, (2020), 107853-107869, (I.F.- **2.49**).
- [3] **Vikas J. Mane**, Shital B. Kale, Shivaji B. Ubale, Vaibhav C. lokhande, Chandrkant D. Lokhande, “Enhanced specific energy of silver doped MnO_2/GO electrodes as facile fabrication symmetric supercapacitor device”, *Mater. Today Chem.*, 20, (2021), 100473-100487, (I.F.- **8.30**).
- [4] **Vikas J. Mane**, Shital B. Kale, Shivaji B. Ubale, Vaibhav C. lokhande, Umakant M. Patil, Chandrkant D. Lokhande, “Lanthanum sulfide-manganese sulfide/graphene oxide ($\text{La}_2\text{S}_3\text{-MnS/GO}$) composite thin film as an electrocatalyst for oxygen evolution reactions”, *J. Solid State Electrochem*, 25, (2021), 1775–1788, (I.F.- **2.64**).
- [5] Dhanaji B. Malavekar, Vaibh C. Lokhande, **Vikas J. Mane**, Shivaji B. Ubale, Umakant M. Patil, Chandrakant D. Lokhande, “Enhanced energy density of flexible asymmetric solid state supercapacitor device fabricated with amorphous

thin film electrode materials”, J. Phys. Chem. Solids, 141, (2020), 109425-109434, (I.F.- 3.99).

- [6] Dhanaji B. Malavekar, Vaibhv C. Lokhande, **Vikas J. Mane**, Shital B. Kale, Ravi N. Bulakhe, Umakant M. Patil, Chandrakant D. Lokhande, “Facile synthesis of layered reduced graphene oxide–copper sulfide (rGO-CuS) hybrid electrode for all solid-state symmetric supercapacitor”, J. Solid State Electrochem, 24, (2020), 2963-2974, (I.F.- 2.64).
- [7] Shivaji B. Ubale, Ravi N. Bulakhe, **Vikas. J. Mane**, Dhanaji B. Malavekar, Insik In, Chandrakant D. Lokhande, “Chemical synthesis of nano-grained ytterbium sulfide thin films for supercapacitor application”, Appl. Nanosci., 10, (2020), 5085–5097, (I.F.- 3.67).
- [8] Priti P. Bagwade, Dhanaji B. Malavekar, Trupti T. Ghogare, Shivaji B. Ubale, **Vikas J. Mane**, Ravi N. Bulakhe, Insik In, Chandrakant D. Lokhande, “A high performance flexible solid-state asymmetric supercapacitor based on composite of reduced graphene oxide@dysprosium sulfide nanosheets and manganese oxide nanospheres”, J. Alloys Compd., 859, (2021), 157829-157842, (I.F.- 5.31).
- [9] Shivaji B. Ubale, Shital B. Kale, **Vikas J. Mane**, Chandrkant D. Lokhande, “SILAR synthesized ytterbium sulfide thin film electrodes for symmetric supercapacitors”, J. Solid State Electrochem, 25, (2021), 1753-1764, (I.F.- 2.64).
- [10] Shivaji B. Ubale, Shital B. Kale, **Vikas J. Mane**, Chandrkant D. Lokhande, “SILAR synthesized ytterbium sulfide @ graphene oxide nanocomposite flexible thin film electrodes for supercapacitor devices applications”, J. Electroanal. Chem., (2021), (I.F.- 4.46).
- [11] **Vikas J. Mane**, Vaibhv C. Lokhande, Shivaji B. Ubale, Ranjit P. Nikam, Priti P. Bagwade, Navnath S. Padalkar, Dattatray S. Dhawale, Chandrkant D. Lokhande, “Facile synthesis of MnS-La₂S₃/graphene oxide composite electrodes for high performance flexible symmetric supercapacitors”, Mater. Today Phys., (2021), (I.F.- 9.29).
- [12] Navaj S. Shaikh, Shivaji B. Ubale, **Vikas J. Mane**, Jasmin S. Shaikh, Vaibhav C. Lokhande, Pongsakorn Kanjanaboos, Supareak Praserttham, Chandrakant D. Lokhande, “Graphene integrated nanomaterials for supercapacitor: conducting polymer, metal oxides, chalcogenides, carbides, nitrides, and MXenes”, J. Alloys Compd., 859, (2021), (I.F.- 5.31).

C) Papers/Poster Presented at National/International Conferences (04):

- [1] **Vikas J. Mane**, Dhanaji B. Malavekar, Shivaji B. Ubale, Chandrakant D. Lokhande, “Synthesis and characterization of manganese dioxide thin films for supercapacitor application”, AMSCA-2018, Savitribai Phule Pune University.
- [2] **Vikas J. Mane**, Dhanaji B. Malavekar, Shital B. Kale, Umakant M. Patil, Chandrakant D. Lokhande, “Economical and high performance Flexible symmetric all solid state supercapacitor”, 4th ICPM-MDF-2019 - Shivaji University), Kolhapur.
- [3] **Vikas J. Mane**, Dhanaji B. Malavekar, Shivaji B. Ubale, Chandrakant D. Lokhande, “Binder free lanthanum doped manganese oxide @ graphene oxide composite as high energy density electrode material for flexible symmetric solid state supercapacitor”, (ICSMN-2020)’, SKN Sinhgad College of Engineering Phandarpur.
- [4] **Vikas J. Mane**, Dhanaji B. Malavekar, Shivaji B. Ubale, Chandrakant D. Lokhande, “Enhanced Specific Energy of Silver Doped MnO₂/Graphene Oxide Electrodes as Facile Fabrication Symmetric Supercapacitor Device”, (ICARE-2020)’, Swami Ramanand Teerth Marathwada University, Nanded.

D) Workshops Attended (03):

- [1] International Web-Seminar on “Recent Trends in Nanostructured Materials Based Devices and Their Applications” organized by (Department of Physics, D. P. Bhosale college, Koregaon, Dist-Satara at **18th July, 2020**).
- [2] International Web-Conference on “Nanostructured Materials for Energy Generation, Storage and Smart Applications”, organized by (Department of Physics Shardabai Pawar College, Shardanagar, Baramati) at **9-10th October 2020**.
- [3] International Seminar Series on “Nanotechnology for Environment and Sustainability”, organized by D. Y. Patil Education Society (Deemed to be University) Kolhapur at **12-13th January 2021**.

LIST OF ABBREVIATIONS

Ad:	Adsorption time
AR:	Analytical grade
BET:	Brunauer-Emmett-Teller
BE:	Binding energy
BJH:	Barrette-Joynere-Halenda
BSE:	Backscattered electrons
CBD:	Chemical bath deposition
Cdl:	Double layer capacitor
CFP:	Carbon fiber paper
Cint:	Intercalation capacity
CNT:	Carbon nano tube
CRT:	Cathode ray tube
Cs:	Specific capacitance
CV:	Cyclic voltammetry
Cy:	Total number of deposition cycles
DWW:	Double distilled water
ED:	Electrodeposition
ED:	Energy density
EDAX:	Energy-dispersive X-ray spectroscopy
EDS:	Energy-dispersive X-ray spectroscopy
EDLC:	Electrical double-layer capacitor
EIS:	Electrochemical impedance spectroscopy
E_K:	Kinetic energy
EMC:	Ethyl methyl carbonate
E_{pa}:	Anodic peak potential
E_{pc}:	Cathodic peak potential
ESR:	Equivalent series resistance
FSS-SCs:	Flexible solid state supercapacitors
FSSSC:	Flexible symmetric solid state supercapacitor
FE-SEM:	Field emission scanning electron microscopy
Fig:	Figure
FTIR:	Fourier transforms infrared spectroscopy
GCD:	Galvanostatic charge-discharge measurement
GO:	Graphene oxide
GSI:	Gigascale integration
hν:	Eemitted photoelectron
I_{pa}:	Anodic peak current
I_{pc}:	Cathodic peak current

IP:	Ionic product
I_{po}:	Oxidation peak current
I_{po}:	Oxidation peak current
I_{pr}:	Reduction peak current
ITO:	Indium doped tin oxide
JCPDS:	Joint Committee of Powder Diffraction Standards
LED:	Light emitting diode
LiCl:	Lithium chloride
MWCNTs:	Multi walled CNTs
NEC:	Nippon Electric Company
NF:	Nickel foam
PRI:	Pinnacle Research Institute
PANI:	Polyaniline
PVP:	Polyvinyl propylene
PVA:	Polyvinyl alcohol
PGEs:	Polymer gel electrolytes
PD:	Power density
PC:	Propylene carbonate
PLD:	Pulsed laser deposition
R_{ct}:	Charge transfer resistance
Re:	Reaction time
Ref:	References
Ri:	Rinsing time
RGO:	Reduced graphene oxide
Rs:	Solution resistance
SWCNTs:	Single walled CNTs
SS-SCs:	Solid state supercapacitors
SP:	Solubility product
S_{BET}:	Specific surface area
Subs:	Substrate
SCs:	Supercapacitor
SILAR:	Successive ionic layer adsorption and reaction
SS:	Stainless steel
SORIO:	Standard Oil Company, Cleveland, Ohio
S_{total}:	Total surface area
TEM:	Transmission electron microscopy
VLSI:	Very large-scale integration
XRD:	X-ray diffraction
XPS:	X-ray photoelectron spectroscopy

LIST OF FIGURES

- Fig. 1.1)** The main differences in the significant basic properties between battery and supercapacitor.
- Fig. 1.2)** (A) Schematic of the capacitor and (B) polarization of dielectric material on the application of external electric field.
- Fig.1.3)** Ragone plot showing the comparative performance of different energy storage devices.
- Fig. 1.4)** The schematic of ordinary electrochemical capacitor.
- Fig. 1.5)** The schematic representation of two different electric charge storage process, (A) electrical double-layer capacitance (EDLC), and (B) pseudocapacitor.
- Fig. 1.6)** The schematic of FSS-SCs device.
- Fig. 2.1)** Schematic diagram of CBD method.
- Fig. 2.2)** Photograph of programmable SILAR coating system used for deposition of thin films.
- Fig. 2.3)** Schematic diagram of SILAR method.
- Fig. 2.4)** Principle of Bragg's law of diffraction.
- Fig. 2.5)** The basic ray diagram of the FTIR spectrometer.
- Fig. 2.6)** Emission of photoelectron radiations in the XPS measurement.
- Fig. 2.7)** Schematic of electron path approaching from various components of FE-SEM.
- Fig. 2.8)** Schematic of electron beam path in TEM.
- Fig. 2.9)** Five types of adsorption isotherms in BET analysis.
- Fig.2.10)** Schematic of the dynamic flow method apparatus used for BET measurements.
- Fig. 2.11)** The CV curve for a reversible single electrode transfer reaction.
- Fig. 2.12)** The schematic of the charge-discharge curve.
- Fig. 2.13)** Typical Nyquist plot for the interface of electrode-electrolyte.
- Fig. 3.1)** (A) Schematic diagram of MnO_2 thin film synthesis using CBD method, (B) the photographs of MnO_2 thin films deposited for different hours (a) 8h, (b) 12h and (c) 16h and (C) the proposed growth mechanism of MnO_2 thin film.
- Fig.3.2)** (A) Schematic diagram of MnO_2 thin film synthesis using SILAR method and (B) the photographs of MnO_2 thin films deposited for different cycles (a) 30, (b) 60 and (c) 90.
- Fig. 3.3)** The XRD patterns of (A) C- MnO_2 8h, C- MnO_2 12h and C- MnO_2 16h and (B) S- MnO_2 30, S- MnO_2 60 and S- MnO_2 90 thin films.

Fig. 3.4) The FT-IR spectra of (A) C-MnO₂8h, C-MnO₂12h and C-MnO₂16h and (B) S-MnO₂30, S-MnO₂60 and S-MnO₂90 thin films.

Fig. 3.5) The FE-SEM pictures of (A-B) C-MnO₂12h and (C-D) S-MnO₂60 thin films at magnifications of 10 kX and 50 kX.

Fig. 3.5) The EDX spectra of (E-F) C-MnO₂12h and S-MnO₂60 thin films.

Fig. 3.6) N₂ adsorption-desorption isotherms of (A) C-MnO₂8h, (B) C-MnO₂12h and C-MnO₂16h, thin films prepared at different time periods and (D) BJH pore size distribution plots of C-MnO₂8h, C-MnO₂12h and C-MnO₂16h powder samples.

Fig. 3.7) N₂ adsorption-desorption isotherms of (A) S-MnO₂30, (B) S-MnO₂60 and (C) S-MnO₂90 thin films prepared at different cycles and (D) BJH pore size distribution plots of S-MnO₂30, S-MnO₂60 and S-MnO₂90 powder samples.

Fig. 3.8) (A) Actual experimental set up consisting of (up) automatic battery cycler with CV cycles graph on monitor and (down) three electrode system and (B) schematic representation of three electrode system.

Fig. 3.9) The cyclic voltammetry curves of (A-C) C-MnO₂8h, C-MnO₂12h and C-MnO₂16h electrodes at scan rate 5-100 mV s⁻¹, (D) CV curves of C-MnO₂8h, C-MnO₂12h and C-MnO₂16h electrodes at scan rate of 100 mV s⁻¹, (E) graph of specific capacitance versus scan rate and (F) the areal specific capacitance of C-MnO₂8h, C-MnO₂12h and C-MnO₂16h electrodes.

Fig. 3.10) The GCD curves of (A-C) C-MnO₂8h, C-MnO₂12h and C-MnO₂16h electrodes at different current densities of 1-4 A g⁻¹, (D) GCD curves for C-MnO₂8h, C-MnO₂12h and C-MnO₂16h electrodes at 1 A g⁻¹ current density, (E) the variation of specific capacitance versus current densities and (F) Nyquist plots of C-MnO₂8h, C-MnO₂12h and C-MnO₂16h electrodes.

Fig. 3.10) (G) The CV curves of long cyclic stability of C-MnO₂12h electrode and (H) the capacitance retention versus cycle number plot of CMnO₂12h electrode.

Fig. 3.11) The CV curves of (A-C) S-MnO₂30, S-MnO₂60 and S-MnO₂90 electrodes at various scan rates from 5 to 100 mV s⁻¹, (D) the CV curves of S-MnO₂30, S-MnO₂60 and S-MnO₂90 electrodes at scan rate at 100 mV s⁻¹, (E) graph of specific capacitance versus scan rates and (F) the areal specific capacitance of S-MnO₂30, S-MnO₂60 and S-MnO₂90 electrodes.

Fig. 3.12) The GCD curves of (A-C) S-MnO₂30, S-MnO₂60 and S-MnO₂90 electrodes at different current densities of 1-4 A g⁻¹, (D) GCD curves for S-MnO₂30, SMnO₂60 and S-MnO₂90 electrodes at 1 A g⁻¹ current density, (E) the variation of specific capacitance versus current densities and (F) Nyquist plots of S-MnO₂30, S-MnO₂60 and S-MnO₂90 electrodes.

Fig. 3.12) The (G) stability CV curves of 5000 cycles S-MnO₂60 electrode and (H) plot of capacitance retention versus cycle number of S-MnO₂60 electrode.

Fig. 3.13) (A) The MnO₂ electrode prepared by CBD method with mechanical flexibility of substrate, (B) C-MnO₂12h electrode (5 X 5 cm²), (C) the painting thin layer of PVA-Na₂SO₄ gel electrolyte on electrode, (D) actual fabricated C-MnO₂12h//PVA-Na₂SO₄//C-MnO₂12h symmetric device, (E)

the mechanical flexibility of FSSSC device and (F) the hydraulic press used to apply pressure on FSSSC device.

Fig. 3.14) (A) Potential window selection in voltage ranging from 0 to 0.9 V, (B) the CV curves of symmetric device at different scan rates 5–100 mV s⁻¹, (C) the graph of specific capacitance versus scan rate, (D) the GCD curves at 4 A g⁻¹ in different voltage range from 0 to 0.9 V, (E) the GCD curves at current densities 2 to 8 A g⁻¹ and (F) the graph of specific capacitance versus current densities.

Fig. 3.15) (A) Ragone plot, (B) Nyquist plots of symmetric device of before and after cycling and (inset shows equivalent circuit), (C) the CV curves of symmetric device at different bending angles of 0-165° at scan rate 100 mV s⁻¹ and (D) the plot of capacitance retention versus cycle number (inset shows stability CV curves of 5000 cycle) of device.

Fig. 3.16) The schematic of (A) flexible symmetric solid state device formation, (B) the demonstration of two series connected symmetric devices charged at + 1.8 V for 30 s, and the discharged through a panel of 211 red LEDs (DYPU CDL GROUP) glows for 160 s and (C) the forward biased I-V characteristics of red LED.

Fig. 4.1) The schematic of deposition of 3%La-MnO₂@GO thin film synthesis using SILAR method.

Fig. 4.2) (A) The XRD patterns of (a) MnO₂, (b) 1% La-Mn, (c) 3%La-Mn, (d) 5%La-Mn and (e) 3%La-MnO₂@GO thin films and (B) GO thin film.

Fig. 4.3) The FT-IR spectra of (A) (a) MnO₂, (b) 1% La-Mn, (c) 3%La-Mn, (d) 5%La-Mn and (e) 3%La-MnO₂@GO thin films and (B) FT-IR spectra of (a) MnO₂@GO and (b) GO thin films.

Fig. 4.4) The FE-SEM pictures of (A-B) MnO₂, (C-D) 3%La-Mn and (E-F) 3%La-MnO₂@GO thin films at magnifications of 10 kX and 50 kX.

Fig. 4.4) The FE-SEM images of (G-H) 1%La-Mn and (I-J) 5%La-Mn thin films at magnifications of 10 kX and 50 kX.

Fig. 4.5) TEM images of (A-B) 3%La-MnO₂@GO powder samples, (C) TEM image of graphene oxide multilayer and (D) HRTEM image of 3%La-MnO₂@GO samples (inset shows SAED image).

Fig. 4.6) (A) The EDX spectrum of 3%La-MnO₂@GO composite electrode, (B) Elemental mapping of 3%La-MnO₂@GO thin film showing distribution of La, C, O, Mn elements, Elemental mapping images of (C) C, (D) O, (E) Mn and (F) La elements.

Fig. 4.7) The contact angles of (A) MnO₂, (B) 3%La-Mn, (C) 3%La-MnO₂@GO, (D) MnO₂@GO and (E) GO thin films.

Fig. 4.8) The XPS spectra of 3%La-MnO₂@GO electrode (A) survey spectrum, (B) Mn 2p spectrum, (C) O 1s spectrum, (D) C 1s spectrum and (E) La 3d spectrum.

Fig. 4.9) (A) BET surface area analysis of MnO₂, 3%La-Mn and 3%La-MnO₂@GO samples, (B) the BJH pore size distribution plots of MnO₂, 3%La-Mn, and

3%La-MnO₂@GO powder samples, (C) the BET surface area analysis of MnO₂@GO and GO samples and (D) the BJH pore size distribution plots of MnO₂@GO and GO powder samples.

Fig. 4.10) (A) The cyclic voltammetry curves of MnO₂, 1%La-Mn, 3%La-Mn, 5%La-Mn and 3%La-MnO₂@GO electrodes at scan rate 100 mV s⁻¹, (B) the CV curves of MnO₂, (C) 1%La-Mn, (D) 3%La-Mn, (E) 5%La-Mn and (F) 3%La-MnO₂@GO electrodes at scan rate of 5-100 mV s⁻¹.

Fig. 4.11) The plot of specific capacitance versus scan rates of MnO₂, 1%La-Mn, 3%La-Mn, 5%La-Mn and 3%La-MnO₂@GO electrodes.

Fig. 4.12) (A) The current density versus square root of potential scan rate for all electrodes MnO₂, 1%La-Mn, 3%La-Mn, 5%La-Mn and 3%La-MnO₂@GO electrodes, (B) 3%La-MnO₂@GO (C) 3%La-Mn, (D) 1%La-Mn, (E) 5%La-Mn and (F) MnO₂ electrodes.

Fig. 4.13) (A) The GCD curves of MnO₂, 1%La-Mn, 3%La-Mn, 5%La-Mn and 3%La-MnO₂@GO electrodes at current density of 1 A g⁻¹, (B) the GCD curves of MnO₂, (C) 1%La-Mn, (D) 3%La-Mn, (E) 5%La-Mn and (F) 3%La-MnO₂@GO electrodes at current densities of 1-4 A g⁻¹.

Fig. 4.14) The specific capacitance with current density of all thin film electrodes.

Fig. 4.15) Nyquist plots of MnO₂, 1%La-Mn, 3%La-Mn, 5%La-Mn and 3%La-MnO₂@GO electrodes.

Fig. 4.16) (A) Stability CV curves of 5000 cycles and (B) the capacitance retention versus cycle number plot of 3%La-MnO₂@GO electrode.

Fig. 4.17) The schematic of flexible symmetric solid state device.

Fig. 4.18) (A) Potential window selection in voltage ranging from 1.0 to 1.8 V, (B) the CV curves of symmetric device at different scan rate 5-100 mV s⁻¹ and (C) the graph of specific capacitance versus scan rates.

Fig. 4.19) (A) The GCD curves at 9 A g⁻¹ at different voltage ranges from 1.0 to 1.8 V, (B) the GCD curves at current densities 8-11 A g⁻¹ and (C) the graph of specific capacitance versus current density of symmetric device.

Fig. 4.20) Ragone plot of FSSSC device

Fig. 4.21) (A) Nyquist plots of symmetric device before and after cycling and (inset shows equivalent circuit) and (B) the EIS spectrum frequency analysis of 3%La-MnO₂@GO electrode.

Fig. 4.22) (A) The CV curves of symmetric device at different bending angles of 0-165° at scan rate 100 mV s⁻¹, (B) the stability CV curves of 5000 cycles of FSSSC device and (C) the plot of capacitance retention versus number of cycles.

Fig. 4.23) (A) Demonstration of two series connected symmetric devices charged at +3.6 V for 30 s and the discharged through a panel of 211 red LEDs (DYPU CDL GROUP) which glows for 3.5 min, (C) the I-V characteristic of 211 red LEDs panel operated as external power source and (D) the I-V characteristics of panel operated on discharging of devices.

- Fig. 5.1)** Schematic diagram of synthesis for Mn-Ag₃/GO thin film by SILAR method.
- Fig. 5.2)** XRD diffraction patterns of (a) Mn, (b) Mn-Ag₁, (c) Mn-Ag₃, (d) Mn-Ag₅ and (e) Mn-Ag₃/GO electrodes.
- Fig. 5.3)** The FT-IR spectra of (a) Mn, (b) Mn-Ag₁, (c) Mn-Ag₃, (d) Mn-Ag₅ and (e) Mn-Ag₃/GO electrodes.
- Fig. 5.4)** The photograph images of contact angles for (A) Mn, (B) Mn-Ag₁, (C) Mn-Ag₃, (D) Mn-Ag₅, (E) Mn-Ag₃/GO and (F) GO thin films.
- Fig. 5.5)** FE-SEM pictures of (A-B) Mn, (C-D) Mn-Ag₃ and (E-F) Mn-Ag₃/GO films at magnifications of 10 kX and 50 kX.
- Fig. 5.5)** The FE-SEM images of (G-H) Mn-Ag₁ and (I-J) Mn-Ag₅ thin films at magnifications of 10 kX and 50 kX.
- Fig. 5.6)** TEM pictures of (A-B) Mn-Ag₃/GO powder sample, (C) HR-TEM picture of GO multilayer and (D) the SAED picture of Mn-Ag₃/GO sample.
- Fig. 5.7)** (A) EDX pattern of Mn-Ag₃/GO thin film, (B) the chemical analysis of Mn-Ag₃/GO thin film representing sharing of Ag, O, Mn and C elements, individual elemental distribution profiles of (C) Ag, (D) O, (E) Mn and (F) C elements.
- Fig. 5.8)** XPS spectra of Mn-Ag₃/GO electrode (A) the XPS survey profiles, (B) Mn 2p spectrum, (C) O 1s spectrum, (D) C 1s spectrum and (E) Ag 3d spectrum.
- Fig. 5.9)** (A) N₂ sorption isotherms for Mn, Mn-Ag₁, Mn-Ag₃, Mn-Ag₅ and Mn-Ag₃/GO samples, (B) the BJH size distribution curves for Mn, Mn-Ag₁, Mn-Ag₃, Mn-Ag₅ and Mn-Ag₃/GO samples, (C) N₂ sorption isotherms of GO sample, and (D) the BJH size distribution curve of GO sample.
- Fig. 5.10)** (A) The CV curves of Mn, Mn-Ag₁, Mn-Ag₃, Mn-Ag₅ and Mn-Ag₃/GO electrodes at 100 mV s⁻¹ scan rate, (B) the CV graphs of Mn, (C) Mn-Ag₁, (D) Mn-Ag₃, (E) Mn-Ag₅ and (F) Mn-Ag₃/GO thin films at 5 to 100 mV s⁻¹ scan rate.
- Fig. 5.11)** (A) The plots of Cs versus scan rates for all electrodes and (B) the plots of areal capacitance versus scan rates of Mn, Mn-Ag₁, Mn-Ag₃, Mn-Ag₅ and Mn-Ag₃/GO electrodes.
- Fig. 5.12)** (A) The GCD plots of Mn, Mn-Ag₁, Mn-Ag₃, Mn-Ag₅ and Mn-Ag₃/GO thin films at 2 A g⁻¹ current density, (B) GCD plot of Mn, (C) Mn-Ag₁, (D) Mn-Ag₃, (E) Mn-Ag₅ and (F) Mn-Ag₃/GO electrodes at 2 to 5 A g⁻¹ current densities.
- Fig. 5.13)** (A) The plots of Cs versus current densities for all electrodes, and (B) the plots of areal capacitance versus current densities of Mn, Mn-Ag₁, Mn-Ag₃, Mn-Ag₅ and Mn-Ag₃/GO electrodes.
- Fig. 5.14)** Nyquist graphs of Mn, Mn-Ag₁, Mn-Ag₃, Mn-Ag₅ and Mn-Ag₃/GO electrodes.
- Fig. 5.15)** (A) The stability of CV curves 5000 cycles for Mn-Ag₃/GO electrode and (B) the graph of capacity retention with cycle number of Mn, Mn-Ag₁, Mn-Ag₃, Mn-Ag₅ and Mn-Ag₃/GO electrodes for 5000 repeated CV cycles.

Fig. 5.16) (A) The cyclic voltammetry curves of GO electrode at 5 to 100 mV s⁻¹ scan rates, (B) the plot of Cs versus scan rate, (C) the areal capacitance versus scan rate, (D) the GCD curves of GO electrode at 1 to 4 A g⁻¹ current densities, (E) the plots of specific capacitance and areal capacitance versus current density and (F) the Nyquist plot of GO electrode.

Fig. 5.17) The schematic of flexible solid state symmetric device formation.

Fig. 5.18) (A) The CV plots of (FSS-SSc) device at various potential windows 0-1.6 V, (B) the CV plots of symmetric device at various scan rates 5-100 mV s⁻¹, (C) the plot of variation Cs with scan rates and (D) the plots of areal capacitance versus scan rates of symmetric device.

Fig. 5.19) (A) The GCD plots at 8 A g⁻¹ with various potential windows, (B) GCD curves at various current densities 8-11 A g⁻¹, (C) the variation of Cs with applied current densities and (D) the plots of areal capacitance versus current densities of symmetric device.

Fig. 5.20) Ragone plot of symmetric device.

Fig. 5.21) (A) The CV curves of symmetric device at different bending angles of 0-165° at scan rate 100 mV s⁻¹, (B) the CV curves for 10,000 cycling stability and (C) the plot of capacity retention with cycle number of FSS-SSC device.

Fig. 5.22) Before and after CV cycling of Nyquist plots and (inset reveals best fitted with equivalent circuit).

Fig. 5.23) (A, B) The photograph two (FSS-SSc) devices attached in series with charged at +3.2 V for 30 s at current density 1 A g⁻¹ and discharged during a panel of 211 LEDs (DYPU CDL GROUP) glows for 180 seconds, (C) the I-V characteristic of 211 red LEDs panel operated as external power source and (D) the I-V characteristics of panel operated on discharging of devices.

LIST OF TABLES

- Table 1.1:** Literature survey on manganese oxide (MnO_2) thin films for SCs.
- Table 1.2:** Literature survey on symmetric FSS–SCs device.
- Table 1.3:** Literature survey on asymmetric FSS–SCs device.
- Table 3.1:** A summary of specific surface area, average pore size and pore volume values of C- MnO_2 , and S- MnO_2 electrodes.
- Table 3.2:** The electrochemical properties of C- MnO_2 and S- MnO_2 electrodes in 1 M Na_2SO_4 electrolyte.
- Table 3.3:** Comparison study of manganese oxide materials using CBD and SILAR methods for supercapacitor application.
- Table 3.4:** Comparison of supercapacitive properties of flexible symmetric supercapacitor device.
- Table 4.1:** A summary of specific surface area, average pore size and pore volume values of MnO_2 , 3%La-Mn, 3%La- MnO_2 @GO, MnO_2 @GO and GO electrodes.
- Table 4.2:** The electrochemical properties for all electrodes.
- Table 4.3:** Comparison of supercapacitive properties of flexible symmetric supercapacitor device.
- Table 5.1:** An outline of specific surface area, average pore size and pore volume values of Mn, Mn-Ag1, Mn-Ag5, Mn-Ag3, Mn-Ag3/GO, and GO electrodes.
- Table 5.2:** The electrochemical properties of Mn, Mn-Ag1, Mn-Ag5, Mn-Ag3, Mn-Ag3/GO, and GO electrodes.
- Table 5.3:** Comparison of supercapacitive studies of FSS-SSC device.
- Table 6.1:** Supercapacitive evaluation of MnO_2 , La- MnO_2 @GO, and MnO_2 -Ag/GO electrodes in aqueous electrolytes and all symmetric FSS-SCs device in PVA- Na_2SO_4 used as gel electrolyte.

CONTENTS

Chapter No.	Title	Page No.
1	General Introduction and Literature Survey	1-25
2	Theoretical Background of CBD, SILAR Methods and Thin Film Characterization Techniques	26-52
3	Manganese Dioxide Thin Films Deposited by Chemical Bath and Successive Ionic Layer Adsorption and Reaction Deposition Methods and Their Supercapacitive Performance	53-83
4	Binder Free Lanthanum Doped Manganese Oxide @ Graphene Oxide Composite as High Energy Density Electrode Material for Flexible Symmetric Solid State Supercapacitor	84-115
5	Enhanced Specific Energy of Silver Doped MnO ₂ / Graphene Oxide Electrodes as Facile Fabrication Symmetric Supercapacitor Device	116-149
6	Summary and Conclusions	150-156
7	Recommendations	157-162

CHAPTER-1

GENERAL INTRODUCTION AND LITERATURE SURVEY

CHAPTER-1

General Introduction and Literature Survey

Sr. No.	Title		Page No.
1.1	General introduction		1
	1.1.1	Energy storage systems	1
	1.1.2	Evolution of supercapacitors	3
	1.1.3	Recent trends in supercapacitor	4
	1.1.4	Working principle of supercapacitor	5
1.2	Types of supercapacitor		6
	1.2.1	Electrochemical double layer capacitance (EDLC)	6
	1.2.2	Pseudocapacitor	7
	1.2.3	Hybrid capacitor	7
1.3	Assembly of supercapacitor		8
	1.3.1	Electrode Material	8
		1.3.1(a) Carbon based materials	9
		1.3.1(b) Conducting polymers	9
		1.3.1(c) Metal oxide	9
	1.3.2	Electrolytes	15
		1.3.2(a) Liquid electrolyte	15
		1.3.2(b) Solid gel electrolyte	16
1.4	Flexible Solid State Supercapacitors (FSS-SCs)		17
1.5	Purpose and orientation of thesis		19
1.6	References		21

1.1 General Introduction

1.1.1 Energy storage systems

Today's environmental problems and reducing fossil fuels, the increasing demand for renewable energy sources has stimulated intense research on energy storage and conversion from unconventional energy sources. With climate changes and the rapid growth of the global economy, energy has become the main focus in scientific and industrial corporations [1]. The renewable clean energy sources are highly basis on the time of day and regional climate situations. Hence, it is the requirement to increase large-scale sustainable and clean energy sources. The electrical energy storage devices are certainly for some modern applications, such as telecommunication systems, hybrid vehicles, transportable electronic devices and military devices [2, 3]. Electrical energy is the most excellent solution and the possibility of changing fossils fuels to control air pollution with the reduction of fossil fuels. Hence, the creation of electrical energy with renewable energy sources is a significant assignment to overcome the trouble related to non-renewable energy sources [4, 5].

To store the electrical energy, battery, capacitor and supercapacitor (SCs) are fundamentally used. The distinctive application for rechargeable batteries is an energy source in customer electronics such as laptops and mobile phones. Though great efforts have been made on the improvement of high-performance batteries and fuel cells, the poor power ability and high maintenance cost have kept them apart from many applications [6, 7]. The charge-discharge rate of batteries is restricted and their electrochemical storage mechanisms depend on the redox reactions of cations, which significantly influence their cycling stability and pulse power delivery [8]. However, the industry tolerates its drawbacks owing to the absence of practical alternatives. In recent times, the demand for high-power applications, which are the restriction of batteries can achieve has increased extensively. The SCs are being developed to solve this problem [9, 10].

The major differences in the significant basic properties between battery and supercapacitor are depicted in **Fig. 1.1**. Suppose we have two containers that store water. One is big but it has a small water flow to release or refill. The other one is small, but it has a bigger water flow to release or refill. The first container represents lithium ion battery, since they have a big capability, but they charge and discharge

slowly. The second container represents SCs, since they have a small capability, but they charge and discharge rapidly.

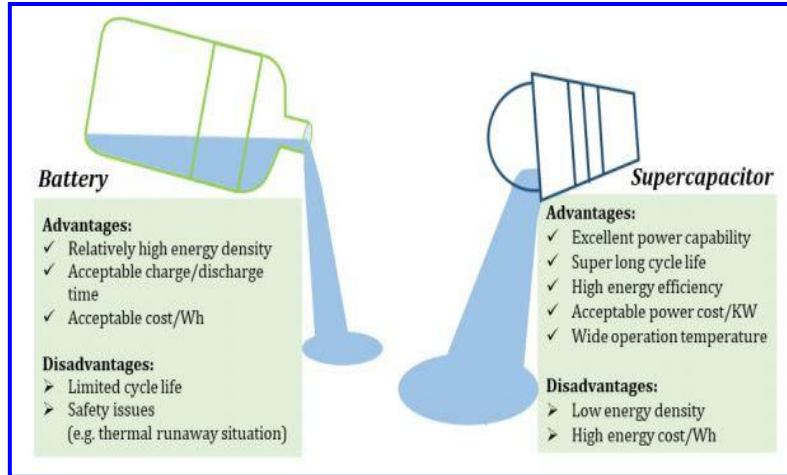


Fig. 1.1) The main differences in the significant basic properties between battery and supercapacitor.

The capacitor is an inactive electrical device, which stores energy as a charge in the electrical field among two metal plates called electrodes. The capacitors are usually can release the accumulated charge and quick consequential in the high power, except cannot store much more energies. The capacitors are mostly included dielectric material in between two metal plates as illustrated in **Fig. 1.2 (A)**. When applied an external voltage, charges stored on the surfaces of both electrodes, which are isolated by an insulating dielectric layer producing an electric field. When applied external electric field enhances electrical charge storage on the metal plates as depicted in **Fig. 1.2 (B)**. Therefore, the capacitors are store relatively low amounts of energy and extensively used in electronic devices [11].

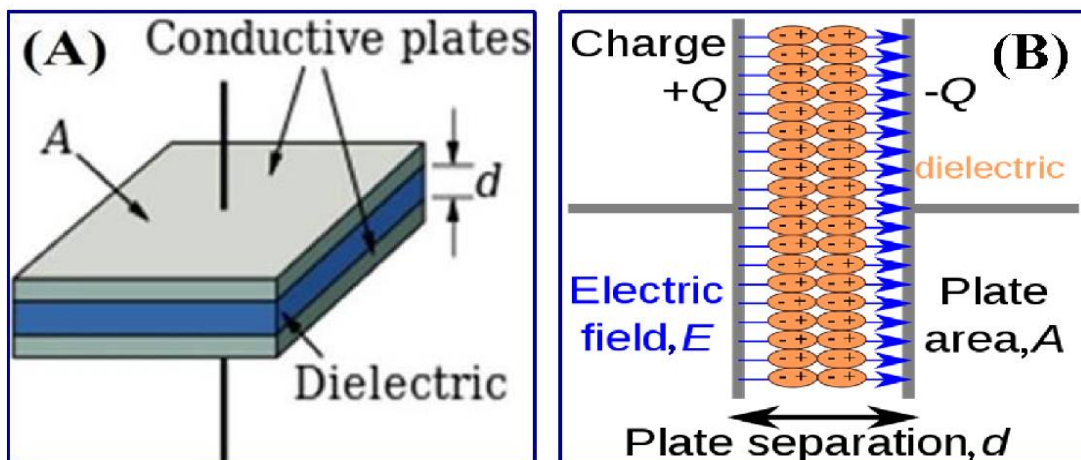


Fig. 1.2) (A) Schematic of the capacitor and (B) polarization of dielectric material on the application of external electric field [11].

Recently, the SCs have huge attention since of their high charge deliver rate, excellent power density, long life span and no short circuit affect. The SCs is a promising electrochemical energy storage technology, which stores high energy density (ED) than capacitor with a high power density (PD) than the batteries. The standard Ragone plot is illustrated in **Fig. 1.3** [12]. Also, charging and discharging SCs have long cycles life (100 times or more) than rechargeable batteries and higher specific capacitance (C_s) of 1 to 2700 F g⁻¹ with lower equivalent series resistance (ESR) than the capacitors [13]. Therefore, various smart applications of SCs are used for high PD such as hybrid cars, cameras for flash equipment, buses, trains, lasers and memory backup devices [14]. Also, it is used in the telecommunication system, satellite system unit, healthcare and medical devices and military devices etc. [15].

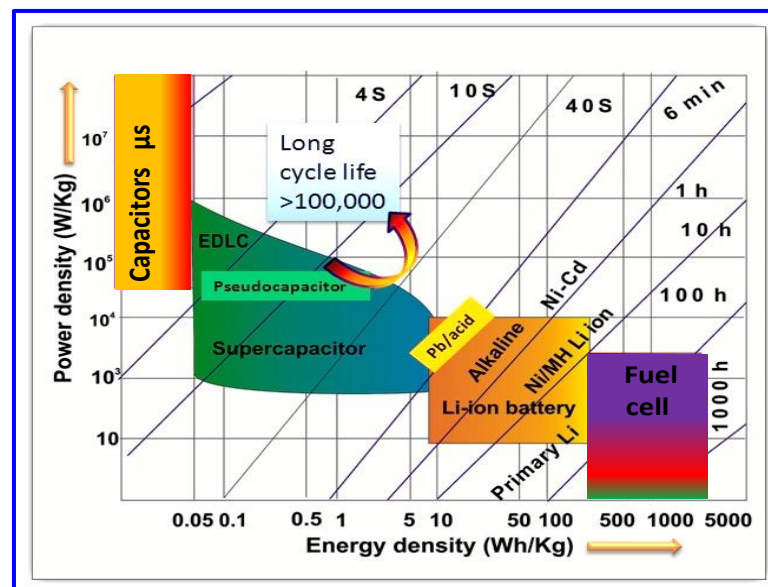


Fig. 1.3) Ragone plot showing the comparative performance of different energy storage devices [12].

1.1.2 Evaluation of supercapacitors

The fundamental idea of charge storage at electrical double-layer capacitor (EDLC) was well known in the 18th century, but primary charge storage technologies with Helmholtz double-layer patented by H. I. Becker in 1957 utilizing porous carbon electrodes in aqueous electrolyte. [16]. Later, in 1966, Standard Oil Company, Cleveland, Ohio (SORIO) multinational has achieved to improve the high energy density technology by using the high surface area porous carbon in non-aqueous electrolytes [17]. In 1971, Nippon Electric Company (NEC), have developed the first commercial SCs and it has brought out the first supercapacitor into the market under

the license of SORIO [18]. Convey has introduced the different principles for charge storage pseudocapacitive behavior of certain materials in 1975 [19]. In 1978, Panasonic Company had developed the ‘Goldcaps’ energy storage devices for memory backup of computers and in 1987 ELNA Company had begun manufacturing their own ‘Dynacap’ supercapacitor device. Both of these companies initiated EDLC SCs. In 1995, NASA demonstrated the vehicle propulsion device in which stored electrical energy as a sole energy source, they utilizing thin metalized polymer film exceed the ED of 10 Wh kg^{-1} [20]. In 1982, a low internal resistance supercapacitor was developed for military applications through the Pinnacle Research Institute (PRI) and which was marketed under the brand name ‘PRI ultracapacitor’ [21]. Today’s, some other companies like NessCap, NCC, ESMA, CAP-XX and Maxwell technologies fabricate the supercapacitor device for different saleable applications.

1.1.3 Recent trends in supercapacitor

The researchers, engineers and scientists around the world are mainly focusing on balancing the ED and PD of SCs in order to without loss of power at once. These SCs will give enhanced performance in consumer electronics, electric vehicles and other application. The researchers are focusing on modifying the developed techniques and materials to further progress the cost-efficiency and power electronics performance of SCs. Furthermore, durability-related worries regarding SCs have been limiting their acceptance in industrial applications to a certain range. A scientist is trying to find substitute materials to enhance the energy density of SCs but not decrease charge and discharge times. If we want to enhance the capability of the SCs, we require expanding the separator and by doing this the time it takes for the electrons to cross the separator enhances, thus increasing the charge and discharge time. The developing SCs appropriate for hybrid electric vehicles or electric vehicles are one of the main important dealing strategies of SCs fabrication companies. The combination of superior active electrode material with appropriate electrolytes successfully enhances both the energy and power capacity of the SCs. Consequently, a smart way to achieve the peak power and ED is the utilization of cost effective pseudocapacitive electrode materials with appropriate electrolytes. The solid state supercapacitors (SS-SCs) with solid polymer electrolyte have been encountered auxiliary interest owing to the benefits of electrolyte leakage, flexibility and relief of treatment as in aqueous electrochemical capacitor [22].

1.1.4 Working principle of supercapacitor

In electrochemical capacitors, electric charge storage depends on the reversible reactions at the interface of electrode/electrolyte. The electrolyte ions through opposite charges are agreed on the electrolyte side as depicted in **Fig. 1.4**. The charge storage mechanism of SCs and the ordinary electrochemical capacitors are the same but the difference in the electrolyte and dielectric material.

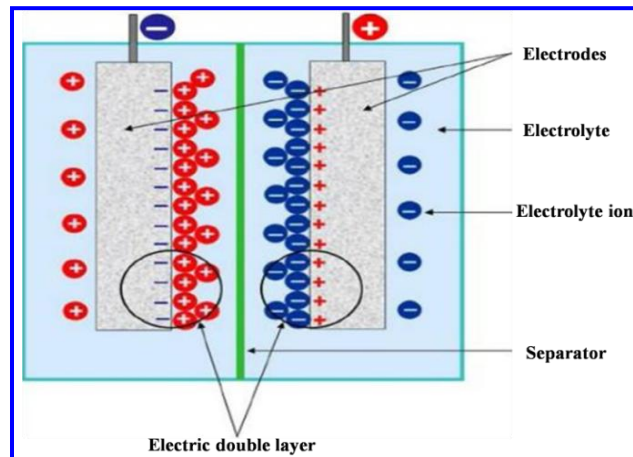


Fig. 1.4) The schematic of ordinary electrochemical capacitor [23].

The higher C_s of the electrochemical capacitor is primarily dependent on the area of the electrode surface and the distance between two plates. The capacitance of an electrochemical capacitor is calculated by the following equation,

$$C = \frac{\epsilon_r \epsilon_0 S}{D} \quad (1.1)$$

where, ' C ', ' ϵ_r ', ' ϵ_0 ', ' S ' and ' D ' are the capacitance of the electrochemical capacitor, dielectric constant of the vacuum, permittivity of the medium, specific surface area of the electrodes and distance between electrolyte ions and the electrode. The ED and PD of electrochemical capacitor are depicted by the following equations,

$$S_E = \frac{0.5 \cdot C_s \cdot (V_C^2 - V_A^2)}{3.6}; \text{and} \quad (1.2)$$

$$S_p = \frac{S_E \cdot 3600}{T_d} \quad (1.3)$$

where, ' C_s ', ' dt ' and ' $V_C - V_A$ ' are the specific capacitance, discharging time and potential window of SCs.

1.2 Types of supercapacitor

According to the charge storage mechanism separates SCs into different categories as EDLCs, pseudocapacitor and hybrid capacitor [24]. The SCs are directed by the same basic equations as an ordinary electrochemical capacitor, except offers high surface area with a porous surface electrode and polymer gel electrolyte to reach at higher Cs. The graphical representation of different types and sub-types of SCs are summarized in **chart 1.1**.

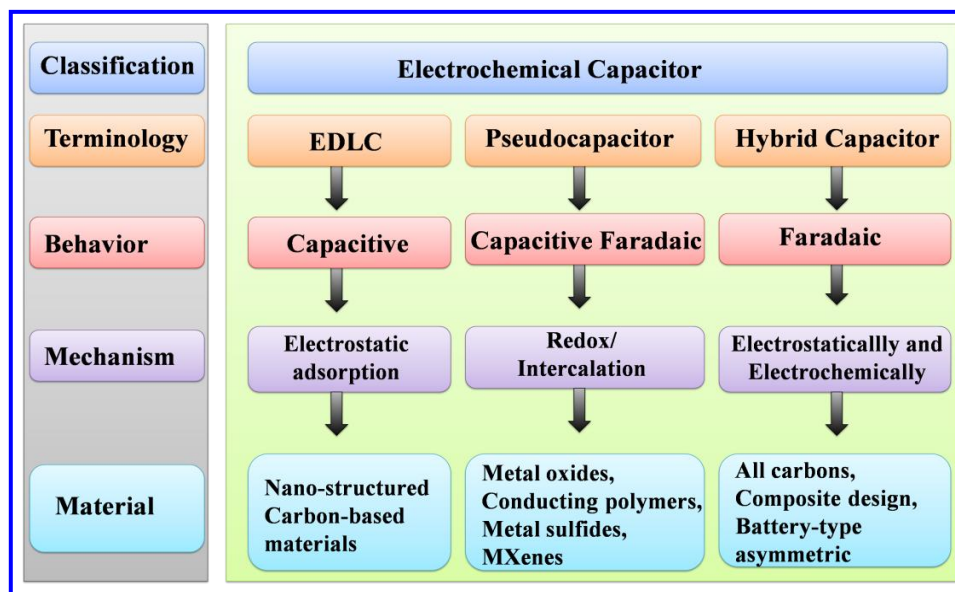


Chart 1.1) Classifications of supercapacitors.

1.2.1 Electric Double Layer Capacitors (EDLC)

In EDLC, the electric charges are gathered in a reversible reaction that is the formation of double layer at the porous carbon-based electrode/electrolyte interface [25]. The EDLC consists of two electrodes divided by an insulating divider and ionically linking with electrolyte [26]. In EDLC, there is no charge transformation, means it stores a charge by reversible adsorption of both anions and cations at the electrode/electrolyte interface as depicted in **Fig. 1.5 (A)**. Therefore, the electrode of EDLC material is immobile at all working voltage. The EDLC has higher PD but very low ED due to faster discharge rate [27]. The electric energy storing capability of EDLC is depends on the electrode materials of surface area and pore-size distribution is accessible to the electrolyte ions. The porous carbon based materials like as reduced graphene oxide, carbon nanotubes, etc. act as an EDLC type electrode. Therefore, research requires focusing on the synthesis condition to increase the performance-increasing elements such as the surface energy, surface area, high electrical conductivity and pore size distribution.

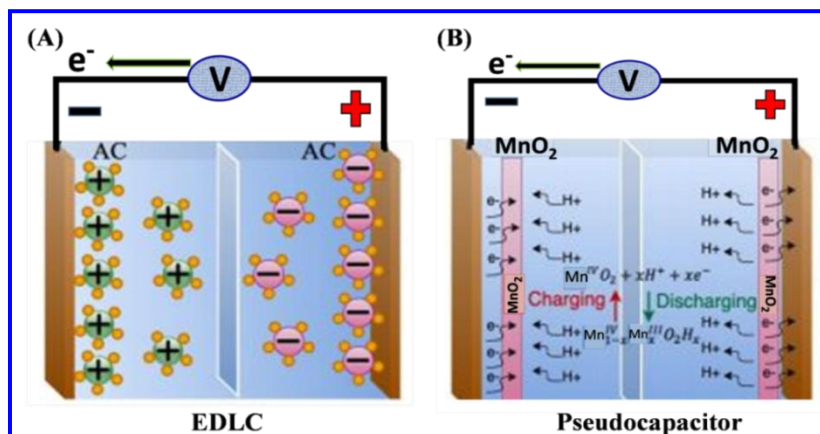


Fig. 1.5) The schematic representation of two different electric charge storage processes, (A) electrical double-layer capacitance (EDLC), and (B) pseudocapacitor [27].

1.2.2 Pseudocapacitor

The pseudocapacitors are depends on the faradic reactions. The oxidation reduction processes take place during charge-discharge of a capacitor, which is a reversible capacitive reaction [28]. The schematic of pseudocapacitor reaction mechanism is illustrated in **Fig. 1.5 (B)**. In the faradic mechanism, charge transformation happens through the double layer as an alternative of the creation of a static double layer. The pseudocapacitive reactions are faradic in origin and storing the electrical energy is very high with reversible redox processes at the electrode surface and electrolyte [29]. The electrochemical performance of the pseudocapacitor depends on the surface area, particle size, the electrical conductivity of the electrode, type of electrolyte and the design of the device. Therefore, the charge storing capacity of pseudocapacitive electrode is very high as compared to the EDLC electrode, except these electrodes have restricted cycling stability and low power density owing to phase change and faradic reactions. Typically, the material like metal oxides, MnO₂ [30], NiO [31] and conducting polymers [32] are used for pseudocapacitor material.

1.2.3 Hybrid capacitor

The hybrid capacitor is recently modernized a gorgeous approach to reaching both higher ED and superior power capability. In hybrid capacitors, one electrode material depends on EDLC category and another is a pseudocapacitive [33]. The mainly fundamental characteristic of hybrid capacitors is depends on two types of energy storage mechanisms that attractive advantage of both non-faradic and faradaic processes [34]. The charge storage processes of hybrid capacitors may refer to capacitive

activities, containing adsorption and desorption ions of reversible redox reaction at the surface of the electrode and electrolyte interface. And faradaic behavior, containing reversible ion intercalation, doping of heteroatoms, reversible processes during the bulk of the electrode materials. Moreover, the hybrid supercapacitor illustrates two types as (a) asymmetric and (b) symmetric supercapacitor. In symmetric SCs, the electrodes of the same category are used. In asymmetric supercapacitor consists of different categories of electrodes, e.g. combination of pseudocapacitive (MnO_2) and EDLC (carbon based). Recently, the battery-type hybrid capacitor is developed, which contains one of the electrode is the capacitive type and another electrode is battery type. This device illustrates the properties of battery as well as capacitor, which signifies superior ED and PD. This is combination opened up a new opportunity for further development in energy storage devices, bridging the gap between the performance of the battery and capacitive EDLC.

1.3 Assembly of supercapacitor

To achieve the higher supercapacitive performance, there is required a selection of active electrode material and electrolyte, the high surface area of the electrode also the packing material of SCs devices. The active electrode material and the conducting electrolyte play a significant function increase the electrochemical performance of SCs.

1.3.1 Electrode Material

To obtain the superior performance of supercapacitor, high specific area, more porous, surface morphology are required for the electrode. The ideal SCs illustrate the following properties for the electrode.

- ❖ The preparation cost of the active electrode is low and non-toxic.
- ❖ The electrical conductivity of electrode material must be better for high performance.
- ❖ The surface area must be high to gives more electroactive material in electrochemical processes.
- ❖ The thermal and chemical stability must be large to obtain maximum electrochemical stability.

Generally, the carbon based electrode materials were employed in EDLC category SCs due to their high surface area, high electrical conductivity and high PD. The metal

oxides and conducting polymers are applied in pseudocapacitor since of their rapid and reversible redox processes.

1.3.1(a) Carbon based materials

The activated carbons, carbon nanotubes and carbon aerogels have been investigated as an electrode material owing to its properties like high conductivity, high thermal and chemical stability. These materials are controlled pore structure, cost effective and the higher active surface of $3000 \text{ m}^2 \text{ g}^{-1}$ [35]. The carbon electrodes are integrated in the EDLC type supercapacitor groups.

1.3.1(b) Conducting polymers

The polyaniline, polypyrrole and polythiophene are the polymers employed as an application for supercapacitor. The conducting polymers can energy storage with not only EDLC but also fast faradic charge transfer processes. The most important of conducting polymer is superior electrical conductivity. Usually, the potential windows of all conducting polymers are stationary. Conducting polymers have various oxidation states and more conductivity than metal oxides and metal hydroxides. These polymers of conductivity can be tuned in an extensive range from 10^4 up to $10^{-10} \text{ S cm}^{-1}$ through different dopants and the doping level. Several reports are accessible in the literature on conducting polymers. Tripathi et al [36] reported a Cs of 137 F g^{-1} for polypyrrole electrode. Dubal et al [37] reported Cs of 586 F g^{-1} and prepared the polypyrrole thin films through the electrodeposition method. 480 F g^{-1} for polypyrrole [38]. The Low charge-discharge cycling stability of polymer materials decreased their use for supercapacitor. Therefore, polymer composite materials are synthesized widely used of carbon-based materials such as polyaniline/graphene [39], and polypyrrole/CNT [40].

1.3.1(c) Metal oxide

In recent years, different metal oxides and hydroxides have fascinated wide attention for SCs applications. Commonly, transitional metals are used as pseudocapacitor electrodes acquiring various oxidation states. The quick and reversible faradic processes at the interface of electrode surface and electrolyte are responsible for high conductivity [41]. The multiple oxidation states of pseudocapacitor have attracted more attention due to its high PD, long cycle life than that of batteries and

high ED than that of dielectric capacitors. The ED of supercapacitor can be improved either by increasing Cs or potential window [42].

The main research focus has been on the improvement of the electrochemical energy storage devices with high energy and power densities along with cycling stability. The transition metal oxides like RuO₂, MnO₂, ZnO, NiO, CuO and conducting polymers are used as electrode materials in supercapacitor [43-46]. The ruthenium oxide (RuO₂) has been extensively studied due to its high electrical conductivity and various oxidation states with a higher potential window of 1.2 V. However, its expensive and toxic nature restricts its implementation into practical applications [47]. Amongst above materials; MnO₂ has drawn great attention due to its inexpensive, eco-friendly nature, earth abundant and high theoretical Cs of 1370 F g⁻¹, as a promising electrode material for SCs [48]. The MnO₂ in the thin film and powder forms has been synthesized by various methods including chemical bath deposition (CBD), hydrothermal and successive ionic layer adsorption and reaction (SILAR) investigated for SCs application [49-51]. The carbon based materials composed with metal oxides have great potential as an electrode owing to their outstanding mechanical, optical and high electrochemical performance [52].

The electrochemical properties of MnO₂ can be easily improved with doping of metal ions [53]. The metals such as Cu, Fe, V, Co, and Ni were successfully doped into the structure of MnO₂ and studied for electrochemical performance [54, 55]. Dubal et al [56] obtained Cs of 328 F g⁻¹ for CBD deposited α -MnO₂ films. Patil et al [57] prepared nano-spheres of α -MnO₂ thin film with Cs of 550 F g⁻¹. Chodankar et al [58] reported Cs of 633 F g⁻¹ with CBD deposited MnO₂ film. Hu et al [59] chemically synthesized nanoporous layered δ -MnO₂ electrode and showed maximum Cs of 447 F g⁻¹. Hu et al [60] prepared nonporous of δ -MnO₂ films using CBD deposited and maximum Cs of 447 F g⁻¹. Singu and Yoon [61] prepared nanosphered α -MnO₂ films using SILAR method and obtained Cs of 262 F g⁻¹. Jana et al [62] reported MnO₂-reduced graphene oxide composite electrode for supercapacitor application with maximum Cs of 987 F g⁻¹. Shaikh et al [63] prepared Mn₃O₄ films using SILAR method and obtained Cs of 371.2 F g⁻¹. Gund et al [64] deposited GO/Mn₃O₄ thin films through SILAR method for supercapacitor with Cs of 344 F g⁻¹. The supercapacitive properties such as the ED and PD of MnO₂ based electrodes with their deposition methods and electrolytes are summarized in **Table 1.1**.

Table 1.1 Literature survey on manganese oxide (MnO₂) thin films for SCs.

Sr. No.	Material	Deposition method	Substrate Used	Electrolyte	Specific capacitance (F g ⁻¹)	Energy density (Wh Kg ⁻¹)	Power Density (kW kg ⁻¹)	Stability (%)	Ref. No.
1	α -MnO ₂	CBD	SS	1 M Na ₂ SO ₄	328	-	-	84 (1000)	[56]
2	α -MnO ₂	CBD	SS	1 M Na ₂ SO ₄	550	61	2.1	92.5 (2000)	[57]
3	α -MnO ₂	CBD	SS	1 M Na ₂ SO ₄	633	65.9	-	95 (2000)	[58]
4	δ -MnO ₂	CBD	SS	1 M Na ₂ SO ₄	229	-	-	83 (1000)	[59]
5	δ -MnO ₂	CBD	SS	0.5 M Na ₂ SO ₄	447	38.3	0.24	87 (1000)	[60]
6	MnO ₂	SILAR	SS	1 M Na ₂ SO ₄	262	18.3	7.99	72 (4000)	[61]
5	MnO ₂ /RGO	SILAR	SS	1 M Na ₂ SO ₄	987	88	23.2	79 (10,000)	[62]
7	Mn ₃ O ₄	SILAR	SS	1 M Na ₂ SO ₄	371.2	17	0.99	94 (4500)	[63]
8	GO/Mn ₃ O ₄	SILAR	SS	1 M Na ₂ SO ₄	344	93	1.0	87 (3000)	[64]
9	Mn ₃ O ₄	Hydrothermal	Carbon-Ti plate	1 M Na ₂ SO ₄	401	-	-	91 (1000)	[65]
10	MnO ₂	Hydrothermal	SS	1 M Na ₂ SO ₄	269	-	-	94 (2000)	[66]
11	δ -MnO ₂	Chelation-mediated method	NF	1 M Na ₂ SO ₄	325	-	-	86 (1000)	[67]
12	MnO ₂	Hydrothermal	NF	1 M LiPF ₆	455	5.7	0.372	97 (2000)	[68]
13	MnO ₂	Hydrothermal	NF	1 M Na ₂ SO ₄	411	-	-		[69]
14	MnO ₂	Hydrothermal	NF	1 M Na ₂ SO ₄	241	-	-	90 (1000)	[70]
15	MnO ₂	Decantation	CFP	1 M Na ₂ SO ₄	306	21	67.8	95 (6000)	[71]

16	α -MnO ₂	Hydrothermal	CFP	1 M Na ₂ SO ₄	251	-	-	98 (3000)	[72]
17	MnO ₂	ED	SS	1 M Na ₂ SO ₄	237	2.3	0.59	-	[73]
18	MnO ₂	ED	SS	1 M Na ₂ SO ₄	345	3.4	0.6	-	[74]
19	α -MnO ₂	Hydrothermal	CFP	1 M Na ₂ SO ₄	118	-	-	42 (1000)	[75]
20	MnO ₂	ED	Nickel plate	0.5 M Na ₂ SO ₄	347	-	-	90 (1500)	[76]
21	MnO ₂	ED	ITO	0.5 M Na ₂ SO ₄	1018	90.5	2.0	-	[77]
22	α -MnO ₂	ED	SS	0.5 M Na ₂ SO ₄	338	-	-	-	[78]
23	MnO ₂	Hydrothermal	NF	1 M Na ₂ SO ₄	295	24.0	1.0	8 (1000)	[79]
24	Mn ₃ O ₄	precipitation	SS	1 M Na ₂ SO ₄	322	-	-	77	[80]
25	Mn ₃ O ₄	SILAR	SS	1 M Na ₂ SO ₄	314	-	-	-	[81]
26	Mn ₃ O ₄	CBD	SS	1 M Na ₂ SO ₄	193	-	-	-	[82]
27	Mn ₃ O ₄	ED	SS	0.5 M Na ₂ SO ₄	235	-	-	-	[83]
28	Mn ₃ O ₄	PLD	SS	0.1 M Na ₂ SO ₄	210	-	-	-	[84]
29	MnO _x	PLD	SS	1 M Na ₂ SO ₄	213	-	-	-	[85]
31	MnO ₂	Hydrothermal	CPF	1 M Na ₂ SO ₄	461	21.3	13.33	-	[86]

Specifications: Methods (ED-Electrodeposition, CBD- Chemical bath deposition, SILAR- Successive ionic layer adsorption and reaction, PLD- Pulsed laser deposition), GO- Graphene oxide, RGO- Reduced graphene oxide, Substrates (NF-Nickel foam, CFP- Carbon fiber paper, SS-Stainless steel, ITO- Indium doped tin oxide).

Table 1.2 Literature survey on symmetric FSS– SCs device.

Sr. No	Symmetric Supercapacitor Electrode	Polymer Gel Electrolyte	Specific Capacitance (F g^{-1})	Energy Density (Wh kg^{-1})	Power Density (kW kg^{-1})	Stability (%) (cycles)	Ref. No.
1.	rGO@LaCe-MnO ₂	Na ₂ SO ₄	61	21.96	4	50 (3000)	[93]
2.	MWCNTs/MnO ₂	PVA-Na ₂ SO ₄	204	23.3	-	80 (2500)	[94]
3.	Au-MnO ₂ /CNT	Na ₂ SO ₄	68	4.5	33	-	[95]
4.	MnO ₂	PVP-LiClO ₄	110	23	1.9	92 (2200)	[96]
5.	Graphene@carbon cloth	PVA-H ₂ SO ₄	11.8	1.64	0.67	-	[97]
6.	α -MnO ₂	CMC-Na ₂ SO ₄	145	16	2.5	88 (2500)	[98]
7.	PCNP2	H ₂ SO ₄ /PVA	226	7.9	0.1	92 (5000)	[99]
8.	MnO ₂ @CNTs/Ni	Na ₂ SO ₄	145	33.6	30.2	82 (1000)	[100]
9.	3%La-MnO ₂ @GO	PVA-Na ₂ SO ₄	140	64	1	90 (5000)	[101]
Specifications: CNT- Carbon nano tubes, MWCNTs- Multi walled CNTs, rGO- Reduced graphene oxide, FSS- Flexible solid state, PVA- Polyvinyl alcohol, La-Lanthanum, Ce-Cerium, MnO ₂ - Manganese oxide, Au- Aluminium, Ni-Nickle, %- Percentage							

Table 1.3 Literature survey on asymmetric FSS– SCs device.

Sr. No	Supercapacitor Symmetric Electrode	Polymer Gel Electrolyte	Specific Capacitance (F g^{-1})	Energy Density (Wh kg^{-1})	Power Density (kW kg^{-1})	Stability (%) (cycles)	Ref. No.
1.	CNTs/MnO ₂ //CNTs/PANI	Na ₂ SO ₄ /PVP	-	24.8	1.20	-	[102]
2.	CoSe ₂ //MnO ₂	LiCl/PVA	1.77 F cm^{-3}	0.58 mWh cm^{-3}	0.282 W cm^{-3}	94.8 (2000)	[103]
3.	ZnO@MnO ₂ //RGO	LiCl/PVA	0.52 F cm^{-3}	0.23 mWh cm^{-3}	0.133 W/cm^3	98.5 (5000)	[104]
4.	SWCNTs//RuO ₂	H ₃ PO ₄ /PVA	138	18.8	96	60-70 (1000)	[105]
5.	Carbon aerogel//Co ₃ O ₄	KOH-PVA	57.4	17.9	0.75	85 (1000)	[106]
6.	Graphene(ILCMG)// RuO ₂ –IL-CMG	H ₂ SO ₄ /PVA	175	19.7	0.68	-	[107]
Specifications: CNT- Carbon nano tubes, SWCNTs- Single walled CNTs, RGO- Reduced graphene oxide, PVA- Polyvinyl alcohol, PVP- Polyvinyl propylene, LiCl –Lithium chloride, PANI-Polyaniline, MnO ₂ - Manganese oxide, H ₃ PO ₄ -Phosphoric acid.							

Table 1.1 demonstrates electrochemical performance of MnO_2 electrodes. These electrochemical parameters of MnO_2 based electrodes material signify the future scope of metal oxides in supercapacitor electrode fabrication. The higher electrochemical stability of MnO_2 is the main advantages, but it will be resolved using a composite of metal oxides with carbon based materials. The electrochemical performance of electrode materials depends on surface morphology of electrode material. The potential window plays a significant role to enhance the Cs of electrode material.

1.3.2 Electrolytes

The electrolyte is an intermediate that conducts electricity and which is created by dissolving the substance in a proper ionizing solvent such as water. The electrolyte has a distinctive significance in the supercapacitor, as it decides the ED of the SCs. The PD and ED are mostly related to the operating potential window of the SCs and determined through the electrolyte. In brief, electrolytes are categorized into two groups viz. liquid and solid electrolytes. Every electrolyte has its benefits and drawbacks.

1.3.2(a) Liquid electrolyte

The liquid electrolytes are categorized into two types; as aqueous and organic electrolytes. The aqueous electrolytes are extensively used to develop the SCs, owing to their uncomplicated preparation, environment friendly, inexpensive and high ionic conductivity ($\sim 10^{-3} \text{ S cm}^{-1}$). But, a restricted operating potential window (1.23 V) of aqueous electrolyte reserves a limit on the performance of SCs. The operating potential of organic electrolytes can achieve 3 V, except they are related to protection risks since of the flammability and very toxic behavior. Their realistic energy density is too low and the majority of them are less than 5 Wh kg^{-1} . The most important explanation is the capacitance is not large sufficient owing to the bulky size of the organic molecules (15-20 Å). These aqueous and organic liquid electrolytes have several general disadvantages. The SCs manufacture with these types of electrolytes needed expensive packaging substances and techniques to evade the probable leakage of electrolytes, as mainly of the electrolytes is corrosive and highly toxic.

It is quite tricky to fabricate a flexible and small supercapacitor utilizing liquid electrolytes. One more restriction is that the evaporation of liquid electrolyte

successfully decreases the energy storing capability of the SCs. Thus, it is necessary to search for a new electrolyte system that is more appropriate as related to the liquid electrolyte.

1.3.2(b) Solid gel electrolyte

The research during the field of solid electrolytes includes analysis of physical and chemical activities of the solids with quick ion movement in the bulkiness as well as their technological features. The solid electrolytes are also known as the ‘superionic solids’ or rapid ion conductors’. The solid electrolytes demonstrate the enormous extent to develop all-solid-state mini/micro electrochemical devices viz. fuel cells, SCs, batteries, photoelectrochemical, sensors, solar cells, etc. These solid electrolytes have the subsequent characteristics.

These electrolytes possess very low-temperature ionic conductivity of an order of 10^{-12} to 10^{-16} S cm⁻¹ and generally, they are measured as an insulator. The numbers of exertions were prepared to enhance the range of ionic conductivity by doping, but with very restricted success. The polymer electrolytes are defined as polymeric membranes, which possess the ion transport effects corresponding to the liquid electrolyte. The significance of polymer electrolytes with other solid electrolytes are in terms of ease of formation, high ionic conductivity ($\sim 10^{-3}$ S cm⁻¹) with mechanical flexibility at room temperature [87]. The ion transportation in this electrolyte primarily directed by the thermally created point deficiency such as Frenkel and Schottky defects. Therefore, the function of the dependable solid-state electrochemical appliance, polymer electrolyte should possess the following characteristics;

The high ionic conductivity in the range of 10^{-3} S cm⁻¹, ions are the principle charge carriers, high thermal, chemical and electrochemical durability, high mechanical strength, more compatibility, and acts as a separator.

On the basis of physio-chemical activities several methods are approved for the synthesis of polymer electrolytes. These are classified into various types such as plasticized polymer electrolytes, solvent-swollen polymer electrolytes, rubbery electrolytes and polymer gel electrolytes (PGEs) [88]. In the last years, the PGEs have predominately utilized to fabricate the SCs, as it demonstrates both the cohesive properties of solid and diffusive transfer activities of the liquid [89]. Generally, the PGEs are formed by trapping the liquid electrolyte in the polymeric gel. This ionic

conduction takes place through the movement of liquid electrolytes, where as polymer gives mechanical integrity to PGEs. With the gel-like nature and much smaller liquid content, it is predicted that PGEs are low reactive than their liquid electrolyte equivalents [90]. The advantages of PGEs have high ionic conductivity, mechanical flexibility, large potential window (3 V) and thermal stability. Frequently used organic solvent as plasticizers are ethylene carbonate (EC), propylene carbonate (PC) and ethyl methyl carbonate (EMC), but organic solvents are in general often expensive, flammable and highly toxic. Hence, the replacing of an organic solvent with an aqueous solvent is highly appropriate. The aqueous gel electrolytes can also significantly decrease the device cost.

1.4 Flexible Solid State Supercapacitors (FSS-SCs)

The growing demand for renewable off-grid energy sources, mobile electronic devices and electric vehicles entail high energy storage devices. The rechargeable batteries and FSS-SCs devices are suitable for the fabrication of microelectronics. The flexible SS-SCs combined with exceptionally long life span, high PD, safety, environmental friendliness, flexibility and stability are useful for electric charge storage appliances. The schematic diagram of FSS-SCs is shown in **Fig. 1.6**. The current collector with a thin layer of active material acts as one electrode. When the device is symmetric then two electrodes are of same types and the device is asymmetric, when two electrodes are of different types of materials. The solid gel electrolyte acts as a separator as well as conducting medium and all this assembly is packed in appropriate packaging materials [91].

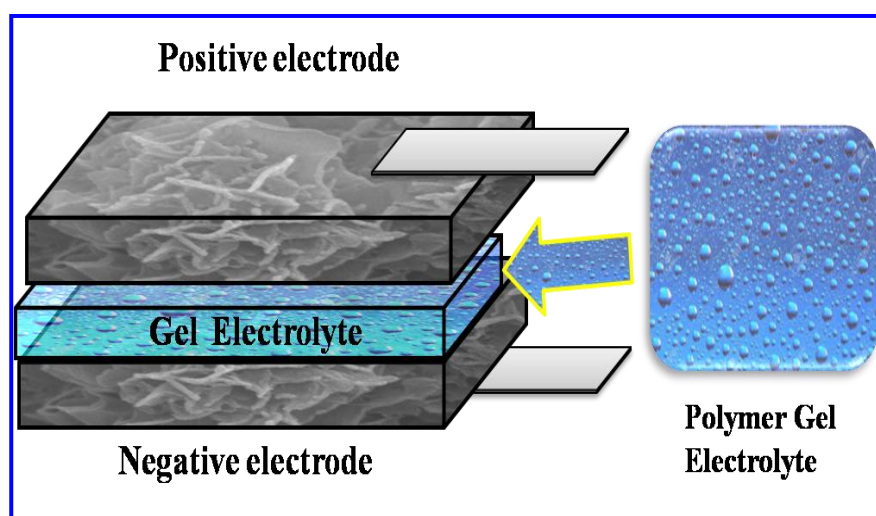


Fig. 1.6) The schematic of FSS-SCs device [91].

The previous paragraph shows the use aqueous, organic or ionic liquids as electrolytes in supercapacitor. The SCs based on liquid electrolyte, suffers from leakage of electrolyte and electrochemical cycling instability. Therefore, the proper packaging of SCs is a very significant task. The high cost of packing materials is required to avoid the leakage of electrolyte. Moreover, due to liquid electrolyte, the size of supercapacitor decreases up to certain limit which restricts the use of device in smaller electronic part. The liquid organic electrolytes are poisonous and harmful to human being. Furthermore, liquid electrolytes have more water content, which generates evaporation of electrolyte at high temperature. Recently, the new class of energy storage devices like FSS-SCs achieved greater attraction owing to its higher storage and cycling stability. The FSS- SCs have a number of advantages over the conventional supercapacitor like light-weight, small-size, convenient, excellent reliability, ease of handling, wide operating potential window and high temperatures. For fabrication of FSS-SCs devices, flexible electrode and polymer gel electrolyte are required, which can be hold their properties even at bending or twisting. Generally, the FSS-SCs devices are two types as symmetric and asymmetric FSS- SCs on the basis of electrode fabrication.

Mostly, symmetric FSS-SCs have the same positive and negative electrodes which are stacked with polymer gel electrolyte [92]. The overall capacitance of the supercapacitor device is estimated by the following equation,

$$1/C = 1/C_1 + 1/C_2 \quad (1.4)$$

where, 'C', 'C₁' and 'C₂' are the overall capacitance, positive and negative electrodes of the supercapacitor, respectively. **Table 1.2** illustrates the results obtained for symmetric FSS-SCs devices.

Table 1.2 shows electrochemical performance of symmetric FSS-SCs. The numbers of reports are available on symmetric FSS- SCs to increase the ED and operating potential window of the FSS- SCs device. It is observed that additional attempts are needed to improve the electrochemical performance of symmetric FSS-SCs supercapacitor.

The improvement of ED and operating potential window of symmetric FSS-SCs device without trailing of PD with electrochemical cycling stability is required. One of the ways to enhance the electrochemical performance with extensive potential

window is to fabricate an asymmetric device with two various electrodes. In this one electrode of EDLC type properties and other pseudocapacitive properties are used to increase ED and PD, respectively. Supercapacitive performance of asymmetric FSS-SCs device depends on the electrochemical characteristics of both electrodes. **Table 1.3** illustrates the results achieved for asymmetric FSS-SCs devices.

The low Cs of carbon based material reserved restrictions on the overall capacitance of the asymmetric FSS- SCs device. Consequently, as an alternative to carbon based materials, pseudocapacitive materials having a negative operating potential window are used as a negative electrode, to overcome the restrictions of carbon based materials.

1.5 Orientation and purpose of the dissertation

The SCs devices are required for the electric charge storage in devices with configuration of small size flexible and portable electronic. Therefore, the SCs are significant in new technology owing to their properties like high energy efficiencies, high specific power, superior cycle life and faster charge-discharge rates. The prime requirements of electrodes in SCs are higher electrical conductivity, well-defined redox states and porous microstructure with a high surface area.

The trend of recent research is focused on transition metal oxide with carbon based materials because of their good electrical conductivity, high value of ED, PD, and electrochemical stability. Among all these, transition metal oxides are largely explored as an active electrode material, in which MnO_2 is most studied material and has very promising potential towards addressing the problems in the area of SCs. The metal oxide with carbon based materials SCs are an important incoming class of electrochemical capacitors, likely to deliver high ED at high charging-discharging rates. Improvements in the operating potential window, specific capacitance and energy density of these electrodes significantly increase the overall electrochemical efficiency of the supercapacitor. To prepare this type of electrode material, a simple, inexpensive and convenient chemical route is important to maintain cost of supercapacitor cell. Among various other deposition methods, CBD and SILAR have many advantages. Also, these methods are generally used for large area deposition, which is beneficial for device fabrication.

The present work is focused on the fabrication of FSS-SCs devices using the MnO_2 thin films as flexible electrodes and PGEs as an electrolyte. These configurations of FSS-SCs will be tested for the usefulness of active electrode material on the device level. In present work first aim to synthesis of MnO_2 composite thin films by simple chemical methods and characterize these thin films with various physiochemical characterization techniques. In the synthesis of the electrode material, the preparative parameters like as concentration of precursor solution, pH of solution, temperature of the bath, time of deposition are optimized. The simple chemical methods (CBD and SILAR) can provide additive-less and binder-free thin film electrodes by improving the interfacial contact of active material and flexible stainless steel (SS) substrates. Also, corrosion and oxidation of metallic substrates can be restricted using low temperature deposition methods.

Furthermore, the well adherent and uniform MnO_2 composite thin films will be evaluated for phase analysis, structural clarification, compositional analysis, surface, and microstructural analysis will be carried out. The X-ray diffraction (XRD) technique will be used for the phase confirmation of material and chemical bonding in prepared material will be studied by fourier transform infrared spectroscopy analysis (FTIR). The surface morphological evaluation of thin film material will be carried out using the field emission scanning electron microscopy (FE-SEM) technique. The energy-dispersive X-ray spectroscopy (EDS) technique will be used for confirmation of elemental composition. The X-ray photoelectron spectroscopy (XPS) technique will be employed for the identification of chemical composition, and oxidation states. Transmission electron microscopy (TEM) study will be carried out for the particle size investigation of material. To further examine the specific surface area and pore size distribution of the electrode material, surface area analysis will be carried out using Brunauer-Emmett-Teller (BET) measurement. The electrochemical performances of the electrodes will be investigated by cyclic voltammetry (CV), galvanostatic charge-discharge measurement (GCD), and electrochemical impedance spectroscopy (EIS) using an electrochemical workstation.

1.4 References

- [1] K. Oldham, J. Myland, Academic Press Inc, New York, (1994), 1-496.
- [2] S. Chen, J. Zhu, X. Wu, Q. Han, X. Wang, ACS Nano., 4, (2010), 2822-2830.
- [3] X. Xie, K. Lee, J. Wang, K. Loh, Energy Environ. Sci., 4, (2011), 3960-3965.
- [4] J. Tao, N. Liu, W. Ma, L. Ding, L. Li, J. Su, Y. Gao, Sci. Rep., 3, (2013), 2286-2293.
- [5] J. Oh, H. Yuan, H. Branz, Nat Nanotechnol., 7, (2012), 743-748.
- [6] L. Feng, Y. Zhu, H. Ding, C. Ni, J. Power Sources, 267, (2014), 430-444.
- [7] A. Nishino, J. Power Sources, 60, (1996), 137-147.
- [8] Y. Xiang, S. Lu, S. Jiang, Chem. Soc. Rev., 41, (2012), 7291-7321.
- [9] C. Liu, F. Li, L. Ma, H. Cheng, Adv. Mater., 22, (2010), 28-62.
- [10] D. Dubal, N. Chodankar, D. Kim, P. Gomez-Romero, Chem. Soc. Rev., 47, (2018), 2065-2129.
- [11] http://commons.wikimedia.org/wiki/File:Capacitor_schematic_with_dielectric.svg. (accessed 2014-04-03).
- [12] P. Simon, Y. Gogotsi, Nat. Mater., 7, (2008), 845-854.
- [13] D. Dubal, J. Kim, Y. Kim, R. Holze, C. D. Lokhande, W. Kim, Energy Technol., 2, (2014), 325-341.
- [14] C. Lethien, J. Bideau, T. Brousse, Energy Environ. Sci. 12, (2019), 96-115.
- [15] A. Burke, J. Power Sources, 91, (2000), 37-50.
- [16] K. Han, Q. Wang, Elsevier Inc., Amsterdam, 10, (2012), 811-829.
- [17] H. I. Becker, Low voltage electrolytic capacitors. U.S., Patent, 2800616, (1957).
- [18] R. A. Rightmire, Electrical energy storage apparatus. U.S., Patent, 3288641, (1966).
- [19] B. Conway, J. Electrochem. Soc., 138, (1991), 1539-1548.
- [20] H. C. De Long, R. T. Carlin, U. S. Patent, 5,585,999 Dec., 17, (1996).
- [21] H. Heubauma, F. Biermannb, Energy Policy, 87, (2015), 229-239.
- [22] X. Lu, M. Yu, G. Wang, Y. Tong, Y. Li, Energy Environ. Sci., 7, (2014), 2160-2181.
- [23] S. Chang, Z. Zainal, K. Tan, N. Yusof, W. Yusoff, S. Prabakaran, Ceram. Int., 41, (2015), 1-14.
- [24] X. Lang, A. Hirata, T. Fujita, M. Chen, Nat. Nanotechnol., 6, (2011), 232-236.

- [25] J. Miller, A. Burke, *Electrochem. Soc Interface*, 17, (2008), 53-57.
- [26] X. Du, L. Wang, W. Zhao, Y. Wang, T. Qi, C. Li, *J. Power Sources*, 323, (2016), 166-173.
- [27] K. Jost, G. Dion, Y. Gogotsi, *J. Mater. Chem. A*, 2, (2014), 10776-10787.
- [28] G. Zheng, M. Chen, J. Yin, H. Zhang, X. Liang, J. Zhang, *Int. J. Electrochem. Sci.*, 14, (2019), 2345-2362.
- [29] V. Birss, B. Conway, J. Wojtowicz, *J. Power Sources*, 66, (1997), 1-14.
- [30] Q. Chen, Y. Meng, C. Hu, Y. Zhao, H. Shao, N. Chen, L. Qu, *J. Power Sources*, 247, (2014), 32-39.
- [31] Y. Qian, R. Liu, Q. Wang, J. Xu, D. Chen, G. Shen, *J. Mater. Chem. A*, 2, (2014), 10917-10922.
- [32] G. Snook, P. Kao, A. Best, *J. Power Sources*, 196, (2011), 1-12.
- [33] R. Rakhi, N. Alhebshi, D. Anjum, H. Alshareef, *J. Mater. Chem. A*, 2, (2014), 16190-16198.
- [34] Y. Shao, M. El-Kady, J. Sun, *Chem. Rev.*, 118, (2018), 9233-9280.
- [35] M. Hakamada, T. Abe, M. Mabuchi, *J. Power Sources*, 325, (2016), 670-674.
- [36] S. Tripathi, A. Kumar, S. Hashmi, *Solid State Ion.*, 177, (2006), 2979-2985.
- [37] D. Dubal, S. Lee, J. Kim, W. Kim, C. D. Lokhande, *J. Mater. Chem.*, 22, (2012), 3044-3052.
- [38] X. Du, X. Hao, Z. Wang, X. Ma, G. Guan, A. Abuliti, G. Ma, S. Liu, *Synth Met.*, 175, (2013), 138-145.
- [39] J. Zang, S. Bao, C. Li, H. Bian, X. Cui, Q. Bao, C. Sun, J. Guo, K. Lian, *J. Phys Chem C*, 112, (2008), 14843-14847.
- [40] J. Boback, A. Lewenstam, A. Ivaska, *J. Electroanal Chem.*, 489, (2000), 17-27.
- [41] L. Zhang, X. Zhao, *Chem. Soc. Rev.*, 38, (2009), 2520-2531.
- [42] Z. Fan, J. Yan, T. Wei, L. Zhi, G. Ning, T. Li, F. Wei, *Adv. Funct. Mater.*, 21, (2011), 2366-2375.
- [43] J. Wang, F. Kang, B. Wei, *Prog. Mater. Sci.*, 74, (2015), 51-124.
- [44] Q. Ren, Y. Zhang, H. Lu, Y. Wang, W. Liu, X. Ji, A. Devi, A. Jiang, D. Zhang, *ACS Appl. Mater. Interfaces*, 10, (2018), 468-476.
- [45] H. Xiao, S. Yao, H. Liu, F. Qu, X. Zhang, X. Wu, *Prog. Nat. Sci. Mater. Int.*, 26, (2016), 271-275.
- [46] V. Senthilkumar, Y. Kim, S. Chandrasekaran, B. Rajagopalan, E. Kim, J. Chung,

- RSC Adv., 5, (2015), 20545-20553.
- [47] U. Patil, S. Kulkarni, V. Jamadade, C. D. Lokhande, J. Alloys and Compd., 509, (2011), 1677-1682.
- [48] X. Zhang, X. Sun, H. Zhang, C. Li, Y. Ma, Electrochim. Acta., 132, (2014), 315-322.
- [49] D. Yan, Z. Guo, G. Zhu, H. Yang, R. Wei, H. Xu, Material let., 82, (2012), 156-158.
- [50] V. Subramanian, H. Zhu, R. Vajtai, P. Ajayan, B. Wei, J. Phys. Chem. B, 109, (2005), 20207-202014.
- [51] B. Sankapal, H. Gajare, S. Karade, R. Salunkhe, D. Dubal, Electrochim. Acta, 192, (2016), 377-384.
- [52] M. Sk, C. Yue, RSC Adv., 4, (2014), 19908-19915.
- [53] T. Xiong, T. Tan, L. Lu, W. Lee, J. Xue, Adv. Energy Mater., 8, (2018), 1-10.
- [54] J. Kang, A. Hirata, L. Kang, X. Zhang, Y. Hou, L. Chen, C. Li, T. Fujita, K. Akagi, M. Chen, Angew. Chem., Int. Ed., 52, (2013), 1664-1667.
- [55] Y. Yang, T. Liu, L. Zhang, J. Mater. Sci.: Mater. Electron., 27, (2016), 6202-6207.
- [56] D. Dubal, R. Holze, P. M. Kulal, J. Mater. Sci., 48, (2013), 714-719.
- [57] A. Patil, A. Lokhande, P. Shinde, C. D. Lokhande, ACS Appl. Mater. Interfaces. 10, (2018), 16636-16649.
- [58] N. Chodankar, G. Gund, D. Dubal, C. D. Lokhande, RSC Adv., 4, (2014), 61503-61513.
- [59] Y. Hu, H. Zhu, J. Wang, Z. Chen, J. Alloys and Compd., 42, (2011), 10234-10240.
- [60] Y. Hu, J. Wang, X. Jaiang, Y. Zheng, Z. Chen, Appl. Surf. Sci., 271, (2013), 193-201.
- [61] B. Singu, K. Yoon, J. Alloys and Compd., 695, (2017), 771-778.
- [62] M. Jana, S. Saha, P. Samanta, N. Murmu, N. Kim, T. Kuila, J. Lee, J. Power Sources, 340, (2017), 380-392.
- [63] A. Shaikh, M. Waikar, R. Sonkawade, Synth. Met., 247, (2019), 1-9.
- [64] G. Gund, D. Dubal, B. Patil, S. Shinde, C. D. Lokhande, Electrochim. Acta., 92, (2013), 205-215.
- [65] B. Li, X. Zhang, J. Dou, C. Hu, Ceram. Int, 45, (2019), 16297-16304.

- [66] X. Zhang, P. Yu, H. Zhang, D. Zhang, X. Sun, Y. Ma, *Electrochim. Acta.*, 89, (2013), 523-529.
- [67] M. Pang, G. Long, S. Jiang, Y. Ji, W. Han, B. Wang, X. Liu, Y. Xi, *Electrochim. Acta.*, 161, (2015), 297-304.
- [68] R. Kalubarme, H. Jadhav, C. Park, *Electrochim. Acta.*, 87, (2013), 457-465.
- [69] F. Li, Y. X. Zhang, M. Huang, Y. Xing, L. L. Zhang, *Electrochim. Acta.*, 154, (2015), 329-337.
- [70] D. Yan, Z. Guo, G. Zhu, Z. Yu, H. Xu, A. Yu, *J. Power Sources*, 199, (2012), 409-412.
- [71] S. He, C. Hu, H. Hou, W. Chen, *J. Power Sources*, 246, (2014), 754-761.
- [72] X. Su, L. Yu, G. Cheng, H. Zhang, M. Sun, X. Zhang, *Appl. Energy*, 153, (2015), 94-100.
- [73] D. Dubal, D. Dhawale, T. Gujar, C. D. Lokhande, *Appl. Surf. Sci.*, 257, (2011), 3378-3382.
- [74] D. Dubal, W. Kim, C. D. Lokhande, *J. Alloy Compd.*, 509, (2011), 10050-10054.
- [75] W. Yao, J. Wang, H. Li, Y. Lu, *J. Power Sources*, 247, (2014), 824-830.
- [76] Y. Li, X. Cai, W. Shen, *Electrochim. Acta.*, 149, (2014), 306-315.
- [77] Y. Zhang, J. Li, F. Kang, F. Gao, X. Wang, *Int. J. Hydrogen Energ.*, 37, (2012), 860-866.
- [78] T. Yousefi, A. Golikand, M. Mashhadizadeh, M. Aghazadeh, *J. Solid State Chem.*, 190, (2012), 202-207.
- [79] Q. Ye, R. Dong, Z. Xia, G. Chen, H. Wang, G. Tan, L. Jiang, F. Wang, *Electrochim. Acta.*, 141, (2014), 286-293.
- [80] B. Raj, A. Asiri, J. Wu, S. Anandan, *J. Alloys Compd.*, 636, (2015), 234-240.
- [81] D. Dubal, D. Dhawale, R. Salunkhe, S. Pawar, C. D. Lokhande, *Appl. Surf. Sci.*, 256, (2010), 4411-4416.
- [82] D. Dubal, D. Dhawale, R. Salunkhe, S. Pawar, V. Fulari, C. D. Lokhande, *J. Alloy Compd.*, 18, (2009), 218-221.
- [83] T. Yousefi, A. Golikand, M. Mashhadizadeh, M. Aghazadeh, *Curr. Appl. Phys.*, 12, (2012), 544-549.
- [84] D. Yang, *J. Power Sources*, 196, (2011), 8843-8849.
- [85] H. Xia, M. O. Lai, L. Lu, *J. Power Sources*, 196, (2011), 2398-2402.
- [86] J. Zhu, W. Shi, N. Xiao, X. Rui, H. Tan, X. Lu, H. Hng, J. Ma, Q. Yan, *ACS*

- Appl. Mater. Interfaces, 4, (2012), 2769-2774.
- [87] S. Sekhon, Bull. Mater. Sci., 26, (2003), 321-328.
- [88] J. Y. Song, Y. Y. Wang, C. C. Wan, J. Power Sources, 77, (1999), 183-197.
- [89] C. Liew, S. Ramesh, A. Arof, Int J. Hydrogen Energ., 39, (2014), 2953-2963.
- [90] G. Pandey, A. Rastogi, C. Westgate, J. Power Sources, 245, (2014), 857-865.
- [91] M. Lazzari, F. Soavi, M. Mastragostino, J. Power Sources, 178, (2008), 490-496.
- [92] G. Wang, L. Zhang, J. Zhang, Chem. Soc. Rev., 41, (2012), 797-828.
- [93] R. Rajagopal, K. Ryu, ChemElectroChem., 5, (2018), 2218-2227.
- [94] N. Chodankar, S. Ji, D. Kim, J. Taiwan Inst Chem Eng., 80, (2017), 503-510.
- [95] A. Reddy, M. Shaijumon, S. Gowda, P. Ajayan, J. Phys. Chem., C 114, (2010), 658-663.
- [96] N. Chodankar, D. Dubal, G. Gund, C. D. Lokhande, Electrochim. Acta., 165, (2015), 338-347.
- [97] S. Wang, B. Pei, X. Zhao, R. Dryfe, Nano Energy, 2, (2013), 530-536.
- [98] N. Chodankar, D. Dubal, G. Gund, C. D. Lokhande, J. of Energy Chem., 25, (2016), 463-471.
- [99] Q. Cai, J. Mao, Y. Li, J. Liu, H. Zhang, J. Huang, T. Wu, Y. Yang, C. Yuan, L. Dai, J. Mater. Chem. A, 8, (2020), 14254-14264.
- [100] P. Sun, H. Yi, T. Peng, Y. Jing, R. Wang, H. Wang, X. Wang, J. of Power Sources, 341, (2017), 27-35.
- [101] V. Mane, D. Malavekar, S. Ubale, R. Bulakhe, Insik In, C. D. Lokhande, Electrochim. Acta., 335, (2020), 135613-135630.
- [102] Y. Jin, H. Y. Chen, M. H. Chen, N. Liu, Q. W. Li, ACS Appl. Mater. Interfaces, 5, (2013), 3408-3416.
- [103] W. Zilong, Z. Zhu, J. Qiu, S. Yang, J. Mater. Chem. C, 2, (2014), 1331-1336.
- [104] N. Yu, M. Q. Zhu, D. Chen, J. Mater. Chem. A, 3, (2015), 7910-7918.
- [105] K. Wang, P. Zhao, X. Zhou, H. Wuab, Z. Wei, J. Mater. Chem., 21, (2011), 16373-16378.
- [106] W. Liu, X. Li, M. Zhu, X. He, J. Power Sources, 282, (2015), 179-187.
- [107] B. Choi, S. Chang, H. Kang, C. Park, H. Kim, W. Hong, S. Lee, Y. Huh, Nanoscale, 4, (2012), 4983-4988.

CHAPTER-2

THEORETICAL BACKGROUND OF CBD, SILAR METHODS AND THIN FILM CHARACTERIZATION TECHNIQUES

CHAPTER-2

Theoretical Background of CBD, SILAR Methods and Thin Film Characterization Techniques

Sr. No.	Title		Page No.
2.1	Introduction		26
2.2	Thin film		26
2.3	Thin film deposition methods		27
	2.3.1	Theoretical background	27
	2.3.1.1	Chemical bath deposition (CBD) methods	30
	2.3.1.2	Thin film deposition mechanisms of CBD method	31
	2.3.1.3	Preparative parameters of CBD method	32
	2.3.1.4	Advantages of CBD method	33
	2.3.2.1	Successive ionic layer adsorption and reaction (SILAR) method	33
	2.3.2.2	Preparative parameters of SILAR method	36
	2.3.2.3	Advantages of CBD method	37
2.4	Thin film characterization techniques		37
	2.4.1	Thin film thickness measurement	37
	2.4.2	X-ray diffraction (XRD) study	38
	2.4.3	Fourier transform-infrared spectroscopy (FT-IR)	39
	2.4.4	X-ray photo emission spectroscopy (XPS)	40
	2.4.5	Field-emission scanning electron microscopy (FE-SEM)	41
	2.4.5.1	Scanning process and image formation in SEM	43
	2.4.6	Transmission Electron Microscopy (TEM)	43
	2.4.7	Brunauer-Emmett-Teller (BET) theory	45
2.5	Electrochemical techniques		46
	2.5.1	Cyclic voltammetry (CV)	47
	2.5.2	Galvanostatic charge-discharge (GCD)	48
	2.5.3	Electrochemical impedance spectroscopy (EIS)	49
2.6	References		51

2.1 Introduction

The scientific curiosity and utility of thin films are two-dimensional solids for the massive interest in the analysis of science and technology. The practical development of thin-film is convenient and inexpensive by depositing material on the substrate. The attraction of thin-film devices over bulk materials, because of the low material utilization, easy processing and the practicable use of flexible substrates is increased [1]. The needed properties and flexibility can be attained by selecting a suitable deposition method for thin films. The thin layers of deposited materials are atom-by-atom, ion-by-ion, and molecule-by-molecule with a group of condensation [2]. The two-dimensional classified responsible for the natures of the materials are the physio-chemical properties of the thin-film materials. Thin films are used for technology that has been developed in the field of optics, sensors, electronics, energy storage devices and magnetism [3]. The requirements of innovative and improved thin solid films are one element as well as binary and ternary compounds with controlled parameters and properties.

2.2 Thin film

The thin solid system at the main two dimensional classifies is known as “thin film”. The solid film thickness in the third dimension is lower than the two dimensions. The thin film properties are often differing from the bulk to surface interface effects, which control the overall performance of the films. The films are used for various fields (solar cell, narrowband filter, photo-detectors, electrochemical electrodes, superconductivity, battery electrodes, hard coatings, magnetic films and wear resistance etc.).

2.2.1 Thin Film Technology

Modern technology needs several categories of films for various applications as superconductivity, optical coatings, surface science, microelectronics and magnetism [4]. The films application for the development of communication, informatics, VLSI/GSI and solar energy conversion of microscience related with low dimensional micro and nanomaterial [5]. The films can have different forms such as one or multi-component, alloy/compound or multilayer coatings on substrate of various sizes and shapes [5]. The thin films application of desired properties such as high optical reflection/transmission, wear resistance, hardness, single crystal structure can be

controlled by thin film deposition [6]. The technology of thin films less than 1 micron thickness has made great advances in the last decade. The development increases of thin film technology and industrial demands of reliable films to fulfil the urgent requirements for microelectronic devices. The basic and applied research progress the development and scientific confidence are used for thin films. The addition of new areas of research in the chemistry and solid-state physics of thin films are based on characteristics of the structure, geometry and thickness of films [7].

2.3 Thin film deposition methods

There are two main methods used for the synthesis of thin films that can classify into physical and chemical methods. The physical methods entail vacuum evaporation and sputtering [8, 9]. The chemical methods are subcategories of liquid and gas phases, which are further classified into chemical vapour deposition (CVD) [10], Photo CVD, Laser CVD, chemical bath deposition (CBD) [11], electrodeposition [12] etc. The physical methods have disadvantages such as control of boat temperatures, deposition of the large area, high cost and require must of advanced instruments. The chemical methods are comparatively inexpensive, simple and large scale deposition processes. In these methods concentration of deposition of temperature, solution of pH and deposition of time can be easily controlled. The broad classification of film deposition methods is depicted in **Chart 2.1**.

2.3.1 Theoretical background

1. Concept of solubility and ionic product

The amount of soluble salt XY, in water, forms a saturated solution with X and Y ions in contact with undissolved solid XY and an equilibrium is established in the solution as follows,



From the law of mass action,

$$K_c = \frac{C_{X^+} C_{Y^-}}{C_{XY}} \quad (2.2)$$

Where, C_{X^+} , C_{Y^-} and C_{XY} are the concentrations of X, Y and XY, respectively. The concentration of solid XY is a constant i.e. $C_{XY} = \text{a constant say } K_0$. Therefore, equation (2) becomes,

$$K_c K_0 = C_{X^+} C_{Y^-} \quad (2.3)$$

K_c and K_0 are constant

Therefore, product $K_c K_0 = K_s$ is also constant.

$$K_s = C_{X+} C_{Y-} \quad (2.4)$$

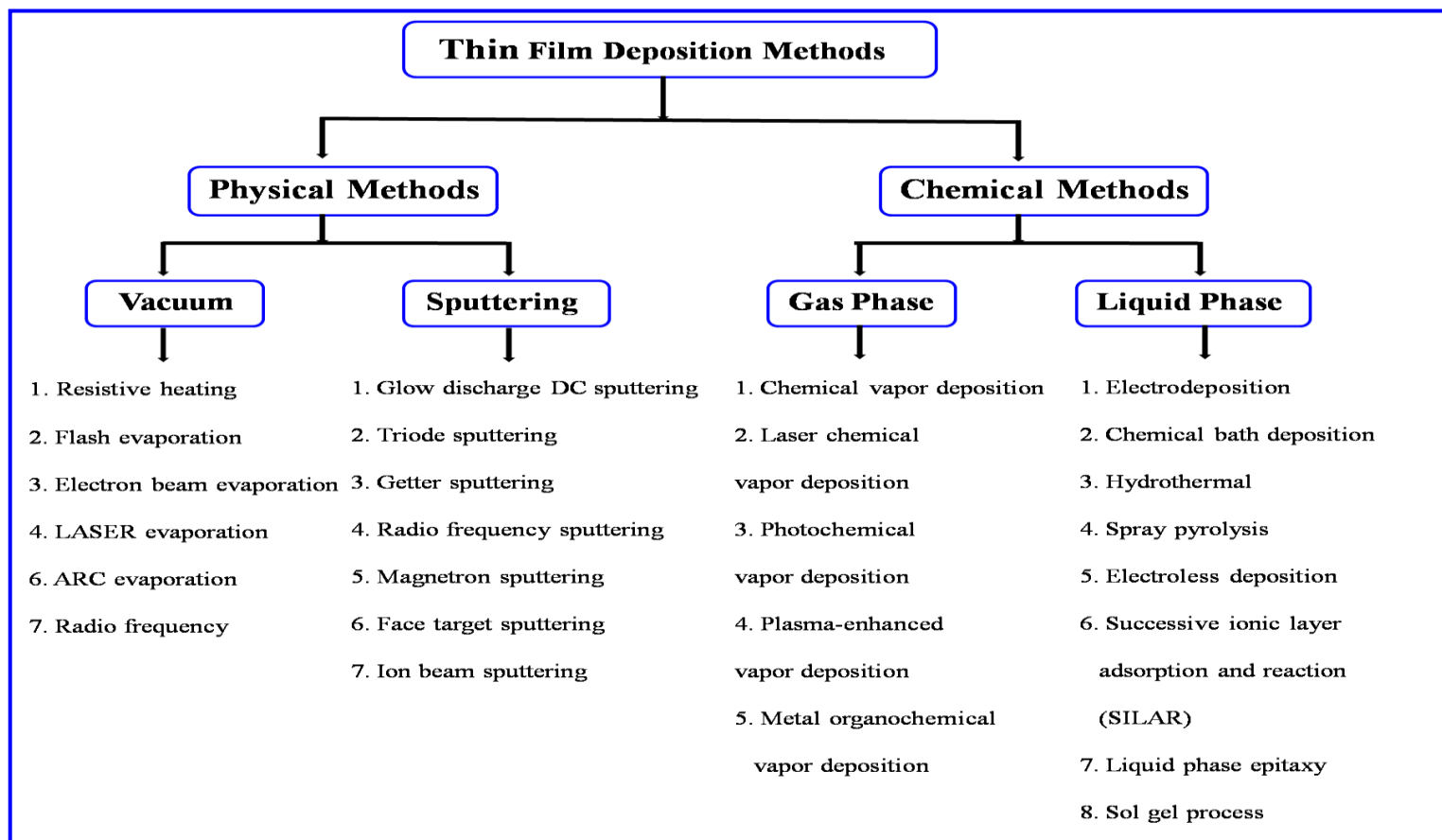
The constant K_s is called solubility product (SP) and $(C_{X+} C_{Y-})$ is called ionic product (IP).

If IP is equal to the SP the solution is in the saturated state. As, if the IP of ions exceeds the SP i.e. the solution becomes supersaturated. In this case, ions merge on the substrate and in the solution to form nuclei. The solvent, temperature and particle size are three significant parameters that affect the SP [13]. The direction of solubility can be changed by temperature. The equilibrium between a precipitate and its corresponding ions in solution allows shift accordingly to either the endothermic or exothermic reaction of the solution. For lower dielectric constant solvent, the solubility of the moderately insoluble substance in water can be reduced by the addition of alcohol or some other water miscible solvent. Particle size decreases and an increase in solubility.

2. Formation of precipitate in the solution

The particle size of a precipitate is distinct to a certain extent by the experimental conditions, superior at the time of its formations. The rate of addition of complexing agents, temperature, reagents concentration and solubility of precipitate at the reaction is affecting particle size. These are associated with the comparative supersaturation of the process. The conditions of supersaturation can be achieved by the lower reaction temperature of an unsaturated solution of the solute in the solutions [14]. The rate of nuclei form in a solution depends on the rate of supersaturation. The nucleation rate increases exponentially in the higher supersaturated solution [13].

Chart 2.1) Classification of thin film deposition methods.



2.3.1.1 Chemical bath deposition (CBD) method

The ordered by consideration of facile, inexpensive, large area thin films are deposited by chemical techniques. Spray pyrolysis, electrophoresis, electrodeposition, dip coating, anodization and chemical bath deposition are some of the chemical techniques for the deposition of thin films from the liquid phase. It is carried out exclusive of refined instrumentation such as a vacuum system with expensive types of equipment [13]. The glass beaker, hot plate and one stirrer can start the deposition process. The primary chemicals are generally accessible and are low-cost materials. The large numbers of any type of substrates are deposited in a single run from chemical deposition. The electrical conductivity of the substrates is not a necessary condition in chemical deposition [13]. Schematic representation of CBD method is depicted in **Fig. 2.1**.

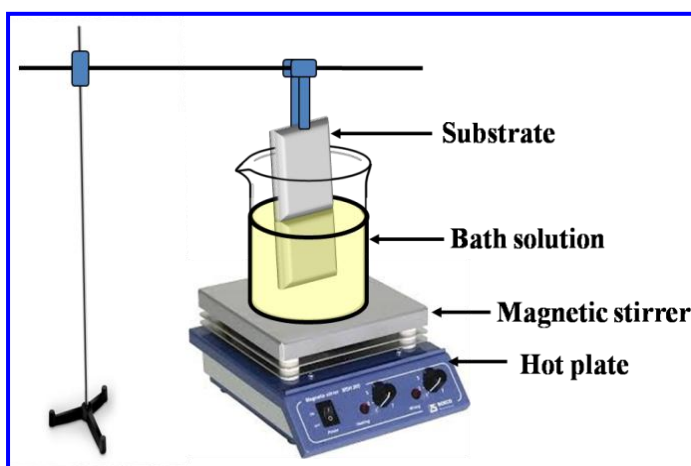


Fig. 2.1) Schematic diagram of CBD method

Consequently, any insoluble surface having free entrance of solution will be coated appropriately using the CBD method. It is a low temperature thin film deposition method; it avoids corrosion of the metallic substrate. The CBD produces uniform pinhole-free material depositions as the solution from which are deposited on the substrate. The stoichiometric formation can be easily achieved since the basic buildings block of thin-film deposition are ions as an alternative to atoms. The preparative factors can be easily restricted and superior direction with enhanced grain structure can be easily gained. There are two main steps included in the deposition of thin film which are particle growth and nucleation. The particle size depends on the precipitate, a number of the molecules and ions essential to create a stable solid phase interact with the solution, called as nucleus [14]. The nucleation arrangement is required for a precipitate formation.

The nucleation conception in solution is the quick corrosion of produced clusters particles and molecules which are collective grown up a reliable film thickness [14]. The deposition of thin film condition depends on the solution concentration, pH, stirring rate and bath temperature. The films growth takes place either by adsorption of colloidal particles and ion-by ion on the substrate. The CBD method is used for deposition of many binary compounds such as MnO, PbO, CuO, Bi₂S₃, CdSe, PbSe, CdS, MoS₂, Ag₂S₃, ZnS, PbS, CuS etc. and ternary compounds such as CdPbSe, CdSSe, CuInSe₂, ZnCo₂O₄, Cu₂SnS₃ etc.

2.3.1.2 Thin film deposition mechanisms of CBD method

There are four possible mechanisms for the thin film deposition depending on the specific procedure and reaction parameters [15].

(1) Ion-by-ion formation

In this method, the ‘ion-by-ion’ mechanism concludes to be the effective one and sequential ionic reactions. The common reaction mechanism is as follows,



The thin film formation of M_mX_n compound is based on the principle of the exceed of ionic product $[M^{n+}] [X^{m-}]$ over the solubility product K_{sp} of M_mX_n , as M_mX_n forms a solid phase. The higher ionic product may be necessary for supersaturation. When ionic product does not pass K_{sp} , no solid phase is created, exceptionally owing to limited variations in the solution. The small solid nuclei dissolve before increasing to a fixed size. Consequently, the reaction is a balancing procedure relatively one-way reaction compound is based on the principle of the exceed of

(2) Cluster (hydroxide) mechanism

The preparative conditions in CBD process are so preferred that the formation of metal hydroxide is avoided. The CBDs are commonly carried out under such conditions, where a metal hydroxide and hydrated oxide are unavoidable. It seems to imply that a precipitate of metal hydroxide $[M(OH)_n]$ is formed at the primary stage in the CBD process. This metal hydroxide formed is either as a colloid than a precipitate and as an adsorbed species on the substrate and not in the bulk of the solution. Here, the metal chalcogenide (M_mX_n) is created by the reaction of the X^{m+} ion with the $M(OH)_n$.



Which follows as,



(3) Complex-decomposition ion-by-ion formation

In this mechanism, the complication of free metal cations (M^{n+}) by thiourea provides M^{n+} thiourea compound ion. This mechanism is useful in acidic solution as thioacetamide decomposition happen at an intermediate pH values, mostly in weak acidic solution ($pH > 2$) has been advised to happen through a thioacetamide compound, than through intermediate sulfide formation.

(4) Complex-decomposition cluster mechanism

The compound decomposition cluster mechanism is functioning on the creation of solid-phase particles as an alternative to directly responding with a free anion. It is the form of an intermediate compound with the anion form reagent. The catalytic result of the solid surface can be the decomposition of thiourea to sulphide species and not catalyze the compound decomposition process.

2.3.1.3 Preparative parameters of CBD method

The various preparative parameters, which limit thin film formation in the CBD method, are clarified in details as follows,

(1) Substrate: The thin film is deposited on the substrate with two states, one at optimized states for metal ion (M^+) and anions (X^-) compound. The second state is based on a single crystalline substrate, which are gives the required condition for the deposition of material. The thin film of the MX complex will be created and the lattice structure is coordinated with the substrate material itself.

(2) Effect of anion concentration: The film thickness of the MX compound increases with anion source concentration. At high concentration, deposition rate of compound MX is enhanced to very high amount so that homogeneous precipitation in the solution becomes in large amount creating less film thickness.

(3) pH of solution: At low pH values, the amount of supersaturation is increased, which so preferred reaction rate of M and X ions to form larger film thickness at low temperature besides.

With increasing pH value, supersaturation decreases to that extent, so that at low temperature very few M and X ions are free to provide MX compound. Therefore, no thin film is formed. With enhancing temperature, the supersaturation rate increases, this increases higher reaction rate and film growth.

(4) Concentration of complexing agent: The function of a complexing agent in this method is to provide ligand to M, which maintains them to form the unsaturated solution. Hence, enhancement in the concentration of complexing agent reduces free metal ion absorption. This decreases film thickness growth rate but increases terminal thickness of film.

(5) Temperature: The metal ion (M^+) and anion (X^-) dissociate at higher rates with enhance in temperature in solution bath. Consequently, at higher temperature of solution M and X ions dissociation rate is more providing rise to more thickness of film, which depends on supersaturation of the solution.

2.3.1.4 Advantages of CBD method

- The great flexibility in substrate selection and drastically decreased manufacturing cost.
- The low temperature processing and possibility for large area depositions.
- Safe process with less ecological danger.
- High reproducibility rate.
- Minimum wastage.

2.3.2.1 Successive ionic layer adsorption and reaction (SILAR) method

In the 1980s, SILAR method was developed to deposit several compound thin films [16, 17]. The comparable SILAR method was reported for the preparation of metal oxide thin films by Ristov et al [18]. The distinctive feature of SILAR is that, it contains of alternative aqueous cationic and anionic solution baths. In principle, it is predictable to grow thin film using an ion-by-ion mechanism through successive adsorption and reaction of a single atomic layer.

In this chemical method, a thin film is produced on a substrate when heterogeneous precipitation occurred on a surface. The chemical method results in the avoidable formation of precipitate in solution. The actual used and schematic representation of the SILAR method as depicted in **Figs. 2.2 and 2.3**. In the SILAR method, thin films are deposited from the inclusion of a substrate in separately located cationic and anionic precursors, and the substrate is rinsed with ion-exchange water through every immersion.

The basic and theoretical background of SILAR is explained in detail in the review article of Pathan and Lokhande [19]. The SILAR method depends on adsorption followed by reaction of ions in a solution and rinsing in DDW during each

immersion to avoid homogenous precipitation. The adsorption is a crucial factor of the SILAR method. It is anticipated that contacts between heterogeneous phases accelerate the growth of materials. Therefore, there are three adsorption systems of liquid-solid, gas-solid and gas-liquid. The SILAR process based on the adsorption in a liquid-solid system. The adsorption is a surface phenomenon (exothermic) facilitated by attractive or chemical forces between solution ions on the surface of a substrate. The cations adsorbed on substrate surface leads to the growth of a monolayer. In this reaction, the adsorbed ion reacts with desired anions leading to the monolayer formation of the desired material. The repeating such cycles, layer-by-layer formation of thin film takes place on the substrate surface. The adsorption process is highly affected by the physical parameters like the nature of the substrate, concentration of the solution, temperature, area of the substrate etc., thus physico-chemical characteristics of a thin film can be changed by varying the above parameters. The SILAR method can form a thin nanocrystalline compact layer over conducting and non-conducting substrates.

In the manually operated SILAR method, the researcher requires to immerse substrate for numbers of cycles in the solution and water. Therefore, it is relatively difficult to manage the time and number of cycles in the manually operated SILAR method. In the automatic unit, the researcher only requires to suspend substrate in a holder and program for necessary dip cycles and duration. The SILAR equipment (Holmarc Opto-Mechatronics Pvt Ltd. India, Model: HO-TH-03A) consists of six beakers on the circular metal tray, of 100 ml each (see Fig. 2.2). Every rinsing beaker can be placed between cationic and anionic salt solutions. After that, substrates can be set on the line with the help of vertical tweezers and maintain on the spindle. The spindle rotates and slides into the Teflon bearing driven by a stepping motor. The retrieval speed as well as period can be set for each beaker. The vertical movement of the spindle is variable; it has different rotation speeds (1-200 rpm) [20].

The SILAR method consists of four beakers system, which is generally used for deposition of binary metal oxide, metal chalcogenides and sulfides formation of thin films. The schematic represents of a SILAR method is shown in Fig. 2.3. In the present work, the coating involves four steps: (I) adsorption of cations from a cationic solution, (II) rinsing for removal of weakly adsorbed ions in DWW, (III) reaction with

anions from the anionic bath and (IV) rinsing for eliminated of weakly bounded ions in DWW.



Fig. 2. 2) Photograph of programmable SILAR coating system used for deposition of thin films.

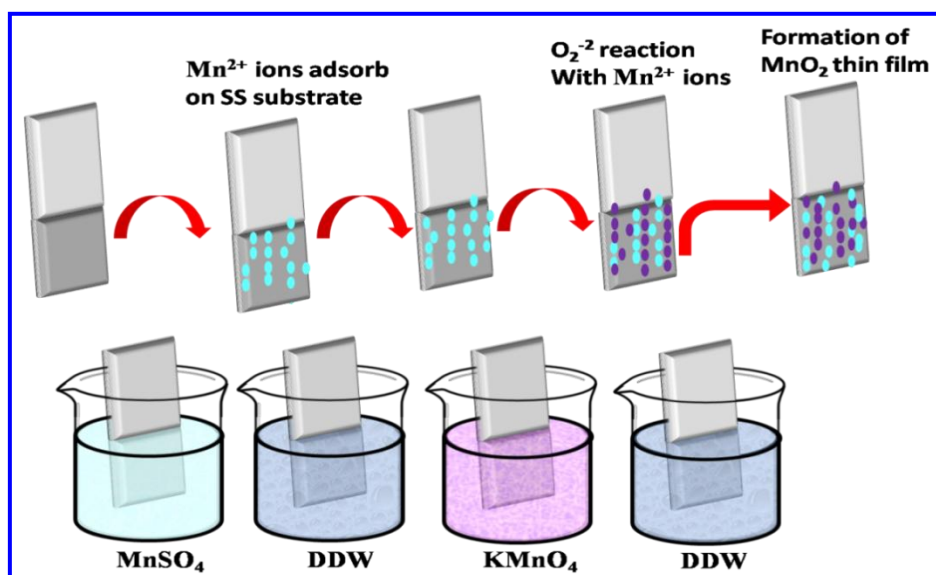


Fig. 2.3) Schematic diagram of SILAR method.

The SILAR methodology is relatively new and less studied, which is based on a consecutive reaction on the substrate surface using various precursors. The rinsing follows every reaction, which enables a heterogeneous reaction between the solid phase and the solvated ions in the solution. The SILAR method entails four steps:

(1) Adsorption: In the SILAR method, the cations represent in the precursor solution are adsorbed on the SS substrate and formation the electric double layer. This layer consists of two layers: the inner (positive charge) and outer (negative charge) layers. The positive layer involves the cations with the negative layer form and opposes the cation ions.

(2) First rinsing: In first rinsing, the loosely bounded ions are rinsed further than the diffusion layer. This effect into saturated electrical double layer.

(3) Reaction: In this step, the chemical interaction among solvated adsorbed cations and anions by immersing the substrate in the solution causes growth of material. Due to the less stability of ions reaction between cation and anion takes place leading to formation of solid phase over substrate.

(4) Second rinsing: In this step, the surplus and unreacted ions and the reaction results as of the diffusion layer are eliminated.

In this method, the adsorption of cations and reaction of anions with preadsorbed cations leads to the deposition of the thin film of required material.

2.3.2.2 Preparative parameters of SILAR method

The deposition rate and thickness depend on the adsorption and reaction time in the solution. The kinetics growth depends the adsorption, time, complexing agent, temperature, rinsing time, pH and concentration of ions. The effect of different deposition conditions as follows:

(1) Concentration of ions: With an increase in precursor concentration, the 'C' and 'D' ion concentration enhances and yields a film of 'CD' with a higher thickness. Moreover, the reaction rate is higher for a high concentration of cation and anion, which leads to enhance in homogeneous precipitation and results in deposition of low 'CD' on the substrate. Therefore, the thickness of film reduces at a high concentration of precursors. Stoichiometric deposition of material can be achieved by varying precursor concentrations.

(2) Rinsing time: In a rinsing bath, the weakly bonded species detached from a substrate surface. A good quality film can be prepared by adequate rinsing time, which is free from unreacted species and loosely bonded compounds.

(3) Temperature: The increases in temperature give driving force to enhance the ion mobility with respective electrode that improved the conductivity of bath solution. The further result is a rise in crystalline size with the reduction in polarization outcomes at a higher temperature. Therefore, with enhanced current density, it is probable to achieve smooth and thin particles deposited at high temperatures. The temperature should be optimized.

(5) Complexing agent: The significant function of complexing agent is to control the delivery of free metal ions for reduction and metal ions buffers. Hence, kinetics growth

rate can be restricted using the complexing agent. The metal ion concentration reduces with raise in complexing agent, hence precipitation and rate of reactions are reduced. The complexing agents of the complex compound provided as a reticent and constant supply of the simple ions required for the discharge at the cathode takes place. The lower metal ion concentrations enable the formation of deposits with small particles and increase the delivering power.

2.3.2.3 Advantages of SILAR method

- The comparatively uniform films can be deposited on any kind of substrates having complex formation.
- The films thickness, deposition rate and morphology can be efficiently restricted by the various preparative conditions.
- The apparatus required is not expensive and does not entail refined equipments and vacuum.
- The method is cost effective and conserves material with it is efficient for deposition over a large area.
- This method is very feasible to dope any elements with the required proportion in the film.
- The method is generally employing at low temperature because various kinds of substrate like metals, semiconductor, insulator and polymer can be used. This prevents corrosion and oxidation of metallic substrates.
- Drawbacks like contamination, interdiffusion, and dopant redistribution, due to the high temperature deposition method can be avoided.

Along with exceeding advantages, SILAR has a fascinating feature that materials can be deposited from aqueous and non-aqueous bath.

2.4 Thin film characterization techniques

The most important is to characterize the sample before their implantation in appliance. The various characterizations include the structural, morphological and surface area. Which required XRD, FT-IR, XPS, FE-SEM, contact angle, and BET surface area techniques.

2.4.1 Thickness measurements:

The deposited thin film of thickness is a very significant parameter for the physical and optical properties of material (band gap, electrical conductivity and conversion efficiency for solar cell application). The film thickness is measured using

different methods such as, gravimetric, direct and optical methods. The area and mass of thin films are measured in this method. Out of these methods gravimetric is simple method, in which one can easily calculate film thickness using following formula [21],

$$t = \frac{M.A}{\rho} \quad (2.8)$$

$$M = m_1 - m_2 \quad (2.9)$$

Where, M , t , A , m_1 , m_2 and ρ are the mass, thickness, area of film, mass of substrate with film and without film and density of film material, respectively. The value of bulk material is generally taken as the bulk density of material in thin film form is smaller. This method is destructive and real density of material varies thin film material.

2.4.2 X-ray diffraction Technique (XRD)

The XRD is a powerful analytical technique used to identify the crystalline phases present in materials and to measure the structural properties (strain, grain size, epitaxial, phase composition, preferred orientation and defect structure) of these phases. The films are amorphous, crystal and polycrystalline structures. The intensities measured with XRD can provide quantitative, accurate information on the atomic arrangements at interfaces (e.g. in multilayers). The XRD is based on constructive interference of monochromatic X-ray and crystalline film. The x-rays are generated by a cathode ray tube, filtered to produce monochromatic radiation, collimated to concentrate and directed toward the sample. The interaction of the incident beam with crystal sample produces constructive interference and diffracted rays are called as Bragg's law [22].

Assume I_1 , I_2 and I_3 is incident beam on the parallel atomic planes of any material, making an opaque angle θ and d is interplanar spacing as depicted in **Fig 2.4**. Further, that the I_1 , I_2 and I_3 x-rays scattering as follows PT_1 , PT_2 and PT_3 path difference. This path difference rays PT_1 , PT_2 equal to $QS + SR$. Therefore, $QS + SR = 2d\sin\theta$ for the constructive interference patterns. The path difference between rays should be equal to integral multiple of wavelength.

$$2d\sin\theta = n\lambda, \quad (2.10)$$

Where, λ is the wavelength of monochromatic X- ray, n is the order of diffraction, θ is the diffraction angle and d is the lattice spacing, respectively. The 'd' values are calculated using above relation for known values of λ , n and θ , respectively.

Bragg's law relates the wavelength of electromagnetic radiation to the diffraction angle and the lattice spacing in a crystalline phase.

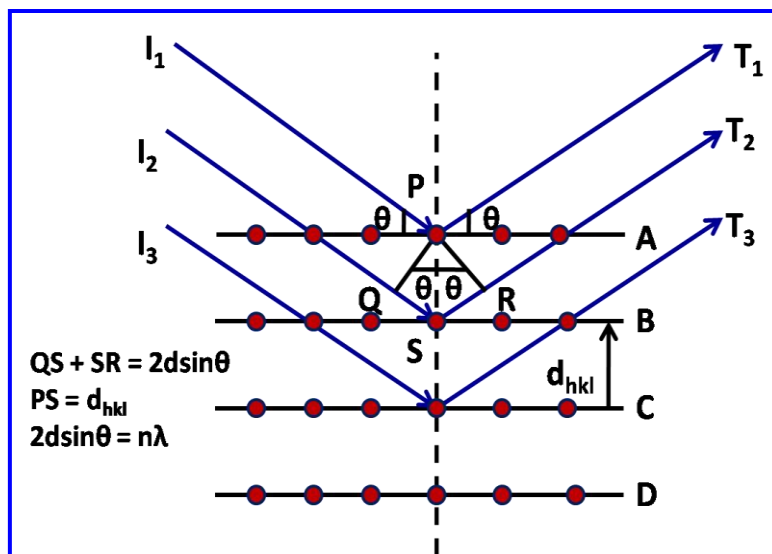


Fig. 2.4) Principle of Bragg's law of diffraction [22].

The XRD data thus obtained are compared to Joint Committee of Powder Diffraction Standards (JCPDS) powder diffraction to the identification of unknown materials. The sample used may be a thin film, powder or single crystal. The crystal size 'D' of the sample is determined through the full width at half maxima of the most intense diffraction plane using Scherrer's equation as [23].

$$D = \frac{K\lambda}{\beta \cdot \cos\theta} \quad (2.11)$$

Where, λ , β , θ and K are wavelength of X-rays, full width of half maxima of peak intensity and Bragg's angle and constant, respectively.

2.4.3 Fourier- Transform Infrared Spectroscopy (FT-IR)

The FTIR is a powerful technique for identifying the functional group and covalent bond information. The spontaneous orientation of the dipole moment materials is studied by the non-destructive tool using infrared spectroscopy that can provide information about inter-atomic forces within the crystal lattice. There are six different ways an organic/inorganic compound can vibrate; symmetrical and anti-symmetrical stretching, wagging, rocking, scissoring and twisting [24]. FTIR spectrometer; Alpha (II) Bruker model is used for characterization and ray diagram of the FTIR displayed in **Fig. 2.5**.

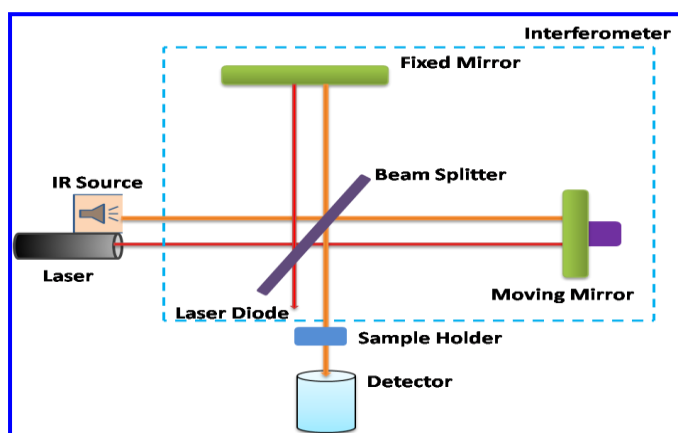


Fig. 2.5) The basic ray diagram of the FTIR spectrometer [24].

The infrared vibrational frequencies with inter-atomic forces correlated and so it is used to investigate functional groups in the material. According to the Planck-Einstein relation, energy transfer between different energy states of molecules can be written as the following equation,

$$\Delta E = h\nu \quad (2.12)$$

Where, h is the Planck constant and ν is frequency. The positive ΔE means the molecule absorbs energy, when ΔE is negative means it emits energy in form of radiation and this emission spectrum is obtained.

When eq. 2.12 is satisfied, an absorption spectrum is obtained, which is a particular molecule under investigation. The spectrum is normally presented as an intensity plot versus frequency and absorption peaks obtain, when eq 2.12 is satisfied. A spectrum close to a visible region comparatively small portion is used for spectroscopic investigations. This portion incorporates UV-Visible and IR regions (1 mm to 10 nm). The different absorption spectra can be observed from atoms and molecules because of the nature of energy levels in transition [25]. The transition of electrons between orbitals of atoms takes place due to the absorption of energy. However, the atoms vibrate in a molecule and it moves due to the absorption of energy [26]. A few transition energies such as rotational, vibrational and electronic are possible to measure. Usually, translational energy can be ignored since it is sufficiently small. The vibrational spectrum is believed to be the unique physical characteristic of molecules. Therefore, the IR spectrum is supposed as a fingerprint for the identification of material [27].

2.4.4 X-ray photoelectron spectroscopy (XPS)

The XPS is the highly sensitive spectroscopic technique, which can identify the surface composition and chemical oxidation states of the elements present in the materials.

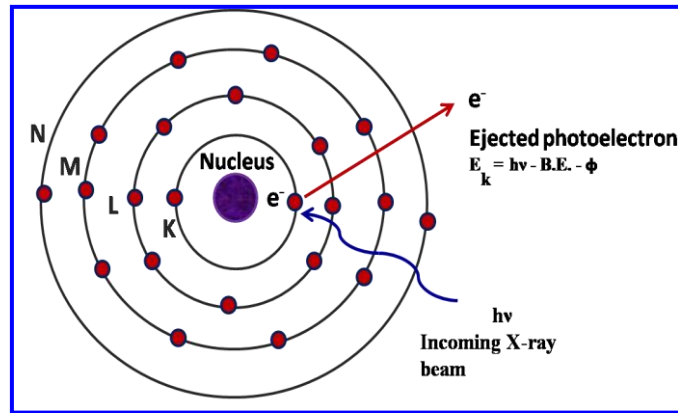


Fig. 2.6) Emission of photoelectron radiations in the XPS measurement [28].

The XPS working by irradiating sample material with a monoenergetic electron beam to be emitted. The working of XPS is based on the principle of photoelectric intensities can be determined by the following equation,

$$E_k = h\nu - B.E. - \phi \quad (2.13)$$

Where, E_k , $h\nu$, B.E. and ϕ are the kinetic energy of emitted photoelectron, the energy of incident x-ray photon, binding energy of electron shell and spectrometer work function, respectively [28].

Usually, the procedures of executing XPS spectroscopy, sample surface are most regularly used x-ray sources Mg $K\alpha$ ($h\nu = 1253.6$ eV) and Al $K\alpha$ radiations ($h\nu = 1486.6$ eV), which sources emission of photoelectron from the sample surface as depicted in **Fig. 2.6**. The electron energy analyzer is to measure the energy of the released photoelectrons. The kinetic energy of these emitted electrons is the element from which the photoelectrons are created. The point and intensity of peaks in an energy spectrum give the quantitative details and required chemical state. The B.E. and photoelectron peak intensity, chemical state and the elemental identity of elements can be determined. The basic requirements of the photoelectron emission experiments are the electron energy analyzer measure the electron flux of energy, x-ray radiation source and vacuum condition for photoelectrons study without disturbance as of gas molecule collision.

2.4.5 Field Emission-Scanning Electron Microscopy (FE-SEM)

The FE-SEM investigates the structure of thin film by bombarding the electron beam with the scanning sample and accumulates slow-motion secondary electrons that

the specimen produces. Hence, secondary electrons are collected, amplified and demonstrated on the computer monitor. The SEM is usually used to study the external structure of targets that are as diverse as samples, metals, rocks and ceramics can be observed in the light microscope. The SEM is a class of electron microscope that pictures of specimen surface by scanning it with high energy electrons in examined patterns. The electron beams interconnect with the atoms those generating signals to contain details about the sample composition, surface topography, and electrical conductivity properties. The various types of signals generated by an SEM involve have backscattered electrons (BSE), secondary electrons, characteristic x-rays, transmitted electrons and light specimens. This type of signal all needs specific detectors for their detection. The signals affect the interaction of the electrons with atoms on the surface of the sample. The most common and standard detection mode is secondary electrons. The SEM can generate very high-resolution images on the specimen surface, shows the information about 1 to 5 nm in size. These SEM micrograph images have a very large depth of field, which is helpful for recognizing the surface structure of the specimen.

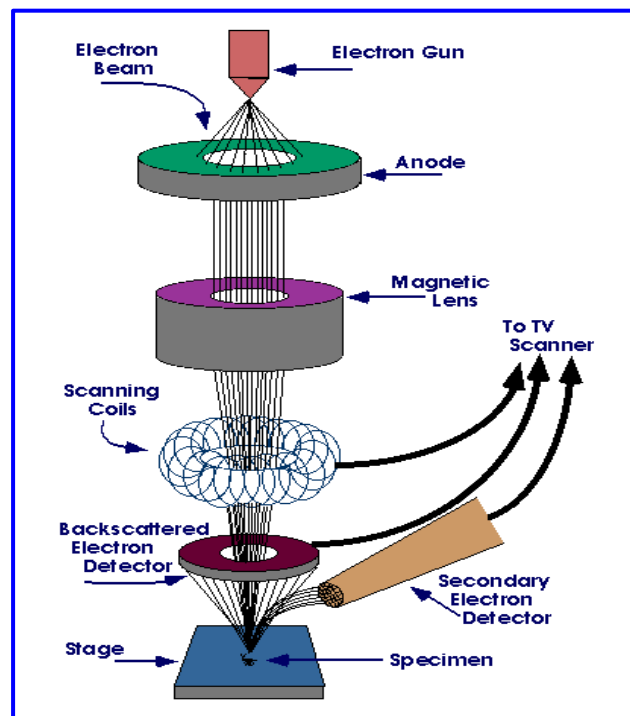


Fig. 2.7) Schematic of electron path approaching from various components of FE-SEM [29].

The possible extensive range of light microscope is ranging about 25 to 250,000 magnification limits. The back scattered electron (BSE) is electron beams that are transmitted from the specimen by elastic scattering. The BSE is frequently used in

investigative SEM along with the spectra prepared from the attribute to x-rays. The intensity of the BSE signal is powerfully associated with the atomic number (Z) of the sample and BSE images can provide details about the division of various elements in the specimen. The same reason BSE imaging can image colloidal gold immune-labels. The characteristic X-ray is transmitted when the beam of electron eliminates an inner shell electron from the specimen, reason a high energy electron to load the shell and free energy. These characteristics are used to recognize the composition and evaluate the profusion of elements in the specimen [29]. Schematic diagram of electron path through various component of FE-SEM is shown in **Fig. 2.7**.

2.4.5.1 Scanning process and image formation in SEM

In the usual SEM, a source of electrons beam is emitted from an electron gun fixed with a tungsten filament. These are two types of emission sources: thermionic and field emitter. The tungsten is generally used in thermionic electron guns since it is inexpensive, low vapour pressure and a high melting point of all metals. The electron field emitters contain lanthanum hexaboride (LaB_6) are used in normal tungsten filament. Typically, the electron beam has an energy range of 500 eV to 40 keV, is focused via two condenser lenses to spot about 0.4 to 5 nm in diameter. The electron passes through couples of scanning coils and couples of deflector plates in the electron column and scanning area of the sample surface. The primary electrons interact with the samples; the electrons lose energy through repetitive scattering and absorption, which expand from less than 100 nm to 5 μm into the surface. The energy changes between electrons and the sample effect in the reflection of high-energy electrons through resilient scattering. The electronic amplifies of different classes are used to amplify the signal, which is shown as variation in brilliance on the cathode ray tube (CRT). The scanning of the CRT is illustrated synchronized with electrons on the sample in the microscope. The picture may be taken by photography from high-resolution CRT in advanced machines. The consequence of the small tip of 100 nm radius is the electric field can be determined to an intense level.

2.4.6 Transmission Electron Microscopy (TEM)

TEM is a microscopy technique in which beam of electron interacts and transmitted through a specimen. The electron beam is radiated by source and focused magnified image with the system of magnetic lenses. The TEM works on the same principle as the SEM. In this case of TEM, the sample is thin, the beam of electrons

emits through the specimen. The formed image is magnified with focused onto the fluorescent screen and is printed photographic film. The advanced machines can be detected images using the charge-coupled device. The wavelength of the electron source is often lower than light, which optimal determination can be achieved for TEM images [30]. Schematic diagram of TEM is shown in Fig. 2.8.

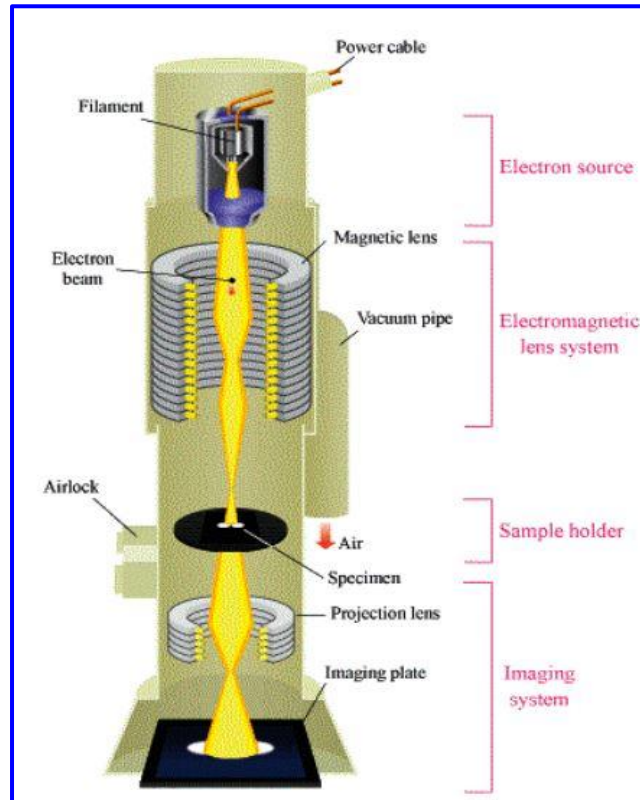


Fig. 2.8) Schematic of electron beam path in TEM [30].

It consists of four parts as following,

- (1) **Electron source:** It consists of anode and cathode. Anode (+ve potential) accelerates a beam of electrons towards the sample specimen located. The cathode (-ve potential) is a tungsten filament heated electromagnetically and emits electrons.
- (2) **Electromagnetic lenses:** It is the combination of an aperture and a magnetic lens. The magnetic lens generates a specific magnetic field, which acts similar to the optical lens and is focused on electrons. The aperture is a thin disc having a diameter of 2 to 100 μm and used for the removal of unnecessary electrons from hitting samples. The electromagnetic system tolerates well determined narrow electron energy transmits to hit the target sample under analysis.
- (3) **Sample holder:** The radiated electrons are passed by the sample without interrelating with it. These depend on the thickness of the sample. The thinner region of the sample will emerge lighter and the thicker region will emerge darker.

(4) Imaging system: All these electrons scattered by the sample will have equal energy. Hence, formed of another electromagnetic lens and display. These electromagnetic lenses are refocusing the electron beam after transmitting by specimen and create enlarging of the image on the projector display.

2.4.7 Brunauer-Emmett-Teller (BET) theory

The adsorption is nothing but adhesive of gas molecules and atoms by some solid surface. The sum of adsorbed gas molecules depends on the revelation of temperature, surface area, gas pressure with the interaction between solid surface and gas molecules. Usually, nitrogen (N_2) is preferred for the BET estimations, because it is acquired more cleanness and strong interaction of solids surface. The amount of N_2 gas is delivered into the sample chamber in stepwise behavior and atmospheric pressure higher than relative pressures is calculated by fractional vacuum condition. When saturation pressure is reached, further adsorption is not probable even in expansion in the system of pressure. The micro porous materials having pore size diameter less than 2 nm is shows such type of isotherm shown in **Fig. 2.9**.

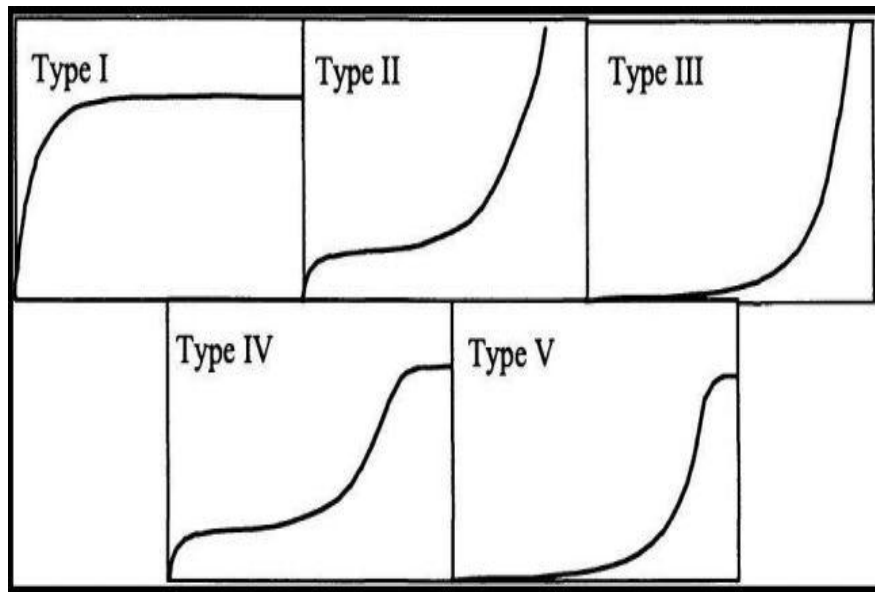


Fig. 2.9) Five types of adsorption isotherms in BET analysis [33].

The accurate pressure gauges are employed to calculate small pressure change owing to the adsorption procedure. The sample material is eliminated from the N_2 atmosphere and heat releases N_2 gas adsorbed from the solid surface. The five types of sorption isotherm are possible [31, 32].

(1) Type I: It is obtained, when $P/P_0 < 1$ and $c > 1$, where P/P_0 is a comparative pressure and c is the BET constant which is associated with an adsorption energy of

initial monolayer and various solid to solid. The microporous materials are less than 2 nm in diameter.

(2) **Type II:** The middle flat portions signify the monolayer structure. The monolayer structure takes place though at a high-pressure capillary condensations system.

(3) **Type III:** Type III is probable when $c < 1$ and directly multilayer structure take place and no multilayer is produced. Hence, the BET is not suitable.

(4) **Type IV:** These curves mentioned when capillary condensation takes place. The low pressure than the saturation pressure gas molecules is reduced in small solid pores. The monolayer structure occurs at low pressure followed through a multilayer structure with an increase in pressure. This type of isotherm reveals mesoporous materials in the range of 2 to 50 nm. The dynamic flow method apparatus used in measurements of BET surface area of material are shown in **Fig. 2.10**.

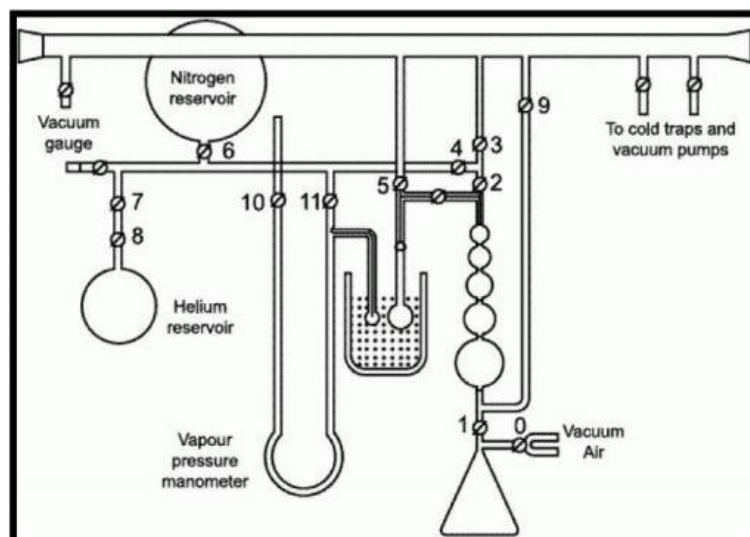


Fig. 2.10) Schematic of the dynamic flow method apparatus used for BET measurements [34].

(5) **Type V:** The type V curve is same as the type IV but not relevant to BET. The specific surface area (S_{BET}) and total surface area (S_{total}) of materials can be estimated as follows,

Where, S , V_m , N and a is the adsorbing species, molar volume of the adsorbate gas, Avogadro's number and mass of the adsorbent [33].

$$S_{BET} = \frac{S_{total}}{a} \quad (2.14)$$

$$S_{total} = \frac{V_m N s}{V} \quad (2.15)$$

2.5. Techniques to evaluate for testing of electrochemical properties

The working of the supercapacitor was examined by cyclic voltammetry (CV), electrochemical impedance spectroscopy (EIS) and galvanostatic charge-discharge techniques are used. These techniques are useful in batteries, sensors, fuel cells, and thus can give information on interfacial capacitance, reaction parameters such as corrosion rates and electrode surface porosity measurements.

2.5.1 Cyclic Voltammetry (CV)

The CV is the widely used technique for analyzing the electrochemical reaction. The CV gives information on a redox reaction, adsorption reaction, redox potential of the active material and heterogeneous electron transfer processes. This potentiostat technique is used to measure the current flowing between working electrode and a counter electrode. The CV curve is plotted as current versus applied potential. In the CV measurements, the electrode potential ramps linearly versus time in cyclic behaviour as depicted in **Fig. 2.11**.

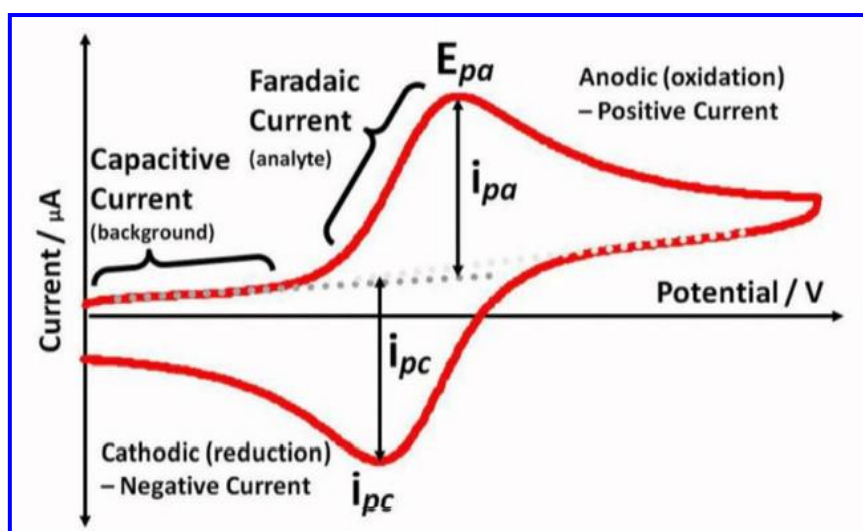


Fig. 2.11) The CV curve for a reversible single electrode transfer reaction [37].

The peak height and width for the specific processes depend on the electrolyte concentration, electrode materials and scan rate [35, 36]. In this study, the CV is used in the illumination of reaction occurring on the electrode surfaces. The reactions occurring on the electrode surface may be reversible and non-redox reactions. The reversible reaction may be physical structure changed of the electrode surface since the reaction occurring owing to the potential application. The classified is non-faradic reaction and adsorption of species to forming an electrical double layer. The redox reaction, E_{pa} , E_{pc} represents peak potentials for an anodic and cathodic reaction. Where, I_{pa} and I_{pc} are represented to peak currents. The scan rates are dependent on the widths, peak potentials and peak amplitude observed in the voltammogram. The CV

technique is useful to study the role of diffusion, adsorption and chemical reaction mechanism [37, 38].

The CV is the renowned technique to evaluate the Cs of supercapacitor [34]. The capacitance of supercapacitor is estimated using the equation,

$$C_s = \frac{1}{mv(V_2-V_1)} \int_{V_1}^{V_2} I(V)dV \quad (2.16)$$

Here, s, (V_2-V_1) , m and I are the scan rate in $mV s^{-1}$, potential window in Volt, mass of active material ($1 cm^2$ area) in $mg cm^2$ and measured current in Ampere, respectively.

2.5.2 Galvanostatic Charge Discharge (GCD)

The GCD technique details charge storage ability of materials with energy storage and power delivery. The constant current is applied to the working electrode and totally charged to higher potential V_2 and discharged through contrary direction current up to lower potential V_1 with the same magnitude. The GCD graph is plotted as applied potential versus time essential for charging and discharging. The specific capacitance, specific energy, specific power GCD cycling stability and columbic efficiency of materials can be determined using the GCD curves. The schematic of charge-discharge curve is shown in **Fig. 2.12**.

To estimation the average capacitance, energy and power density of the electrode material GCD technique is necessary. Moreover, the nature of the electrode material can be determined from the shape of GCD curve. The Cs of the electrode material is determined from the following equation,

$$C_s = \frac{I_d \times T_d}{\Delta V \times m} \quad (2.17)$$

where, ' ΔV ', ' I_d ' and ' T_d ' are referred to voltage of potential in Volt, discharge current in Ampere and discharge time in seconds.

The energy density (ED) and power density (PD) of MnO_2 electrodes are calculated using following equations,

$$E_D = \frac{0.5 \times C_s \times \Delta V}{3.6}; \text{ and} \quad (2.18)$$

$$P_D = \frac{E \times 3600}{T_d} \quad (2.19)$$

where, ΔV is the potential window in (Volt).

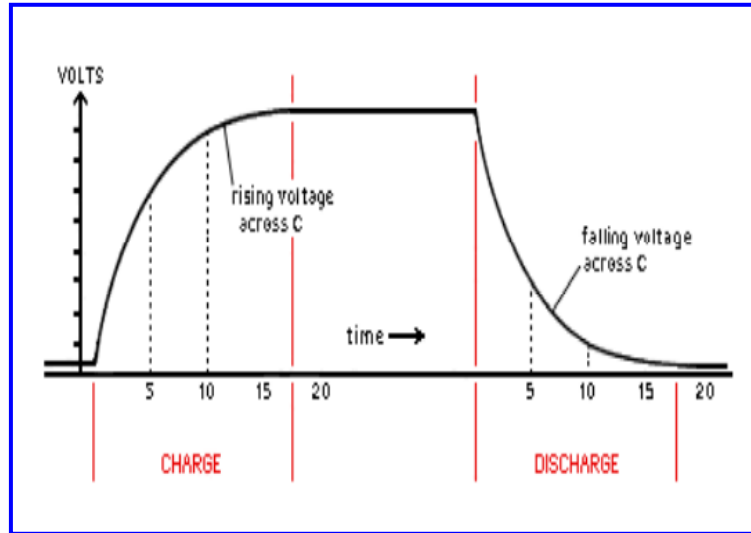


Fig. 2.12) The schematic of the charge-discharge curve [39].

2.5.3 Electrochemical Impedance Spectroscopy (EIS)

The EIS technique is the sinusoidal sign of low amplitude is applied and extensive frequency range, temperature and current response are analyzed. The graph as depicted in **Fig. 2.13** is the most preferred curve for estimating electrochemical impedance with equivalent circuit [40, 41]. The EIS is the main advantage of the plot format which is the consequents of ohmic resistance. In the EIS graph, there is a half semicircle in the high-frequency zone and a straight line in the low-frequency zone. The half semicircle is the parallel combination of capacitance and resistance whereas the straight-line correlates with the Warburg resistance [42]. The various electrochemical term elevated in EIS spectroscopy as follows,

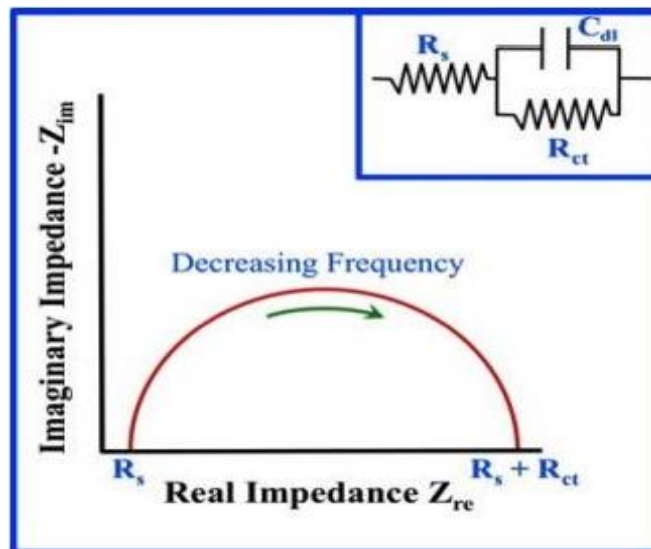


Fig. 2.13) Typical Nyquist plot for the interface of electrode-electrolyte [43].

(1) Electrolyte resistance: The series resistance was often an important factor of the electrochemical impedance. Hence, the three electrode cell compensates for the series resistance between reference and counter electrode. The series resistance between the working and reference electrode must be considered while modeling electrochemical cells. The solution resistance of an ionic solution has a basis on the ionic concentration, temperature, areal geometry and types of ions in which current is carried [43]. The resistor is not dependent on the frequency and does not contain imaginary elements. **Fig. 2.13** shows the equivalent circuit, which contains the low and high frequency components, where, C_{dl} is the double layer capacitor, R_s is solution resistance, R_{ct} is the charge transfer resistance, and Warburg impedance.

(2) Double layer capacitance: The charge transfer occurs from both the mechanism i.e. by faradic as well as non-faradic mechanism. The faradic element occurs from the redox reaction on the electrode surface, while the non-faradic element happens from the C_{dl} . The charge transfer occurs at the interface and which depends upon the rate of electron transfer. The rate of electron transfer depends on the employ of the oxidants and the production of the reductant near the electrode surface.

(3) Charge transfer resistance (R_{ct}): The resistance is created by the single, kinetically controlled electrochemical reaction. **Fig.2.13** shows the half semi-circular loop which is associated with resistance of charge transfer. The current flowing at an electrified interface owing to an electrochemical reaction,

The reversible reaction is as follows,



Where, n is the number of electrons transferred, O is the oxidant, and Red is its reduced product (reductant). The R_{ct} reaction has a certain speed depends on the kind of reaction, the reaction temperature the concentration of the reaction product, and potential.

Diffusion resistance: The diffusion makes impedance called Warburg resistance. The resistance depends on the frequency of the potential perturbation. At lower frequencies, the reactants have to diffuse more distance, which increases the Warburg-impedance. In Nyquist plot, Warburg impedance described by diagonal line with an inclination of 45° arises due to mass transport of ions. The EIS is used as an important characterization technique for applications to many material systems such as fuel cells, corrosion, plating, batteries, etc.

2.6 References

- [1] C. Konigstein, M. Spallart, J. Electrochem Soc. 145, (1998), 337-343.
- [2] B. Conway, V. Birss, J. Wojtowicz, J. Power Sources, 66, (1997), 1-14.
- [3] T. Niesen, M. Guire, Solid State Ion., 151, (2002), 61-68.
- [4] K. Chopra, P. Paulson, V. Dutta, Photovoltaic, 12, (2004), 69-92.
- [5] R. Vook, Int. Met. Rev., 27, (1982), 209-245.
- [6] K. Chopra, S. Das, Springer, Boston, MA., 181, (1983), 275-347.
- [7] D. M. Mattox, Thin Solid Films, 18, (1973), 173-186.
- [8] P. Kalita, B. Sarma, H. Das, Bull. Mater Sci, 26, (2003), 613–617.
- [9] H. Windischmann, Crit. Rev Solid State, 17, (1992), 547-596.
- [10] Q. ji, L. Shi, Q. Zhang, W. Wang, H. Zheng, Y. Zhang, Y. Liu, J. Sun, Appl. Surf. Sci, 387, (2016), 51-57.
- [11] R. Bulakhe, N. Shinde, R. Thorat, S. Nikam, C. D. Lokhande, Curr. Appl. phys, 13, (2013), 1661-1667.
- [12] S. Mishra, K. Saini, C. Kant, M. Pal, Mater Chem Phys, 146, (2014), 324-329.
- [13] R. S. Mane, C. D. Lokhande, Mater Chem Phys., 65, (2000), 1-31.
- [14] C. D. Lokhande, Mater Chem Phys., 27, (1991), 1-43.
- [15] G. Gund, D. Dubal, S. Jambure, S. Shinde, C. D. Lokhande, J. Mater. Chem. A, 1, (2013), 4793-4803.
- [16] S. Kale, R. Mane, H. Pathan, A. Shaikh, O. Jooa, S. Han, Appl Surf Sci., 253, (2007), 4335-4337.
- [17] S. Sartale, C. D. Lokhande, Mater. Chem. Phys., 65, (2001), 63 -67.
- [18] M. Ristov, G. Sinadinovski, I. Grozdanov, Thin Solid Films, 123, (1985), 63-67.
- [19] H. Pathan, C. D. Lokhande, Bull Mater Sci., 27, (2004), 85–111.
- [20] SILAR machine, [https://holmarc.com/silar controller with stirrer. php](https://holmarc.com/silar%20controller%20with%20stirrer.php).
- [21] M. Ohring, Materials Science of Thin Films, Deposition and Structure, Academic Press, New Jersey, (2001), 271-579.
- [22] H. Ibach, H. Luth, Solid-State Physics: An Introduction to Principles of Materials Science, Springer, Berlin, (2009), 67-77.
- [23] B. D. Cullity, Elements of X-ray Diffraction, Addison-Wesely, London, (1956), 1-99.
- [24] J. Preudhomme, P. Tarte, Spectrochim. Acta A, 27, (1971), 1817-1835.

- [25] R. Nyquist, R. Kagel, Infrared spectra of inorganic compounds, 1st edition, Academic Press INC, New York, (1971), 1-109.
- [26] C. Tripp, M. Hair, Langmuir 8, 4, (1992), 1120-1126.
- [27] P. Coates, Appl. Spectrosc. Rev., 31, (1996), 179-192.
- [28] <https://wiki.utep.edu/pages/viewpage.action?pageId=51217144>.
- [29] https://en.wikipedia.org/wiki/Scanning_electron_microscope.
- [30] http://www.hk-phy.org/atomic_world/tem/tem02_e.html.
- [31] H. Sankur, J. Cheung, Appl Phys A, 47, (1988), 271-284.
- [32] R. Sivakumar, R. Gopalakrishnan, M. Jayachandran, C. Sanjeeviraja, Opt Mater, 29, (2007), 679-687.
- [33] N. Hwang, A. Barron, <http://cnx.org/content/m38278/1.1/>.
- [34] <http://particle.dk/methodsanalyticalaboratory/surfaceareabet/surfaceareabettheory/>.
- [35] J. Bard, L. Faulkner, Electrochemical Methods: Fundamentals and Applications (2 ed.), Wiley, (2000-12-18), ISBN 0-471-04372-9.
- [36] S. Nicholson, S. Irving, Anal. Chem., 36, (1964-04-01), 706–723.
- [37] J. Heinze, Angew Chem. Int. Ed. Engl. 23, (11), (1984), 831-847.
- [38] R. Parsons, Chem. Rev. 90, 5, (1990), 813–826.
- [39] https://en.wikipedia.org/wiki/Cyclic_voltammetry.
- [40] <http://www.gamry.com/application-notes/EIS/basics-of-electrochemicalimpedance-spectroscopy/>.
- [41] http://www.ecochemie.nl/download/Applicationnotes/Autolab_Application_Note_EIS06.pdf.
- [42] https://www.jlab.org/conferences/tfsrf/Thursday/Th2_1-EIS%20intro%20Reece.pdf.
- [43] <http://www.gscsg.com/Electrochemical%20Impedance%20Spectroscopy.html>.

CHAPTER-3

**MANGANESE DIOXIDE THIN FILMS
DEPOSITED BY CHEMICAL BATH AND
SUCCESSIVE IONIC LAYER ADSORPTION
AND REACTION DEPOSITION METHODS
AND THEIR SUPERCAPACITIVE
PERFORMANCE**

CHAPTER-3

Manganese Dioxide Thin Films Deposited by Chemical Bath and Successive Ionic Layer Adsorption and Reaction Deposition Methods and Their Supercapacitive Performance

Sr. No.	Title	Page No.
3.1	Introduction	53
Section-A		
Synthesis and characterization of MnO₂ thin films by CBD and SILAR methods.		
3.2 A.1	Introduction	53
3.2.A.2	Experimental details	54
	3.2.A.2.1 Cleaning of substrate	54
	3.2.A.2.2 Chemicals	55
	3.2.A.2.3 Synthesis of MnO ₂ thin film using CBD method	55
	3.2.A.2.4 Synthesis of MnO ₂ thin film using SILAR method	55
	3.2.A.2.5 MnO ₂ film formation in CBD method	55
	3.2.A.2.6 MnO ₂ film formation in SILAR method	56
	3.2.A.2.7 MnO ₂ thin film characterization	57
3.2.A.3	Results and discussion	58
	3.2.A.3.1 XRD analysis	58
	3.2.A.3.2 FT-IR Study	58
	3.2.A.3.3 FE-SEM analysis	69
	3.2.A.3.4 EDX Study	61
	3.2.A.3.5 BET surface area analysis	61
Section-B		
Supercapacitive evaluation of MnO₂ thin films by CBD and SILAR methods.		
3.2.B.1	Introduction	63
3.2.B.2	Experimental setup for supercapacitive evaluation	64
3.2.B.3	Results and discussion	64
	3.2.B.3.1 The CV study (CBD)	65
	3.2.B.3.2 The GCD studies (CBD)	66

	3.2.B.3.3	The EIS study (CBD)	67
	3.2.B.3.4	The stability study (CBD)	68
	3.2.B.3.5	The CV study (SILAR)	69
	3.2.B.3.6	The GCD studies (SILAR)	70
	3.2.B.3.7	The EIS study (SILAR)	71
	3.2.B.3.8	The stability study (SILAR)	72
<p style="text-align: center;">SECTION - C</p> <p>Flexible symmetric solid state supercapacitor (FSSSC) device fabrication and supercapacitive evaluation of C-MnO₂12h thin films.</p>			
3.2.C.1	Introduction		75
3.2.C.2	Experimental details		75
	3.2.C.2.1	Electrode preparation	75
	3.2.C.2.2	Preparation of PVA-Na ₂ SO ₄ gel electrolyte	76
	3.2.C.2.3	Fabrication of flexible symmetric solid state supercapacitor device	76
3.2.C.3	Electrochemical properties of flexible symmetric solid state supercapacitor (FSSSC) device		77
	3.2.C.3.1	The CV study	77
	3.2.C.3.2	The GCD study	78
	3.2.C.3.3	Ragone plot and EIS study	79
	3.2.C.3.4	Mechanical Flexibility and stability study	80
	3.2.C.3.5	Demonstration of symmetric C-MnO ₂ 12h device	80
3.3	Conclusions		81
3.4	References		82

3.1. Introduction

Among the different energy storage devices, pseudocapacitor has attracted more attention due to their high power density, long cycle life than that of batteries and higher energy density than that of dielectric capacitors [1, 2]. The energy density of supercapacitor can be improved either by increasing specific capacitance or potential window [3]. The design and development of high energy density material is a challenging task for researchers. The new active materials such as MnO_2 , NiO , V_2O_5 , CuO , ZnO , etc. showed more specific capacitance, higher energy density and superior electrochemical stability than carbon and conducting polymer based materials [4-7]. The MnO_2 with low cost and high theoretical specific capacitance ($\sim 1380 \text{ F g}^{-1}$), abundant and environmental friendly nature, is a promising electrode material for supercapacitor device [8].

In the past, different chemical deposition methods like chemical bath deposition (CBD), successive ionic layer adsorption and reaction (SILAR), electrodeposition and hydrothermal are used to prepare the nanostructured MnO_2 electrodes [9-12]. The surface morphology plays a significant role for the supercapacitor application, as the electrochemical reactions take place by the surface of active electrode material. In present work, facile and binder free CBD and SILAR methods are employed to MnO_2 thin films deposited on stainless steel substrate. These two methods have preparative parameters such as the pH of solution, concentration of reactants, deposition temperature, deposition cycles and time of deposition.

The present chapter is divided into three sections (Section A, B and C). The Section 'A' deals with the deposition of MnO_2 thin films using facile inexpensive and binder free CBD and SILAR methods and their characterizations. The Section 'B' is associated with the electrochemical performance of MnO_2 thin films testing in aqueous 1 M Na_2SO_4 electrolyte. Section 'C' deals with the fabrication and electrochemical properties of flexible symmetric solid state supercapacitor (FSSSC) device based on MnO_2 thin films.

SECTION - A

Synthesis and characterization of MnO_2 thin films by CBD and SILAR methods

3.2 A.1 Introduction

The electrode material must be inexpensive, scalable processing, high performance with high power density, energy density and good electrochemical rate capability. From these points of view, the MnO_2 electrodes are synthesized by simple, binder-less and low temperature CBD and SILAR methods.

The major advantage of CBD is deposition of adherent, uniform and large scale of substrate mounting devices as well as good reproducibility [13]. The preparative parameters such as surface morphology and thickness of the thin film can be easily controlled by varying preparative parameters such as reaction time, pH, temperature and concentration of precursor. One of the drawbacks of this method is the wastage of solution after every deposition. In usual chemical bath method, a synthesis of thin film on the substrate is carried by excess of ionic product than solubility product. The CBD method requires more time to obtain film due to slow growth rate resulting into low thickness directly affecting electrochemical performance of device.

The SILAR is also an effective method for deposition by layer-by-layer assembling of material with easily control over the thin film thickness and large scale area of on any type of substrate without use of binders [14]. It is based on successive reaction on the substrate surface using different reacting precursor and hence unnecessary bulk precipitation is avoided. In SILAR method, fast growth rate result into inappropriate thickness.

3.2.A.2 Experimental details

3.2.A.2.1 Cleaning of substrate

In chemical methods, the substrate surface with extreme cleanness is the essential to take good quality thin films. Furthermore, the substrate with contamination offers uncontrolled growth on the substrate surface, which leads to the formation of non-uniform thin film.

The conducting substrate is the basic necessity of supercapacitor, the stainless steel (SS) substrate is highly conducting and inexpensive appropriate for supercapacitor application. These SS substrates were cleaned by following procedure,

- 1) Previous to synthesis, the SS substrates of thickness 0.050 mm and dimensions 1 x 5 cm² were polished by zero grade polish paper.

- 2) Then, the substrates were cleaned through acetone by ultrasonication in the double distilled water (DDW) for 10 minutes and air dried at room temperature (300 K).

3.2.A.2.2 Chemicals

All analytical grade (AR) chemicals such as methanol (CH₃OH), manganese sulfates (MnSO₄), and potassium permanganate (KMnO₄) are used without further purification.

3.2.A.2.3 Synthesis of MnO₂ thin film using CBD method

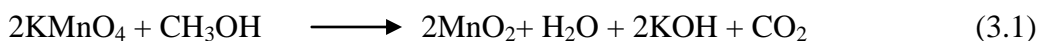
For MnO₂ thin film synthesis, 2 ml methanol was added as reducing agent in 0.1 M KMnO₄ (100 ml) solution. The well cleaned SS substrates were vertically immersed in above bath and kept for different time periods (8, 12, 16 hours) at room temperature (27 °C) [15]. After 8, 12, 16 hours, the SS substrate was taken out from the bath, washed with DDW and dried at room temperature. The dark brown colored MnO₂ thin films are denoted as C-MnO₂8h, C-MnO₂12h and C-MnO₂16h, for 8, 12, 16 hours deposition period, respectively.

3.2.A.2.4 Synthesis of MnO₂ thin film using SILAR method

The MnO₂ thin film was synthesized in an aqueous bath using 0.1 M (50 ml) manganese sulfate as the cationic precursor solution and 0.1 M (50 ml) potassium permanganate as an anionic precursor solution [16]. The SS substrate was successively dipped in cationic and anionic precursor solutions for 10 s each with rinsing between for 10 s in DDW. Such cycles were repeated for 30, 60 and 90 times and corresponding films are denoted as S-MnO₂30, S-MnO₂60 and S-MnO₂90, respectively.

3.2.A.2.5 MnO₂ film formation in CBD method

Initially, in the beaker, 2 ml methanol was added in (100 ml) 0.1 M KMnO₄ solution and SS substrate was immersed at room temperature (27 °C). The precipitation started in solution after 5 h. During precipitation, as time passes the ionic product exceeds the soluble product resulting in coalescence and aggregation of particles. The heterogeneous reaction occurs on the SS substrate to form MnO₂ thin film. The overall chemical reaction is as follow,



At the major phase of reaction, MnO_2 grows on the surface of SS substrate as well as in the bulk solution. The ionic product ($\text{IP} = 3.74 \times 10^{-6}$) represses the solubility product ($\text{SP} = 1.4 \times 10^{-35}$) of MnO_2 within solution for creation of nucleation on the SS substrate. The thickness of thin film slowly increases up to deposition time of 12h. The mass loading is 0.18, 0.3 and 0.32 mg cm^{-2} for 8, 12 and 16 hours time of deposition, respectively. **Fig. 3.1 (A)** schematic represents MnO_2 thin film deposition. **Fig. 3.1 (B)** shows the photographs of MnO_2 thin films at different deposition hours as (a) 8h, (b) 12h and (c) 16h. The **Fig. 3.1 (C)** shows the chemical synthesis process of thin film consisting of steps like nucleation, aggregation, coalescence and growth of ions on the substrate.

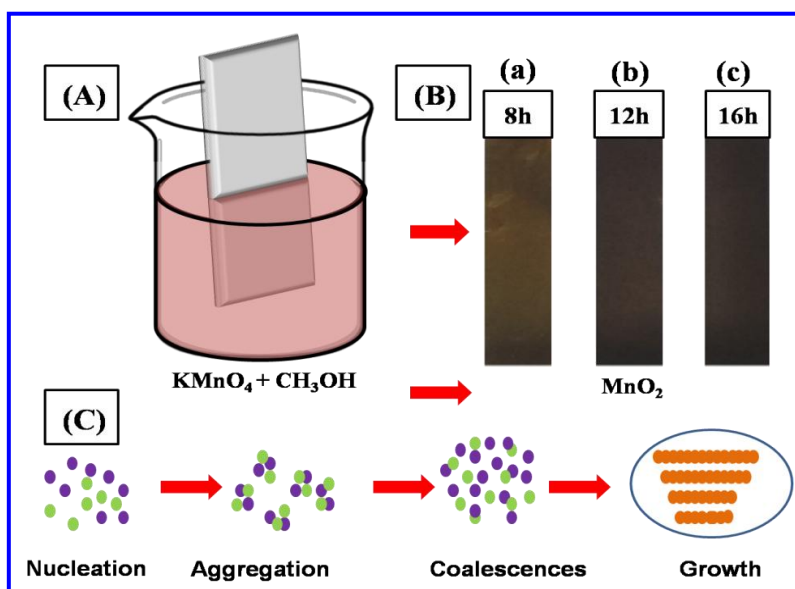


Fig. 3.1) (A) Schematic diagram of MnO_2 thin film synthesis using CBD method, (B) the photographs of MnO_2 thin films deposited for different hours (a) 8h, (b) 12h and (c) 16h and (C) the proposed growth mechanism of MnO_2 thin film.

3.2.A.2.6 MnO_2 film formation by SILAR method

The **Fig. 3.2 (A)** shows the deposition mechanism of MnO_2 thin film by SILAR method. The growth of MnO_2 thin film takes place by ion-by-ion growth process at the nucleation sites on the immersed substrate. For the deposition of MnO_2 thin films, when well cleaned SS substrate is immersed in cationic precursor, the Mn^{2+} ions to form adsorbed on the surface of SS substrate. The substrate is rinsed in DDW to remove the loosely bound Mn^{2+} ions to avoid the homogenous precipitation in the diffusion layer. Further, the SS substrate is dipped in an anionic precursor KMnO_4 solution in which O_2^{2-} ions react with Mn^{2+} ions and form MnO_2 layer on the substrate.

This completes one cycle for deposition of MnO_2 thin film. Such cycles are repeated to increase MnO_2 thin film thickness. The overall deposition reaction can be written as,



In this case, KMnO_4 precursor solution acts as a strong oxidizing agent. The mass loading per cm^2 on substrate is 0.4, 1.0 and 1.2 mg cm^{-2} for 30, 60 and 90 cycles, respectively. The **Fig. 3.2 (B)** shows the photographs of MnO_2 thin films deposited at different cycles (a) 30, (b) 60 and (c) 90.

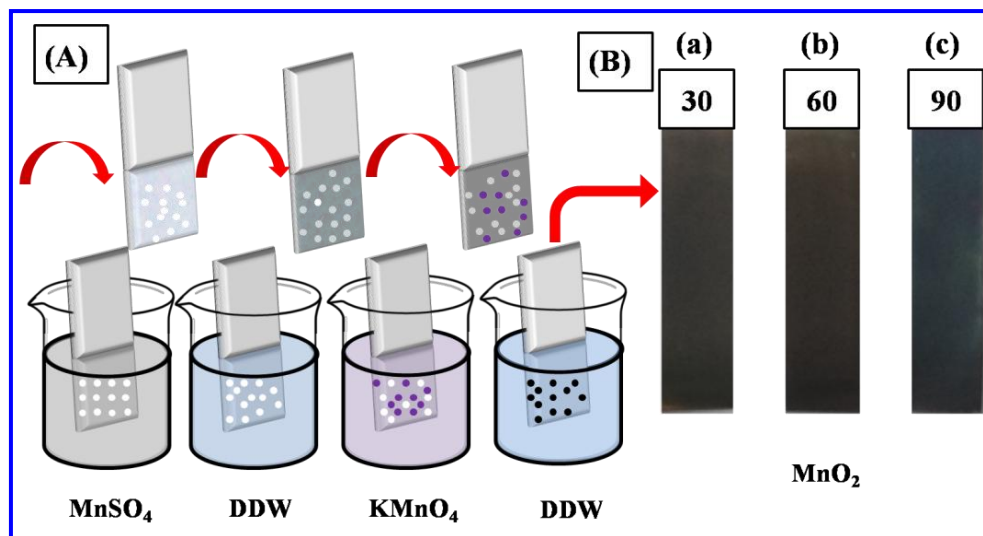


Fig. 3.2) (A) Schematic diagram of MnO_2 thin film synthesis using SILAR method and (B) the photographs of MnO_2 thin films deposited for different cycles (a) 30, (b) 60 and (c) 90.

3.2.A.2.7 MnO_2 thin film Characterization

The MnO_2 thin films were characterized by X-ray diffraction (XRD) studies for structural analysis using Rigaku miniflex-600 new model with $\text{Cu K}\alpha$ ($\lambda = 0.154 \text{ nm}$) radiation, operated at 30 kV through scan rate of $2^\circ/\text{min}$. To observe chemical bonding, the Fourier transform infrared (FT-IR) spectrum of samples was measured using an alpha (II) Bruker instrument. The surface morphology of MnO_2 thin film was studied using field-emission scanning electron microscopy (FE-SEM, JSM-7001F and JEOL) coupled with energy-dispersive X-ray spectroscopy (EDX), (Oxford and X-max). The specific surface area and pore size distribution of thin films were obtained through Brunauer-Emmett-Teller (BET) and Barrette-Joynere-Halenda (BJH) methods using BEL-SORP-II mini method. The electrochemical measurements were carried out using ZIVE MP1 multichannel electrochemical workstation, equipped with three electrodes arrangement consisting of saturated calomel electrode as a reference electrode,

platinum as a counter electrode and MnO_2 thin film as a working electrode in 1M Na_2SO_4 electrolyte.

3.2.A.3 Results and discussion

3.2.A.3.1 XRD analysis

The XRD patterns were used to investigate the crystal structure and phase of deposited MnO_2 thin films. **Fig. 3.3 (A)** shows the XRD patterns of C- MnO_2 8h, C- MnO_2 12h and C- MnO_2 16h thin films on SS substrate. The detected diffraction peaks correspond to (110), (200), (103) and (310) planes of tetragonal phase of α - MnO_2 (JCPDS card no. 44-0141). Similar α - MnO_2 phase was also reported by hydrothermal and CBD methods [17, 18].

The XRD patterns of S- MnO_2 30, S- MnO_2 60 and S- MnO_2 90 samples are displayed in **Fig. 3.3 (B)**. The planes (001), (002) (-111) and (020) correspond to birnessite-type of MnO_2 phase (JCPDS card no. 42-1317). This birnessite-type of MnO_2 phase was reported by Fan et al. [3] and Jana et al. [15] using redox reaction and SILAR methods, respectively. For both methods, the low intense diffraction peaks signify the nanocrystalline nature of MnO_2 thin films. The diffraction peaks denoted by (#) corresponds to SS substrate.

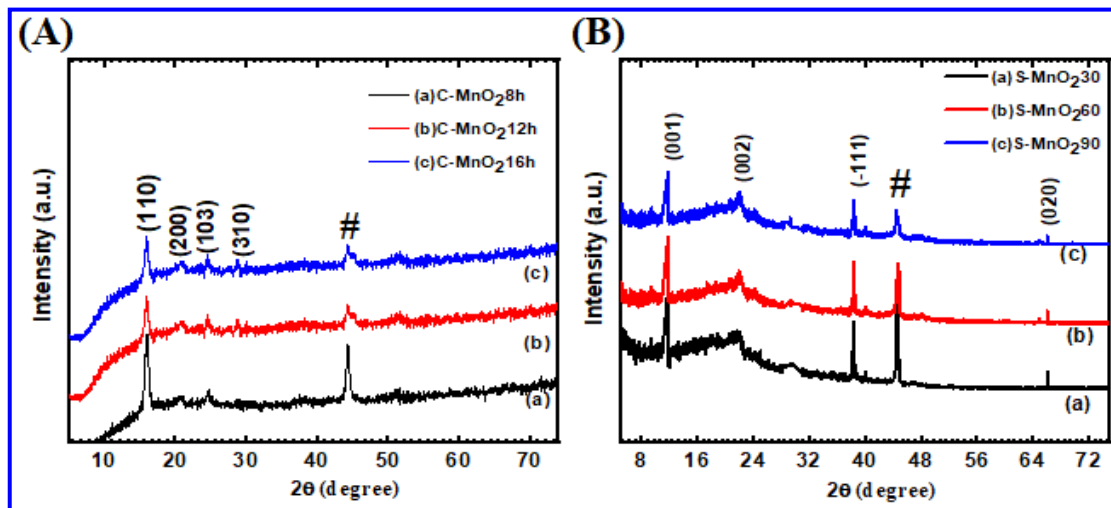


Fig. 3.3) The XRD patterns of (A) C- MnO_2 8h, C- MnO_2 12h and C- MnO_2 16h and (B) S- MnO_2 30, S- MnO_2 60 and S- MnO_2 90 thin films.

3.2.A.3.2 FT-IR Study

The MnO_2 samples were characterized by FT-IR spectroscopic technique within wavelength range $4000\text{--}400\text{ cm}^{-1}$. **Fig. 3.4 (A)** shows the FT-IR absorption spectra of

C-MnO₂8h, C-MnO₂12h and C-MnO₂16h thin films. The broad band at 3382.59 cm⁻¹ indicates -OH stretching vibration mode [19], while the absorption peaks at 1631.57 and 1516 cm⁻¹ certify the -C-O bending vibrations joining with Mn atoms [20]. A number of small incorporation peaks around the 1291.30 and 1053.01 cm⁻¹ are due to the twisting vibration of O-H bonds connected through Mn atoms [21]. The incorporation peaks at 621.75 cm⁻¹ is related to linking mode with Mn-O stretching mode [21].

Fig. 3.4 (B) shows FT-IR spectra of S-MnO₂30, S-MnO₂60 and S-MnO₂90 samples. The broad intense peak at 3380.34 cm⁻¹ is due to the -OH stretching vibrations mode of the MnO₂ [22]. The absorption peaks at 1610.77 and 1348.02 cm⁻¹ allocated towards the bending vibrations of the surface -C-O ions linked with Mn atoms. The two broad absorption peaks at 764.56 and 621.75 cm⁻¹ are the Mn-O stretching mode [23].

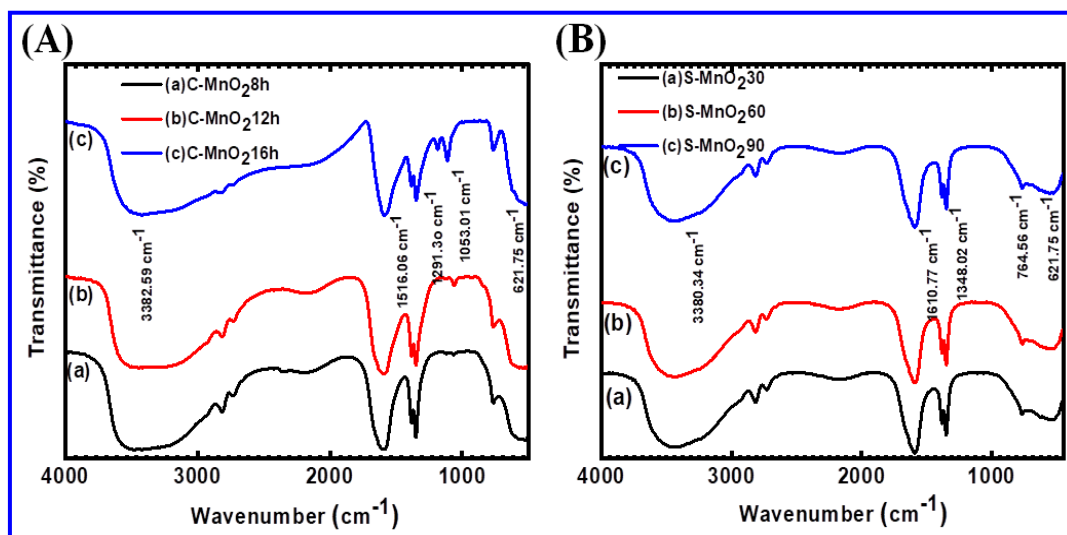


Fig. 3.4) The FT-IR spectra of (A) C-MnO₂8h, C-MnO₂12h and C-MnO₂16h and (B) S-MnO₂30, S-MnO₂60 and S-MnO₂90 thin films.

3.2.A.3.3 FE-SEM analysis

The FE-SEM is used for study of morphology of MnO₂ samples deposited by CBD and SILAR methods and morphology of C-MnO₂12h and S-MnO₂60 films are shown at two different magnifications in **Fig. 3.5 (A-D)**. The surface morphology of C-MnO₂12h thin film shows fine grained nanoparticles with a size between 60-80 nm, as illustrated in **Fig. 3.5 (A-B)**. As seen in the image, randomly oriented and non-uniform clusters are formed with nanoparticles. Gund et al. [24] observed thin microporous structure consisting of very fine nanosheets of MnO₂ with CBD method

and Patil et al. [25] obtained spherical shaped nanoparticles for α - MnO_2 by CBD method. The nanostructured surface morphology of thin film may provide more electrochemical active sites and enhance the rate of intercalation/deintercalation of electrolyte ions, which favors the charge storage mechanism in the electrode material.

The surface morphology of S- $\text{MnO}_2/60$ thin film shows the grains with approximate size of 30-40 nm formed with agglomerated particles as shown in **Fig. 3.5 (C-D)**. All these agglomerated particles are interconnected. The particles with irregular size and shape are randomly oriented in the grains. Singu et al. [14] obtained nanosphere MnO_2 thin films using SILAR method. Jana et al. [16] prepared hierarchical MnO_2 nanorods and Dubal et al. [26] converted surface morphology of SILAR deposited MnO_2 film from interlocked cubes to porous nanowalls. The C- $\text{MnO}_2/12\text{h}$ electrode has slow growth rate and takes 12h to develop fine grained nanoparticles on the SS substrate. The high growth rate (40 minutes) of S- $\text{MnO}_2/60$ electrode results into formation of agglomerated densely packed surface morphology. Hence, the change in surface area of MnO_2 films is due to the different growth rates under different optimized conditions in both the methods.

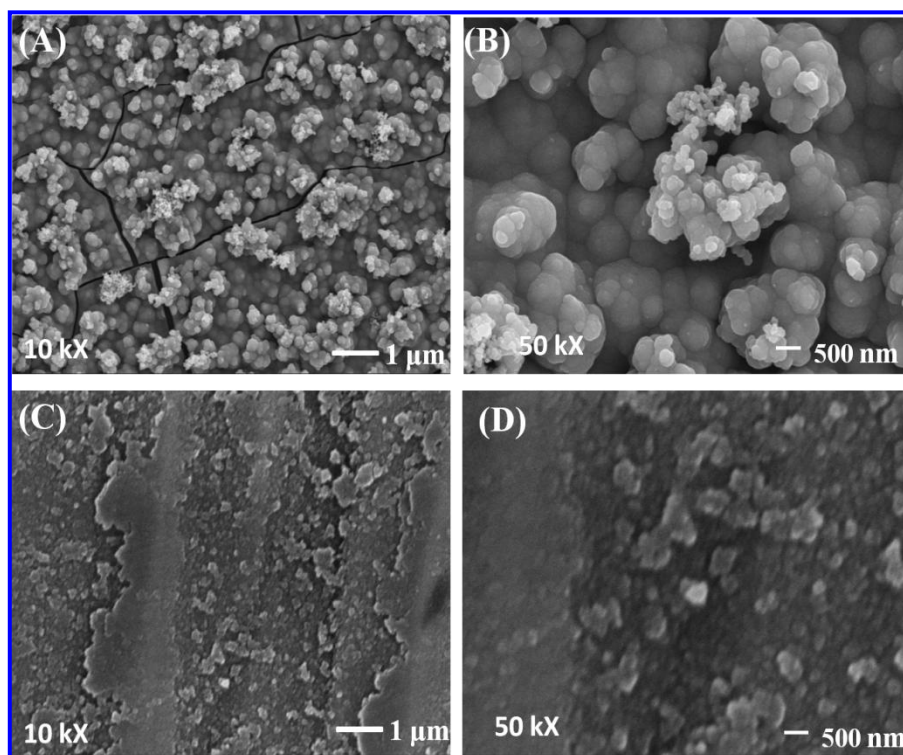


Fig. 3.5) The FE-SEM pictures of (A-B) C- $\text{MnO}_2/12\text{h}$ and (C-D) S- $\text{MnO}_2/60$ thin films at different magnifications of 10 kX and 50 kX.

3.2.A.3.4 The EDX Study

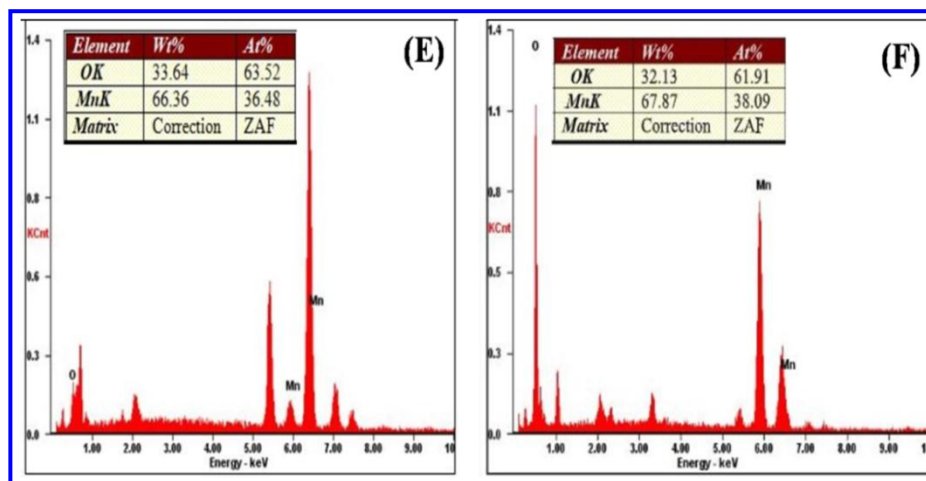


Fig. 3.5) The EDX spectra of (E-F) C-MnO₂12h and S-MnO₂60 thin films.

The EDX analysis spectrum of C-MnO₂12h thin film displayed in **Fig. 3.5 (E)** shows peaks from O and Mn elements without any other impurities. Inset table reveals weight percentage of (Mn - 66.36%, O - 33.64%) and atomic percentage of (Mn - 36.48%, O - 63.52%) for Mn and O elements. The EDX analysis spectrum of S-MnO₂60 electrode is shown in **Fig. 3.5 (F)**. Inset table shows weight (Mn - 67.87%, O - 32.13%) and atomic (Mn - 38.09%, O - 61.91%) percentages of Mn and O elements. This analysis confirms the formation of MnO₂ thin film on the SS substrate.

3.2.A.3.5 BET surface area analysis

The BET surface area and pore size distribution results in **Fig. 3.6 (A-C)** are obtained from N₂ adsorption-desorption isotherm analysis at 77 K. The distinct hysteresis loops are studied with relative pressure ranging from 0.2 to 1.0 P/P₀ for C-MnO₂8h, C-MnO₂12h and C-MnO₂16h electrodes are shown in **Fig. 3.6 (A-C)**. The samples of C-MnO₂8h, C-MnO₂12h and C-MnO₂16h show type-IV isotherm with a H₃ hysteresis loop which revealing the mesoporous surface structure [27]. The specific surface areas of 144, 192 and 132 m² g⁻¹ are obtained for C-MnO₂8h, C-MnO₂12h and C-MnO₂16h electrodes. The pore size distributions with mesoporous structure of C-MnO₂8h, C-MnO₂12h and C-MnO₂16h electrodes with the pore radii 13.65, 11.37 and 18.89 nm, respectively are shown in **Fig. 3.6 (D)**. Patil et al. [15] obtained specific surface area of 75 m² g⁻¹ with mesoporous structure for CBD MnO₂ thin film. The estimated values of specific surface area, pore size and pore volume are presented in **Table 3.1**.

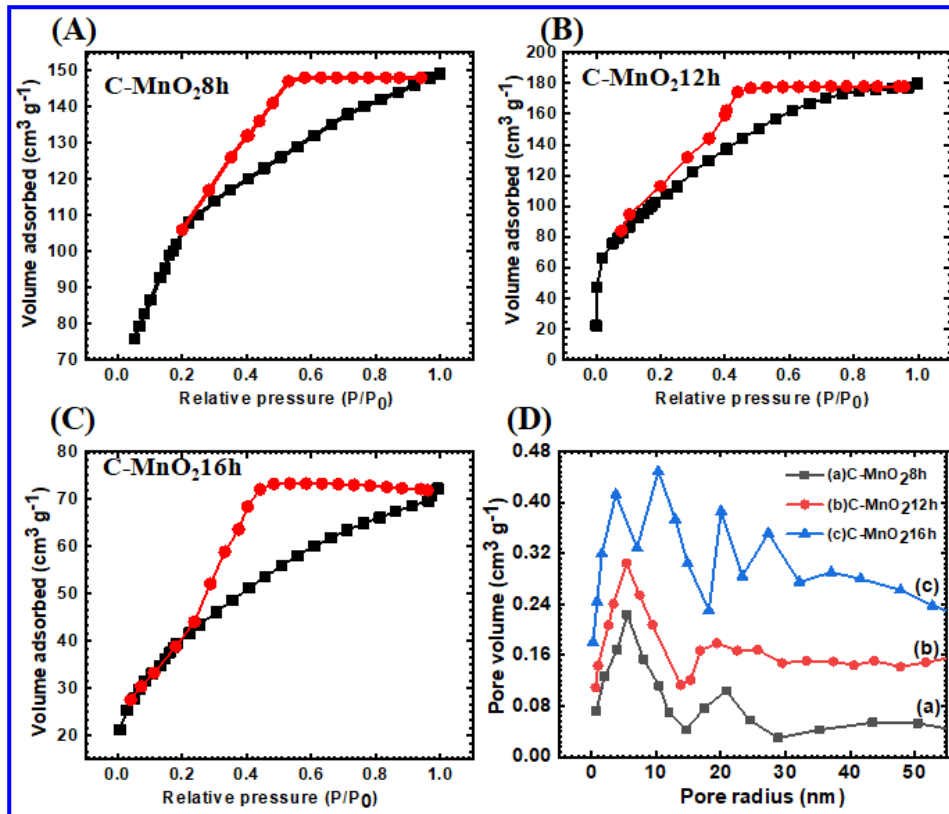


Fig. 3.6) N₂ adsorption-desorption isotherms of (A) C-MnO₂8h, (B) C-MnO₂12h and C-MnO₂16h thin films prepared at different time periods and (D) BJH pore size distribution plots of C-MnO₂8h, C-MnO₂12h and C-MnO₂16h powder samples.

Table 3.1: A summary of specific surface area, average pore size and pore volume values of C-MnO₂ and S-MnO₂ electrodes.

Sr. No.	Samples	Specific surface area m ² g ⁻¹	Average pore size (nm)	Pore volume m ³ g ⁻¹
1	C-MnO ₂ 8h	144	13.65	0.113
2	C-MnO ₂ 12h	192	11.37	0.276
3	C-MnO ₂ 16h	132	18.89	0.219
4	S-MnO ₂ 30	77	17.24	0.151
5	S-MnO ₂ 60	78	12.57	0.185
6	S-MnO ₂ 90	49	20.43	0.148

The above table illustrates that C-MnO₂12h and S-MnO₂60 electrodes have more active surface area and high pore volume as compared to other samples. Furthermore, FE-SEM images demonstrate that the surface morphology of C-MnO₂12h electrode consists of fine grained particles where as S-MnO₂60 electrode shows agglomerated and densely packed morphology.

Similarly, the BET characterization of S-MnO₂30, S-MnO₂60 and S-MnO₂90 electrodes obtained from N₂ adsorption-desorption isotherm are shown in **Fig. 3.7 (A-C)**. The distinctive type-II isotherm with a H₄ hysteresis loop characteristic depicted for samples reveals macro/mesoporous surface structure [28]. The small hysteresis loop observed for all electrodes in the range from 0.8 to 1.0 P/P₀, also indicates the existence of a macro/mesoporous structure [29]. The specific surface areas of S-MnO₂30, S-MnO₂60 and S-MnO₂90 electrode are 77, 78 and 49 m² g⁻¹ respectively. The pore size distribution of S-MnO₂30, S-MnO₂60 and S-MnO₂90 electrodes with pore radius of 17.24, 12.57 and 20.43 nm, respectively is shown in **Fig. 3.7 (D)**. The estimated values of specific surface area, pore size and pore volumes are presented in **Table 3.1**.

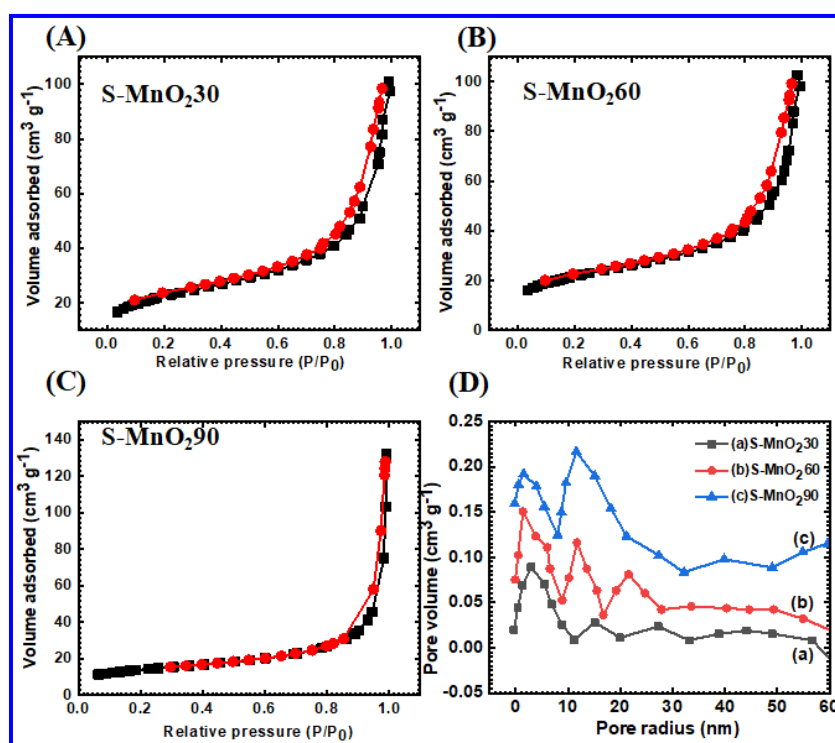


Fig. 3.7) N₂ adsorption-desorption isotherms of (A) S-MnO₂30, (B) S-MnO₂60 and (C) S-MnO₂90 thin films prepared at different cycles and (D) BJH pore size distribution plots of S-MnO₂30, S-MnO₂60 and S-MnO₂90 powder samples.

SECTION – B

Supercapacitive evaluation of MnO₂ thin films by CBD and SILAR methods

3.2.B.1 Introduction

The present section deals with the electrochemical measurements of CBD and SILAR prepared MnO₂ thin films in 1 M Na₂SO₄. This section includes the CV, GCD

and EIS measurements. These electrochemical tests are essential to decide the superior electrode material for fabrication of supercapacitor device. Moreover, the effect of scan rate, current density and electrochemical durability of MnO_2 thin films are investigated.

3.2.B.2 Experimental setup for supercapacitive measurements

For investigation of electrochemical measurements of MnO_2 thin films, the three electrode system was used which include MnO_2 thin film, platinum plate and saturated calomel electrode (SCE) as a working electrode, counter electrode and reference electrode, respectively in 1 M Na_2SO_4 electrolyte. The working electrode for electrochemical measurement was dipped in electrolyte up to area of 1 cm^2 . **Fig. 3.8 (A, B)** shows the actual experimental set up and schematic for the electrochemical study, respectively. The supercapacitive properties of MnO_2 electrode such as specific capacitance, energy density, power density and electrochemical stability were studied using CV, GCD and EIS techniques. The CV and GCD studies were conducted to evaluate the ZIVE MP1 electrochemical workstation. The EIS measurement was conducted to evaluate the electrochemical workstation ZIVE MP1 multichannel in the range of frequency from 0.001 Hz to 1 MHz with AC amplitude of 10 mV.

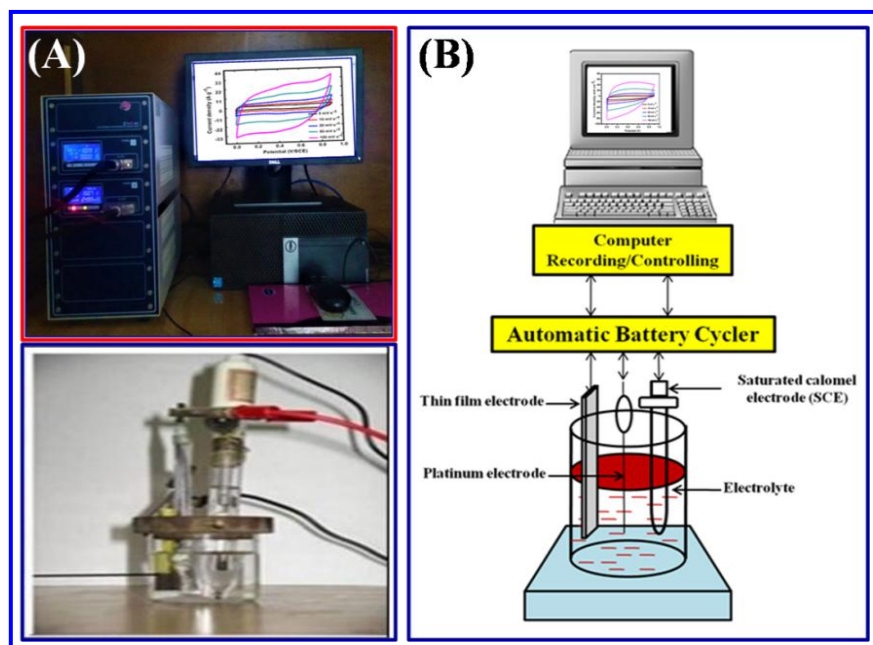


Fig. 3.8) (A) Actual experimental set up consisting of (up) automatic battery cyclers with CV cycles graph on monitor and (down) three electrode system and (B) schematic representation of three electrode system.

3.2.B.3 Results and discussion

3.2.B.3.1 The CV study (CBD)

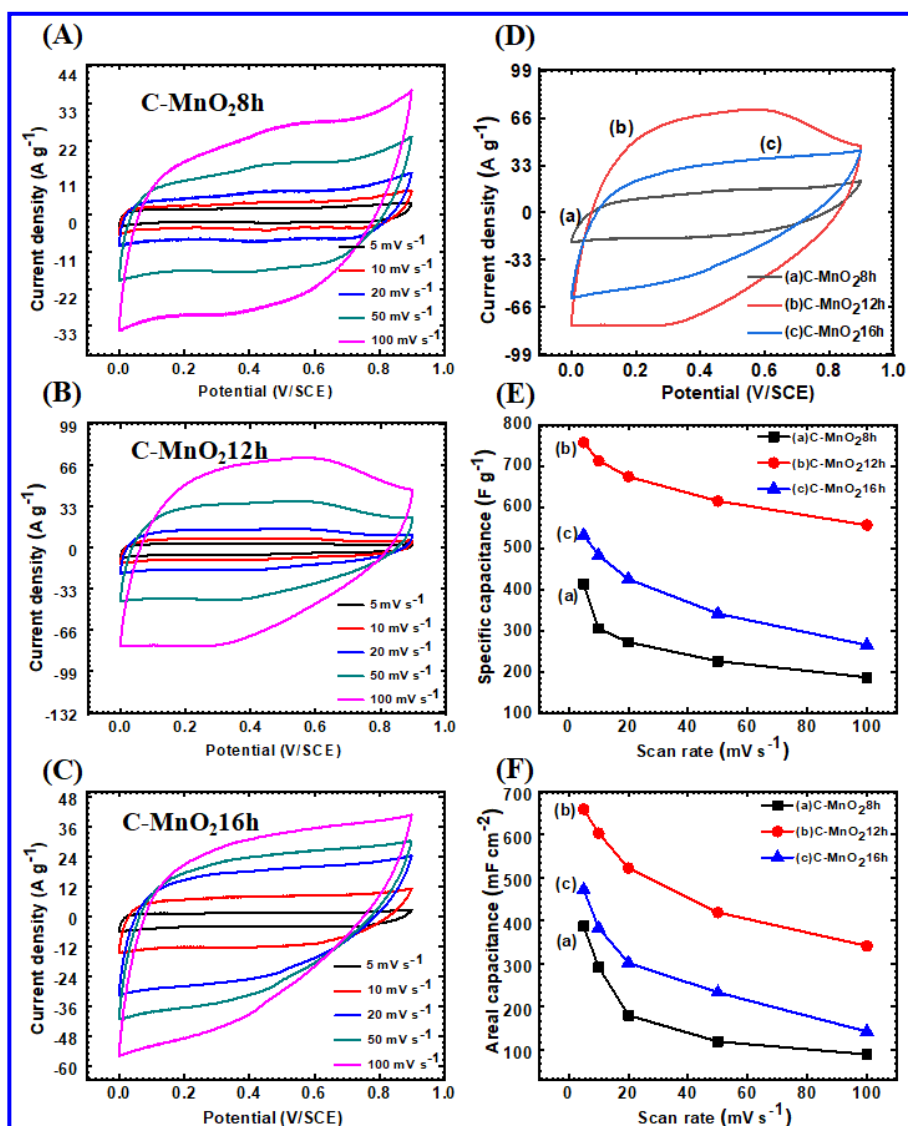


Fig. 3.9) The cyclic voltammetry curves of (A-C) C-MnO₂8h, C-MnO₂12h and C-MnO₂16h electrodes at scan rate 5-100 mV s⁻¹, (D) CV curves of C-MnO₂8h, C-MnO₂12h and C-MnO₂16h electrodes at scan rate of 100 mV s⁻¹, (E) the graph of specific capacitance versus scan rate and (F) the plot of areal capacitance versus scan rate of C-MnO₂8h, C-MnO₂12h and C-MnO₂16h electrodes.

Fig. 3.9 (A-C) shows the CV curves of C-MnO₂8h, C-MnO₂12h and C-MnO₂16h electrodes at scan rates from 5 to 100 mV s⁻¹ in the potential window of 0 to +0.9 V/SCE. The shape of all CV curves reflects nearly symmetric and rectangular shape, similar to the ideal capacitive behavior. The C-MnO₂12h electrode shows larger current area under CV curves than C-MnO₂8h and C-MnO₂16h electrodes at 100 mV s⁻¹ scan rate, as shown in **Fig. 3.9** (D). The increase in current passing through the scan rate exhibits the exceptional use of electrode substance with electrolyte owing the electrochemical reaction [30]. The effect of scan rate on specific capacitance is

illustrated in **Fig. 3.9 (E)**. The maximum values of specific capacitance observed for C-MnO₂8h, C-MnO₂12h and C-MnO₂16h electrodes are 413, 757 and 532 F g⁻¹, respectively at 5 mV s⁻¹ scan rate. The areal specific capacitance versus scan rate is shown in **Fig. 3.9 (F)**. The areal specific capacitances calculated as 387, 659 and 472 mF cm⁻², respectively. The redox reactions depend on the intercalation/deintercalation rate of protons and alkali cations from the electrolyte. The highest specific capacitance obtained for lower scan rate is ascribed to more working ions reaching the active surface, promoting the effective interaction among the ions between inner and outer side of the electrode [31].

3.2.B.3.2 The GCD studies (CBD)

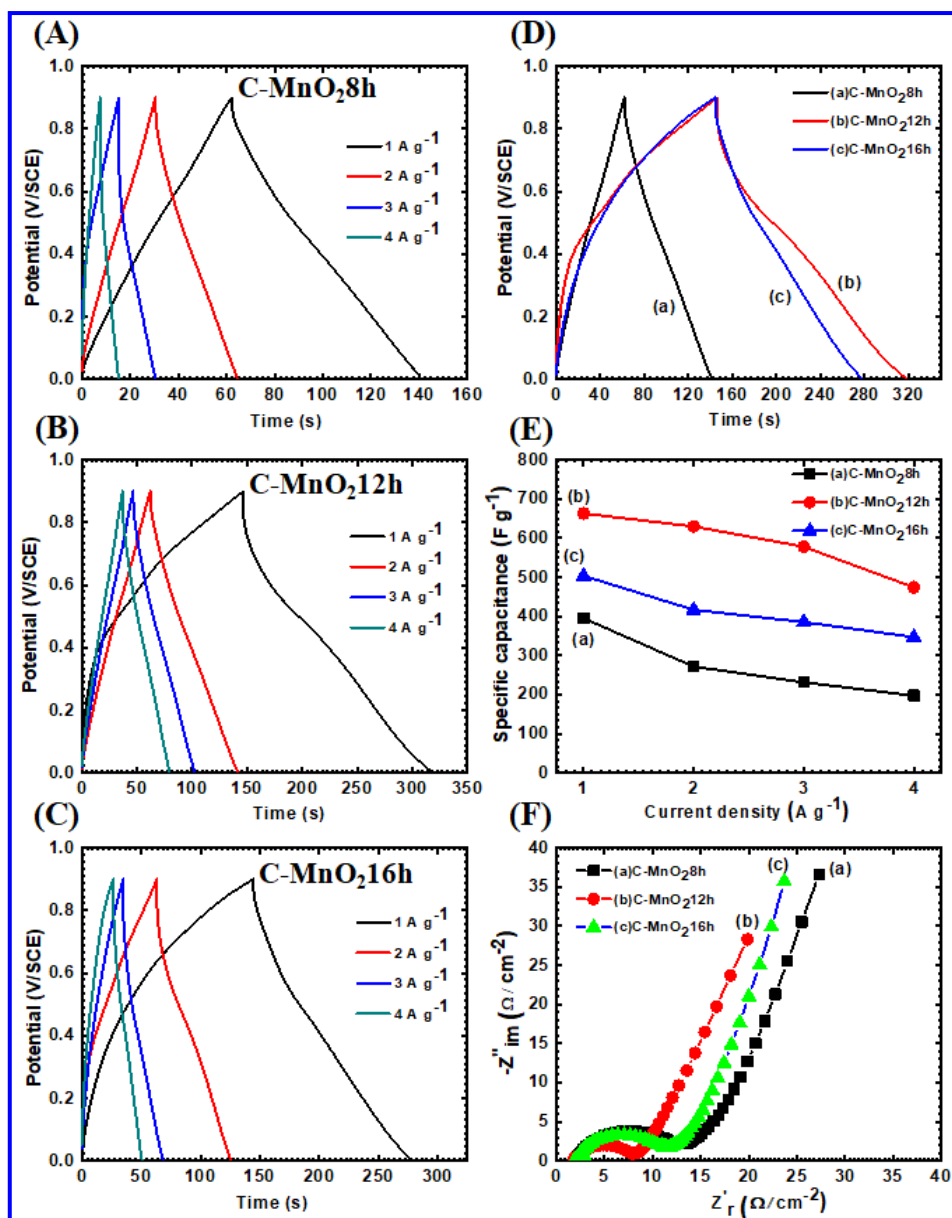


Fig. 3.10 The GCD curves of (A-C) C-MnO₂8h, C-MnO₂12h and C-MnO₂16h electrodes at different current densities of 1-4 A g⁻¹, (D) GCD curves for C-MnO₂8h, C-MnO₂12h and C-MnO₂16h electrodes at 1 A g⁻¹ current density, (E) the variation of specific capacitance versus current densities and (F) Nyquist plots of C-MnO₂8h, C-MnO₂12h and C-MnO₂16h electrodes.

Fig. 3.10 (A-C) displays the galvanostatic charge-discharge (GCD) curves of C-MnO₂8h, C-MnO₂12h and C-MnO₂16h electrodes by passing current densities between 1-4 A g⁻¹ within potential window 0 to +0.9 V/SCE. The GCD curves of C-MnO₂8h electrode shows maximum charging and discharging time than the C-MnO₂12h and C-MnO₂16h electrodes at 1 A g⁻¹ current density, as depicted in **Fig. 3.10 (D)**. The triangular-shape of charge-discharge curves with a slight curvature is almost symmetric, again demonstrating the pseudocapacitive performance. It is observed that, specific capacitance decreases with enhancing the scan rate and current density. The variation of specific capacitance versus current density is demonstrated in **Fig. 3.10 (E)**. The specific capacitance obtained for C-MnO₂8h, C-MnO₂12h and C-MnO₂16h electrodes are 395, 662 and 503 F g⁻¹, respectively at 1 A g⁻¹ current density.

3.2.B.3.3 The EIS study (CBD)

The electrochemical impedance measurement is the study of resistive and capacitive components of MnO₂ electrode with consequence of the supercapacitive characteristics. The **Fig. 3.10 (F)** shows the Nyquist plots of C-MnO₂8h, C-MnO₂12h and C-MnO₂16h electrodes in frequency range of 0.1 kHz to 1 MHz with bias potential 10 mV. All Nyquist plots consists of partial semicircle in high frequency region and straight line in low frequency region. The slope of straight line in the low frequency region at 45° gives Warburg resistance (W). The Nyquist plots of MnO₂ display the small semicircle in the high frequency region indicating the low series resistance (R_s) and charge transfer resistance (R_{ct}). This is mainly ascribed to its good diffusion rate due to higher surface area. The solution resistance (R_s) values of 2.13, 2.11 and 2.25 Ω/cm⁻² and charge transfer resistance (R_{ct}) of 13.1, 7.5 and 11.3 Ω/cm⁻² are observed for C-MnO₂8h, C-MnO₂12h and C-MnO₂16h electrodes, respectively, as illustrated in **Table 3.2**. As known, the smaller R_{ct} means faster charge transfer rate in the reversible reaction between electrode and electrolyte. Therefore, being a C-MnO₂12h electrode of smaller R_{ct} among all samples has superior charge transfer rate. The high specific surface area can increase charge transfer rate, enhance contact area between electrode and electrolyte, so as to decrease the charge transfer resistance [32].

3.2.B.3.4 The stability study (CBD)

The good cycling stability of the electrode is prime requirement for real supercapacitor application. Long cycling stability of C-MnO₂12h electrode studied in 1 M Na₂SO₄ electrolyte by the cyclic voltammetry measurement at scan rate of 100 mV s⁻¹ for 5000 of CV cycles is demonstrated in **Fig. 3.10 (G)**. The capacitive retention of 95% is observed for C-MnO₂12h electrode. The capacitive retention versus cycle number plot of C-MnO₂12h electrode is shown in **Fig. 3.10 (H)**. The small decrement in the specific capacitance up to 5000 CV cycles can be credited to degradation of active substance through redox reaction of active material into electrolyte during charging-discharging.

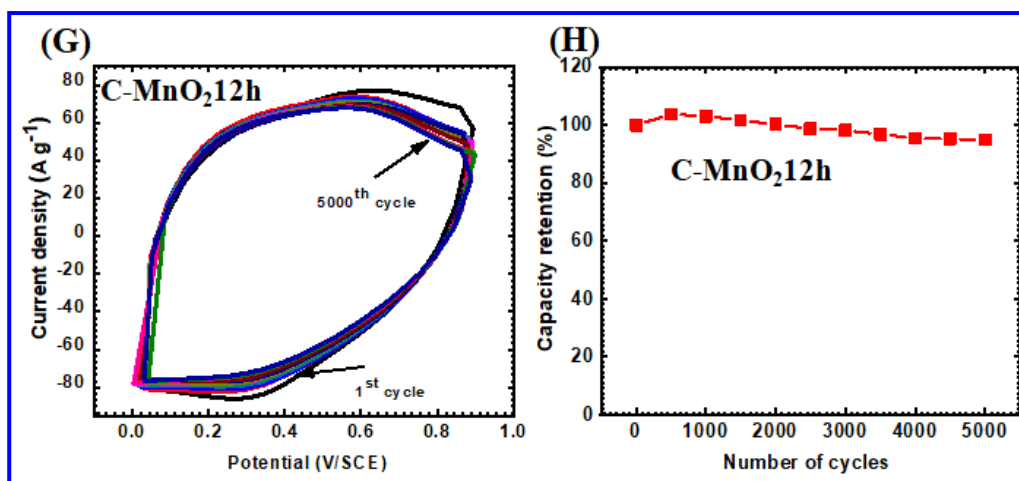


Fig. 3.10 (G) The CV curves of long cyclic stability of C-MnO₂12h electrode and (H) the capacitance retention versus cycle number plot of CMnO₂12h electrode.

Table 3.2: The electrochemical properties of C-MnO₂ and S-MnO₂ electrodes in 1 M Na₂SO₄ electrolyte.

Sr. No.	Sample	Specific capacitance (F g ⁻¹)	Capacity retention (%)	R _{ct} (Ω/cm ⁻²)	R _s (Ω/cm ⁻²)	Areal capacitance (mF cm ⁻²)
1	C-MnO ₂ 8h	413	89	13.1	2.13	387
2	C-MnO ₂ 12h	757	95	7.5	2.11	659
3	C-MnO ₂ 16h	564	61	11.3	2.25	472
4	S-MnO ₂ 30	383	77	83.5	1.70	353
5	S-MnO ₂ 60	512	88	24.4	1.15	435
6	S-MnO ₂ 90	294	90	180.2	2.69	153

3.2.B.3.5 The CV study (SILAR)

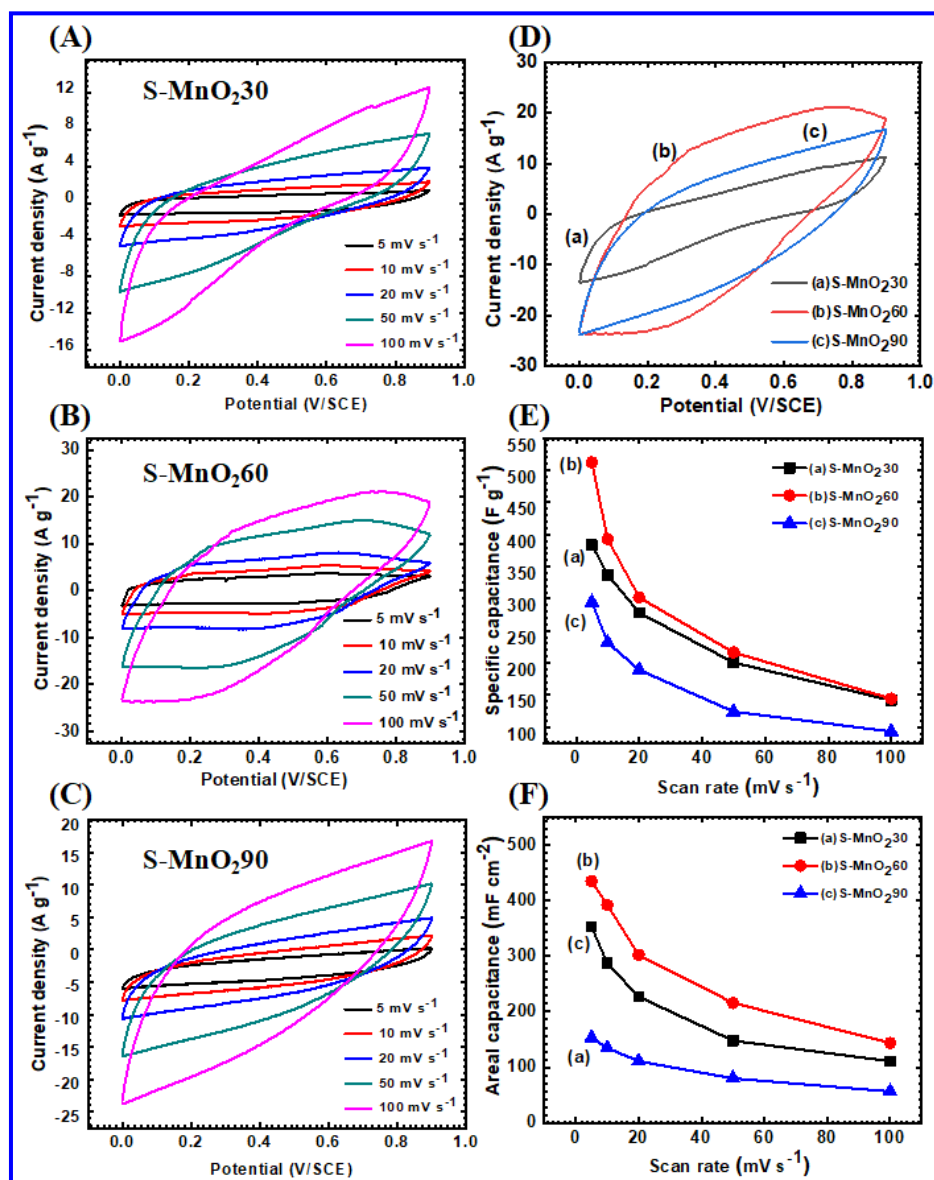


Fig. 3.11) The CV curves of (A-C) S-MnO₂30, S-MnO₂60 and S-MnO₂90 electrodes at various scan rates from 5 to 100 mV s⁻¹, (D) the CV curves of S-MnO₂30, S-MnO₂60 and S-MnO₂90 electrodes at scan rate of 100 mV s⁻¹, (E) graph of specific capacitance versus scan rates and (F) the plot of areal capacitance versus scan rates of S-MnO₂30, S-MnO₂60 and S-MnO₂90 electrodes.

The CV curves of S-MnO₂30, S-MnO₂60 and S-MnO₂90 electrodes analyzed within a potential range of 0 to +0.9 V/SCE at scan rates of 5 to 100 mV s⁻¹ are shown in **Fig. 3.11 (A-C)**. The CV curves are symmetric and area under CV curve confirms the storage of electrical charge of pseudocapacitive behavior [33]. The CV curve of S-MnO₂60 electrode shows the largest area as compared to S-MnO₂30 and S-MnO₂90 electrode at constant scan rate of 100 mV s⁻¹, as depicted in **Fig. 3.11 (D)**. The electrochemical measurements reveal that MnO₂ thin film obtained after 60 cycles

consist of mesoporous size with increased specific capacitance. The graph of specific capacitance versus scan rate is shown in **Fig. 3.11 (E)**. The specific capacitance of 383, 512 and 294 F g^{-1} are obtained for S-MnO₂30, S-MnO₂60 and S-MnO₂90 electrodes, respectively at scan rate of 5 mV s^{-1} . The areal specific capacitance versus scan rate is depicted in **Fig. 3.11 (F)**. The areal specific capacitances are 353, 435 and 153 mF cm^{-2} , at 5 mV s^{-1} scan rates. At low scan rate, all electrode active material takes part in slow redox reactions with inner and outer surface of MnO₂ electrode. At high scan rates, only outer surface S-MnO₂60 electrode is provided for fast redox reaction. Hence, at a low scan rate, specific capacitance is high.

3.2.B.3.6 The GCD studies (SILAR)

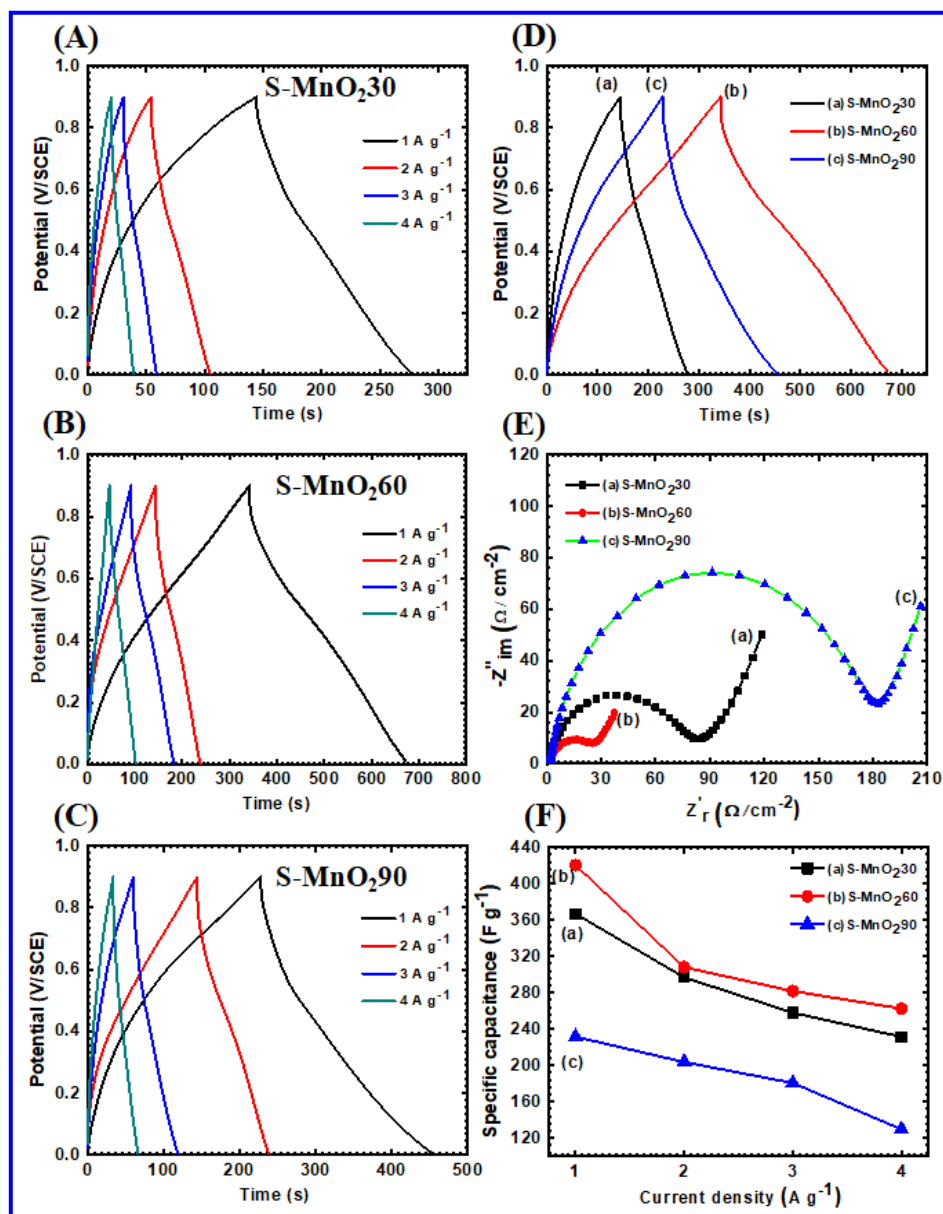


Fig. 3.12) The GCD curves of (A-C) S-MnO₂30, S-MnO₂60 and S-MnO₂90 electrodes at different current densities of 1–4 A g⁻¹, (D) GCD curves for S-MnO₂30, S-MnO₂60 and S-MnO₂90 electrodes at 1 A g⁻¹ current density, (E) the variation of specific capacitance versus current densities and (F) Nyquist plots of S-MnO₂30, S-MnO₂60 and S-MnO₂90 electrodes.

Fig. 3.12 (A-C) shows the GCD of S-MnO₂30, S-MnO₂60 and S-MnO₂90 electrodes at current densities from 1–4 A g⁻¹ within potential range of 0 to +0.9 V/SCE. The GCD curves of S-MnO₂60 electrode shows maximum charging and discharging time than the S-MnO₂30 and S-MnO₂90 electrodes at 1 A g⁻¹ current density, as depicted in **Fig. 3.12 (D)**. It is clear that the good non-linear and symmetric characteristics of GCD curves reveal the excellent electrochemical reversibility and ideal charge-discharge properties for all electrodes. The variation of specific capacitance versus current density is demonstrated in **Fig. 3.12 (E)**. The specific capacitances of 366, 420 and 231 F g⁻¹ at current density 1 A g⁻¹ is obtained for S-MnO₂30, S-MnO₂60 and S-MnO₂90 electrodes, respectively.

3.2.B.3.7 The EIS study (SILAR)

The electrochemical impedance spectroscopy (EIS) plots are analysed in the frequency range of 0.1 kHz to 1 MHz with bias potential of 10 mV. All Nyquist plots shown in **Fig. 3.12 (F)** consist of partial semicircle in high frequency region and straight line in low frequency region. All electrodes exhibited similar shape in a semicircle high frequency region and straight line at low frequency region. The solution resistance (R_s) values of 1.70, 1.15 and 2.69 Ω/cm^{-2} and charge transfer resistance (R_{ct}) of 83.5, 24.4 and 180.2 Ω/cm^{-2} are observed for S-MnO₂30, S-MnO₂60 and S-MnO₂90 electrodes, respectively as illustrated in **Table 3.2**. The S-MnO₂60 electrode displays lower charge transfer resistance (R_{ct}) than the S-MnO₂30 and S-MnO₂90 electrodes.

3.2.B.3.8 The stability study (SILAR)

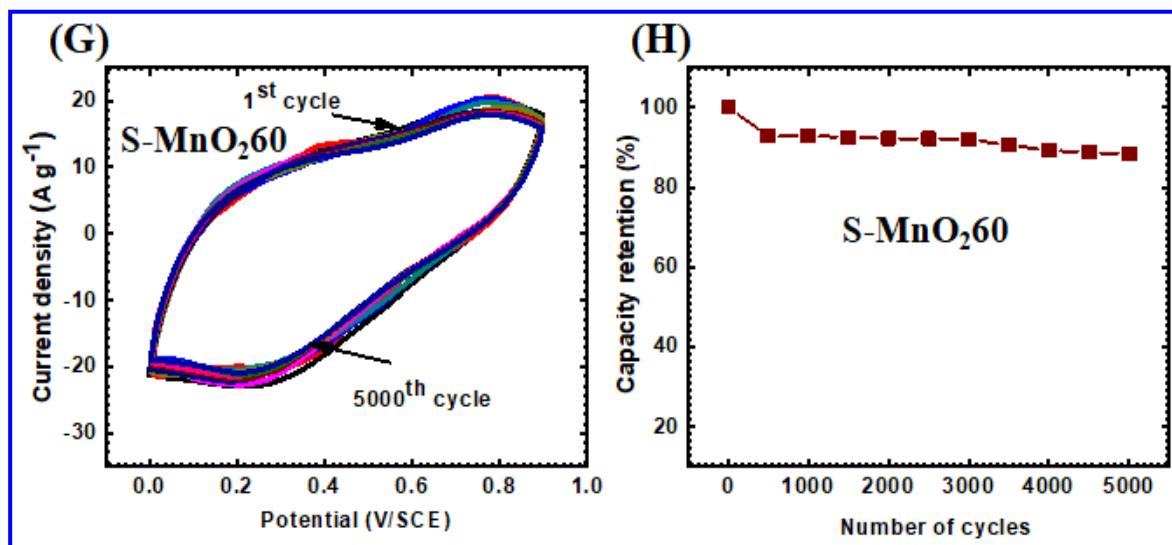


Fig. 3.12 (G) The stability CV curves of 5000 cycles S-MnO_{2.60} electrode and (H) plot of capacitance retention versus cycle number of S-MnO_{2.60} electrode.

The long-term cycling stability of S-MnO_{2.60} electrode studied by the cyclic voltammetry measurement at scan rate of 100 mV s⁻¹ for 5000 CV cycles is demonstrated in **Fig. 3.12 (G)**. The capacitive retention of 88% is observed for S-MnO_{2.60} electrode. The capacitive retention versus cycle number plot for S-MnO_{2.60} electrode is shown in **Fig. 3.12 (H)**. The comparison study of manganese oxide materials using CBD and SILAR methods for supercapacitor application is presented in **Table 3.3**.

Hu et al. [9] chemically synthesized nanoporous layered α -MnO₂ electrode and showed maximum specific capacitance of 447 F g⁻¹. Chodankar et al. [13] reported specific capacitance of 633 F g⁻¹ with CBD-MnO₂ method. Patil et al. [15] prepared nano-spheres of α -MnO₂ thin film with specific capacitance of 550 F g⁻¹. Singu et al. [14] prepared nanosphered α -MnO₂ using SILAR method and obtained specific capacitance of 262 F g⁻¹. Jana et al. [16] reported MnO₂-reduced graphene oxide composite electrode for supercapacitor application with maximum specific capacitance of 987 F g⁻¹. Dubal et al. [21] reported stepwise conversion of SILAR deposited Mn₃O₄ films into birnessite MnO₂ electrode for supercapacitor with specific capacitance of 314 F g⁻¹. Chen et al. [31] obtained specific capacitance of 550 F g⁻¹ for CBD deposited α -MnO₂ films.

Table 3.3: Comparison study of manganese oxide materials using CBD and SILAR methods for supercapacitor application.

Sr. No.	Deposited Material	Methods	Substrate	Electrolyte	Capacitance (F g ⁻¹)	Ref. No.
1.	δ -MnO ₂	CBD	SS	1 M Na ₂ SO ₄	447	[9]
2.	α -MnO ₂	CBD	SS	1 M Na ₂ SO ₄	633	[13]
3.	MnO ₂	SILAR	SS	1 M Na ₂ SO ₄	262	[14]
4.	α -MnO ₂	CBD	SS	1 M Na ₂ SO ₄	550	[15]
5.	MnO ₂ /RGO	SILAR	SS	1 M Na ₂ SO ₄	987	[16]
6.	MnO ₂	SILAR	SS	1 M Na ₂ SO ₄	314	[21]
7.	δ -MnO ₂	CBD	SS	1 M Na ₂ SO ₄	550	[31]
8.	α -MnO ₂	CBD	SS	1 M Na ₂ SO ₄	757	Present work
9.	Birnessite phase MnO ₂	SILAR	SS	1M Na ₂ SO ₄	512	Present work

Table 3.4: Comparison of supercapacitive properties of flexible symmetric supercapacitor device.

Sr. No	Supercapacitor Symmetric Electrode	Gel Electrolyte	Specific Capacitance (F g^{-1})	Energy Density (Wh kg^{-1})	Power Density (kW kg^{-1})	Stability (%) (cycles)	Ref. No.
3.	$\alpha\text{-MnO}_2/\text{FSS}$	PVA- Na_2SO_4	67.3	15.3	13	87.2 (1500)	[15]
1.	rGO@LaCe- MnO_2	Na_2SO_4	61	21.96	4	50 (3000)	[39]
2.	MWCNTs/ MnO_2	PVA- Na_2SO_4	204	23.3	-	80 (2500)	[40]
4.	MnO_2	PVP- LiClO_4	110	23	1.9	92 (2200)	[41]
5.	Graphene@carbon cloth	PVA- H_2SO_4	11.8	1.64	0.67	-	[42]
6.	Au- MnO_2/CNT	Na_2SO_4	68	4.5	33	-	[43]
7.	C-$\text{MnO}_2$12h	PVA-Na_2SO_4	128	14	0.2	90 (5000)	Present Work

SECTION - C

Flexible symmetric solid state supercapacitor (FSSSC) device fabrication and supercapacitive evaluation of C-MnO₂12h thin films.**3.2.C.1 Introduction**

The modern portable and flexible small size electronic equipments are required in fabrication of recent energy storage devices [34, 35]. The flexible symmetric solid state supercapacitor FSSSC device is one of the most hopeful energy storage devices and have been widely investigated recently [36-38]. The mechanical flexibility, inexpensive, light-weight, highly reliable, ease of handling and environment– friendly energy storage of supercapacitors are useful in portable and commercialized energy storage devices [1]. There is an essential to enhance the electrochemical performance of the FSSSC device which depends upon the active electrode material, electrolyte and supporting substrates. Among the different energy storage devices, pseudocapacitors have attracted more attention due to their high power density, long cycle life, low cost and good stability than that of batteries and higher energy density than that of dielectric capacitors [2].

In this chapter, MnO₂ thin films are prepared by using CBD and SILAR methods. In order to select the superior MnO₂ thin film to fabricate FSSSC device, electrochemical performance of best MnO₂ thin films was optimized [CBD (C-MnO₂12h) and SILAR (S-MnO₂60)] and compared. **Table 3.2** illustrates the electrochemical parameters of C-MnO₂12h and S-MnO₂60 thin films, which assist to choose the superior electrode to fabricate the symmetric FSSSC device. The results of C-MnO₂12h thin film are superior to S-MnO₂60 thin film, therefore C-MnO₂12h thin film was chosen to fabricate the FSSSC device.

The present section deals with the performance of symmetric FSSSC device fabricated using C-MnO₂12h thin film as cathode and anode electrodes with PVA-Na₂SO₄ gel as electrolyte as well as a separator. The section also deals with fabrication and electrochemical performance evaluation of symmetric FSSSC supercapacitor device.

3.2.C.2 Experimental details**3.2.C.2.1 Electrode Preparation**

The CBD method was employed to prepare C-MnO₂12h thin films on flexible SS substrate. The preparative parameters to prepare C-MnO₂12h thin films are described in (Section 3.2.A.2.3).

3.2.C.2.2 Preparation of PVA-Na₂SO₄ gel electrolyte

The PVA-Na₂SO₄ gel electrolyte is used in supercapacitor devices [15]. To prepare PVA based gel electrolyte, 6 gm of polyvinyl alcohol (PVA) was dissolved in 60 ml DDW at temperature of 353 K with constant stirring for 4 h to form clear and viscous solution, followed by drop-by-drop addition of 1 M Na₂SO₄ solution. This mixture was kept under constant stirring for 3 h to form uniform PVA-Na₂SO₄ gel electrolyte.

3.2.C.2.3 Fabrication of flexible symmetric solid state supercapacitor device

The flexible symmetric solid state device was assembled using C-MnO₂12h thin films with area of 5 x 5 cm². The schematic of fabricated C-MnO₂12h symmetric FSSSC device is showing in **Fig. 3.13**. The edges of electrode were sealed with plastic tape to avoid the short circuit. Then, to fabricate supercapacitor device, each electrodes painted by polyvinyl alcohol (PVA-Na₂SO₄) gel electrolyte was stacked on to each another and packed together using transparent plastic strips to avoid leakage. Moreover, the whole device was placed under hydraulic press at a pressure of 1 ton for 30 min. Such solid state device was tested using different electrochemical techniques.

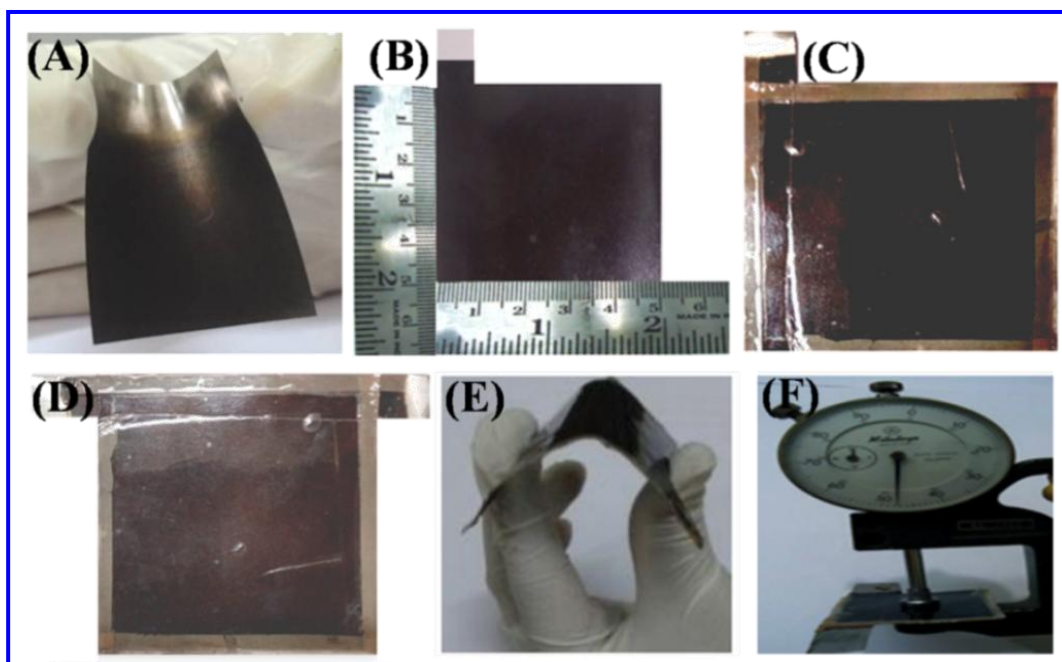


Fig. 3.13) (A) The MnO₂ electrode prepared by CBD method with mechanical flexibility of substrate, (B) C-MnO₂12h electrode (5 X 5 cm²), (C) the painting thin layer of PVA–Na₂SO₄ gel electrolyte on electrode, (D) actual fabricated C-MnO₂12h//PVA–Na₂SO₄//C-MnO₂12h symmetric device, (E) the mechanical flexibility of FSSSC device and (F) the hydraulic press used to apply pressure on FSSSC device.

3.2.C.3 Electrochemical properties of flexible symmetric solid state supercapacitor (FSSSC) device

3.2.C.3.1 The CV study

The CV curves of FSSSC device in potential window from 0 to 0.9 V at scan rate of 100 mV s⁻¹ are illustrated in **Fig. 3.14 (A)**. The nature of CV curves do not distort with changing scan rate, indicating promising charge-discharge performance for symmetric device. The CV curves in potential window from 0 to 0.9 V at various scan rate of 5-100 mV s⁻¹ are shown in **Fig. 3.14 (B)**. The high specific capacitance (C_s) at low scan rate is due to more utilization of active material and time for electrochemical reaction. The value of C_s of FSSSC device is 122 F g⁻¹ at scan rate of 5 mV s⁻¹. The plot of variation of C_s with scan rate is shown in **Fig. 3.14 (C)**. The observed specific capacitance values of FSSSC device in current work are comparatively higher than reported for earlier symmetric as shown devices in **Table 3.4**. Rajagopal et al. [39] reported hydrothermal synthesized rGO-mixed LaCe-MnO₂ nanocomposite electrodes with specific capacitance of 61 F g⁻¹. The MWCNTs/MnO₂ electrode was reported with maximum specific capacitance values of 204 F g⁻¹ using electrodeposition method [40]. The report on MnO₂ electrode showed maximum specific capacitance values of 110 F g⁻¹ for CBD method [41]. Wang et al. [42] reported graphene@carbon cloth supercapacitor electrode with maximum specific capacitance of 11.8 F g⁻¹ using electrophoretic deposition method. Also, Au-MnO₂/CNT composite electrode by electrodeposition method showed electrochemical specific capacitance of 68 F g⁻¹ electrode [43].

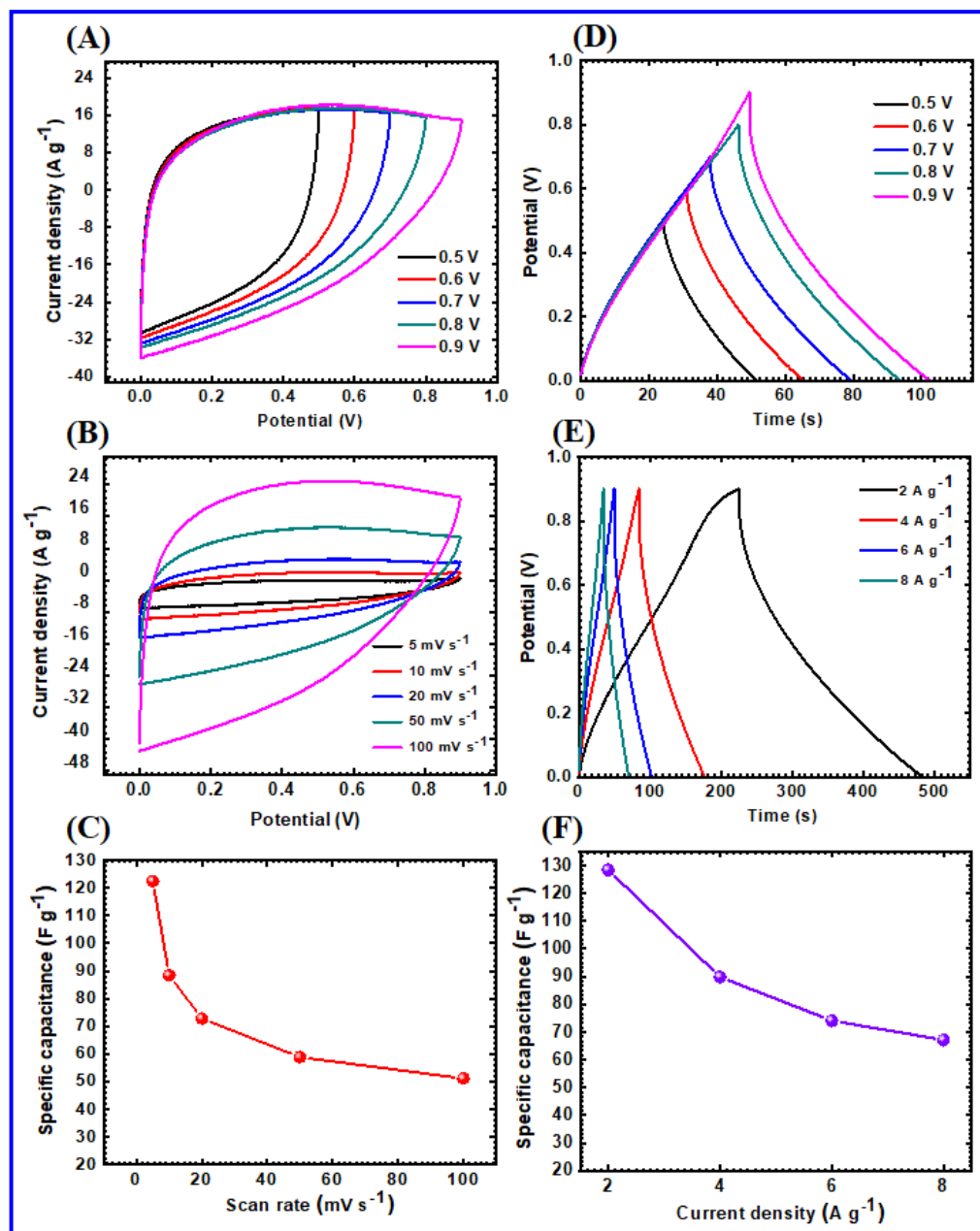


Fig. 3.14 (A) Potential window selection in voltage ranging from 0 to 0.9 V, (B) the CV curves of symmetric device at different scan rates 5–100 mV s⁻¹, (C) the graph of specific capacitance versus scan rate, (D) the GCD curves at 4 A g⁻¹ in different voltage range from 0 to 0.9 V, (E) the GCD curves at current densities 2 to 8 A g⁻¹ and (F) the graph of specific capacitance versus current densities.

3.2.C.3.2 The GCD study

The GCD curves of FSSSC device in potential windows from 0 to +0.9 V at constant current density of 4 A g⁻¹ is plotted in **Fig. 3.14 (D)**. The GCD curves of FSSSC device at current densities of 2, 4, 6 and 8 A g⁻¹ within operating potential window from 0 to 0.9 V are shown in **Fig. 3.14 (E)**. A good triangular shaped GCD curves are observed at all current densities signifying ideal supercapacitive behaviour.

The calculated C_s versus current density is depicted in **Fig. 3.14 (F)** which demonstrates maximum C_s of 128 F g^{-1} at current density of 2 A g^{-1} .

3.2.C.3.3 Ragone plot and EIS study

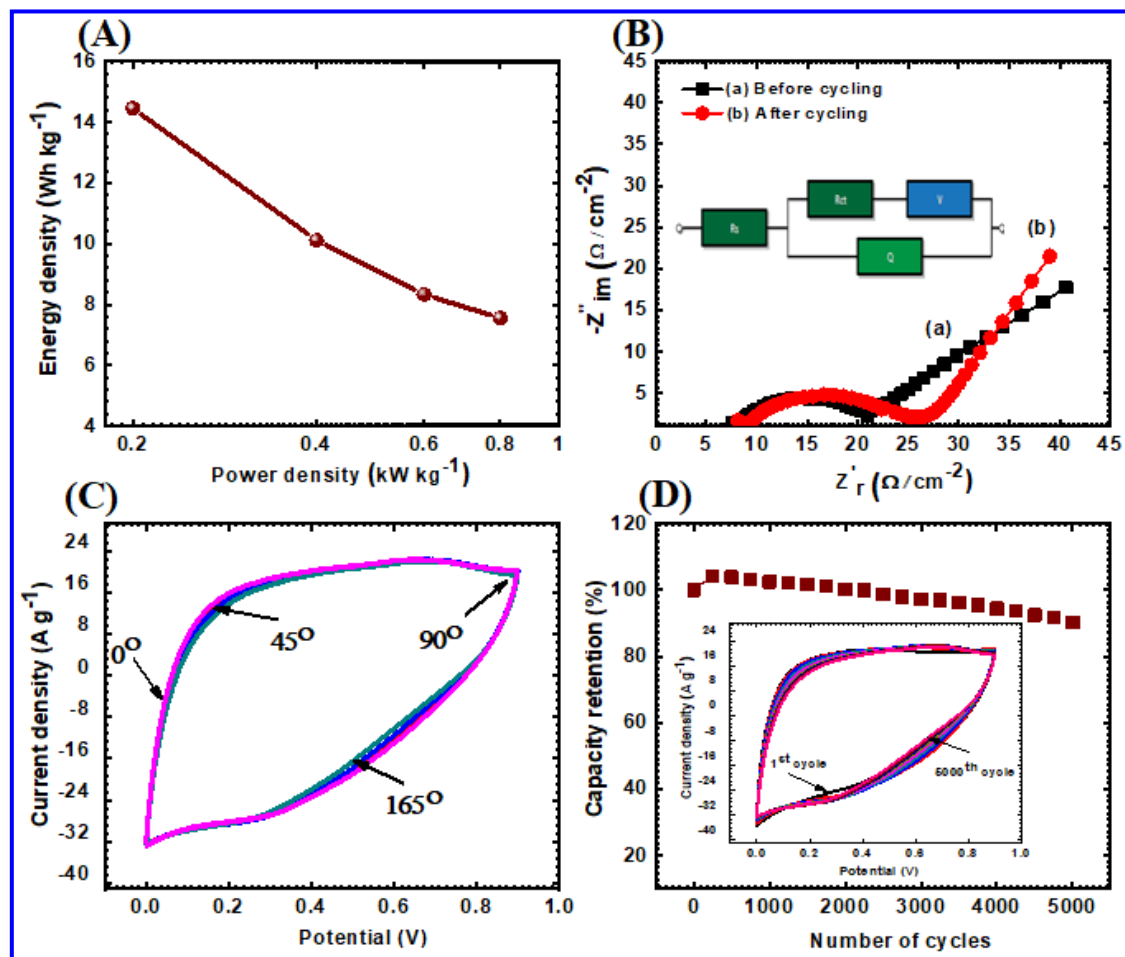


Fig. 3.15 (A) Ragone plot, (B) Nyquist plots of symmetric device of before and after cycling and (inset shows equivalent circuit), (C) the CV curves of symmetric device at different bending angles of 0-165° at scan rate 100 mV s^{-1} and (D) the plot of capacitance retention versus cycle number (inset shows stability CV curves of 5000 cycle) of device.

The ED and PD calculated from GCD curves are displayed in **Fig. 3.15 (A)**. The device shows maximum ED of 14.4 Wh kg^{-1} and PD 0.2 kW kg^{-1} , respectively. The C-MnO₂12h electrode showed excellent electrochemical performance due to high surface area, high electrical conductivity and low charge transfer resistance.

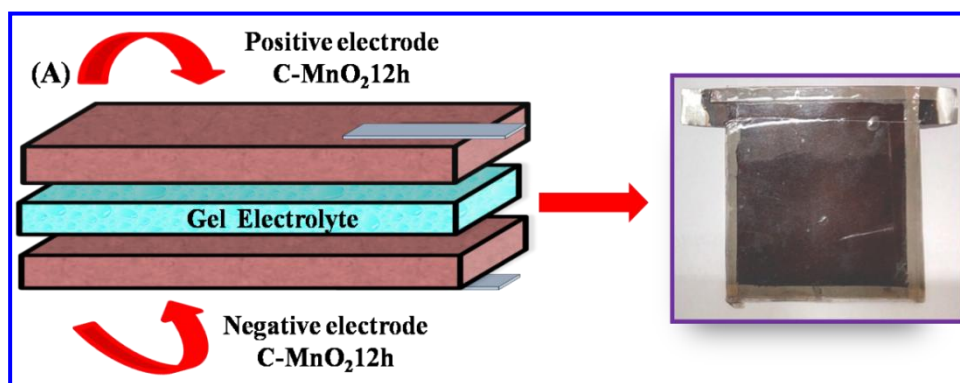
Nyquist plots of FSSSC device before and after 5000 CV cycling are shown in **Fig. 3.15 (B)** and inset image shows equivalent circuit. The C-MnO₂12h electrode shows nearly similar shape in the high frequency region before and after cycling stability. However, **Fig. 3.15 (B)** shows the values of $R_s = 7.4 \text{ Ω/cm}^{-2}$ and $R_{ct} = 21.26$

Ω/cm^{-2} for C-MnO₂12h electrode before cycling which is slightly lower than after cycling (R_s 8.5/ $\Omega \text{ cm}^{-2}$ and R_{ct} 27.99 Ω/cm^{-2}).

3.2.C.3.4 Mechanical flexibility and stability studies

The mechanical flexibility and resilience are important factors to make supercapacitor useful for domestic applications. Here, we have tested the electrochemical performance of FSSSC to insure its preservation of electrochemical properties after bending. The CV plots of bending positions of device at 0, 45, 90, and 165° are shown in **Fig. 3.15 (C)**. The capacitive retention versus cycle number plots of FSSSC device is represented in **Fig. 3.15 (D)**. Furthermore, 5000 CV cycles are repeated to test the stability FSSSC device (Inset of **Fig. 3.15 (D)**). The maximum capacitive retention 90% is observed after 5000 CV cycles. This signifies the excellent adhesion of active electrode material with proper interface between gel electrolyte and electrode material.

3.2.C.3.5 Demonstration of symmetric C-MnO₂12h device



The schematic of flexible symmetric solid state device formation is depicted in **Fig. 3.16 (A)**. The practical demonstration of fabricated large area (5 x 5 cm²) series connected symmetric devices is showed in **Fig. 3.16 (B)**. One device has +0.9 V operating potential window, so the series combination of the two devices gives a total potential up to +1.8 V. Initially, these FSSSC devices are charged with a potential of +1.8 V for 30 s and discharged through panel of 211 red LEDs (DYPU CDL GROUP) which glowed for 160 seconds. **Fig. 3.16 (B)** shows photographs captured at discharging of symmetric device. The measured storing output power of device is 0.364 mWcm⁻² which signifies excellent charge storing capability. Forward biased I-V characteristics of red LED is shown in **Fig. 3.16 (C)** for comparison.

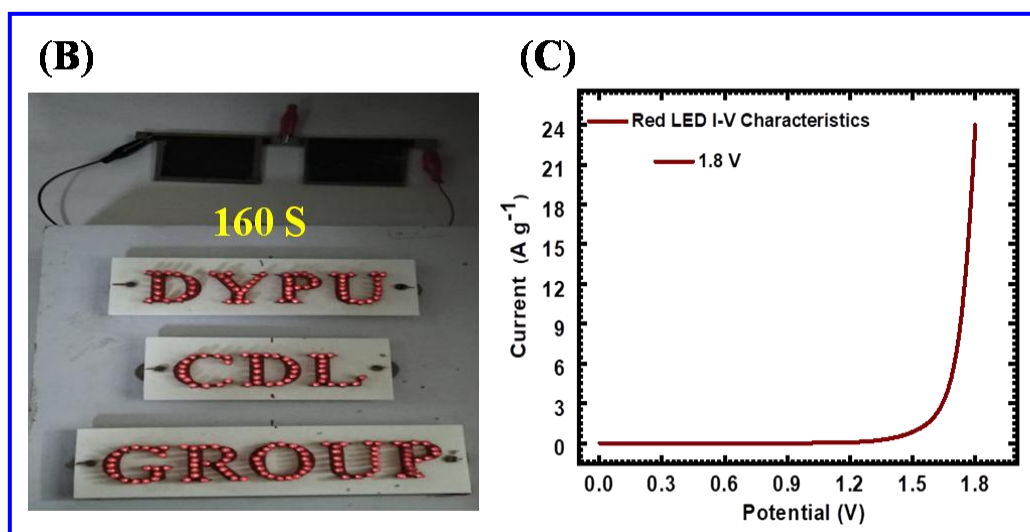


Fig. 3.16 The schematic of (A) flexible symmetric solid state device formation, (B) the demonstration of two series connected symmetric devices charged at + 1.8 V for 30 s, and the discharged through a panel of 211 red LEDs (DYPUCDL GROUP) glows for 160 s and (C) the forward biased I-V characteristics of red LED.

3.3 Conclusions

The present work is a comparative study of properties and their supercapacitance performance of MnO₂ thin films deposited using CBD and SILAR methods. The CBD method results into fine grain nano-particles with α -MnO₂ phase. The CBD α -MnO₂ films deposited for 12 hours showed maximum specific capacitance values of 757 F g⁻¹ as compared to SILAR deposited \square -MnO₂ films. The EIS measurement showed that highly porous C-MnO₂ electrode provides low charge transfer resistance, for easy access to ions for intercalation/deintercalation as compared to S-MnO₂ electrodes. The CV stability showed excellent capacity retention of 95% for C-MnO₂12h electrode after 5000 cycles. These results show that CBD deposited α -MnO₂ film exhibits better performance than SILAR deposited \square -MnO₂ films. The flexible symmetric solid state supercapacitor device with configuration of C-MnO₂12h//PVA-Na₂SO₄//C-MnO₂12h showed maximum specific capacitance of 128 F g⁻¹ with ED 14 Wh kg⁻¹ at PD 0.2 kW kg⁻¹. In addition, FSSSC device exhibited capacitive retention of 90% for 5000 CV cycles. This device is feasible for practical applications as it can store energy of 0.364 mW cm⁻² and is able to glow 211 red LEDs (DYPUCDL GROUP) for period of 160 s with two devices connected in series.

3.4 References

- [1] L. Zhang, X. Zhao, Chem. Soc. Rev. Chem. Soc. Rev., 38, (2009), 2520-253.
- [2] A. Yang, Y. Xue, Y. Zhang, X. Zhang, H. Zhao, X. Li, Y. He, Z. Yuan, J. Mater. Chem., 22, (2012), 112-117.
- [3] Z. Fan, J. Yan, T. Wei, L. Zhi, G. Ning, T. Li, F. Wei, Adv. Funct. Mater., 21, (2011), 2366-2375.
- [4] Y. Wang, J. Guo, T. Wang, J. Shao, D. Wang, Y. Yang, Nanomater., 5, (2015), 1667-1689.
- [5] B. Sankapal, H. Gajare, S. Karade, R. Salunkhe, D. Dubal, Electrochim. Acta, 192, (2016), 377-384.
- [6] M. Huang, F. Li, J. Ji, Y. Zhang, X. Zhao, X. Gao, CrystEngComm., 16, (2014), 2878-2884.
- [7] Y. Zhang, M. Huang, F. Li, Z. Wen, Int. J. Electrochem. Sci., 8, (2013), 8645-8661.
- [8] S. Devaraj, N. Munichandraiah, Solid-State Lett., 8, (2005), A373-A377.
- [9] Y. Hu, H. Zhu, J. Wang, Z. Chen, J. Alloys and Compd., 42, (2011), 10234-10240.
- [10] S. Sartale, C. Lokhande, Mater. Chem. Phys., 72, (2001), 101-104.
- [11] H. Sun, D. Qin, S. Huang, X. Guo, D. Li, Y. Luo, Q. Meng, Energ. Environ. Sci., 4, (2011), 2630-2637.
- [12] W. Cui, C. Ge, Z. Xing, A. Asiri, X. Sun, Electrochim. Acta, 137, (2014), 504-510.
- [13] N. Chodankar, G. Gund, D. Dubal, C. Lokhande, RSC Adv., 4, (2014), 61503-61513.
- [14] B. Singu, K. Yoon, J. Alloys and Compd. 695, (2017), 771-778.
- [15] A. Patil, A. Lokhande, P. Shinde, C. Lokhande, ACS Appl. Mater. Interfaces, 10, (2018), 16636-16649.
- [16] M. Jana, S. Saha, P. Samanta, N. Murmu, N. Kim, T. Kuila, J. Lee, J. Power Sources, 340, (2017), 380-392.
- [17] C. Chen, W. Fu, C. Yu, Mater. Lett., 82, (2012), 133-136.
- [18] M. Ghaemi, F. Ataherian, A. Zolfaghari, S. Jafari, Electrochim. Acta, 53, (2008), 4607-4614.
- [19] C. Julien, M. Massot, C. Poinson, Acta, 60, (2004), 689-700.
- [20] D. Dubal, D. Dhawale, R. Salunkhe, S. Pawar, C. Lokhande, Appl. Surf. Sci., 256, (2010), 4411-4416.
- [21] M. Ocana, Colloid. Polym. Sci., 278, (2000), 443-449.
- [22] Y. Kang, B. Kim, H. Chung, W. Kim, Synth. Met., 160, (2010), 2510-2514.
- [23] D. Dubal, C. D. Lokhande, Ceram. Int., 39, (2013), 415-423.

- [24] G. Gund, D. Dubal, N. Chodankar, J. Cho, P. Romero, C. Park, C. Lokhande, *Nature*, 5, (2015), 12454-1-12454-13.
- [25] A. Patil, V. Lokhande, U. Patil, P. Shinde, C. Lokhande, *ACS Sustainable Chem. Eng.*, 6, (2018), 787-802.
- [26] D. Dubal, D. Dhawale, R. Salunkhe, C. Lokhande, *J. Electroanal. Chem.*, 647, (2010), 60-65.
- [27] X. Li, Q. Li, Y. Wu, M. Rui, H. Zeng, *ACS Appl. Mater. Inter.*, 7, (2015), 19316-19323.
- [28] J. Yan, Z. Fan, T. Wei, J. Cheng, B. Shao, K. Wang, L. Song, M. Zhang, *J. Power Sources*, 194, (2009), 1202-1207.
- [29] G. Gund, D. Dubal, S. Shinde, C. Lokhande, *ACS Appl. Mater. Interfaces*, 6, (2014), 3176-3188.
- [30] J. Zhao, B. Guan, B. Hu, Z. Xu, D. Wang, H. Zhang, *Electrochim. Acta.*, 230, (2017), 428-437.
- [31] X. Chen, H. Song, Z. Zhang, Y. He, *Electrochim. Acta.*, 117, (2014), 55-61,
- [32] Y. Hu, J. Wang, X. Jaiang, Y. Zheng, Z. Chen, *Appl. Surf. Sci.*, 271, (2013), 193-201,
- [33] N. Chodankar, D. Dubal, G. Gund, C. Lokhande, *J. of Energy Chem.*, 25, (2016), 463-471.
- [34] P. Simon, Y. Gogotsi, *Nat. Mater.*, 7, (2009), 320-329.
- [35] H. Wang, Y. Liang, T. Mirfakhrai, Z. Chen, H. Casalongue, H. Dai, *Nano Res.*, 4, (2011) 729-736.
- [36] X. Li, T. Zhao, Q. Chen, P. Li, K. Wang, M. Zhong, J. Wei, D. Wu, B. Wei, H. Zhu, *Phys. Chem. Chem. Phys.*, 15, (2013), 17752-17757.
- [37] C. Meng, C. Liu, L. Chen, C. Hu, S. Fan, *Nano Lett.*, 10, (2010), 4025–4031.
- [38] G. Xiong, C. Meng, R. Reifengerger, P. Irazoqui, T. Fisher, *Adv. Energy Mater.*, 4, (2014), 1300515-1300524.
- [39] R. Rajagopal, K. Ryu, *ChemElectroChem*, 5, (2018), 2218-2227,
- [40] N. Chodankar, S. Ji, D. Kim, *J. Taiwan Inst Chem Eng.*, 80, (2017), 503-510.
- [41] N. Chodankar, D. Dubal, G. Gund, C. Lokhande, *Electrochim. Acta*, 165, (2015), 338-347.
- [42] S. Wang, B. Pei, X. Zhao, R. Dryfe, *Nano Energy*, 2, (2013), 530-536.
- [43] A. Reddy, M. Shaijumon, S. Gowda, P. Ajayan, *J. Phys. Chem. C*, 114, (2010), 658-663.

CHAPTER-4

**BINDER FREE LANTHANUM DOPED
MANGANESE OXIDE @ GRAPHENE OXIDE
COMPOSITE AS HIGH ENERGY DENSITY
ELECTRODE MATERIAL FOR FLEXIBLE
SYMMETRIC SOLID STATE
SUPERCAPACITOR**

HAPTER-4

Binder Free Lanthanum Doped Manganese Oxide @ Graphene Oxide Composite as High Energy Density Electrode Material for Flexible Symmetric Solid State Supercapacitor

Sr. No.	Title	Page No.
4.1	Introduction	84
Section- A Synthesis and characterization of lanthanum doped manganese oxide @ graphene oxide thin films using SILAR method.		
4.2 A.1	Introduction	85
4.2.A.2	Experimental details	85
	4.2.A.2.1 Chemicals	85
	4.2.A.2.2 Synthesis of Graphene oxide (GO)	85
	4.2.A.2.3 Synthesis of GO thin film	86
	4.2.A.2.4 Synthesis of MnO ₂ and La-doped MnO ₂ thin films	86
	4.2.A.2.5 Synthesis of La-doped 3%MnO ₂ @GO thin film	86
	4.2.A.2.6 Thin film characterizations	87
4.2.A.3	Results and discussion	88
	4.2.A.3.1 XRD analysis	88
	4.2.A.3.2 FT-IR analysis	89
	4.2.A.3.3 FE-SEM analysis	90
	4.2.A.3.4 TEM analysis	92
	4.2.A.3.5 EDX analysis	93
	4.2.A.3.6 Surface Wettability	93
	4.2.A.3.7 The XPS study	94
	4.2.A.3.8 BET analysis	95
Section- B Supercapacitive evaluation of MnO₂, La-doped MnO₂ and La-MnO₂@GO thin films by SILAR method.		
4.2.B.1	Introduction	97
4.2.B.2	Results and discussion	97

	4.2.B.2.1	The CV studies	97
	4.2.B.2.2	The GCD studies	100
	4.2.B.2.3	The EIS studies	102
	4.2.B.2.4	The stability studies	103
<p style="text-align: center;">SECTION- C</p> <p>Flexible solid state symmetric supercapacitor (FSSSC) device fabrication and supercapacitive evaluation of 3%La-MnO₂@GO thin films.</p>			
4.2.C.1	Introduction		103
4.2.C.2	Experimental details		104
	4.2.C.2.1	Electrode Preparation	104
	4.2.C.2.2	Preparation of PVA-Na ₂ SO ₄ gel electrolyte	104
	4.2.C.2.3	Fabrication of flexible solid state symmetric supercapacitor device	104
4.2.C.3	Electrochemical properties of flexible solid state symmetric supercapacitor (FSSSC) device		105
	4.2.C.3.1	The CV studies	105
	4.2.C.3.2	The GCD studies	106
	4.2.C.3.3	Ragone plots	107
	4.2.C.3.4	The EIS studies	109
	4.2.C.3.5	Mechanical flexibility and stability studies	110
	4.2.C.3.6	Practical demonstration of symmetric FSSSC device	111
4.3	Conclusions		112
4.4	References		113

4.1. Introduction

Portable and small supercapacitors are essential in assembly of recent energy storage devices, which show mechanical flexibility, light weight and low-cost [1]. The main research focus has been on improvement of electrochemical energy storage device with high energy and power densities along with cycling stability. The transition metal oxides like RuO_2 , MnO_2 , ZnO , NiO , CuO , SnO_2 and conducting polymers are used as electrode materials in supercapacitor [2-8]. The Ceramics and MXenes ($\text{M}_{n+1}\text{X}_n\text{T}_x$ where, M shows a transition metal, X is carbon or nitrogen and T_x represents surface terminations) also emerging materials for energy storage with excellent electrochemical properties due to their high rate charge transfer. The properties of these materials are excellent due to the formation of plane to point network which results in to high electrical conductivity. However, these materials require complicated and high temperature processing which makes it disagreeable material for large scale production at low cost [9].

The 2D single layered graphene oxide has more fascinating properties such as excellent electrical conductivity, high mechanical strength, high surface area and low cost [10]. Many researchers have focused on the preparation of carbon materials composite with metal oxides and conducting polymers [11]. In order to solve these problems, carbon based materials composed with metal oxides have great potential as an electrode owing to their outstanding mechanical, optical and high electrochemical performance [12].

The electrochemical properties of MnO_2 can be easily improved with doping of metal ions [13]. The metals such as Cu, Fe, V, Co, and Ni have been successfully doped into the structure of MnO_2 and studied for electrochemical performance [14, 15]. In recent years, rare earth metals are investigated due to their unique optical, magnetic and excellent semiconductor properties. The rare earth metal oxides exhibit various composition, structure and presence of 4f electrons. The rare earth La_2O_3 compound has been studied for optical, gas sensor and gate dielectric applications [16].

The present chapter is divided into three sections (Sections A, B and C). In the present work, MnO_2 , La-doped MnO_2 and $\text{La-MnO}_2@\text{GO}$ composite thin films are synthesized using facile, inexpensive and binder free successive ionic layer adsorption and reaction (SILAR) method and their characterizations are discussed in Section 'A'.

The crystal structure, morphology and chemical composition are investigated. The Section 'B' is associated with the electrochemical performance of MnO_2 , La-doped MnO_2 and $\text{La-MnO}_2@\text{GO}$ thin films in 1 M Na_2SO_4 electrolyte. Section 'C' deals with the flexible solid state symmetric supercapacitor device configuration of $\text{SS}/3\%\text{La-MnO}_2@\text{GO}/\text{PVA-Na}_2\text{SO}_4/3\%\text{La-MnO}_2@\text{GO}/\text{SS}$ is fabricated and their electrochemical performance.

SECTION – A

Synthesis and characterization of MnO_2 , La-doped MnO_2 and $\text{La-MnO}_2@\text{GO}$ thin films using SILAR method

4.2 A.1 Introduction

The present section deals with the synthesis and characterization of MnO_2 , La-doped MnO_2 and $\text{La-MnO}_2@\text{GO}$ composite thin films by simple and economical SILAR method.

4.2.A.2 Experimental details

4.2.A.2.1 Chemicals

All analytical grade (AR) chemicals such as manganese sulfates (MnSO_4), lanthanum chloride (LaCl_3), potassium permanganate (KMnO_4) natural graphite flex, sulphuric acid (H_2SO_4 98%), hydrogen peroxide (H_2O_2 30%), sodium nitrate (NaNO_3) and hydrochloric acid (HCl 35.4%) were procured from Thomas Baker Ltd. India and used as received. The double distilled water (DDW) was used as a solvent.

4.2.A.2.2 Synthesis of Graphene Oxide (GO)

Graphene oxide (GO) was prepared using modified Hummers method [17]. Graphite flake (5 g) and NaNO_3 (2.5 g) were added into 120 ml of concentrated H_2SO_4 in an ice bath with stirring for 30 minutes after that slowly adding KMnO_4 (15 g) in the mixture with stirring for 150 minutes. After that, the mixture was stirred for 720 minutes at a temperature of 300 K in a water bath. The mixture was diluted with 800 ml of DDW. Successively, 150 ml of diluted 30% H_2O_2 was added drop wise to the deep brown mixture to reduce the residual KMnO_4 after which color of the mixture became bright yellow. For purification, the mixture was washed with HCl and DDW several times. Then, the suspension was centrifuged at 10,000 rpm several times for 20

min. Further, the GO was exfoliated in DDW using the ultrasonic bath. Finally, the homogeneously dispersion of brown colored of graphene oxide solution was obtained and used for the deposition of thin films.

4.2.A.2.3 Synthesis of GO thin film

Layer-by-Layer (LBL) method was used for the preparation of GO thin films. Typically, 1 mg ml^{-1} GO was exfoliated in 50 ml DDW using the ultrasonic bath at 30 min for homogeneously dispersion. After, the ultrasonication a well-dispersed brown colored GO solution. Further, the precleaned SS substrate is vertically immersed in GO solution for 50 s to adsorb GO sheets and air dried for 40 s. These LBL deposition cycles were repeated 60 times to get uniform GO film on the substrate.

4.2.A.2.4 Synthesis of MnO_2 and La-doped MnO_2 thin films

The MnO_2 and 1, 3, 5 volume % La-doped MnO_2 film electrodes were synthesized using SILAR method at room temperature (300 K). In typical synthesis, separately prepared 0.05 M LaCl_3 and 0.05 M MnSO_4 solutions were mixed in various volumetric ratios as 0:50, 0.5:49.5, 1.5:48.5 and 2.5:47.5 to obtain final solution of 50 ml. For deposition of MnO_2 and La-doped MnO_2 thin films, above mixed solutions were used as a cationic precursor and 0.03 M KMnO_4 solution as an oxidizing agent. Initially, the well cleaned SS substrate was dipped in cationic solutions for 10 s to adsorb La^{3+} and Mn^{2+} ions, followed by rinsing in DDW for 10 s to remove loosely bound ions. Then, the SS substrate was dipped in KMnO_4 solution for 10 s to form MnO_2 or La- MnO_2 film and again rinsed in DDW for 10 s to remove unreacted and loosely bound species from SS substrate. After 50 cycles, film of MnO_2 or La-doped MnO_2 was coated on SS substrate. These films were denoted as MnO_2 , 1%La-Mn, 3%La-Mn, 5%La-Mn, for 0, 1, 3 and 5 % volumetric ratios of LaCl_3 solutions, respectively.

4.2.A.2.5 Synthesis of 3%La-doped in MnO_2 @GO thin films

Typically, 1 mg ml^{-1} of GO was dispersed in 50 ml DDW with the sonication for 30 min. The LaCl_3 and MnSO_4 solutions in volumetric ratio 1.5:48.5 ml were mixed and used as cationic precursor and KMnO_4 solution was used as anionic precursor. The SS substrate was immersed in solution of GO for 50 s and air dried for 40 s to deposit GO sheets on SS substrate. Further, this substrate was dipped in

cationic solution for 10 s to adsorb $\text{La}^{3+}\text{-Mn}^{2+}$ ions on GO sheets followed by rinsing in DDW for 10 s to remove loosely bound $\text{La}^{3+}\text{-Mn}^{2+}$ ions. After that, the substrate was immersed in KMnO_4 solution for 10 s to form layer of 3% $\text{La-MnO}_2\text{@GO}$ material on SS substrate. Further, substrate was rinsed in DDW for 10 s to remove excess and unreacted species. Such 50 cycles were repeated to get uniform 3% $\text{La-MnO}_2\text{@GO}$ composite film. The schematic of deposition of 3% $\text{La-MnO}_2\text{@GO}$ film is shown in Fig. 4.1.

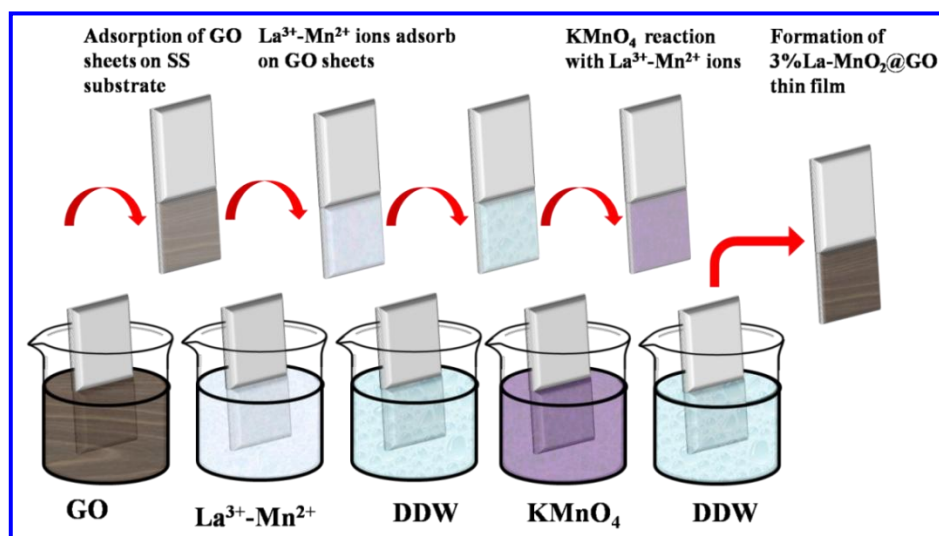


Fig. 4.1) The schematic of deposition of 3% $\text{La-MnO}_2\text{@GO}$ thin film synthesis using SILAR method.

4.2.A.2.6 Thin film characterizations

The structural analysis of MnO_2 , 1, 3, 5 % La-doped MnO_2 and 3% $\text{La-MnO}_2\text{@GO}$ thin films was carried out using X-ray diffraction (XRD) technique by Rigaku miniflex-600 new model with $\text{Cu K}\alpha$ ($\lambda = 0.154 \text{ nm}$) radiation, operated at 30 kV through scan rate of $2^\circ/\text{min}$. To study chemical bonding in deposited materials, the Fourier transform infrared (FT-IR) spectra of samples were recorded using an alpha (II) Bruker instrument. The field-emission scanning electron microscopy (FE-SEM, JEOL-6360, Japan) coupled with energy dispersive X-ray spectroscopy (EDX), (Oxford, X-max) was used to observe the surface morphology and chemical composition. The contact angle measurement was carried out using Rame Hart-500 advanced goniometer to observe the hydrophilic/hydrophobic nature of thin film electrodes. The specific surface area and pore size distribution were obtained through Brunauer-Emmett-Teller (BET) and Barrette-Joyner-Halenda (BJH) methods using BEL-SORP-II mini method. The ZIVE MP1 multichannel electrochemical workstation

equipment was used to measure the supercapacitive properties of thin film electrodes in 1M Na₂SO₄ electrolyte using three electrode system and flexible solid state symmetric supercapacitor device configuration of SS/3%La-MnO₂@GO/PVA-Na₂SO₄/3%La-MnO₂@GO/SS.

4.2.A.3 Results and discussion

4.2.A.3.1 XRD analysis

The XRD patterns of (a) MnO₂, (b-d) 1, 3, 5 % La-doped MnO₂ and (e) 3%La-MnO₂@GO thin films on SS substrate are shown in **Fig. 4.2 (A)**. The two major peaks in MnO₂ XRD patterns at $2\theta = \sim 21.9^\circ$ and $2\theta = \sim 28.6^\circ$ correspond to planes of (110) and (310) tetragonal phase of α -MnO₂ (JCPDS card no. 14-0140) [18]. The low intensity of XRD peaks confirms lower crystalline nature of MnO₂ thin films. The XRD patterns (b-d) related to La doping do not show any peak corresponding to the pure lanthanum or compounds such as La₂O₃ or LaO₃ phases. With La doping slight shift of $\sim 0.5^\circ$ in peak positions is observed along with increase in peak intensities, as the ionic radius of La³⁺ (0.106 nm) is higher than Mn⁴⁺ (0.54 nm). Small amount of La³⁺ ions introduced into MnO₂ lattice interface leads to the shift of diffraction peaks. In the XRD pattern of 3%La-MnO₂@GO thin film (**Fig. 4.2 (e)**) the peak at $2\theta = \sim 11.2^\circ$ corresponds to GO (001) plane [17]. The low intense diffraction peaks in present XRD patterns signify the nanocrystalline nature which is essential for supercapacitor application [19]. **Fig. 4.2 (B)** the XRD peak at $2\theta = \sim 11.2^\circ$ corresponds to GO (001) plane is confirms [17]. The peak marked by sign ‘#’ corresponds to the SS substrate.

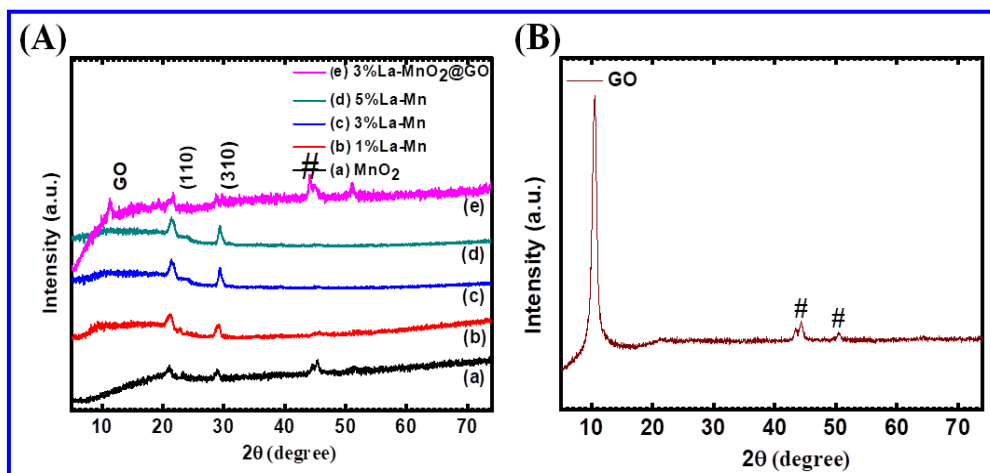


Fig. 4.2) (A) The XRD patterns of (a) MnO₂, (b) 1% La-Mn, (c) 3%La-Mn, (d) 5%La-Mn and (e) 3%La-MnO₂@GO thin films and (B) GO thin film.

4.2.A.3.2 FT-IR analysis

The FT-IR technique was used to identify functional groups and bonding nature of (a) MnO_2 , (b-d) 1, 3, 5 % La-doped MnO_2 and (e) 3%La- MnO_2 @GO thin films as depicted in **Fig. 4.3 (A)** in the wavelength range 4000 to 400 cm^{-1} . The proportion of La into the MnO_2 is negligible due to which there is no significant change in the FT-IR spectra of (a-d) electrodes. The broad peak at wavelength 3374.5 cm^{-1} indicates stretching vibrations and weak peak at 1604.2 cm^{-1} shows bending vibrations of -OH group of adsorbed water molecules at surface [20]. The absorption peak at 1344.6 cm^{-1} is attributed to -C-O bending vibration connecting with Mn atoms [21]. The peak at 625.7 cm^{-1} corresponds to stretching vibrations of Mn-O bond [22]. The bonding present in the **Fig. 4.3 A (e)** shows the formation of La doped MnO_2 @GO composite thin films. The peak at 1634 cm^{-1} corresponds to surface oxygen groups of stretching vibration mode [23]. The peak at 1546 cm^{-1} is assigned to C=C skeletal vibration of GO sheets [24]. In addition, the absorption bands around 1230 and 1039 cm^{-1} in the composite material are assigned to the existence of -C-O-C epoxy and C-O alkoxy groups [25]. These characteristic bands confirm the formation of MnO_2 , La-doped MnO_2 and 3%La- MnO_2 @GO composite thin films.

The appearance of broad peak at 559.25 cm^{-1} of MnO_2 @GO corresponding to the bending and stretching vibration of Mn-O confirms the presence of MnO_2 over GO sheets [26]. Also, the peak at 766.56 cm^{-1} corresponds to the coupling mode between Mn-O stretching modes of 766.56 cm^{-1} . The peak at 766.56 cm^{-1} is with lower intensity in comparison to MnO_2 @GO **Fig. 4.3 B (a)**. FT-IR spectrum confirms the successful oxidation of GO as shown in **Fig. 4.3 B (b)**. Some functional groups such as O-H, -C-OH, -COOH and -C-O are found. A broad peak in FT-IR between 3500 and 2500 cm^{-1} in FT-IR spectrum of GO is due to the carboxyl O-H stretching mode [27]. The absorption peak at O-H stretching peak at 3399.89 cm^{-1} over the OH stretch of carboxylic acid, due to the occurrence of absorbed water molecules and alcohol groups [27]. The FT-IR peak related to 2816.53 cm^{-1} is due the asymmetric and symmetric CH_2 stretching mode of GO while the peaks around 1633.41 and 1588.09 cm^{-1} are related to C=C stretches from unoxidized graphitic domain [17]. The peak at 1300.89 cm^{-1} corresponds to C-OH stretch of alcohol group and 1095.85 cm^{-1} is due to C-O stretching vibrations of C-O-C [28, 29]. On the other hands, the peaks corresponding to -COOH, -C-O epoxy and -C-O alkoxy peaks are absent [30].

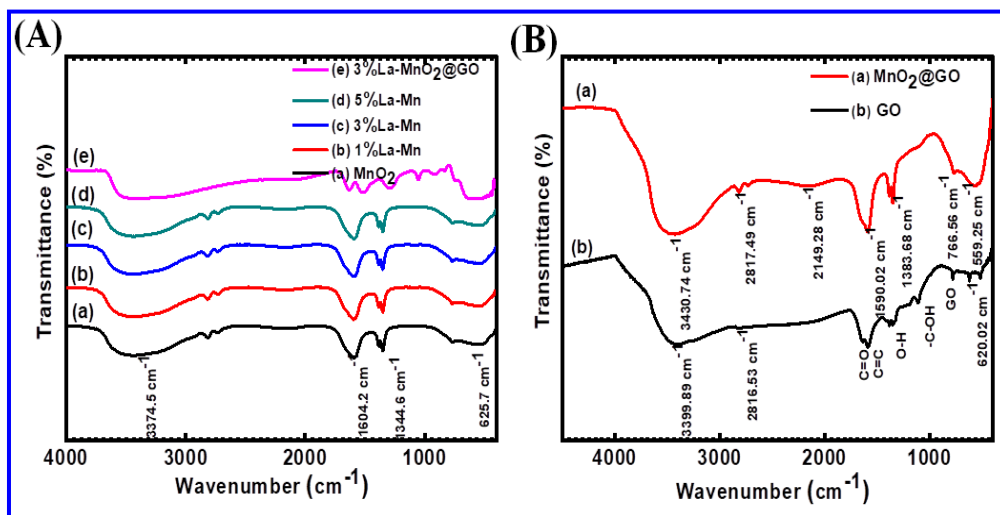


Fig. 4.3) The FT-IR spectra of (A) (a) MnO_2 , (b) 1% La-Mn, (c) 3% La-Mn, (d) 5% La-Mn and (e) 3% La-MnO₂@GO thin films and FT-IR spectra (B) of (a) MnO_2 @GO and (b) GO thin films.

4.2.A.3.3 FE-SEM analysis

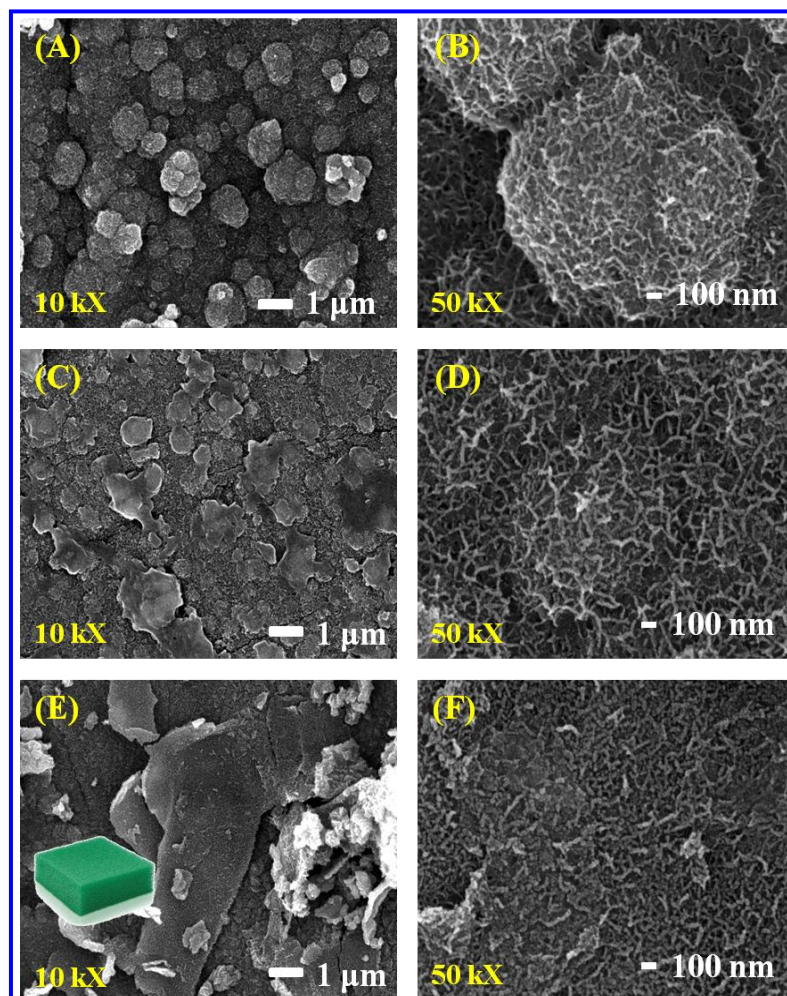


Fig. 4.4) The FE-SEM pictures of (A-B) MnO_2 , (C-D) 3% La-Mn and (E-F) 3% La-MnO₂@GO thin films at magnifications of 10 kX and 50 kX.

In **Fig. 4.4**, the FE-SEM images of (A-B) MnO_2 , (C-D) 3%La- MnO_2 and (E-F) 3%La- MnO_2 @GO composite films at magnification of 10 kX and 50 kX give details of surface topography. **Fig. 4.4 (A)** depicts the formations of micro-spheres of MnO_2 particles within the range of 1-1.5 μm . At higher magnification (50 kX), **Fig. 4.4 (B)** shows that these spheres have sponge-like structure which may provide 3-D access to the electrolyte ions for intercalation-deintercalation process. **Fig. 4.4 (C)** illustrates that the doping of La in MnO_2 changes surface morphology from spheres to the plates-like with size in the range of 1-1.2 μm , but retains its sponge-like structure as shown in **Fig. 4.4 (D)**. The morphology of 3%La- MnO_2 @GO thin film is shown in **Fig. 4.4 (E-F)**. The GO sheets are uniformly covered by the micro porous La-doped MnO_2 nanoparticles forming sponge-like structure. The green structure at the bottom shows sponge-like crystalline and porous material formation in **Fig. 4.4 (E)**. Decrease in the pore depth and size seen in surface structure of 3%La- MnO_2 @GO thin film reveal modification due to the composition with GO.

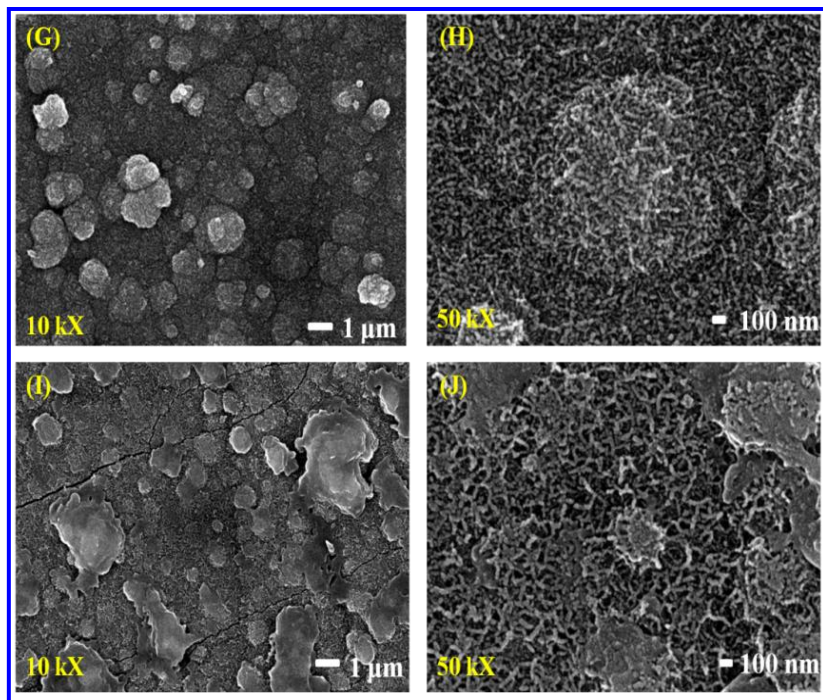


Fig. 4.4) The FE-SEM images of (G-H) 1%La-Mn and (I-J) 5%La-Mn thin films at magnifications of 10 kX and 50 kX.

FE-SEM images of 1%La-Mn and 5%La-Mn are shown as supporting information in **Fig. 4.4. (G-H) and (I-J)**. The FE-SEM image of 1%La-Mn shown in **Fig. 4.4 (G)** depicts the formations of micro-spheres of 1%La-Mn particles having size in the range of 1-1.3 μm . At high magnification of 50 kX, surface structure like corn shell-like particles. The SEM images for 5%La-Mn thin film displays plate-like

structure (10 kX) and cracked microstructures (50 kX). The La doping concentration increases the growth rate of the reaction with increases nucleation rate, and the surface converts into inactive growth with overgrown particles on the SS substrate.

4.2.A.3.4 TEM analysis

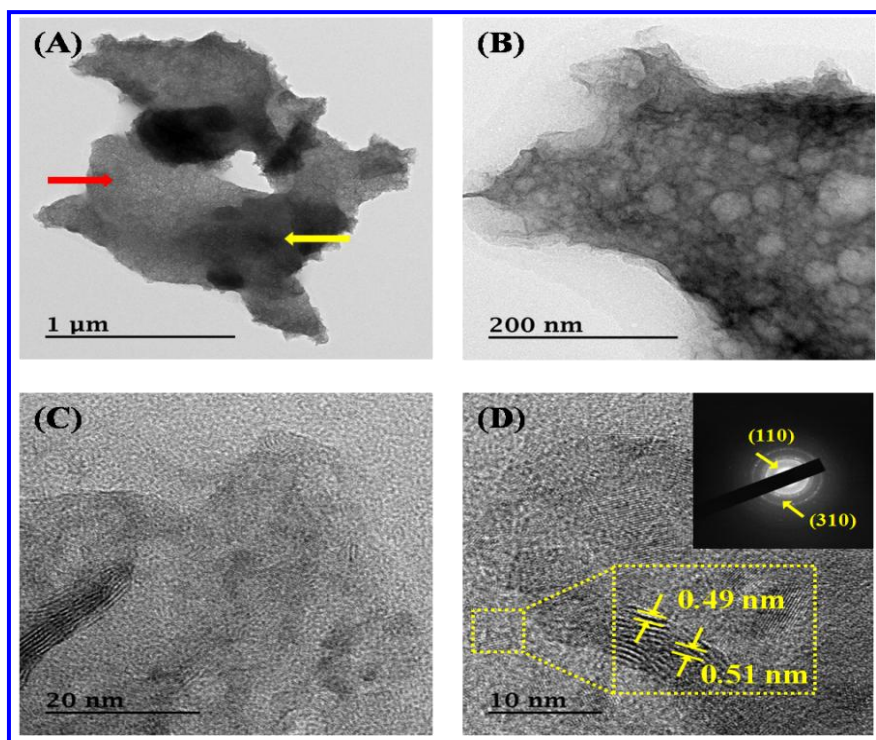


Fig. 4.5) TEM images of (A-B) 3%La-MnO₂@GO powder samples, (C) TEM image of graphene oxide multilayer and (D) HRTEM image of 3%La-MnO₂@GO samples (inset shows SAED image).

Transmission electron microscopy (TEM) is employed to further characterize microstructure to confirm nanocrystalline structure of 3%La-MnO₂@GO. The TEM in **Fig. 4.5 (A)** shows that La-MnO₂ spongy-like particles (yellow arrows) are formed on the thin semi-transparent graphene sheets (red colour arrows) indicating the growth of flake-like La-MnO₂ particles on the graphene sheets. The formation of high density small sized nanoparticles is confirmed by TEM image (**Fig. 4.5 (B)**). The porous nanoparticles in the range of 30-40 nm are mostly spherical in shape as seen in **Fig. 4.5 (B)**. The TEM images of the graphene sheets exhibits 6-7 layered thick GO as shown in **Fig. 4.5 (C)**. The high resolution HR-TEM image shown in **Fig. 4.5 (D)** further confirms the ultrathin nanosheets structures. The inter-planer crystal spacings 0.51 and 0.49 nm correspond to the crystal planes of (110) and (310) of La-MnO₂. Inset SAED pattern clearly identifies the (110) and (310) planes of MnO₂.

4.2.A.3.5 EDX analysis

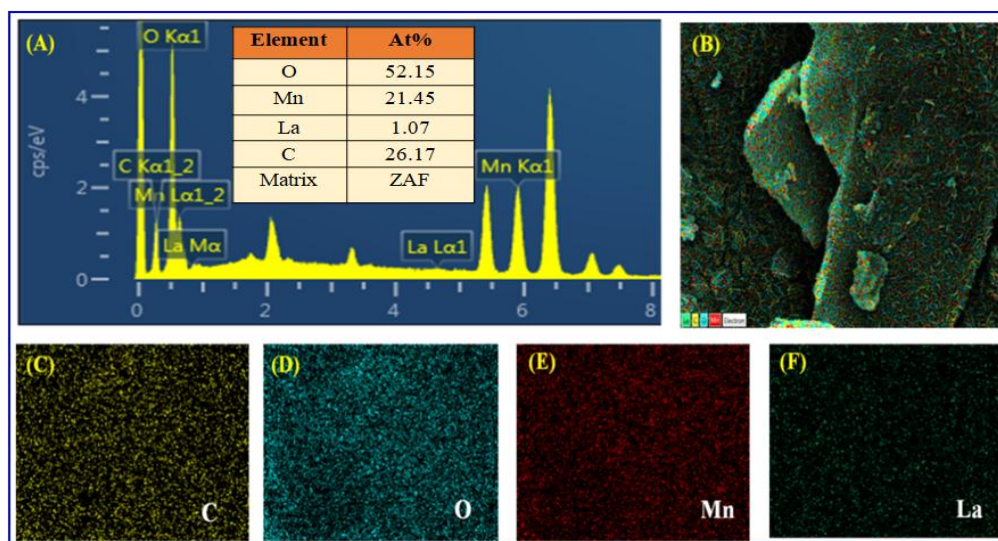


Fig. 4.6 (A) The EDX spectrum of 3%La-MnO₂@GO composite electrode, (B) Elemental mapping of 3%La-MnO₂@GO thin film showing distribution of La, C, O, Mn elements, Elemental mapping images of (C) C, (D) O, (E) Mn and (F) La elements.

The EDX spectrum of 3%La-MnO₂@GO thin film displayed in **Fig. 4.6 (A)** shows peaks from C, O, Mn and La elements without any other impurities. Elemental mapping of 3%La-MnO₂@GO thin film shown in **Fig. 4.6 (B)** convinces that all the elements are distributed uniformly. The individual elemental mapping images of C, O, Mn and La are shown in **Fig. 4.6 (C-F)** precisely give quantitative elemental distribution. This analysis confirms the formation of 3%La-MnO₂@GO thin film on the SS substrate. Non labelled peaks belong to the steel substrate.

4.2.A.3.6 Surface Wettability

The interfacial properties between water and electrode are characterized by contact angle measurement. If the wettability is high, the contact angle (θ) is low and the surface is hydrophilic. On the opposite side, if the wettability is low, the contact angle (θ) is high and surface is hydrophobic. Such low contact angle may be due to the porous morphology of 3%La-MnO₂@GO thin film. The water contact angles of MnO₂, 3%La-Mn, 3%La-MnO₂@GO, MnO₂@GO and GO thin film electrodes as denoted in **Fig. 4.7 (A-E)**. The La doping decreases the contact angle of MnO₂ film from 76°, 60°, 25°, 32° and 49° for MnO₂, 3%La-Mn, 3%La-MnO₂@GO, MnO₂@GO and GO thin films, respectively indicating hydrophilic nature of the electrodes. Lower water contact angle is beneficial to improve the electrochemical performance of the electrode [31].

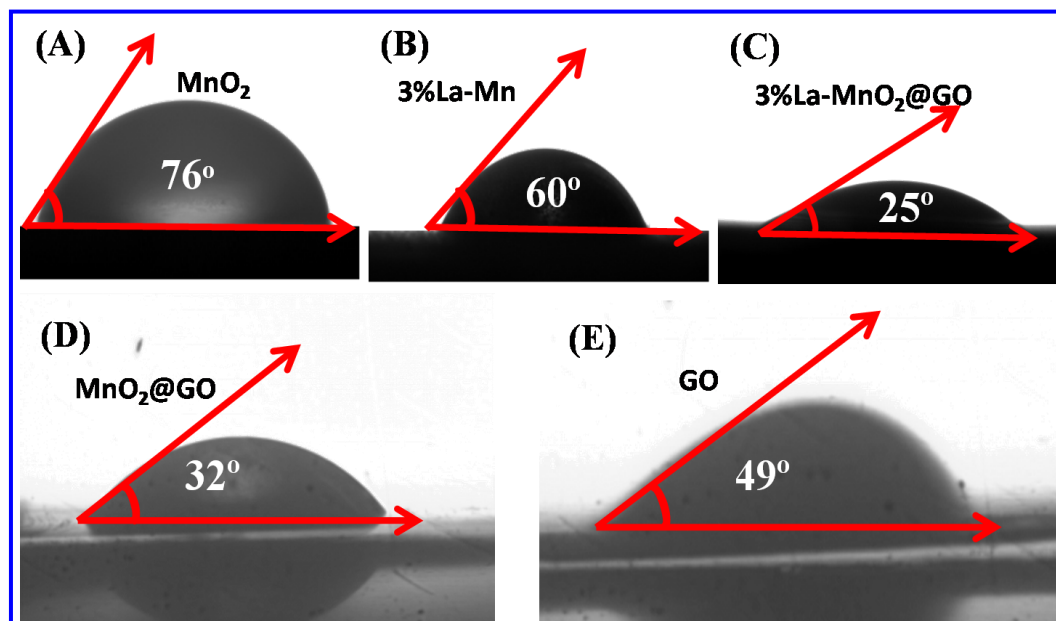


Fig. 4.7) The contact angles of (A) MnO_2 , (B) 3%La-Mn, (C) 3%La- MnO_2 @GO, (D) MnO_2 @GO and (E) GO thin films.

4.2.A.3.7 The XPS study

The XPS survey spectrum of 3%La- MnO_2 @GO composite thin film in **Fig. 4.8 (A)** shows the presence of Mn, O, C and La element peaks confirming composition of thin film. The **Fig. 4.8 (B)** represents Mn 2p peak divided into two sublevels as $2p_{3/2}$ and $2p_{1/2}$ corresponding to binding energies located at 642.2 and 653.7 eVs, respectively to Mn^{4+} oxidation state with an energy gap of (11.7 eV), a characteristic of MnO_2 phase [32]. The **Fig. 4.8 (C)** represents the XPS spectrum of O 1s state peak at 529.6 eV indexed to O^{2-} state of Mn-O-Mn and other peaks at 531.3 and 533.3 eVs are accredited to the C=O and C-O bonding energies, respectively [33]. The XPS spectrum of C 1s indicates peaks at 284.2, 286.4 and 287.9 eVs corresponding to C-C/C=C, -C-OH and -COOH bond energies, respectively as shown in **Fig. 4.8 (D)**. This confirms sp^2 hybridization of the carbon and the presence of hydroxide and carboxylic group on the surface of the GO sheets [34]. The La 3d spectrum in **Fig. 4.8 (E)** displays two energy peaks of the $3d_{3/2}$ and $3d_{5/2}$ located at 852.1 and 835.4 eVs, respectively indicating La^{3+} oxidation state with an energy gap of (16.7 eV), a characteristic of LaO_3 phase [35]. The atomic percent of oxygen (52.15%) is 2.4 times of Mn (21.45%) corresponding to formation of MnO_2 . The La is successfully doped into MnO_2 with atomic weight percent (1.07%). The 3%La-doped MnO_2 is decorated on GO is confirmed by presence of carbon (26.17%). The 5%La-doped MnO_2 leads to actually doping of 2.19% La into MnO_2 .

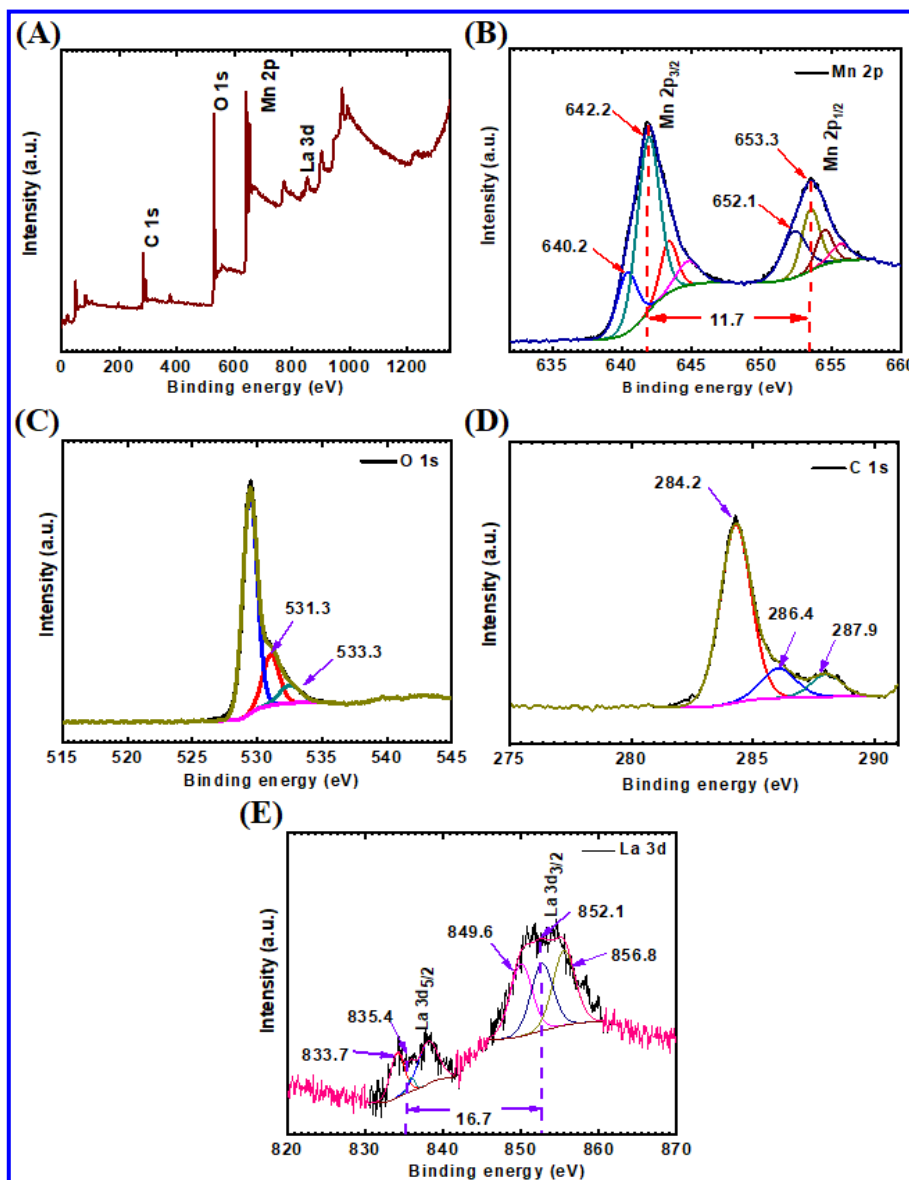


Fig. 4.8) The XPS spectra of 3%La-MnO₂@GO electrode (A) survey spectrum, (B) Mn 2p spectrum, (C) O 1s spectrum, (D) C 1s spectrum and (E) La 3d spectrum.

4.2.A.3.8 The BET analysis

To investigate specific surface area and pore size distribution of MnO₂, 3%La-Mn and 3%La-MnO₂@GO electrodes, N₂ adsorption-desorption isotherms measured at 77 K are shown in **Fig. 4.9 (A)**. The type-IV isotherm with a H₃-type hysteresis loop characteristic depicted for electrode in relative pressure range 0.4-1.0 p/p₀ may be attributed to mesoporous nature [36]. The Brunauer-Emmett-Teller (BET) specific surface area of 149.2 m² g⁻¹ for 3%La-MnO₂@GO is higher than that of MnO₂ (49.7 m² g⁻¹) and 3%La-Mn (86.4 m² g⁻¹) samples. The maximum surface area of 3%La-MnO₂@GO may be due to the interconnected 3-D nanosheets with mesoporous

structure. Gund et. al. [37] reported porous surface morphology of $\text{GO}/\text{Mn}_3\text{O}_4$ electrode with surface area of $94 \text{ m}^2 \text{ g}^{-1}$. The pore size distribution showing mesoporous structure of MnO_2 , 3%La-Mn and 3%La-MnO₂@GO electrodes with the pore radii as 21.47, 18.55 and 15.59 nm, respectively are shown in **Fig. 4.9 (B)**. The 3%La-MnO₂@GO electrode with increased surface area and pore radius provides more electroactive sites for reversible redox reactions in energy storage process.

In **Fig. 4.9 (C)** shows MnO_2 @GO electrode show type-IV isotherm with a H_3 hysteresis loop characteristic revealing mesoporous surface structure [32, 36]. The samples of GO isotherm of type-II formed with hysteresis loop at high relative pressure. The specific surface areas of 139 and $258 \text{ m}^2 \text{ g}^{-1}$ for MnO_2 @GO and GO electrodes, respectively are obtained. The pore size distribution with mesoporous structure of MnO_2 @GO and GO electrodes with the pore radii 16.86 and 12.34 nm, respectively are shown in **Fig. 4.9 (D)**. The estimated values of specific surface area, pore size and pore volumes are presented in **Table 4.1**.

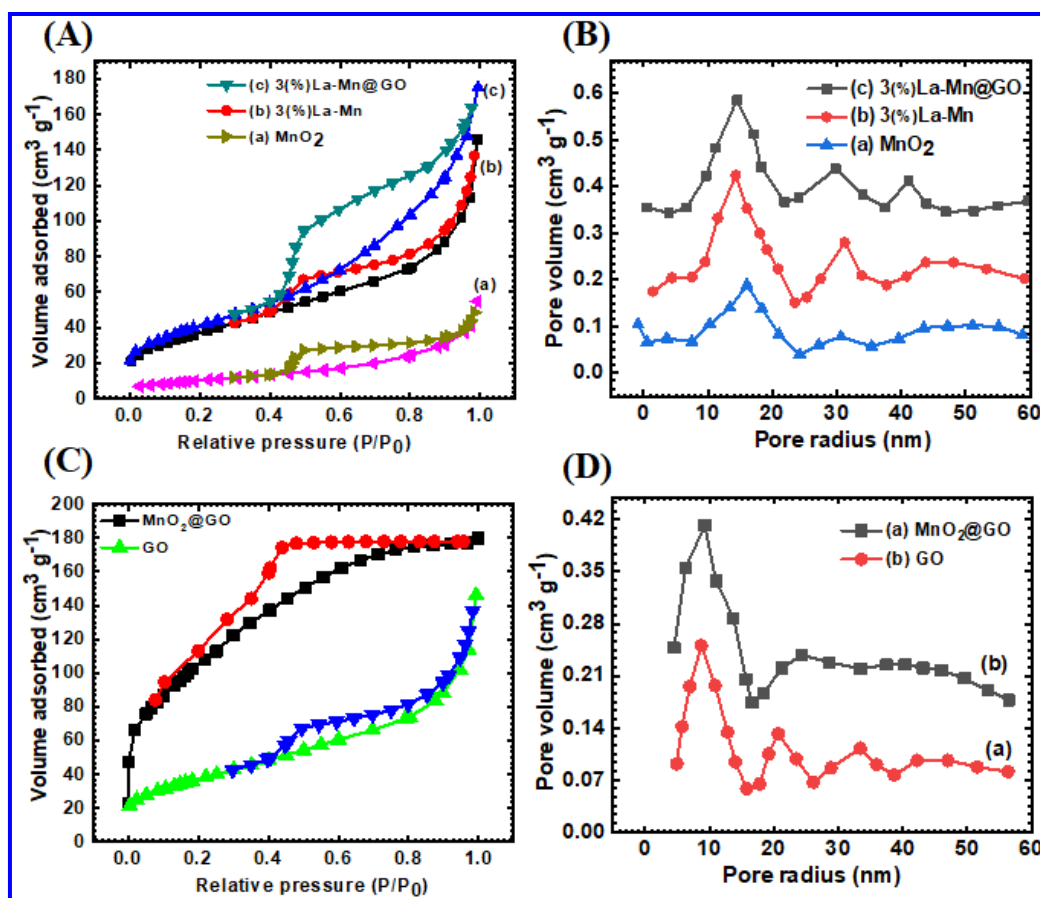


Fig. 4.9 (A) BET surface area analysis of MnO_2 , 3%La-Mn and 3%La-MnO₂@GO samples, (B) the BJH pore size distribution plots of MnO_2 , 3%La-Mn and 3%La-MnO₂@GO powder samples, (C) the BET surface area analysis of

MnO₂@GO and GO samples and (D) the BJH pore size distribution plots of MnO₂@GO and GO powder samples.

Table 4.1: A summary of specific surface area, average pore size and pore volume values of MnO₂, 3%La-Mn, 3%La-MnO₂@GO, MnO₂@GO and GO electrodes.

Sr. No.	Sample	Specific surface area m ² g ⁻¹	Average pore size (nm)	Pore volume m ³ g ⁻¹
1	MnO ₂	49	21.47	0.082
2	3%La-Mn	86	18.55	0.219
3	3%La-MnO ₂ @GO	149	15.59	0.265
4	MnO ₂ @GO	137	16.86	0.113
5	GO	250	12.34	0.276

SECTION – B

Supercapacitive evaluation of MnO₂, La-doped MnO₂ and La-MnO₂@GO thin films by SILAR method

4.2.B.1 Introduction

In present section, the electrochemical performance of MnO₂, La-doped MnO₂ and La-MnO₂@GO thin films was tested in 1 M Na₂SO₄ electrolyte. The effect of various La doping concentrations on the electrochemical performance of MnO₂ thin films is studied using CV, GCD, cycling stability and EIS analysis.

4.2.B.2 Results and discussion

4.2.B.2.1 The CV studies

Fig. 4.10 (A) displays the CV curves within potential range -0.2 to 0.9 V/SCE for MnO₂, 1%La-Mn, 3%La-Mn, 5%La-Mn and 3%La-MnO₂@GO composite thin film electrodes at scan rate of 100 mV s⁻¹. Notably, the 3%La-MnO₂@GO electrode has a larger area under CV curve with highest peak current as compared to other thin film electrodes, resulting high charge-storage capability [38]. **Fig. 4.10 (B-F)** displays the CV curves of MnO₂, 1%La-Mn, 3%La-Mn, 5%La-Mn and 3%La-MnO₂@GO thin films at different scan rates from 5-100 mV s⁻¹. All thin film electrodes display almost rectangular shape of CV curves demonstrating pseudocapacitive nature of charge storage. The specific capacitances of 342, 428, 548, 486, 729 F g⁻¹ are observed for

MnO₂, 1%La-Mn, 3%La-Mn, 5%La-Mn and 3%La-MnO₂@GO electrodes, respectively at scan rate of 5 mV s⁻¹. The increasing specific capacitance of 3%La-MnO₂@GO is due to the well interconnected mesoporous and sponge-like porous structure which can facilitates facile insertion/reinsertion of Na⁺ ions, which can ensure the sufficient faradic reactions for energy storage.

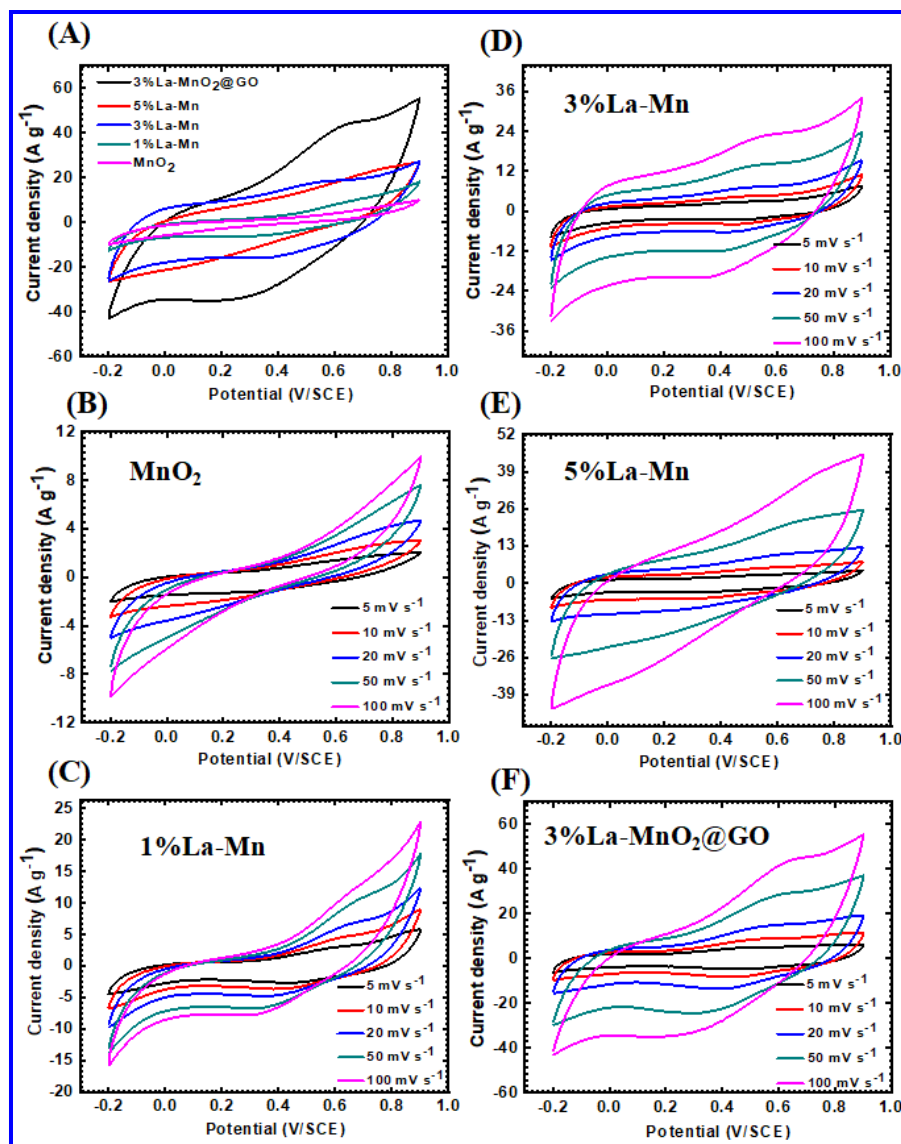


Fig. 4.10 (A) The cyclic voltammetry curves of MnO₂, 1%La-Mn, 3%La-Mn, 5%La-Mn and 3%La-MnO₂@GO electrodes at scan rate 100 mV s⁻¹, (B) the CV curves of MnO₂, (C) 1%La-Mn, (D) 3%La-Mn, (E) 5%La-Mn and (F) 3%La-MnO₂@GO electrodes at scan rate of 5-100 mV s⁻¹.

The specific capacitance variation with scan rate is shown in **Fig. 4.11**. With increase in the scan rate, the area under CV curve also increases, but C_s decreases as the electrochemical insertion/reinsertion reactions happens only on the outer surface of electrode material.

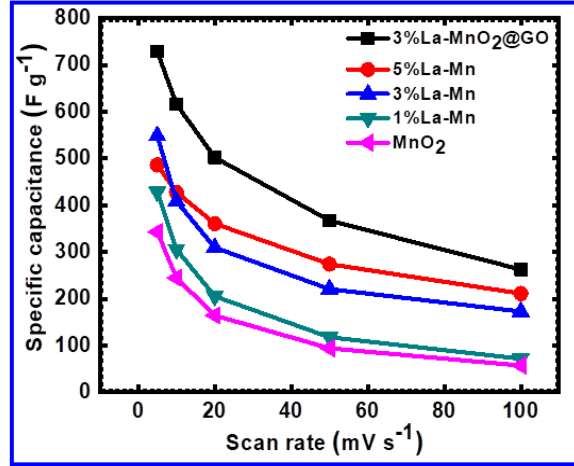


Fig. 4.11) The plot of specific capacitance versus scan rates of MnO₂, 1%La-Mn, 3%La-Mn, 5%La-Mn and 3%La-MnO₂@GO electrodes.

The reversibility of intercalation process is strongly dependent on potential range of operation [39]. The realistic consideration is switching of the limiting stage predominance of kinetic stage over diffusion is observed in current dependent electrode polarization. The assessment of sodium ion diffusion coefficient in accordance with the Randles Shevchik eq. (4.1) is modified by the introduction of the correction parameter z , obtained from the E_c for 3%La-MnO₂@GO electrode [40].

$$i_p = 0.4463 v^{\frac{1}{2}} \frac{z^{\frac{1}{2}} n^{\frac{3}{2}} F^{\frac{3}{2}}}{R^{\frac{1}{2}} T^{\frac{1}{2}}} c_o D_{av}^{\frac{1}{2}} \quad (4.1)$$

where, n is number of electrons, v is potential scan rate, F is the Faraday constant, T is absolute temperature, R is gas constant and C_o is the initial concentration of sodium available for extraction in the material. The D values calculated from these data are $1.92 \times 10^{-12} \text{ cm}^2 \text{ s}^{-1}$ for anodic and $1.64 \times 10^{-12} \text{ cm}^2 \text{ s}^{-1}$ for cathodic processes.

The plots of peak current versus square root at different scan rates of (MnO₂, 1%La-Mn, 3%La-Mn, 5%La-Mn and 3%La-MnO₂@GO) electrodes are depicted in **Fig. 4.12 (A)**. The oxidation peak current (I_{po}) and reduction peak current (I_{pr}) show the anodic and cathodic peak current densities, respectively. It is found that anodic and cathodic peak currents increase directly with increasing potential scan rates [41]. The peak current densities of 100 and 25 A g⁻¹ are observed for 3%La-MnO₂@GO electrode at 100 mV s⁻¹ scan rate for cathodic and anodic sides, respectively as shown in **Fig. 4.12 (B)**. Hence, the plots of peak current separation with square root at different scan rates for all electrodes are illustrated in **Fig. 4.12 (B-F)**.

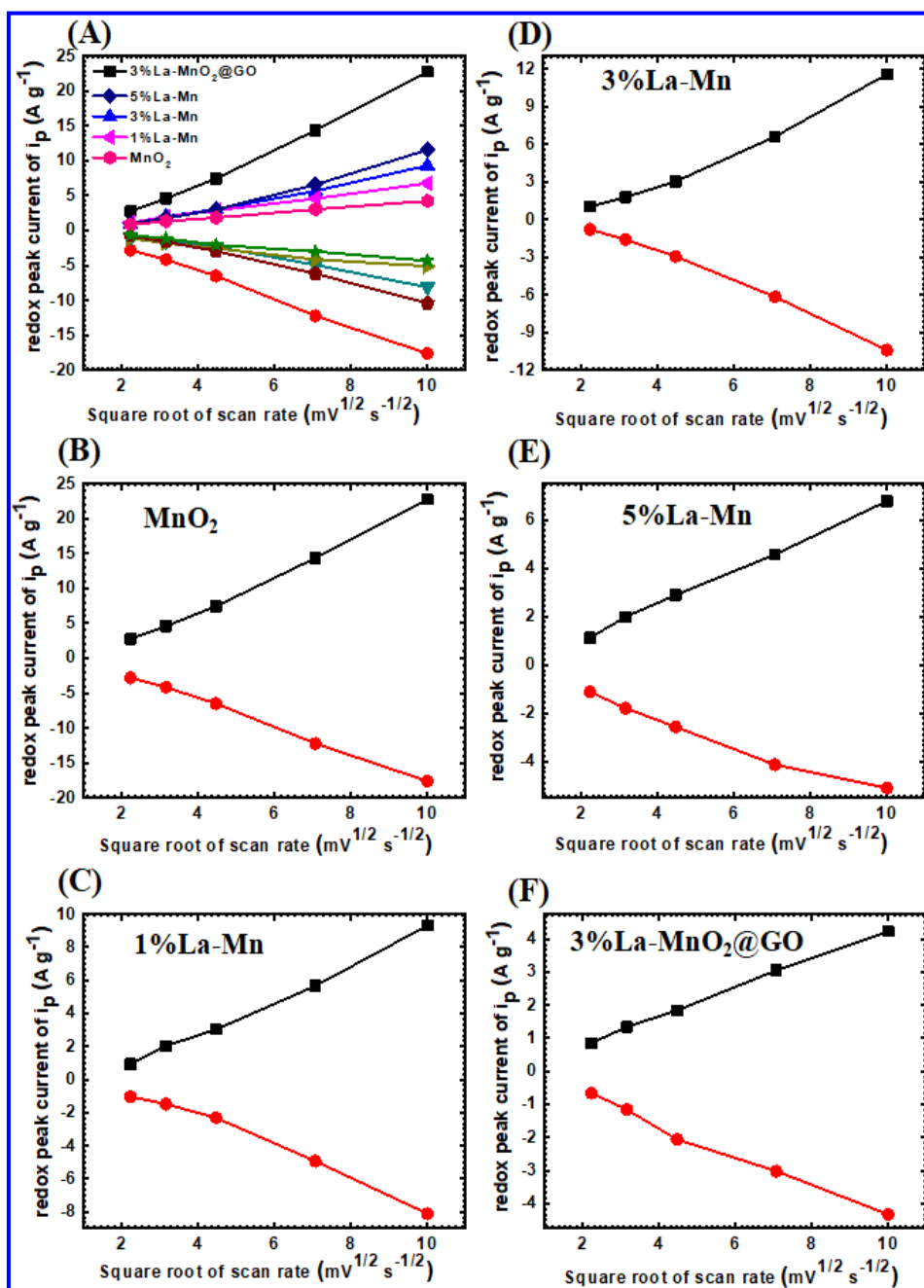


Fig. 4.12) (A) The current density versus square root of potential scan rate of all electrodes MnO_2 , 1%La-Mn, 3%La-Mn, 5%La-Mn and 3%La-MnO₂@GO electrodes, (B) 3%La-MnO₂@GO (C) 3%La-Mn, (D) 1%La-Mn, (E) 5%La-Mn and (F) MnO_2 electrodes.

4.2.B.2.2 The GCD studies

Fig. 4.13 (A) shows the GCD curves of thin film electrodes at current density of 1 A g^{-1} in potential window of 0 to +0.9 V/SCE. It is seen that, symmetrical and triangular shape of GCD curves reveals the pseudocapacitive nature of thin film electrodes. The Fig. 4.13 (B-F) displays the GCD curves of MnO_2 , 1%La-Mn, 3%La-Mn, 5%La-Mn and 3%La-MnO₂@GO at different current densities from 1-4 A g^{-1} , signifying good

electrochemical reversibility. The charge-discharge behaviour is nearly ideal along with low iR drop for all thin film electrodes.

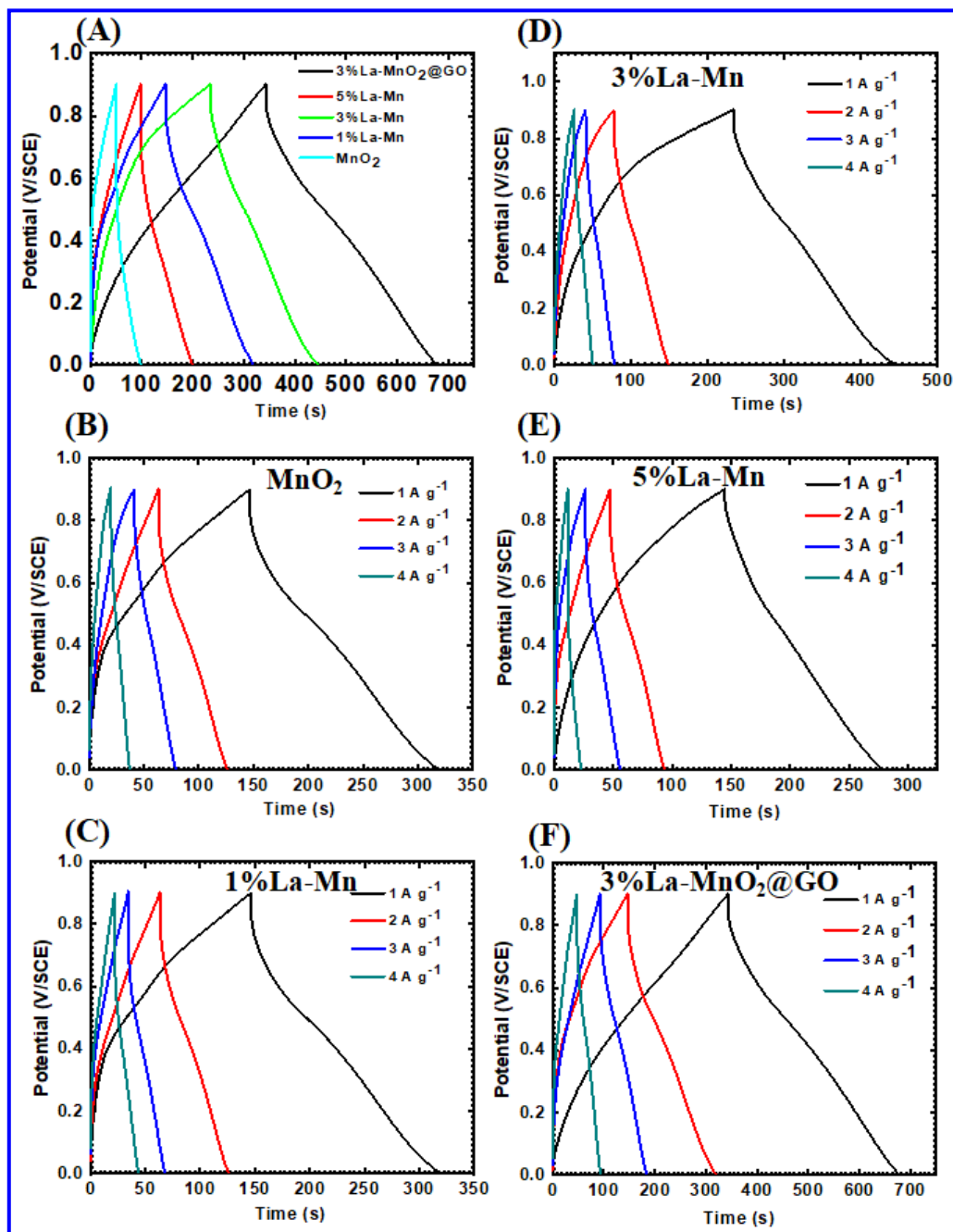


Fig. 4.13 (A) The GCD curves of MnO₂, 1%La-Mn, 3%La-Mn, 5%La-Mn and 3%La-MnO₂@GO electrodes at current density of 1 A g⁻¹, (B) the GCD curves of MnO₂, (C) 1%La-Mn, (D) 3%La-Mn, (E) 5%La-Mn and (F) 3%La-MnO₂@GO electrodes at current densities of 1-4 A g⁻¹.

The values of C_s are 313, 392, 491, 379 and 627 F g⁻¹ for MnO₂, 1%La-Mn, 3%La-Mn, 5%La-Mn and 3%La-MnO₂@GO electrodes, respectively at current density of 1 A g⁻¹. The graph of specific capacitance with current density of thin film electrodes are depicted in **Fig. 4.14**.

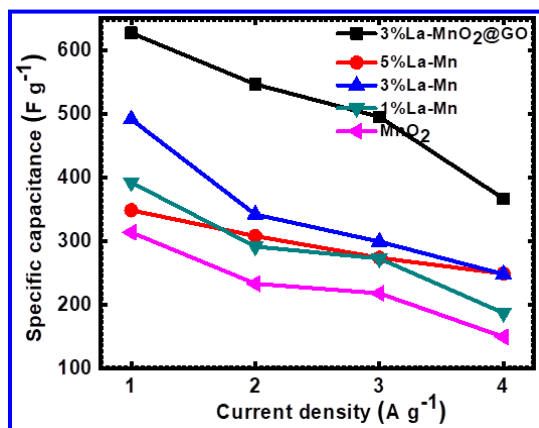


Fig. 4.14) The specific capacitance with current densities of all thin film electrodes.

4.2.B.2.3 The EIS studies

The EIS plots are analysed in the frequency range of 0.1 kHz to 1 MHz with bias potential of 10 mV. All Nyquist plots shown in **Fig. 4.15** consist of partial semicircle in high frequency region and straight line in low frequency region. The slope of straight line in the low frequency region at 45° gives Warburg resistance (W). This is mainly ascribed to its good diffusion rate due to higher surface area. The solution resistance (R_s) of 1.9, 1.6, 1.4, 2.5 and 1.2 Ω/cm^2 and charge transfer resistance (R_{ct}) of 107, 30.6, 7.1, 38.4 and 6.5 Ω/cm^2 are observed for MnO₂, 1%La-Mn, 3%La-Mn, 5%La-Mn and 3%La-MnO₂@GO electrodes, respectively as illustrated in **Table 4.2**. As is known, the smaller R_{ct} means faster charge transfer rate in the reversible reaction between electrode and electrolyte. Therefore, being a 3%La-MnO₂@GO electrode of smaller R_{ct} among all samples, has superior charge transfer rate. The high specific surface area can increase charge transfer rate, enhance contact area between electrode and electrolyte, so as to decrease the charge transfer resistance [42].

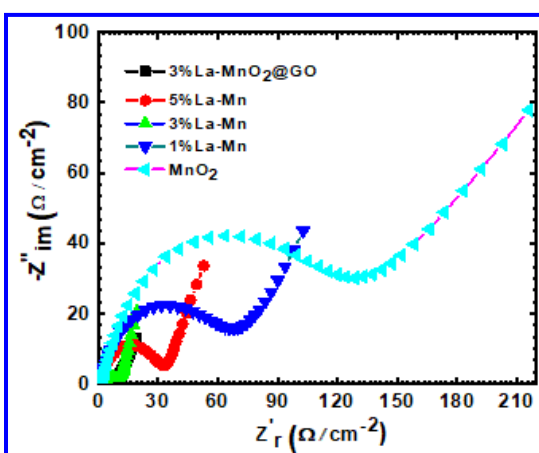


Fig. 4.15) Nyquist plots of MnO₂, 1%La-Mn, 3%La-Mn, 5%La-Mn and 3%La-MnO₂@GO electrodes.

Table 4.2: The electrochemical properties for all electrodes.

Sr. No.	Sample	Specific capacitance (F g ⁻¹)	Capacitive retention (%)	R _{ct} (Ω/cm ⁻²)	R _s (Ω/cm ⁻²)
1	MnO ₂	342	80.83	107	1.9
2	1%La-Mn	428	89.63	30.6	1.6
3	3%La-Mn	548	93.49	7.1	1.4
4	5%La-Mn	486	92.24	38.4	2.3
5	3%La-MnO ₂ @GO	729	94.39	6.2	1.2

4.2.B.2.4 The stability studies

The electrochemical stability of all electrodes are measured up to 5000 cycles at scan rate of 100 mV s⁻¹ in 1 M Na₂SO₄ electrolyte. The long-life stability of 3%La-MnO₂@GO electrode is illustrated in **Fig. 4.16 (A)**. Additionally, the capacitive retention of 94.39% is obtained as shown in **Fig. 4.16 (B)**, which is higher than other samples. The results signify that the incorporation of La and GO enhances cycling stability of MnO₂ electrodes. The calculated capacity retention values of all electrodes are shown in **Table 4.2**.

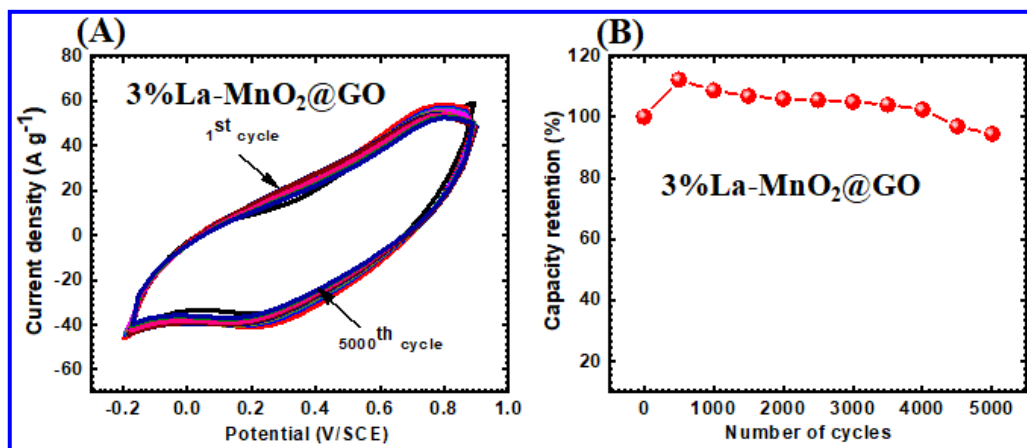


Fig. 4.16) (A) Stability CV curves of 5000 cycles and (B) the plot of capacitance retention versus number of cycles for 3%La-MnO₂@GO electrode.

SECTION - C

Flexible symmetric solid state supercapacitor (FSSSC) device fabrication and supercapacitive evaluation of 3%La-MnO₂@GO thin films.

4.2.C.1 Introduction

In this chapter, the MnO_2 , La-doped MnO_2 and $\text{La-MnO}_2@\text{GO}$ thin films have been prepared using SILAR method. **Table 4.2** illustrates the electrochemical parameters of 3% $\text{La-MnO}_2@\text{GO}$ thin films, which assists to choose the superior electrode to fabricate the symmetric FSSSC device.

The present section deals with high performance symmetric FSSSC device fabricated using 3% $\text{La-MnO}_2@\text{GO}$ thin film as cathode and anode electrodes with PVA- Na_2SO_4 gel as electrolyte as well as a separator. The section ‘C’ deals with fabrication and electrochemical performance evaluation of symmetric FSSSC device.

4.2.C.2 Experimental details

4.2.C.2.1 Electrode Preparation

The SILAR method was employed to prepare the 3% $\text{La-MnO}_2@\text{GO}$ thin films on flexible SS substrates. The preparative parameters to synthesis of 3% $\text{La-MnO}_2@\text{GO}$ thin films are described in (Section 4.2.A.2.5).

4.2.C.2.2 Preparation of PVA- Na_2SO_4 gel electrolyte

The PVA- Na_2SO_4 gel electrolyte was used for flexible symmetric solid state device. To prepare PVA based solid state gel electrolyte, 6 gm of polyvinyl alcohol (PVA) was dissolved in 60 ml DDW at temperature of 353 K with constant stirring for 4 h to form clear and viscous solution, followed by drop-by-drop addition of 1 M Na_2SO_4 20 ml solution. This mixture was kept under constant stirring for 3 h to form uniform PVA- Na_2SO_4 viscous gel like solution. This viscous solution was used as a gel electrolyte to fabricate the 3% $\text{La-MnO}_2@\text{GO}$ symmetric device.

4.2.C.2.3 Fabrication of flexible symmetric solid state supercapacitor device

The flexible symmetric solid state device was assembled using two 3% $\text{La-MnO}_2@\text{GO}$ thin films as cathode and anode electrodes with PVA- Na_2SO_4 gel as electrolyte as well as a separator. The electrodes with area of $5 \times 5 \text{ cm}^2$ were prepared and used as the electrode for fabrication of symmetric (FSSSC) device. The edges of electrode were sealed with plastic tape to evade the short circuit. In order to fabricate symmetric device, both electrodes painted by PVA- Na_2SO_4 gel electrolyte were stacked on to each other to form symmetric supercapacitor device. After packing using plastic strip, symmetric supercapacitor device was placed in a hydraulic press at a

pressure of 1 ton for 30 min and tested by electrochemical techniques. The schematic of flexible symmetric solid state device is shown in Fig. 4.17.

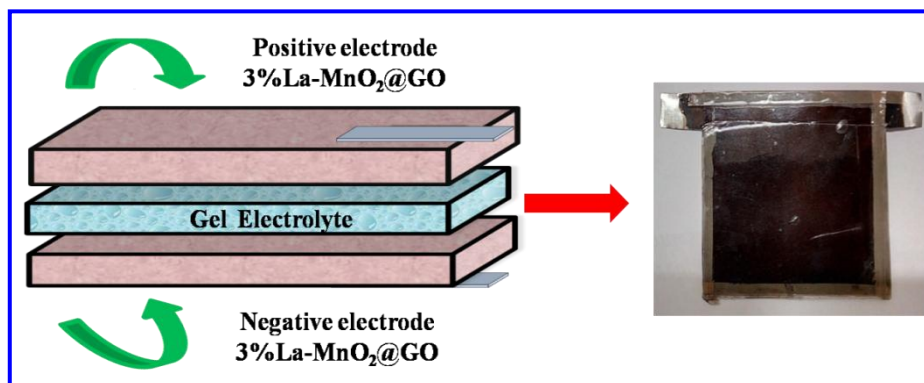


Fig. 4.17) The schematic of flexible symmetric solid state supercapacitor device.

4.2.C.3 Electrochemical properties of flexible symmetric solid state supercapacitor (FSSSC) device

The electrochemical performance of an FSSSC device is measured by two electrode system using 3%La-MnO₂@GO thin film as cathode and anode electrodes with polymer gel as electrolyte as well as separator.

4.2.C.3.1 The CV studies

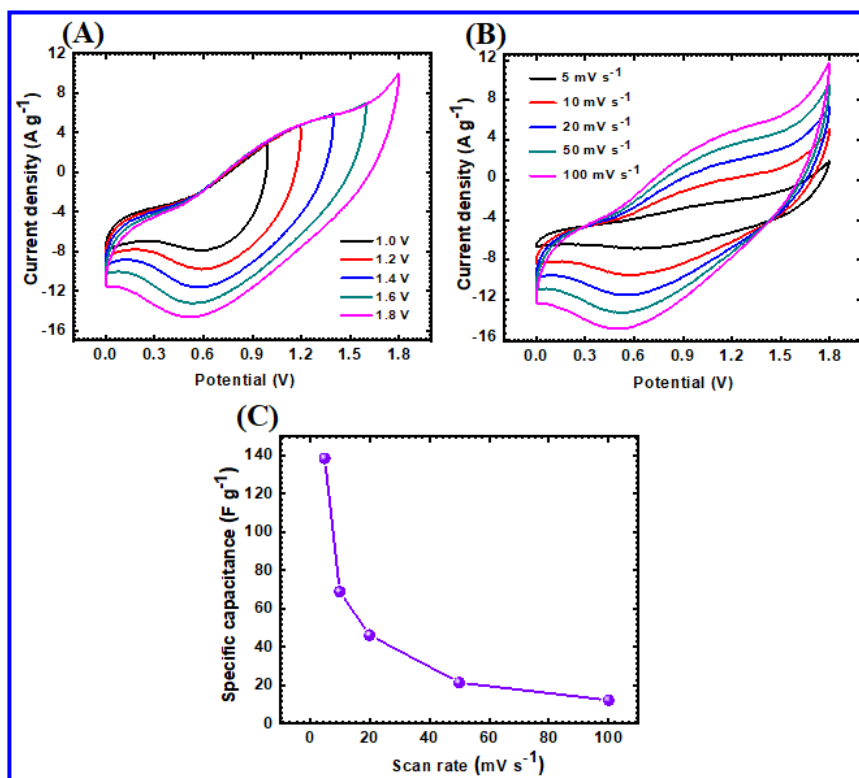


Fig. 4.18) (A) Potential window selection in voltage ranging from 1.0 to +1.8 V, (B) the CV curves of symmetric device at different scan rate 5-100 mV s⁻¹ and (C) the graph of specific capacitance versus scan rates.

Flexible symmetric solid state (FSSSC) device fabricated with 3%La-MnO₂@GO as cathode and anode is evaluated for supercapacitive properties. The CV curves of FSSSC device in potential window from 1 to +1.8 V at scan rate of 100 mV s⁻¹ are illustrated in **Fig. 4.18 (A)**. The CV curves are not distorted with changing scan rate, indicating promising charge-discharge performance for symmetric device. The CV curves in potential window from 0 to +1.8 V at various scan rate of 5-100 mV s⁻¹ are shown in **Fig. 4.18 (B)**. As more electroactive electrode material contributes in electrochemical reaction at low scan rate, due to availability of time, it gives high specific capacitance compared to higher scan rate. The value of C_s of FSSSC device is 138 F g⁻¹ at scan rate of 5 mV s⁻¹. The plot of variation of C_s with scan rate is shown in **4.18 (C)**.

4.2.C.3.2 The GCD studies

The GCD curves of FSSSC device in potential windows from 1 to +1.8 V at constant current density of 9 A g⁻¹ are plotted in **Fig. 4.19 (A)**. The GCD curves of FSSSC device at current densities of 8, 9, 10 and 11 A g⁻¹ within operating potential window of 0 to +1.8 V are shown in **Fig. 4.19 (B)**. A good triangular shaped GCD curves are observed at all current densities signifying ideal supercapacitive behavior. The calculated C_s versus current density is depicted in **Fig. 4.19 (C)** which demonstrates maximum C_s of 133 F g⁻¹ at current density 8 A g⁻¹.

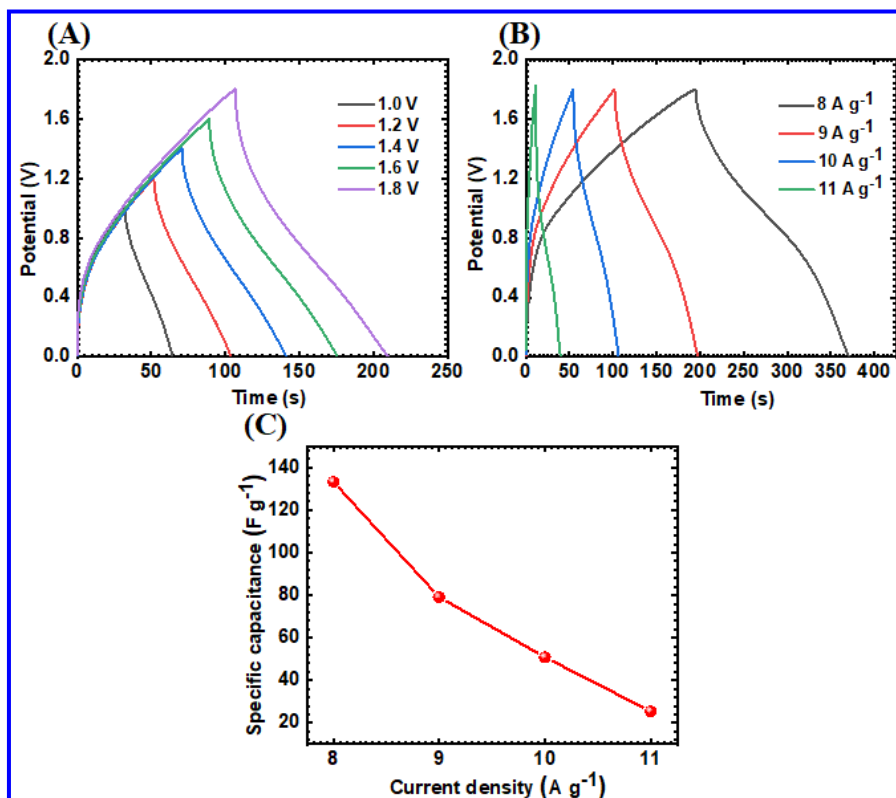


Fig. 4.19) (A) The GCD curves at 9 A g^{-1} different voltage ranges from 1.0 to +1.8 V, (B) the GCD curves at current densities 8-11 A g^{-1} and (C) the graph of specific capacitance versus current density of symmetric device.

4.2.C.3.3 The Ragone plot

The ED and PD calculated from GCD curves are displayed in **Fig. 4.20**. The device shows maximum ED and PD of 64 Wh kg^{-1} and 1 kW kg^{-1} , respectively. The excellent electrochemical performance of 3%La-MnO₂@GO electrode compared to other electrodes is due to high electrical conductivity of nanosheets, and uniform distribution on MnO₂ nanospheres of spongy-like network providing electrolyte ions rapid electrochemical reaction. The observed ED and PD values of FSSSC devices in current work are comparatively higher than reported for earlier symmetric devices in **Table 4.3**. Rajagopal et al. [43] reported ED and PD of rGO-mixed LaCe-MnO₂ nanocomposite electrode as 21.96 Wh kg^{-1} and 4 kW kg^{-1} , respectively. Chodankar et al. [44] reported ED of 23.3 Wh kg^{-1} for MWCNTs/MnO₂ electrode. Reddy et al. [45] obtained ED and PD of 4.5 Wh kg^{-1} and 33 kW kg^{-1} , respectively for Au-MnO₂/CNT electrode. Patil et al. [49] obtained ED 15.3 Wh kg^{-1} and PD 13 kW kg^{-1} for α -MnO₂/FSS electrode. Sun et al. [50] reported ED and PD of MnO₂@CNTs/Ni electrode as 33.6 Wh kg^{-1} and 30.2 kW kg^{-1} , respectively.

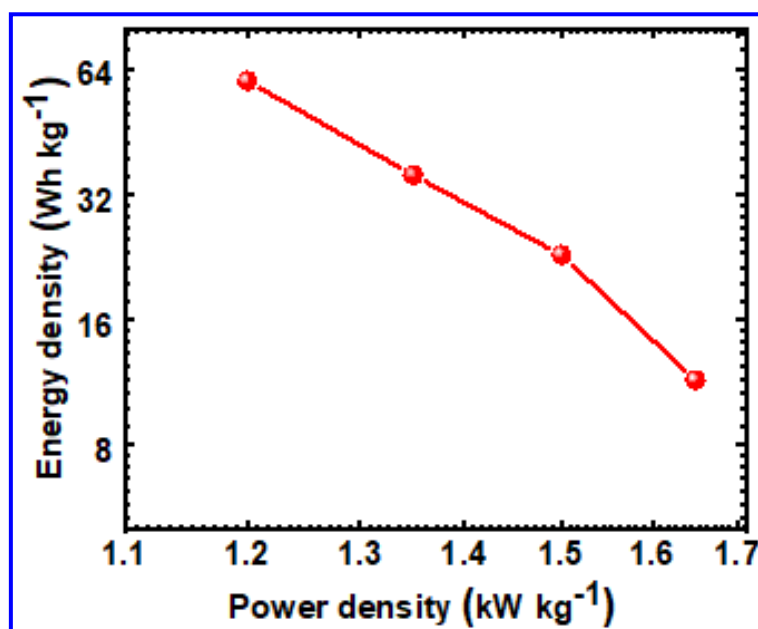


Fig. 4.20) Ragone plot of FSSSC device.

Table 4.3: Comparison of supercapacitive properties of flexible symmetric supercapacitor device.

Sr. No	Supercapacitor Symmetric Electrode	Gel Electrolyte	Specific Capacitance (F g^{-1})	Energy Density (Wh kg^{-1})	Power Density (kW kg^{-1})	Stability (%) (cycles)	Ref. No.
1.	rGO@LaCe-MnO ₂	Na ₂ SO ₄	61	21.96	4	50 (3000)	[43]
2.	MWCNTs/MnO ₂	PVA-Na ₂ SO ₄	204	23.3	-	80 (2500)	[44]
3.	Au-MnO ₂ /CNT	Na ₂ SO ₄	68	4.5	33	-	[45]
4.	MnO ₂	PVP-LiClO ₄	110	23	1.9	92 (2200)	[46]
5.	Graphene@carbon cloth	PVA-H ₂ SO ₄	11.8	1.64	0.67	-	[47]
6.	α -MnO ₂	CMC-Na ₂ SO ₄	145	16	2.5	88 (2500)	[48]
7.	α -MnO ₂ /FSS	PVA-Na ₂ SO ₄	67.3	15.3	13	87.2 (1500)	[49]
8.	MnO ₂ @CNTs/Ni	Na ₂ SO ₄	145	33.6	30.2	82 (1000)	[50]
9.	3% La-MnO ₂ @GO	PVA-Na ₂ SO ₄	138	60	1.2	90 (5000)	Present Work

4.2.C.3.4 The EIS studies

Nyquist plots of FSSSC device before and after 5000 CV cycling is shown in **Fig. 4.21 (A)** (inset image shows equivalent circuit). The EIS contribution is important in analysis of electrochemical performance and considerable factor to know resistance to the charge transportation. The choice of equivalent circuit for modelling the impedance spectra of intercalation electrode is the key point in interpretation of EIS data [51]. The key factors corresponding to this process are involved in the equivalent circuit. **Fig. 4.21 (A)** shows an example of processing of an experimental impedance spectrum of intercalation electrode and the equivalent circuit used for this purpose. The circuit consists of several parts that model the impedance of all electrode structure listed. The solution resistance (R_s) represents the electrolyte resistance. The equivalent circuit of the pseudo-capacitive involves charge transfer resistance (R_{ct}) parallel to charge (Q) [52]. The diffusion of La^{3+} and Mn^{2+} ions in an electrolyte gives a straight line in low frequency region which describes the Warburg constant (W). The 3%La-MnO₂@GO electrode shows nearly similar shape in the high frequency region before and after cycling stability. In contrast, from **Fig. 4.21 (A)** 3%La-MnO₂@GO electrode displays an R_s value of ($0.2 \Omega/cm^{-2}$) and R_{ct} value ($34.7 \Omega/cm^{-2}$) before cycling which are lower than $R_s = 0.3 \Omega/cm^{-2}$ and $R_{ct} = 41.9 \Omega/cm^{-2}$ after cycling. This may be attributed to the surface modification of electrode during cycling.

The EIS spectrum analysis of experimental point of 3%La-MnO₂@GO electrode is shown in **Fig. 4.21 (B)**. The solution resistance (R_s) is considerable high with value of $2 \Omega/cm^{-2}$ at frequency 100 KHz. The charge transfer resistance (R_{ct}) shows an ideal curve with initial resistance $2.8 \Omega/cm^{-2}$ at 3.16 KHz, middle resistance $5.1 \Omega/cm^{-2}$ at 0.158 KHz, and final resistance 9.03 at frequency 2.5 Hz. The Warburg resistance increased from $11.21 \Omega/cm^{-2}$ at frequency 1.25 Hz to $19.4 \Omega/cm^{-2}$ at frequency 0.1 Hz. The equivalent circuit is drawn considering diffusion parameters of EIS spectrum. The diffusion coefficient of sodium ions (D) and intercalation capacity C_{int} values are used for further calculation. The kinetics of diffusion transport processes in electrolyte can be calculated using the modified Warburg formula [53]. The D value obtained from the EIS method was $0.96 \times 10^{-13} cm^2 s^{-1}$.

$$D = \left(\frac{\left| \frac{de}{dc} \right|}{nFSW} \right)^2 \quad (4.2)$$

Where, S is the true surface area of active material of electrode and W is the Warburg

constant, determined from the diffusion impedance. The intercalation capacity dependence is calculated using relation.

$$C_{\text{int}} = FL \left| \frac{dc}{dE} \right|_E \quad (4.3)$$

where, L is the thickness of layer or particle size of electrode material.

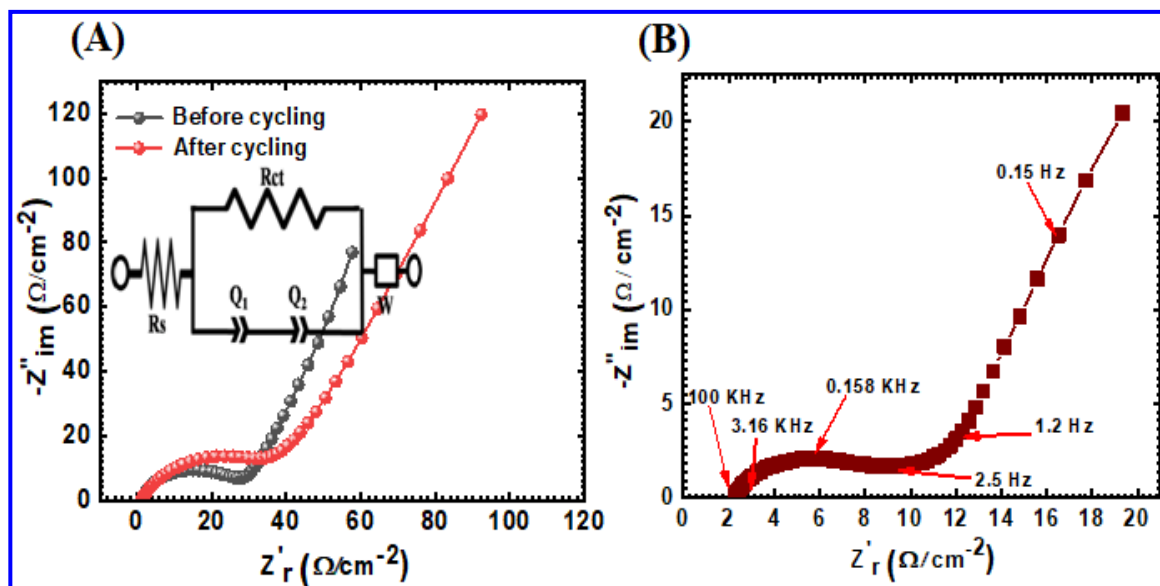


Fig. 4.21 (A) Nyquist plots of symmetric device before and after cycling and (inset shows equivalent circuit) and (B) the EIS spectrum frequency analysis of 3%La-MnO₂@GO electrode.

4.2.C.3.5 Mechanical flexibility and stability studies

The mechanical flexibility of the symmetric device without losing its supercapacitive performance is significantly useful for application of device. The mechanical flexibility of FSSSC device is tested by measuring CV curves at different bending positions. The bending positions of device at angles of 0, 45, 90, and 165° are shown in **Fig. 4.22 (A)**. Furthermore, CV cycles are taken up to 5000 cycles to test the stability FSSSC device as depicted in **Fig. 4.22 (B)**. The capacitive retention versus cycle number plots of FSSSC device is represented in **Fig. 4.22 (C)**. The maximum capacitive retention 90% is observed after 5000 CV cycles. It signifies the excellent adhesion of active electrode material with proper interface between gel electrolyte and electrode material.

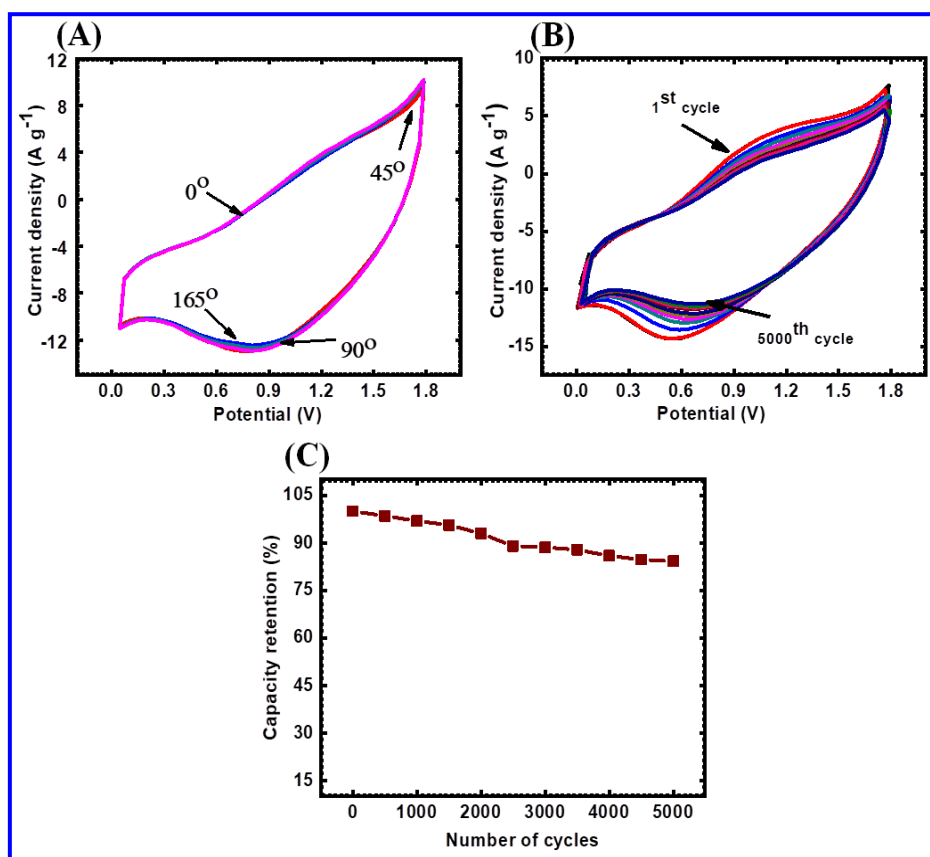


Fig. 4.22 (A) The CV curves of symmetric device at different bending angles of 0-165° at scan rate 100 mV s⁻¹, (B) the stability CV curves of 5000 cycles of FSSSC device and (C) the plot of capacitance retention versus number of cycles.

4.2.C.3.6 Practical demonstration of symmetric FSSSC device

The practical demonstration of fabricated two (5 x 5 cm²) series connected symmetric devices is displayed in **Fig. 4.23 (A)**. One device has +1.8 V operating potential window, so the series combination of the two devices gives a total potential up to +3.6 V. Initially, these FSSSC devices are charged with a potential of +3.6 V for 30 s and discharged through panel of 211 red LEDs. After 30 s charge, during discharging of FSSSC device, LEDs panel glows for more than 3.5 minutes. **Fig. 4.23 (A)** displays photograph captured at discharging of symmetric device. The measured storing output power of device is 744 mW cm⁻² which signifies excellent charge storing capability. The I-V characteristic of 211 red LEDs panel operated as external power source is shown in **Fig. 4.23 (B)**. At the voltage of 1.7 V, LED panel starts glowing with a current of 8 mA. The I-V characteristic of panel during on discharging of devices is illustrated in **Fig. 4.23 (C)**. The discharge current slowly decreases from 225 to 85 mA, while voltage decreases from +3.6 to +1.7 V in 3.5 min. Similarly, output power also decreases from 744 to 180 mW cm⁻².

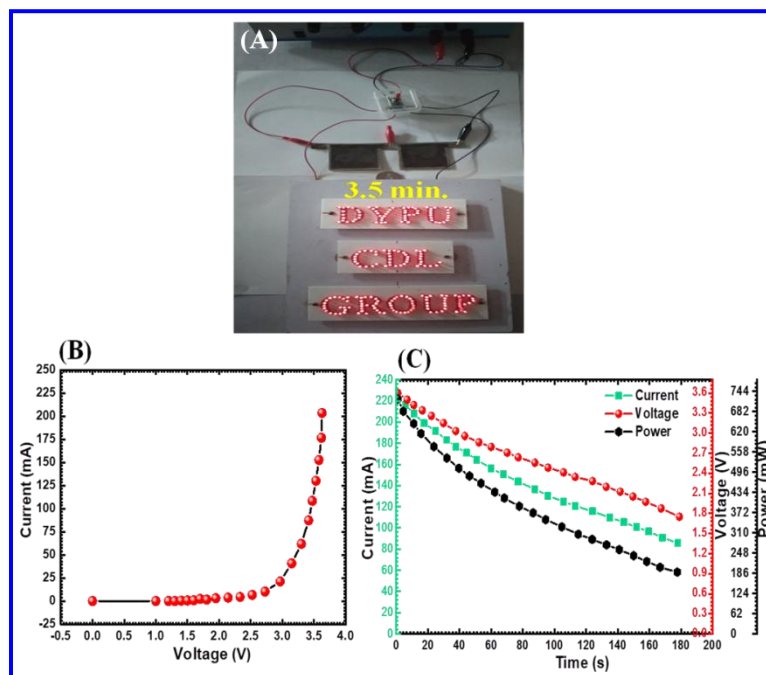


Fig. 4.23) (A) Demonstration of two series connected symmetric devices charged at +3.6 V for 30 s and the discharged through a panel of 211 red LEDs (DYP, U, CDL, GROUP) which glows for 3.5 min, (C) the I-V characteristic of 211 red LEDs panel operated as external power source and (D) the I-V characteristics of panel operated on discharging of devices.

4.3 Conclusions

In present work, the successful synthesis of MnO_2 and La doped $\text{MnO}_2@\text{GO}$ a composite electrode was carried out on SS substrate using SILAR method. The La doping in MnO_2 increased electrochemical activities and GO sheets as a backbone which modified surface morphology of 3%La- $\text{MnO}_2@\text{GO}$ thin film electrode giving rise in surface area of $149.2 \text{ m}^2 \text{ g}^{-1}$. The maximum electrochemical specific capacitance of 729 F g^{-1} at a scan rate of 5 mV s^{-1} with capacitive retention of 94.39% for 5000 CV cycles were obtained for 3%La- $\text{MnO}_2@\text{GO}$ electrode. The flexible symmetric solid state supercapacitor device with configuration of 3%La- $\text{MnO}_2@\text{GO} // \text{PVA-Na}_2\text{SO}_4 / 3\% \text{La-MnO}_2@\text{GO}$ in operating potential window +1.8 V showed specific capacitance of 138 F g^{-1} with ED and PD of 64 Wh kg^{-1} and 1 kW kg^{-1} , respectively. In addition, FSSSC device exhibited capacitive retention of 90% for 5000 CV cycles. Two series connected symmetric devices successfully stored output energy of 744 mW cm^{-2} for 3.5 min when charged at +3.6 V for 30 s and followed by discharged through 211 red LEDs (DYP, U, CDL, GROUP). This work demonstrates that 3%La- $\text{MnO}_2@\text{GO}$ is a promising electrode material for charge storage device application.

4.4 References

- [1] X. Xie, K. Lee, J. Wang, K. Loh, *Energy Environ. Sci.*, 4, (2011), 3960-3965.
- [2] V. Subramaniana, S. Halla, P. Smith, B. Rambabu, *Solid State Ion*, 75, (2004), 511-515.
- [3] J. Wang, F. Kang, B. Wei, *Prog. Mater. Sci.*, 74, (2015), 51-124.
- [4] Q. Ren, Y. Zhang, H. Lu, Y. Wang, W. Liu, X. Ji, A. Devi, A. Jiang, D. Zhang, *ACS Appl. Mater. Interfaces*, 10, (2018), 468-476.
- [5] H. Xiao, S. Yao, H. Liu, F. Qu, X. Zhang, X. Wu, *Prog. Nat. Sci. Mater. Int.*, 26, (2016), 271-275.
- [6] V. Senthilkumar, Y. Kim, S. Chandrasekaran, B. Rajagopalan, E. Kim, J. Chung, *RSC Adv.*, 5, (2015), 20545-20553.
- [7] S. Lim, N. Huang, H. Lim, *Ceram. Int.*, 39, (2013), 6647-6655.
- [8] L. Wang, X. Feng, L. Ren, Q. Piao, J. Zhong, Y. Wang, H. Li, Y. Chen, B. Wang, *J. Am. Chem. Soc*, 137, (2015), 4920-4923.
- [9] I. Ivanishcheva, A. Ivanishchev, A. Dixit, *Monatshefte Chem-Chemic*, 150, (2019), 489-498.
- [10] C. Liu, Z. Yu, D. Neff, A. Zhamu, B. Jang, *Nano Lett.*, 10, (2010), 4863-4868.
- [11] X. Zhou, J. Zhang, H. Wu, H. Yang, J. Zhang, S. Guo, *J. Phys. Chem., C*, 115, (2011), 11957-11961.
- [12] M. Sk, C. Yue, *RSC Adv.*, 4, (2014), 19908-19915.
- [13] T. Xiong, T. Tan, L. Lu, W. Lee, J. Xue, *Adv. Energy Mater.*, 8, (2018), 1-10.
- [14] J. Kang, A. Hirata, L. Kang, X. Zhang, Y. Hou, L. Chen, C. Li, T. Fujita, K. Akagi, M. Chen, *Angew. Chem., Int. Ed.*, 52, (2013), 1664-1667.
- [15] Y. Yang, T. Liu, L. Zhang, *J. Mater. Sci. Mater. Electron*, 27, (2016), 6202-6207.
- [16] Q. Mu, Y. Wang, *J. Alloys and Compd.*, 509, (2011), 396-401.
- [17] M. Jana, S. Saha, P. Samanta, N. Murmu, N. Kim, T. Kuila, J. Lee, *J. Mater. Chem., A* 4, (2016), 2188-2197.
- [18] H. Zhao, Y. Dong, P. Jiang, G. Wang, J. Zhang, K. Li, C. Feng, *New J. Chem.*, 38, (2014), 1743-1750.
- [19] N. Chodankar, G. Gund, D. Dubal, C. D. Lokhande, *RSC Adv*, 4, (2014), 61503-61513.
- [20] Y. Hu, H. Zhu, J. Wang, Z. Chen, *J. of Alloys and Compd.*, 42, (2011), 10234-10240.

- [21] M. Ocana, Colloid. Polym. Sci., 278, (2000), 443-449.
- [22] S. Radhakrishnan, H. Kim, B. Kim, Sens. Actuators B, 233, (2016), 93-99.
- [23] N. Zhang, J. Sun, D. Jiang, T. Feng, Q. Li, Carbon, 47, (2009), 1214-1219.
- [24] T. Szabo, O. Berkesi, I. Dekany, Carbon, 43, (2005), 3186-3189.
- [25] A. Bourlinos, D. Gournis, D. Petridis, T. Szabo, A. Szeri, I. Dekany, Langmuir, 19, (2003), 6050-6055.
- [26] M. Mahmoudian, Y. Alias, W. Basiruna, P. Woi, M. Sookhakian, Sensor Actuat B-Chem, 201, (2014), 526-534.
- [27] Z. Moe, Y. Sun, H. Chen, P. Zhang, D. Zuo, Y. Liu, H. Li, Polymer, 46, (2005), 12670-12676.
- [28] H. Guo, X. Wang, Q. Qian, F. Wang, X. Xia, ACS Nano, 448, (2009), 3, 2653-2659.
- [29] T. Zhang, D. Zhang, Bull. Mater. Sci., 34, (2011), 589-594.
- [30] T. Emiru, D. Ayele, Egypt. Jour. Bas. App. Sci., 4, (2019), 74-79.
- [31] R. Sun, A. Nakajima, A. Fujishima, T. Watanabe, K. Hashimoto, J. Phys. Chem. B, 105, (2001), 1984-1990.
- [32] M. Tanveer, C. Cao, I. Aslam, Z. Ali, F. Idrees, W. Khan, M. Tahir, S. Khalid, G. Nabi, A. Mahmood, J. Chem., 39, (2015), 1459-1468.
- [33] M. Pang, G. Long, S. Jiang, Y. Ji, W. Han, B. Wang, X. Liu, Y. Xi, Electrochimica Acta., 161, (2015), 297-304.
- [34] M. Jana, J. Kumar, P. Khanra, P. Samanta, H. Koo, N. Murmu, T. Kuila, J. Power Sources, 303, (2016), 222-233.
- [35] A. Yadav, A. Lokhande, R. Pujari, J. Kim, C. D. Lokhande, Colloid Interface .J .59-51 ,(2016) ,484 ,.Sci
- [36] X. Li, Q. Li, Y. Wu, M. Rui, H. Zeng, ACS Appl. Mater. Inter, 7, (2015), 19316-19323.
- [37] G. Gund, D. Dubal, B. Patil, S. Shinde, C. D. Lokhande, Electrochim. Acta., 92, (2013), 205-215.
- [38] S. Kong, K. Cheng, T. Ouyang, Y. Gao, K. Ye, G. Wang, D. Cao, Electrochim. Acta., 226, (2017), 29-39.
- [39] A. Ivanishchev, I. Ivanishcheva, A. Dixit, R. J. of Electrochem, 55, (2019), 719-737.
- [40] A. Ivanishcheva, A. shakov, I. Ivanishcheva, A. Churikovb, A. Mironovc, S. Fedotovc, N. Khasanova, E. Antipov, Electrochim Acta, 230, (2017), 479-491.

- [41] A. Ivanishchev, A. Churikov, A. Ushakov, *Electrochimica Acta*, 122, (2014), 187-196.
- [42] J. Zhao, B. Guan, B. Hu, Z. Xu, D. Wang, H. Zhang, *Electrochim. Acta.*, 230, (2017), 428-437.
- [43] R. Rajagopal, K. Ryu, *ChemElectroChem*, 5, (2018), 2218-2227.
- [44] N. Chodankar, S. Ji, D. Kim, *J. of the Taiwan Institute of Chemical Engineers*, 80, (2017), 503-510.
- [45] A. Reddy, M. Shaijumon, S. Gowda, P. Ajayan, *J. Phys. Chem. C*, 114, (2010), 658-663.
- [46] N. Chodankar, D. Dubal, G. Gund, C. D. Lokhande, *Electrochim. Acta.*, 165, (2015), 338-347.
- [47] S. Wang, B. Pei, X. Zhao, R. Dryfe, *Nano Energy*, 2, (2013), 530-536.
- [48] N. Chodankar, D. Dubal, G. Gund, C. D. Lokhande, *J. of Energy Chem.*, 25, (2016), 463-471.
- [49] A. Patil, A. Lokhande, P. Shinde, C. D. Lokhande, *ACS Appl. Mater. Interfaces*, 10, (2018), 16636-16649.
- [50] P. Sun, H. Yi, T. Peng, Y. Jing, R. Wang, H. Wang, X. Wang, *J. of Power Sources*, 341, (2017), 27-35.
- [51] A. Ivanishchev, I. Bobrikov, I. Ivanishcheva, O. Ivanshina, *J. Electroana Chem.*, 821, (2018), 140-151.
- [52] A. Ivanishchev, A. Churikov, A. Ivanishchev, A. Ushakov, M. Sneha, P. Babbar, A. Dixit, *J. of Electrochem.*, 53, (2017), 706-712.
- [53] A. Ivanishchev, A. Churikov, I. Ivanishcheva, A. Ushakov, *Data, Ionics*, 22, (2016), 483-501.

CHAPTER-5

**ENHANCED SPECIFIC ENERGY OF SILVER
DOPED MnO_2 /GRAPHENE OXIDE ELECTRODES
AS FACILE FABRICATION SYMMETRIC
SUPERCAPACITOR DEVICE**

CHAPTER-5

Enhanced Specific Energy of Silver Doped MnO₂/Graphene Oxide Electrodes as Facile Fabrication Symmetric Supercapacitor Device

Sr. No.	Title	Page No.
5.1	Introduction	116
Section- A Synthesis and characterization of MnO₂, Ag-doped MnO₂ and MnO₂-Ag/GO thin films using SILAR method.		
5.2 A.1	Introduction	117
5.2.A.2	Experimental details	117
	5.2.A.2.1 Chemicals	117
	5.2.A.2.2 Deposition of MnO ₂ and Ag-doped MnO ₂ thin films	117
	5.2.A.2.3 Depositions of 3 vol.% Ag-doped MnO ₂ /GO composite films	118
	5.2.A.2.4 Physical and electrochemical characterizations	119
5.2.A.3	Results and discussion	119
	5.2.A.3.1 XRD analysis	119
	5.2.A.3.2 FT-IR analysis	120
	5.2.A.3.3 Wettability test	121
	5.2.A.3.4 FE-SEM study	122
	5.2.A.3.5 TEM study	124
	5.2.A.3.6 The EDX study	124
	5.2.A.3.7 The XPS study	125
	5.2.A.3.8 Brunauer-Emmett-Teller study	126
Section- B Supercapacitive evaluation of MnO₂, Ag-doped MnO₂ and MnO₂-Ag/GO thin films by SILAR method.		
5.2.B.1	Introduction	128
5.2.B.2	Results and discussion	128
	5.2.B.2.1 The CV studies	128
	5.2.B.2.2 GCD studies	130

	5.2.B.2.3	The EIS studies	133
	5.2.B.2.4	The stability studies	134
	5.2.B.2.5	Supercapacitive performance of GO electrode	135
SECTION- C			
Flexible solid state symmetric supercapacitor (FSS-SSC) device fabrication and supercapacitive evaluation of Mn-Ag₃/GO thin films.			
5.2.C.1	Introduction		139
5.2.C.2	Experimental details		139
	5.2.C.2.1	Electrode Preparation	139
	5.2.C.2.2	Fabrication of FSS-SSC device	139
5.2.C.3	Electrochemical properties of flexible solid state symmetric supercapacitor (FSS-SSC) device		140
	5.2.C.3.1	The CV studies	140
	5.2.C.3.2	The GCD studies	141
	5.2.C.3.3	Ragone plot	142
	5.2.C.3.4	Mechanical flexibility and stability studies	143
	5.2.C.3.5	The EIS studies	144
	5.2.C.3.6	Practical demonstration of symmetric FSS-SSC device	145
5.3	Conclusions		146
5.4	References		147

5.1. Introduction

The modern gadgets like portable electronics, medical devices, smart-phones, memory backup devices, load levelling and hybrid vehicles require fast high power contribute which is not possible with rechargeable batteries [1-3]. The supercapacitor is an attractive electrochemical device which meets the requirements of all modern electronic and electrical devices [4, 5].

The transition metal oxides and hydroxides exhibit pseudocapacitance and are easy to fabricate, and investigate as compared with polymer based supercapacitors [6]. The electrode material with high surface area and high electric conductivity results in excellent electrochemical performance [7]. Manganese dioxide (MnO_2) is one of the most fascinating materials for consideration (for making a composite thin film with graphene oxide) owing to its inexpensiveness, environmental compatibility, and natural abundance. It is an attractive material used in many fields such as supercapacitors, batteries, and catalysts [8-10]. The supercapacitors performance of MnO_2 was improved by doping with transition metals such as Co, V, Fe, Cu and Ni [11, 12]. Generally, the heteroatom dopants are changes the electronic, and physicochemical properties of carbon based materials, which then alters the Na^+ storage behavior (adsorption, de/insertion on the electrode surface) [13, 14].

In recent years, noble metals like ruthenium, palladium, rhodium, osmium, iridium, silver, gold, platinum etc. are doped into the matrix of MnO_2 to improve its electronic conductivity [15, 16]. The carbon based materials doped with noble metals are attractive electrode materials in the field of supercapacitor because of their good electrical conductivity, and electrochemical stability [17]. Amongst these, silver (Ag) is a soft and glossy transition metal, which has higher electrical conductivity with reflectivity than other metals [18]. Among all other noble metals, Ag is very attractive due to its lower cost. However, in present work quantity of Ag doped into the MnO_2 is the very less (1 to 5%) while the corresponding increment in Cs of MnO_2 is large. The bulk synthesis of the GO could reduce the production cost. The doping of Ag with the GO composite can increase the cost of a material by 1 to 5% but the value of Cs increases 200%. The Ag doping can increase the proton transmission during the

electrodes. Consequently, Ag-doped MnO_2 electrodes showed increase in Cs due to quick and reversible redox reaction [19].

The present chapter is divided into three sections (Sections A, B and C). In the present work, MnO_2 , Ag-doped MnO_2 and MnO_2 -Ag/GO composite thin film are synthesized using successive ionic layer adsorption and reaction (SILAR) method and their characterization is discussed in Section 'A'. The Section 'B' is associated with the electrochemical performance of MnO_2 , Ag-doped MnO_2 and MnO_2 -Ag/GO thin films testing in 1 M Na_2SO_4 electrolyte. The Section 'C' deal with the symmetric flexible solid state supercapacitor device configuration of SS/ MnO_2 -Ag/GO//PVA- Na_2SO_4 / MnO_2 -Ag/GO/SS and their electrochemical performance is evaluated.

SECTION - A

Synthesis and characterization of MnO_2 , Ag-doped MnO_2 and MnO_2 -Ag/GO thin films using SILAR method.

5.2 A.1 Introduction

The present section deals with the synthesis and characterization of MnO_2 , Ag-doped MnO_2 and MnO_2 -Ag/GO composite thin films by SILAR method using different doping concentrations.

5.2.A.2 Experimental details

5.2.A.2.1 Chemicals

The AR grade chemicals such as potassium permanganate (KMnO_4), manganese sulfate (MnSO_4), natural graphite flake with a particle size of 150 μm , polyvinyl acetate (PVA) and silver nitrate (AgNO_3) were procured from Thomas Baker Ltd. India.

5.2.A.2.2 Deposition of MnO_2 and Ag-doped MnO_2 thin films

The MnO_2 and 1, 3, 5 vol% Ag-doped MnO_2 thin films were prepared by SILAR method. A 0.03 M anionic KMnO_4 solution was formulated by dissolving in 50 ml DDW. Similarly, individually prepared 0.05 M cationic solution (serving Mn^{2+} and Ag^{1+} ions) was prepared by dissolving different volumetric ratios of MnSO_4 and AgNO_3 in 50 ml DDW. Firstly, the precleaned SS substrate was immersed alternately in cationic and anionic solutions for 15 s each. Further every immersion, the SS substrate was rinsed in DDW for 10 s to eliminate weakly bound Mn^{2+} and Ag^{1+} ions.

These four steps are regarded as one SILAR cycle. Such 60 cycles were repeated to achieve uniform deposition of MnO_2 thin film at room temperature (300 K). The deposited thin films are indicated as Mn, 1 vol% Ag-doped Mn (Mn-Ag1), 3 vol% Ag-doped Mn (Mn-Ag3), and 5 vol% Ag-doped Mn (Mn-Ag5) for 50:0, 49.5:0.5, 48.5:1.5 and 47.5:2.5 volumetric ratios, respectively. The mass loadings of 0.28, 0.37, 0.56, and 0.57 mg cm^{-2} are obtained for Mn, Mn-Ag1, Mn-Ag3, and Mn-Ag5 thin films, respectively.

5.2.A.2.3 Depositions of 3 vol% Ag-doped MnO_2 /GO composite films

The GO was synthesized by modified Hummer's method [20]. The anionic solution KMnO_4 was formulated by dissolving in 50 ml DDW and cationic solution (serving Mn^{2+} and Ag^{1+} ions) was prepared by dissolving MnSO_4 and AgNO_3 in 50 ml DDW in volumetric ratio as 48.5:1.5. The SS substrate dipped in GO solution for 60 s to adsorb GO sheets and air dried for 50 s. Then, the substrate was immersed in separately placed cationic and anionic solution for 15 s to adsorption of Mn^{2+} and Ag^{1+} ions. Further every immersion, the SS substrate was rinsed through DDW to eliminate weakly bound Mn^{2+} and Ag^{1+} ions. Thus the first SILAR cycle was completed. After, repeating 60 cycles uniform Mn-Ag3/GO thin films were achieved. The mass loadings of 0.78 and 0.25 mg cm^{-2} are obtained for Mn-Ag3/GO and GO thin films, respectively. High mass loading for Mn-Ag3/GO electrode is due to the fast reaction process at the electrode surface. Schematic diagram of synthesis for Mn-Ag3/GO thin film by SILAR method is shown in Fig. 5.1.

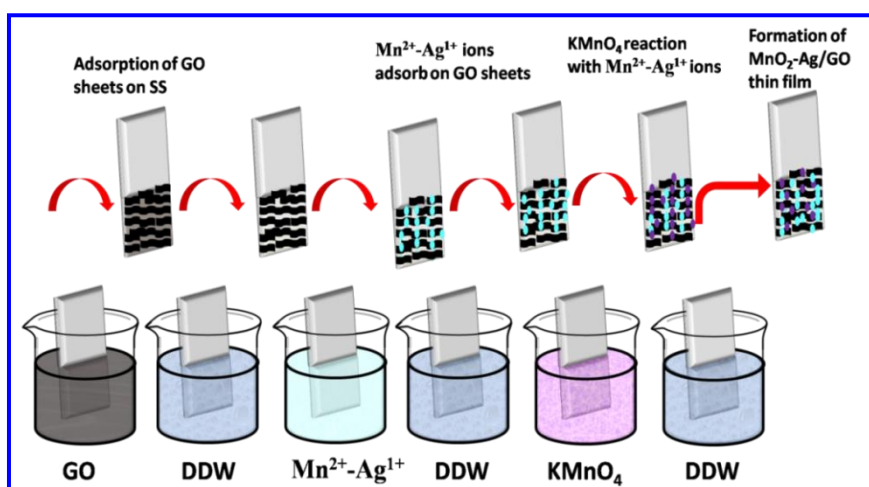


Fig. 5.1) Schematic diagram of synthesis for Mn-Ag3/GO thin film by SILAR method.

5.2.A.2.4 Physical and electrochemical characterizations

The XRD was investigated with Cu K α radiation ($\lambda = 0.154$ nm), operated at 30 kV during 2°/min. The FT-IR spectra of all samples were analyzed using alpha (II) Bruker unit. Surface morphology and elemental composition were studied by field-emission scanning electron microscopy (FE-SEM) (Philips SEM-XL30 Netherlands) with energy dispersive X-ray spectroscopy (EDX). High-resolution transmission electron microscopy (HRTEM) profiles with selected area electron diffraction (SAED) patterns were obtained by JEOL ARM-200F (JEOL, U.S.). Wettability test was used to find the nature of films by Rame Hart-500 advanced goniometer. Elemental composition and chemical states of samples were investigated by X-ray photoelectron spectroscopy (XPS) (K-alpha Thermo Fisher Scientific, U.K.). The pore size distribution and surface area of the product were calculated with Barrette-Joynere-Halenda (BJH) and Brunauer-Emmett-Teller (BET) by BEL-SORP-II instrument. The ZIVE MP1 multichannel workstation measurements were conducted to evaluate the electrochemical performance of electrodes in 1M Na₂SO₄ electrolyte using three electrode cell configuration. The FSS-SSC device fabrication of SS/MnO₂-Ag₃/GO//PVA-Na₂SO₄//MnO₂-Ag₃/GO/SS was tested in two electrode system.

5.2.A.3 Results and discussion

5.2.A.3.1 XRD analysis

The XRD study was carried out to investigate the phase and crystal structure of thin film material. The XRD spectra of Mn, Mn-Ag₁, Mn-Ag₃, Mn-Ag₅ and Mn-Ag₃/GO electrodes on surface of SS substrate are revealed in **Fig. 5.2 (a-e)**. The observed diffraction peaks located at 28.98°, 56.68°, and 64.87° correspond to the (110), (211), and (002) crystal planes of β -type tetragonal MnO₂ (JCPDS card no. 24-0735) [21]. The weak intensity of diffraction peaks shows low crystalline structure of MnO₂ electrodes [20]. The diffraction peaks (**b-d**) associated with Ag doping do not depict any peak matching to the crystalline silver or composite materials. The decrease in intensity and broadness of diffraction peaks are observed with increased silver doping into MnO₂. In **Fig. 5.2 (e)**, the peak observed at an angle of $2\theta = \sim 11.20^\circ$ corresponds to GO (001) plane [22] owing to the formation of functional groups on the

GO sheets. No additional peaks other than SS substrate are observed in XRD patterns. The peaks highlighted with # symbol in the XRD spectra are due to SS substrate.

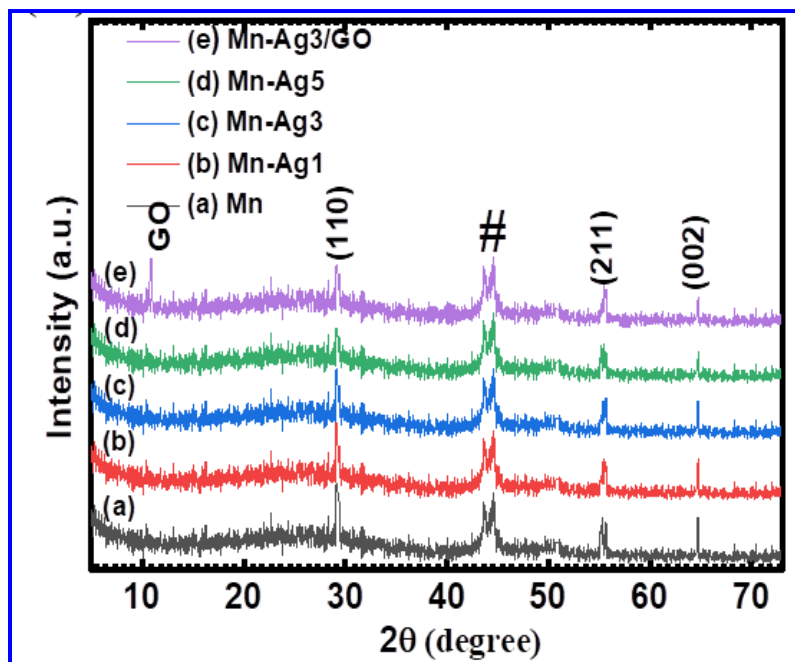


Fig. 5. 2) XRD diffraction patterns of (a) Mn, (b) Mn-Ag1, (c) Mn-Ag3, (d) Mn-Ag5 and (e) Mn-Ag3/GO electrodes.

5.2.A.3.2 FT-IR analysis

Fig. 5.3 (a-e) shows the FT-IR spectra of Mn, Mn-Ag1, Mn-Ag3, Mn-Ag5 and Mn-Ag3/GO composite electrodes in the wavelength range from 400 to 4000 cm^{-1} . Due to small percentage of Ag doping into MnO_2 there is no considerable peak shifts in **Fig. 5.3 (a-d)**. The intense peaks at about 3427.65, and 1596.13 cm^{-1} signify stretching vibrations and bending vibrations of O-H group present on the surface of electrodes, respectively [23]. The peak at 1343.20 cm^{-1} is ascribed to -C-O bending vibration linking with Mn atoms [24]. The strong absorptions peak at 618.35 cm^{-1} is owing to accompanying and stretching vibrations of Mn-O bond [25]. **Fig. 5.3 (e)** shows the FT-IR pattern of Mn-Ag3/GO thin film. The peak at 1609 cm^{-1} is due to by oxygen groups of stretching vibration [26]. The peak at 1596.13 cm^{-1} is due to C=C skeletal vibration to the surface of GO sheets [27]. In addition, the strong absorption peaks at 1343.20, and 1124.43 cm^{-1} are specified the presence of C-O alkoxy, and -C-O-C epoxy groups [28]. These characteristic peaks corroborate the preparation of Ag-doped MnO_2 and Mn-Ag3/GO electrodes.

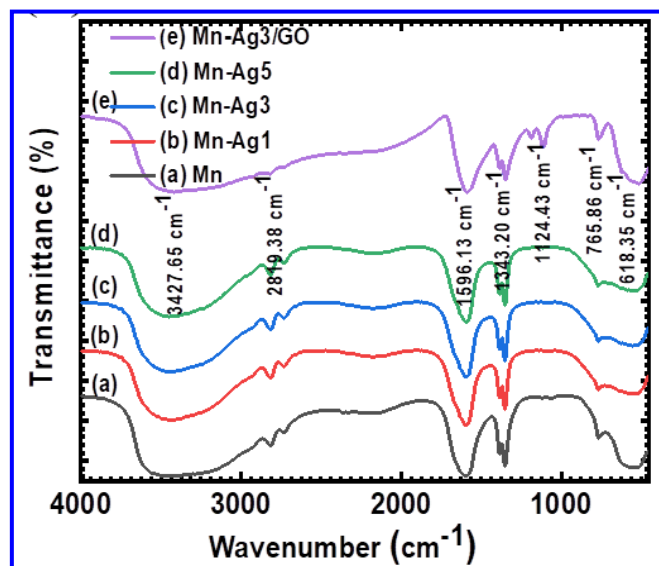


Fig. 5.3) The FT-IR spectra of (a) Mn, (b) Mn-Ag1, (c) Mn-Ag3, (d) Mn-Ag5 and (e) Mn-Ag3/GO electrodes.

5.2.A.3.3 Wettability test

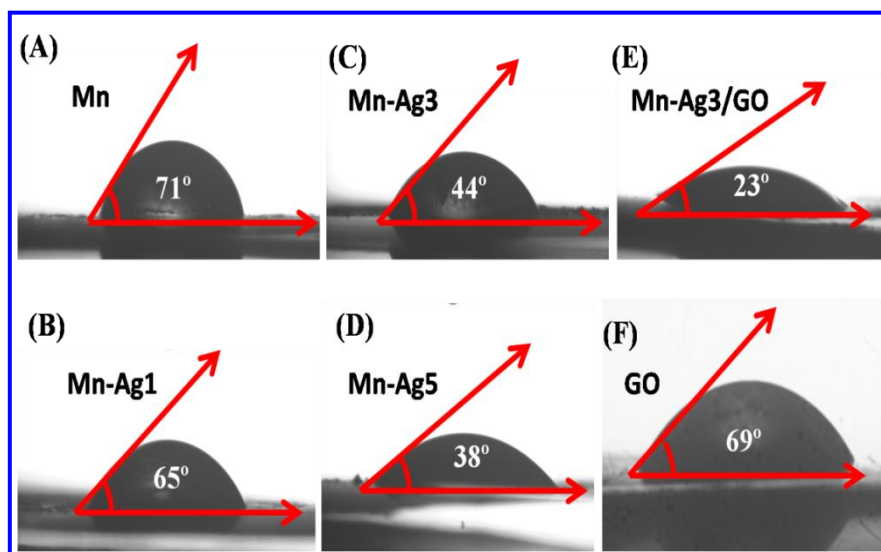


Fig. 5.4) The photograph images of contact angles for (A) Mn, (B) Mn-Ag1, (C) Mn-Ag3, (D) Mn-Ag5, (E) Mn-Ag3/GO and (F) GO electrodes.

The mass and charge transfer are affected by the contact angle between the liquid and electrode surface. The wettability measurement of water droplets on the surface of Mn, Mn-Ag1, Mn-Ag3, Mn-Ag5, Mn-Ag3/GO, and GO thin films are illustrated in **Fig. 5.4 (A-F)**. Also, as Ag doping increases, the water contact angles decreases. The values of water contact angles of 71°, 65°, 44°, 38°, 23° and 69° obtained for Mn, Mn-Ag1, Mn-Ag3, Mn-Ag5, Mn-Ag3/GO and GO electrodes, respectively signify the hydrophilic nature of films. The cause for the change in liquid contact angle is

accredited to the morphology of electrodes achieved by Ag doping. The low water contact angle of Mn-Ag₃/GO film may be due to the porous morphology. The lower wettability is favorable for the supercapacitive activities [29].

5.2.A.3.4 FE-SEM study

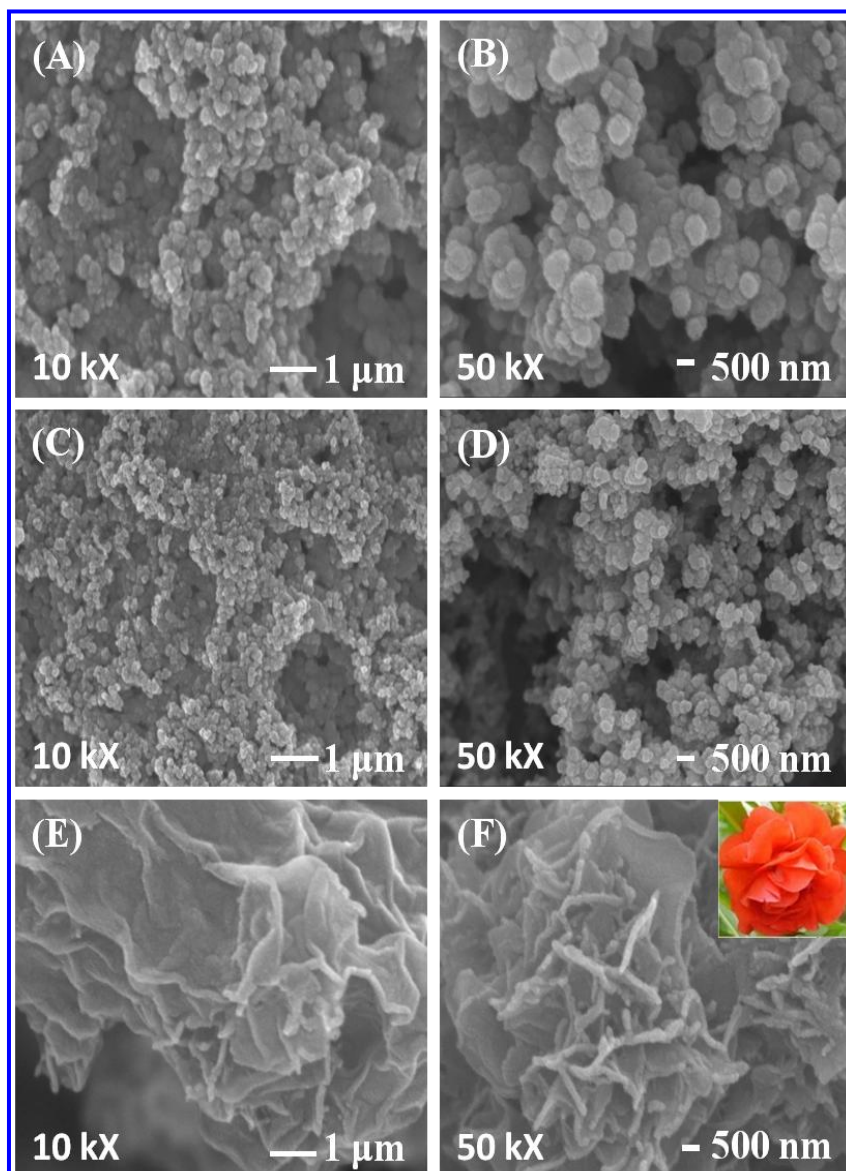


Fig. 5.5) FE-SEM pictures of (A-B) Mn, (C-D) Mn-Ag₃ and (E-F) Mn-Ag₃/GO films at magnifications of 10 kX and 50 kX.

The surface morphologies of MnO₂ and Ag doped MnO₂ samples on the surface of SS substrate are observed by FE-SEM images. **Fig. 5.5 (A-F)** shows the FE-SEM profiles of Mn, Mn-Ag₃ and Mn-Ag₃/GO electrodes at magnifications of 10 kX and 50 kX. **Fig. 5.5 (A-B)** illustrates the formations of a structure due to the interconnected

nanospheres of MnO_2 on the substrate. The interconnected nanosphere structure helps in quick transfer of charge. The 3% Ag doped MnO_2 shows formation of spherical fine porous nanoparticles with size in the range of 60-70 nm [Fig. 5.5 (C-D)]. The flower-like morphology due to layered nanosheets of Mn-Ag3/GO sample is depicted in Fig. 5.5 (E-F). Fig. 5.5 (F) reveals the porous nature of Ag-doped MnO_2 particles over GO sheets. The 2D nanosheets interconnected to each other also provide highly active surface area for ion insertion/desertion at electrode and electrolyte interface. The Mn-Ag3/GO electrode enhances the rate of electrochemical reactions which improves energy storage capacity for SCs application.

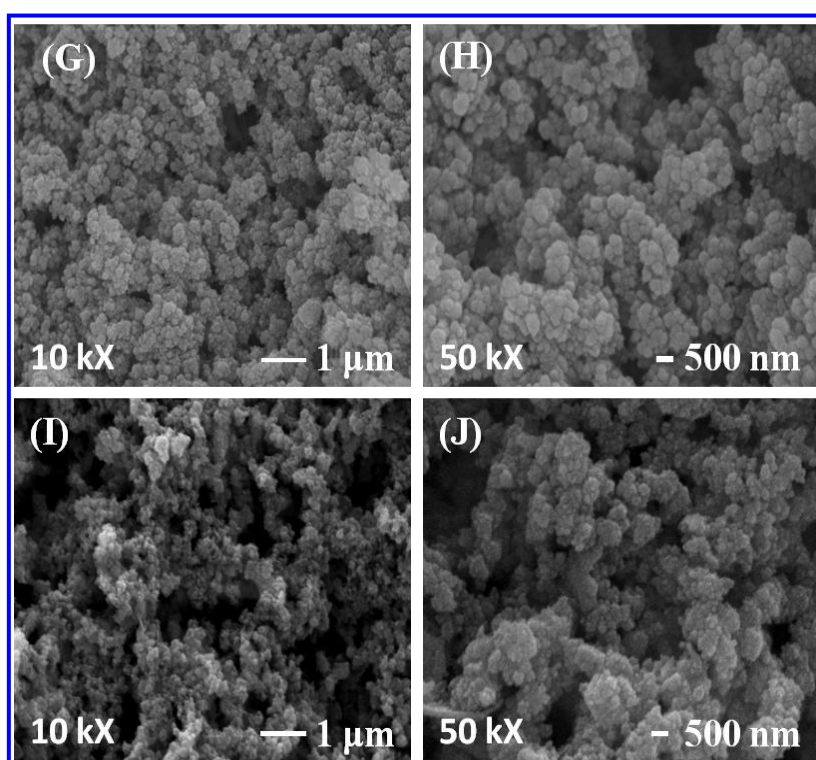


Fig. 5.5) The FE-SEM images of (G-H) Mn-Ag1 and (I-J) Mn-Ag5 thin films at magnifications of 10 kX and 50 kX.

The FE-SEM images of Mn-Ag1 shown in Fig. 5.5 (G-H) depicts the formation of Mn-Ag1 spherical nano-particles having size in the range of 70-80 nm. The surface morphology of Mn-Ag5 thin film displays the formation of nanoparticles with size in the range of 40-50 nm as demonstrated in Fig. 5.5 (I-J). Such nanoparticles collected of large nanoparticles like surface morphology may decrease the electro active surface area and porosity. The Ag doping concentration increases the growth rate of the reaction, nucleation rate increases, and the surface converts into inactive growth with overgrown particles on the SS substrate.

5.2.A.3.5 TEM study

The TEM technique was investigated to further examine the specific microstructure of Mn-Ag3/GO electrode. **Fig. 5.6 (A)** displays the formation of sponge-like Mn-Ag nanoparticles on the GO sheets. The thin semitransparent GO sheets with red color arrow and yellow arrow signify the growth of Mn-Ag nanoparticles on the graphene sheets as depicted in **Fig. 5.6 (B)**. The HR-TEM profile in **Fig. 5.6 (C)** confirms thin nanosheets with structural assembly. Also, the interplanar spacings of 0.403, and 0.476 nm corresponding to (211), and (110) planes of MnO_2 are in agreement of interplanar spacing determined from XRD technique. The selected area electron diffraction (SAED) pattern in Fig. 5 (D) clearly identifies the (110), and (211) planes of MnO_2 .

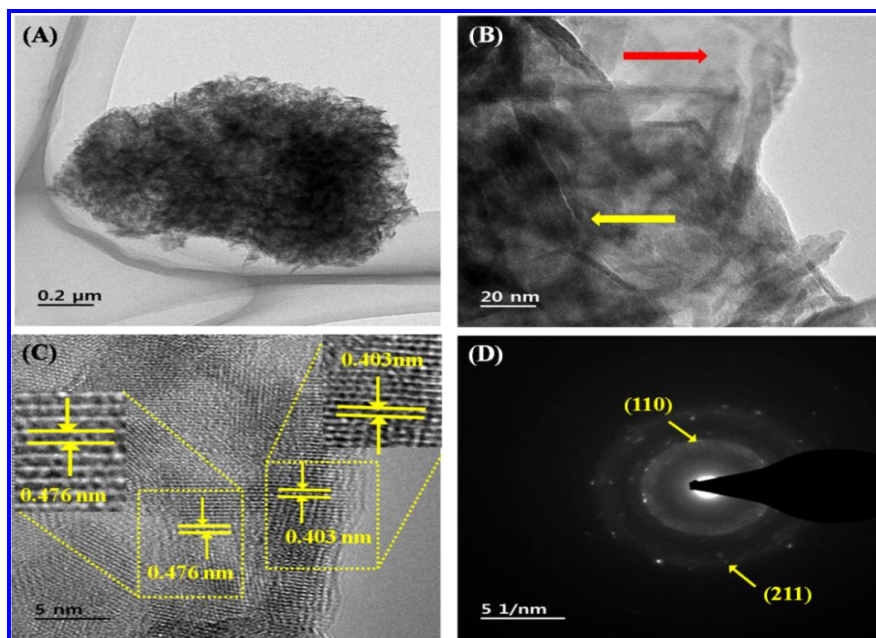


Fig. 5.6) TEM pictures of (A-B) Mn-Ag3/GO powder sample, (C) HR-TEM picture of GO multilayer, and (D) the SAED picture of Mn-Ag3/GO sample.

5.2.A.3.6 The EDX study

The EDX pattern (**Fig. 5.7 (A)**) was used for elemental composition analysis of Mn-Ag3/GO electrode with a table of composition in atomic percentage. The peaks of C, O, Ag, and Mn elements are obtained. The elemental composition analysis of Mn-Ag3/GO electrode is demonstrated in **Fig. 5.7 (B)**. The individual elemental mappings of Ag, O, Mn, and C are shown in **Fig. 5.7 (C-F)**. Such reliable evidences confirm the successful 2.13% atomic percentage doping of Ag into the Mn-Ag3/GO thin film. The

XPS study confirms the atomic percent of oxygen (42.24 %) as 2.0 times of Mn (21.54%) in Mn-Ag₃/GO electrode. The decoration of Ag₃ doped MnO₂ on GO is confirmed by presence of carbon (34.49%).

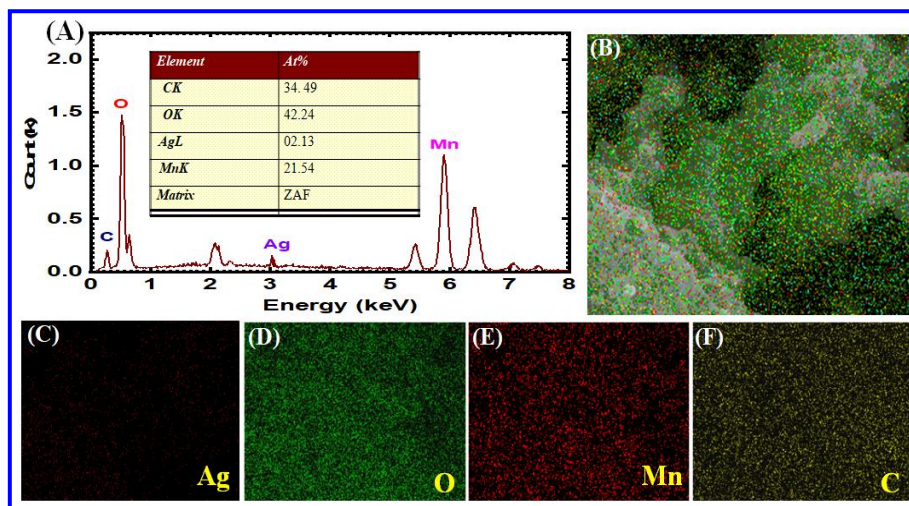


Fig. 5.7) (A) EDX pattern of Mn-Ag₃/GO thin film, (B) the chemical analysis of Mn-Ag₃/GO thin film representing sharing of Ag, O, Mn, and C, elements, individual elemental distribution profiles of (C) Ag, (D) O, (E) Mn, and (F) C elements.

5.2.A.3.7 The XPS study

The chemical state and elemental composition of materials were analyzed by XPS spectra. The XPS survey scan profile of Mn-Ag₃/GO electrode in **Fig. 5.8 (A)** reveals the coexistence of elements of Mn 2p, O 1s, Ag 3d, and C 1s peaks which support the results of EDX mapping. **Fig. 5.8 (B)** shows the Mn 2p peak energies of two substates as 2p_{1/2}, and 2p_{3/2} with spin energy difference of 11.8 eV, which suggest the existence of β -MnO₂ developed on the SS substrate [30]. The components of satellite peaks at 643.1, and 654.9 eV are accredited to Mn⁴⁺ oxidation state. The **Fig. 5.8 (C)** represents the O 1s XPS spectrum of peak located at 531.4 eV, which correspond to the oxygen state of Mn-O-Mn and other peaks at 529.8, and 532.5 eV are attributed to the C=O, and C-O bond energies [31]. The C 1s spectrum specifies the peaks located at 283.1, 284.6, and 286.7 eV to -C-OH, -COOH, and C-C/C=C bonding energies, respectively as depicted in **Fig. 5.8 (D)**. The carbon sp² hybridization confirms epoxy, hydroxyls, and carbonyl groups present on the surface of GO sheets [32]. The spectrum of Ag is depicted in **Fig. 5.8 (E)**. The two satellite peaks ascribed at 366.1, and 372.2 eV specified to 3d_{3/2} and 3d_{5/2}, indicate Ag¹⁺ oxidation state with

spin energy difference of 6 eV [33].

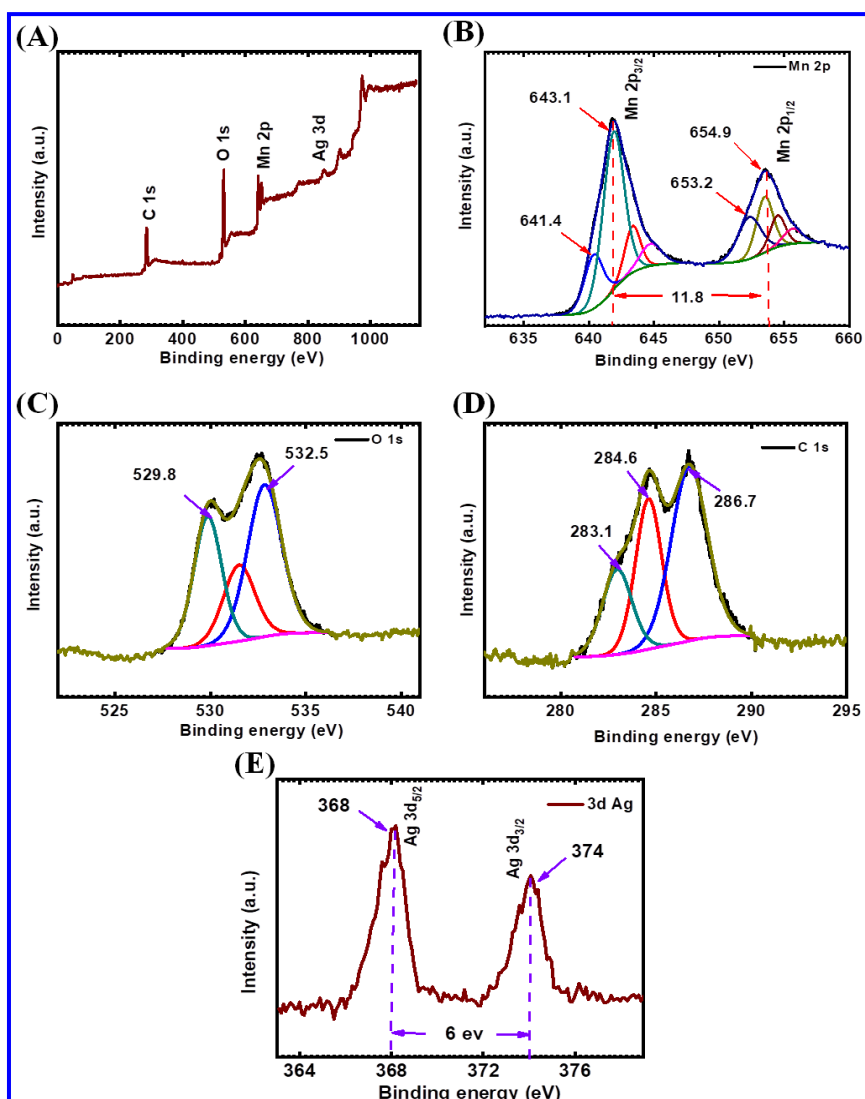


Fig. 5.8) XPS spectra of Mn-Ag3/GO electrode (A) the XPS survey profiles, (B) Mn 2p spectrum, (C) O 1s spectrum, (D) C 1s spectrum, and (E) Ag 3d spectrum.

5.2.A.3.8 The BET study

The textural characteristics of Mn, Mn-Ag1, Mn-Ag3, Mn-Ag5 and Mn-Ag3/GO electrodes investigated by the N₂ sorption isotherms recorded at 77 K are demonstrated in **Fig. 5.9 (A)**. The N₂ sorption isotherms are characterized as type IV with a H₃ hysteresis curve representing the existence of mesoporous nature [34]. A discrete hysteresis loop in pressure range of 0.4-1.0 p/p₀ can be accredited to mesoporous structure. The specific surface areas calculated using the BET are 47, 82, 156, 140 and 192 m² g⁻¹ for Mn, Mn-Ag1, Mn-Ag3, Mn-Ag5 and Mn-Ag3/GO electrodes, respectively. The Mn-Ag3/GO sample shows highest surface area as compared to other

samples. The Barrett-Joyner-Halenda (BJH) pore distribution graphs of all samples with the mesoporous nature are illustrated in **Fig. 5.9 (B)**. Remarkably, Mn-Ag3/GO electrode showed largest BET surface area, total pore volume, and pore radius. The Ag doped MnO₂ and Mn-Ag3/GO samples showed the changes in the surface area owing to the effectively Ag doping. The determined values of BET surface area, pore volume, and pore radius are presented in **Table 5.1**. As can be seen from **Table 5.1**, with an increase in Mn-Ag3/GO electrode, the surface area, and pore volume increase till the nanoporous morphology formation takes place on the GO sheets. The higher BET surface area, average pore volume, and minimum pore radius of the GO composite electrodes with more active sites on the surface appears to be responsible for the maximum specific capacitance value of Mn-Ag3/GO sample.

The surface area, and pore-size characterization of GO sample were verified by measuring the N₂ adsorption-desorption isotherms as shown in **Fig. 5.9 (C)**. From this, the surface area was found to be 227 m² g⁻¹. Furthermore, the pore volume distribution curve as a function of the pore size calculated by the BJH method is shown in **Fig. 5.9 (D)**. The average pore size of 13.20 nm confirms a mesoporous structure GO sample [35].

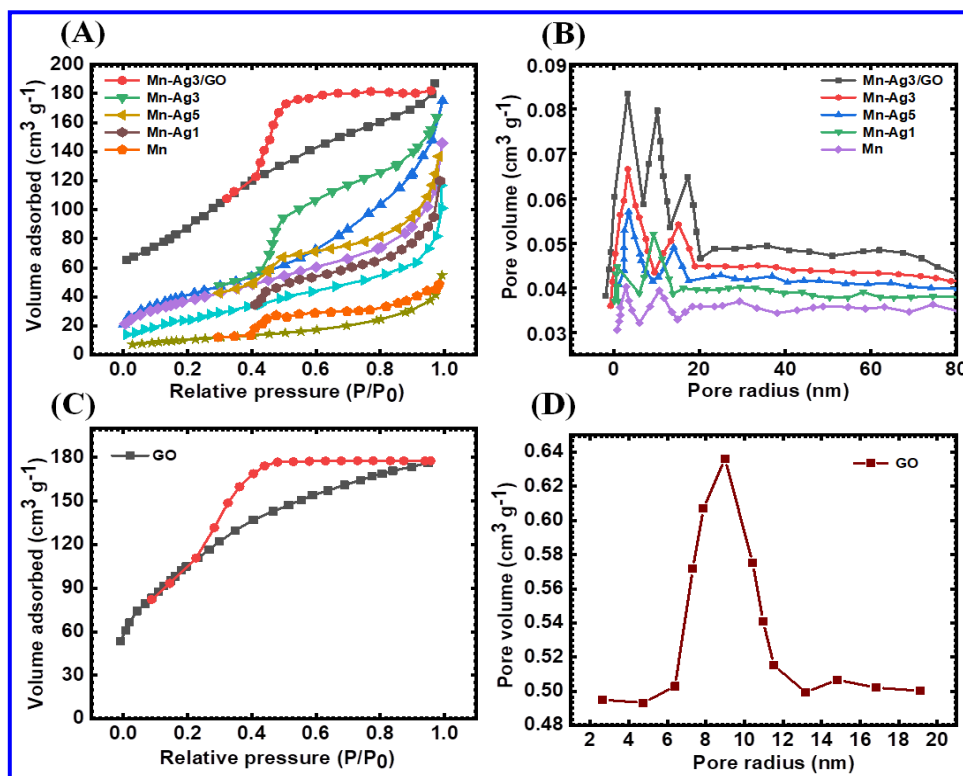


Fig. 5.9) (A) N₂ sorption isotherms for Mn, Mn-Ag1, Mn-Ag3, Mn-Ag5 and Mn-Ag3/GO samples, (B) the BJH size distribution curves for Mn, Mn-Ag1, Mn-Ag3, Mn-Ag5 and Mn-Ag3/GO samples, (C) N₂ sorption isotherms of GO sample and (D) the BJH size distribution curve of GO sample.

Table 5.1: An outline of specific surface area, average pore size and pore volume values of Mn, Mn-Ag1, Mn-Ag3, Mn-Ag5, Mn-Ag3/GO and GO electrodes.

Sr. No.	Sample	Specific surface Area (m ² g ⁻¹)	Average pore size (nm)	Pore volume (m ³ g ⁻¹)
1	Mn	47	12.5	0.149
2	Mn-Ag1	82	7.42	0.137
3	Mn-Ag3	156	2.31	0.039
4	Mn-Ag5	140	3.98	0.082
5	Mn-Ag3/GO	192	1.57	0.019
6	GO	227	13.20	0.620

SECTION – B

Supercapacitive evaluation of MnO₂, Ag-doped MnO₂ and MnO₂-Ag/GO thin films by SILAR method

5.2.B.1 Introduction

In present section, the electrochemical performance of MnO₂, Ag-doped MnO₂ and MnO₂-Ag/GO thin films testing in 1 M Na₂SO₄ electrolyte. The effect of various Ag doping concentrations on the electrochemical performance of MnO₂ thin films is studied by CV, GCD, cycling stability and EIS analysis.

5.2.B.2 Results and discussion

5.2.B.2.1 The CV studies

Fig. 5.10 (A) shows the CV graphs recorded between potential range of 0 to +0.9 V/SCE for Mn, Mn-Ag1, Mn-Ag3, Mn-Ag5 and Mn-Ag3/GO composite electrodes at 100 mV s⁻¹ scan rate. The Mn-Ag3/GO thin film has a highest enclosed area under CV graph and maximum current compared to other thin films with significant more charge storage ability [36]. **Fig. 5.10 (B-F)** demonstrates the CV

graphs of Mn, Mn-Ag1, Ag-Mn3, Mn-Ag5 and Mn-Ag3/GO electrodes at 5 to 100 mV s^{-1} scan rates, respectively. The shapes of the CV curves are unchanged at higher scan rates, implying pseudocapacitive nature of all electrodes. The CV curves of composite materials are of rectangular nature which indicate pseudocapacitor behavior. The larger area under the CV curves signifies the higher current response and good specific capacitance. The Cs of 483, 596, 786, 664, and 877 F g^{-1} are obtained for Mn, Mn-Ag1, Mn-Ag3, Mn-Ag5 and Mn-Ag3/GO thin films, respectively at a scan rate of 5 mV s^{-1} . The higher capacitance of the electrode depends upon percentage of doping and composite with graphene oxide.

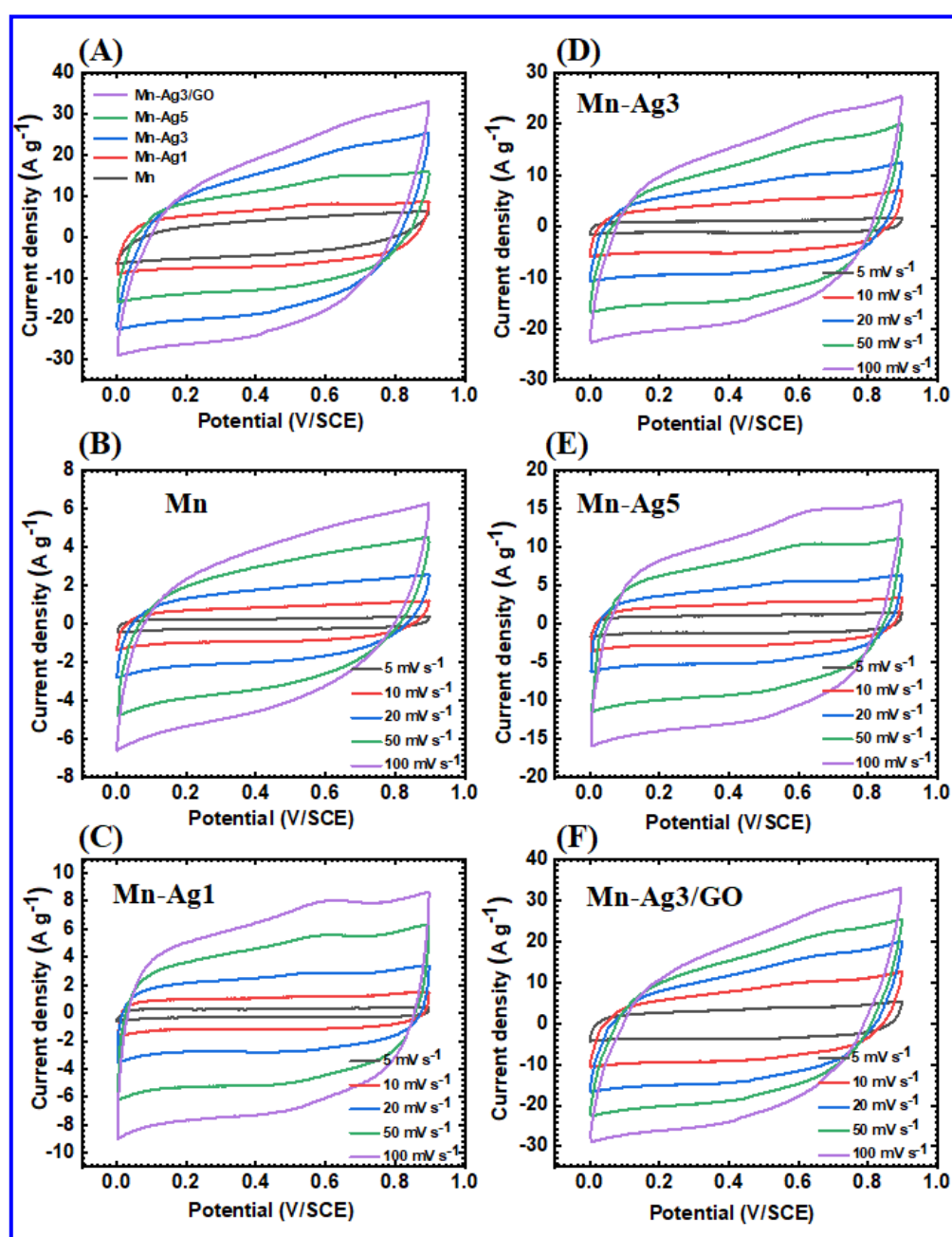


Fig. 5.10 (A) The CV curves of Mn, Mn-Ag1, Mn-Ag3, Mn-Ag5 and Mn-Ag3/GO electrodes at 100 mV s^{-1} scan rate, (B) the CV graphs of Mn, (C) Mn-Ag1, (D) Mn-Ag3, (E) Mn-Ag5 and (F) Mn-Ag3/GO thin films at 5 to 100 mV s^{-1} scan rate.

The Cs variation versus scan rate for all electrodes as depicted in **Fig. 5.11** (A). The Mn-Ag3 composited with graphene oxide (Mn-Ag3/GO) electrode shows the maximum specific capacitance which is attributed to high conductivity, large active surface area and mesoporous nature [37]. The Mn-Ag3/GO electrode illustrated a high areal capacitance of 684 mF cm^{-2} at 5 mV s^{-1} . The variation of areal capacitance for all electrodes with scan rate is shown in **Fig. 5.11** (B). The supercapacitors with high areal capacitance are significantly preferred for integrating with thin wearable and flexible electronic devices. Hence, the present Mn-Ag3/GO supercapacitor electrode is a possible candidates for wearable and flexible device applications. The areal capacitances for electrodes are depicted in **Table 5.2**.

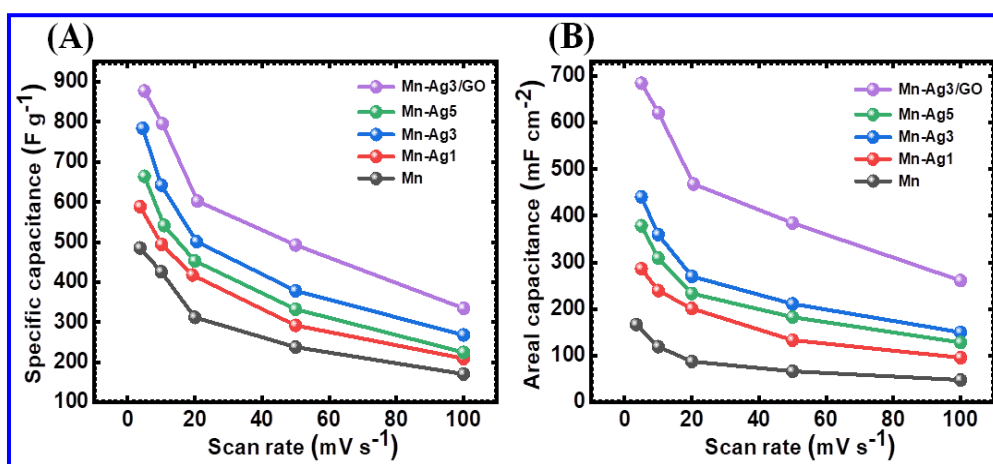


Fig. 5.11 (A) The plots of Cs versus scan rates for all electrodes, and (B) the plots of areal capacitance versus scan rates of Mn, Mn-Ag1, Mn-Ag3, Mn-Ag5 and Mn-Ag3/GO electrodes.

5.2.B.2.2 The GCD studies

The GCD measurements are carried out to find out the charge storage capability of all thin film electrodes. **Fig. 5.12** (A) displays the GCD graphs at 2 A g^{-1} current density in operating potential windows of 0 to $+0.9 \text{ V/SCE}$ of all electrodes. The charge-discharge curves show the good capacitive behavior suggesting the quick reversible reactions at the electrode/electrolyte interface [38]. The Mn-Ag3/GO electrode shows longer charge-discharge time than the other samples at the same current density of 2 A g^{-1} . **Fig. 5.12** (B-F) reveals the GCD graphs of Mn, Mn-Ag1,

Mn-Ag3, Mn-Ag5 and Mn-Ag3/GO at various current densities from 2 to 5 A g⁻¹. The Cs of all samples increases as the current density decreases. It is generally due to the slow reversible process and diffusion rate of the electrolyte at high current density [39]. The GCD performance is almost ideal along with small iR drop for each sample. The Cs determined from GCD curves are 476, 600, 793, 662, and 868 F g⁻¹ for Mn, Mn-Ag1, Mn-Ag3, Mn-Ag5 and Mn-Ag3/GO electrodes, respectively at 2 A g⁻¹ current density. The Mn-Ag3/GO thin film has the maximum specific capacitance. The Cs of the supercapacitor electrodes decreases as the current density increases.

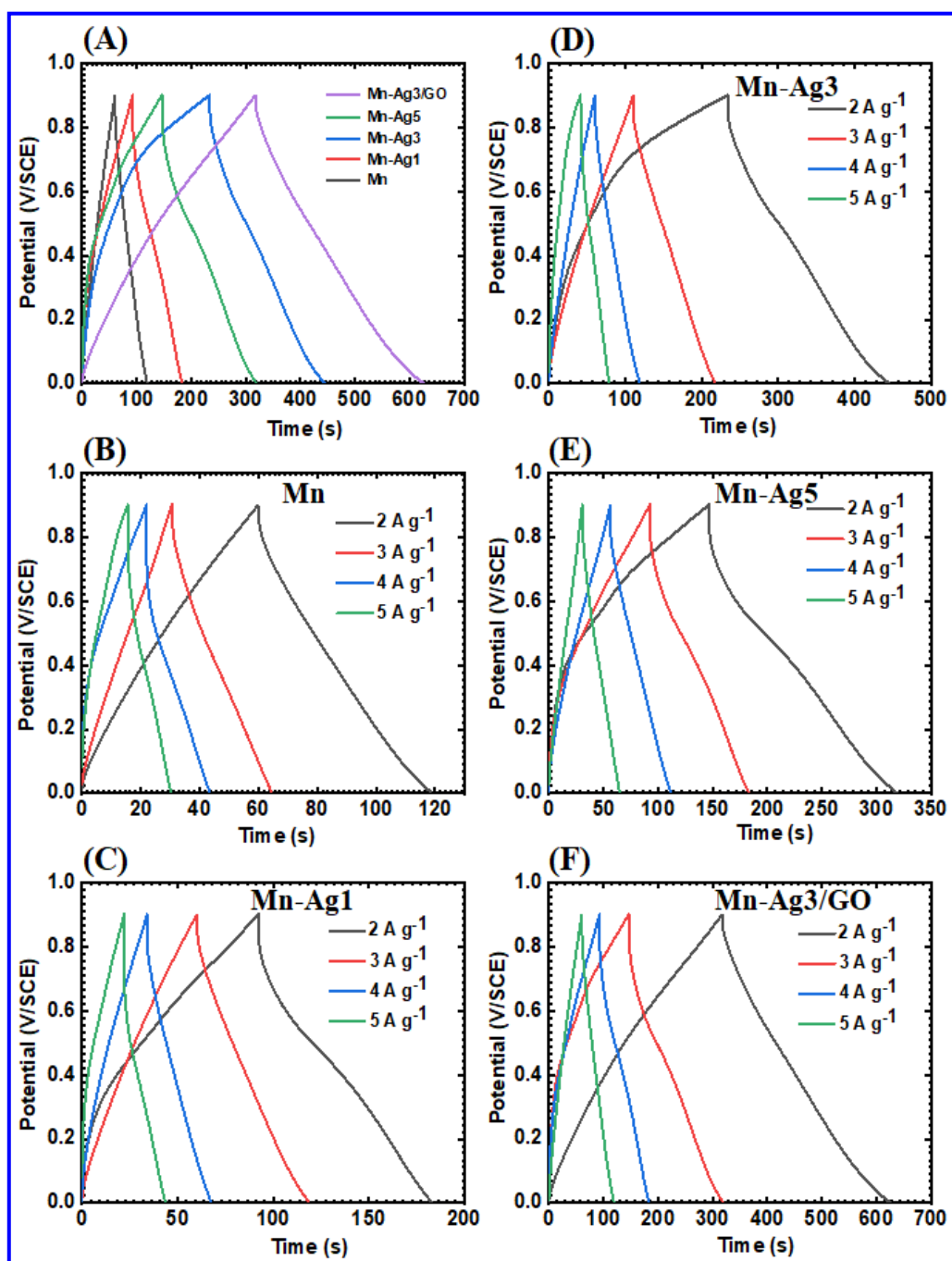


Fig. 5.12) (A) The GCD plots of Mn, Mn-Ag1, Mn-Ag3, Mn-Ag5 and Mn-Ag3/GO thin films at 2 A g⁻¹ current density, (B) GCD plot of Mn, (C) Mn-Ag1, (D) Mn-Ag3, (E) Mn-Ag5 and (F) Mn-Ag3/GO electrodes at 2 to 5 A g⁻¹ current densities.

The plots of C_s with various current densities of all electrodes are depicted in **Fig. 5.13 (A)**. Hence, the gravimetric capacitance depends on the mass loading of electrode. The C_s increases with the increase of mass loading of active materials. The performance of electrode depends upon electroactive species which undergo faradic redox reaction limited to the electrode-electrolyte interface [40]. At a current density of 2 A g⁻¹, the Mn-Ag3/GO electrodes showed areal capacitance of 677 mF cm⁻², which declined to 333 mF cm⁻² at a current density of 5 A g⁻¹. The graph of areal capacitance versus applied current density of all electrodes is shown in **Fig. 5.13 (B)**. The variation of specific capacitance, rate capability, and areal capacitance of these electrodes are illustrated in **Table 5.2**.

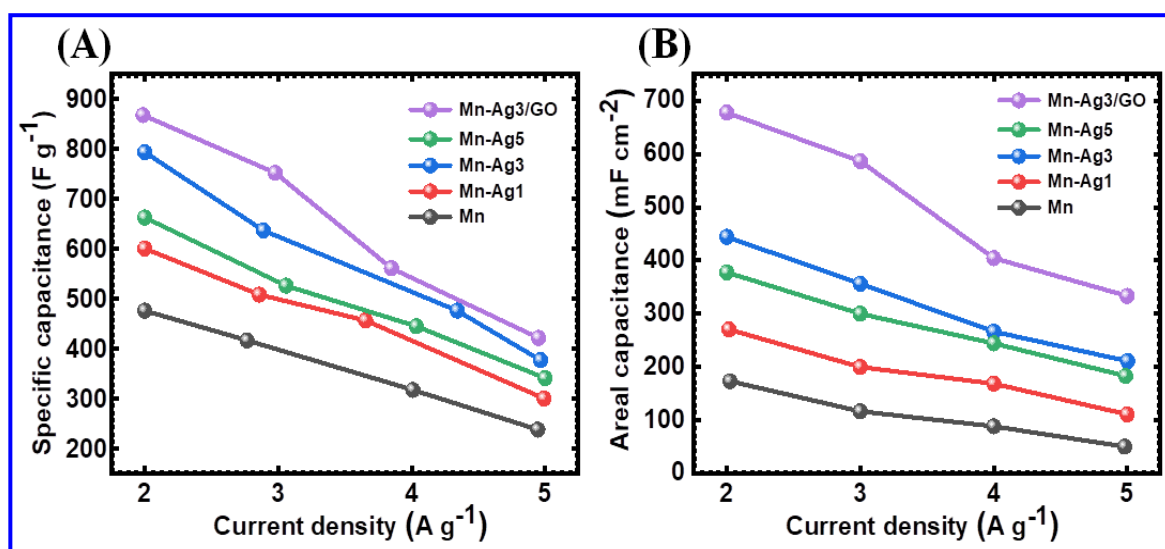


Fig. 5. 13) (A) The plots of C_s versus current densities for all electrodes and (B) the plots of areal capacitance versus current densities of Mn, Mn-Ag1, Mn-Ag3, Mn-Ag5 and Mn-Ag3/GO electrodes.

The MnO₂-Ag3/GO composite electrode showed maximum C_s value of 877 F g⁻¹. The fast charge transfer process of this composite material is responsible for highest specific capacitance. The porous structure of GO in the composite material gives large number of active sites for redox reactions as it contains several hydrophilic functional groups which facilitate smooth ion transportation to the inner material, which increases the overall capacitance. The high surface area, and large pore volume of GO composite materials with more active sites and quick electrolyte ion transfer contribute to control

electrochemical double layer capacitor (EDLC). The uniform MnO_2 -Ag nanoparticles grown on the surface of GO sheets lead to increase the specific surface area and the electrical conductivity of material.

5.2.B.2.3 The EIS studies

The Nyquist graphs are studied in the range of frequency from 0.001 Hz to 1 MHz with amplitude of 10 mV to estimate the electrical conductivity and ion diffusion of the electrode materials. **Fig. 5.14** shows that all Nyquist graphs consist of partial semicircles in high frequency domain and straight lines in small frequency domain indicate an ideal capacitive behavior [41]. The slope of the lower frequency domain at 45° carried out to find out Warburg resistance (W). The equivalent series resistance (R_s) values of 1.7, 1.5, 1.1, 1.3, and $0.9 \Omega/\text{cm}^{-2}$ with charge transfer resistance (R_{ct}) values of 39.2, 24.7, 13.5, 14.9, and $5.3 \Omega/\text{cm}^{-2}$ obtained for Mn, Mn-Ag1, Mn-Ag3, Mn-Ag5 and Mn-Ag3/GO thin films, respectively are depicted in **Table 5.2**. The low R_{ct} values are due to the higher charge transfer rate in the redox reaction between electrolyte and electrode. It is observed that Mn-Ag3/GO electrode has a low diffusion rate with high electrical conductivity. Therefore, Mn-Ag3/GO electrode with low R_{ct} value exhibits excellent charge transfer ability. The surface area of this electrode also leads to an increase in charge transfer rate which raises contact between electrolyte and surface of electrode [42].

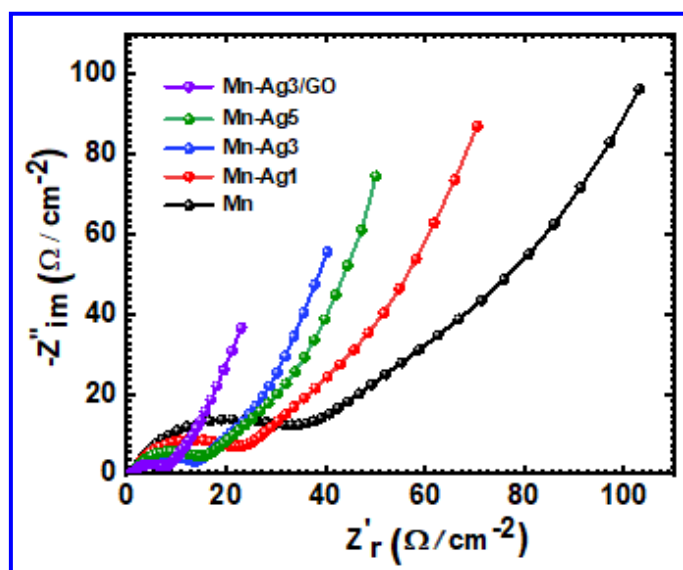


Fig. 5.14 Nyquist graphs of Mn, Mn-Ag1, Mn-Ag3, Mn-Ag5 and Mn-Ag3/GO electrodes.

5.2.B.2.4 The stability studies

The cycling stability of all electrodes was recorded at 100 mV s^{-1} scan rate in $1 \text{ M Na}_2\text{SO}_4$ aqueous electrolyte over 5000 CV cycles. The long-term cycling stability of Mn-Ag3/GO composite thin film is shown in **Fig. 5.15 (A)**. Furthermore, the capacity retention of 94.57 % is revealed in **Fig. 5.15 (B)**. The executive pseudocapacitive contribution can be connected with the superior rate capability of the $\text{MnO}_2\text{-Ag3/GO}$ electrode as shown in **Table 5.2**. The better supercapacitive activity of Mn-Ag3/GO thin film indicates a best candidate for charge storage material. The cycling stability of MnO_2 thin film is improved by the incorporation of Ag and GO. The capacitive retention values are demonstrated in **Table 5.2**. Chodankar et al [7] reported 88% cyclic retention over 2500 cycles for chemically synthesized $\alpha\text{-MnO}_2$ thin film. Mane et al [43] reported 90% capacity retention after 5000 cycles for SILAR deposited La- $\text{MnO}_2\text{@GO}$ composite thin film. Zhi et al [44] reported 90% capacitance retention over 10,000th cycles for chemical vapor deposition synthesized Ag/3D-graphene foam-ordered mesoporous carbon (Ag-GF-OMC) electrode. Kumar et al [45] reported 89% retention in capacitance after 5000 cycles for DC sputtered nickel (Ni) coated anodic aluminum oxide (AAO) $\alpha\text{-MnO}_2\text{/Ni-AAO}$ electrode.

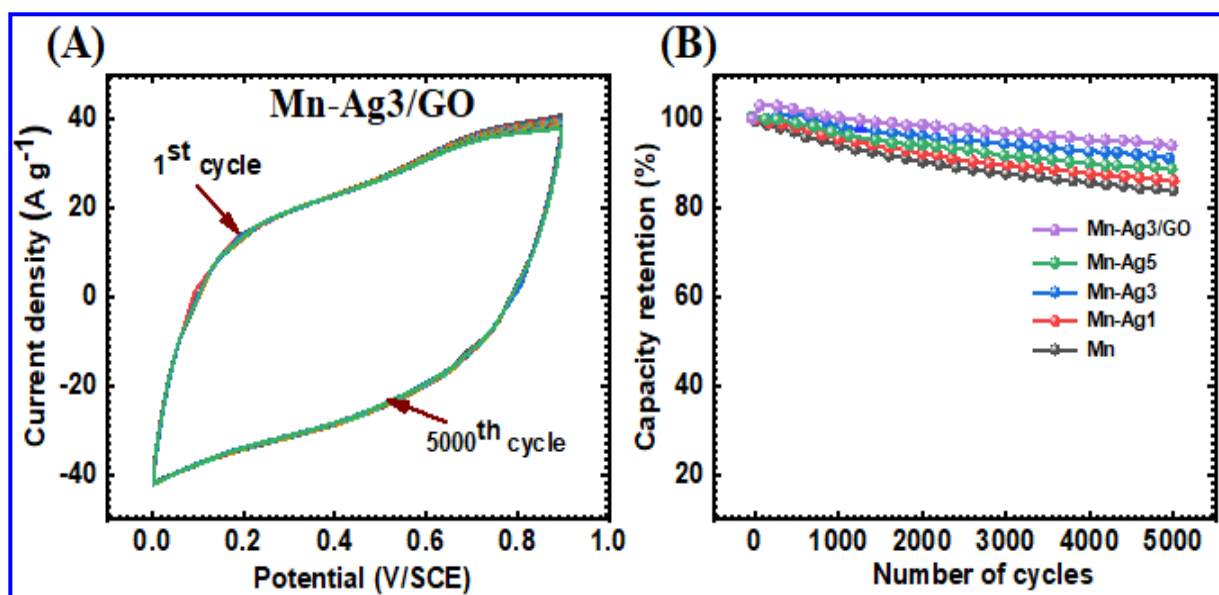


Fig. 5.15 (A) The stability of CV curves 5000 cycles for Mn-Ag3/GO electrode and (B) the graph of capacity retention with cycle number of Mn, Mn-Ag1, Mn-Ag3, Mn-Ag5 and Mn-Ag3/GO electrodes for 5000 repeated CV cycles.

5.2.B.2.5 Supercapacitive performance of GO electrode

The cyclic voltammetry measurement is performed to analyze the supercapacitive performance of GO electrode using a three-electrode cell configuration system with a negative potential window of -1.0 to 0 V/SCE in 1 M Na₂SO₄ electrolyte. **Fig. 5.16 (A)** shows the CV curves of GO electrode in the scan rates range of 5-100 mV s⁻¹, respectively. The rectangular CV curves of GO thin films show the capacitive behavior. The Cs of GO electrode decreases with an increasing scan rate as shown in **Fig. 5.16 (B)**. The GO electrode shows high Cs of 195 F g⁻¹ within the range of potential window between -1.0 – 0.0 V at 5 mV s⁻¹ scan rate. The GO electrode showed a maximum areal capacitance of 48 mF cm⁻² at 5 mV s⁻¹, and the variation in the areal capacitance with scan rate is shown in **Fig. 5.16 (C)**. The slow decrease of the Cs values can be due to the charge resistive activities of the thin film material at the high scan rates and to the diffusion ion charge transport lagging behind the electronic mobility.

The GCD curves of GO electrode are recorded at various current densities from 1-4 A g⁻¹ in the potential range -1 to 0 V/SCE as depicted in **Fig. 5.16 (D)**. The curves are triangular due to carbon-based materials. During the charging and discharging steps, the charge curve of GO electrode is almost symmetric to its corresponding discharge counterpart with a small internal resistance (iR) drop, indicating the pseudocapacitive contribution along with the double layer contribution. At a current density of 1 A g⁻¹, the GO electrode demonstrated a maximum areal capacitance of 50 mF cm⁻² (Cs = 200 F g⁻¹), which declined to 28 mF cm⁻² (80 F g⁻¹) at current density of 4 A g⁻¹. The plots of specific capacitance and areal capacitance versus current densities of GO electrode are illustrated in **Fig. 5.16 (E)**. During the GCD of GO electrode, the charge-discharge time period enhanced at the lower current density due to completely occupy the active sites between the interface of electrode and electrolyte by ions.

Electrochemical impedance spectroscopy (EIS) is the most helpful test for the study of Cs. The Nyquist plots of GO electrode using the EIS in the frequency range from 100 kHz to 0.01 Hz are demonstrated in **Fig. 5.16 (F)**. The Nyquist plots of GO electrode have an almost vertical line in the low-frequency region, indicating a capacitive behavior. From high-frequency region, the solution resistance (R_s) and from low frequency charge transfer resistances are calculated. The diameter of semicircle corresponds to charge transfer resistance (R_{ct}) caused by the redox reaction on the surface of the electrode. The GO electrode shows the low values of R_s (1.6 Ω/cm⁻²),

and R_{ct} ($12.4 \Omega/\text{cm}^2$). These low values are responsible for high capacitance of GO electrode using the interaction between active material and electrolyte.

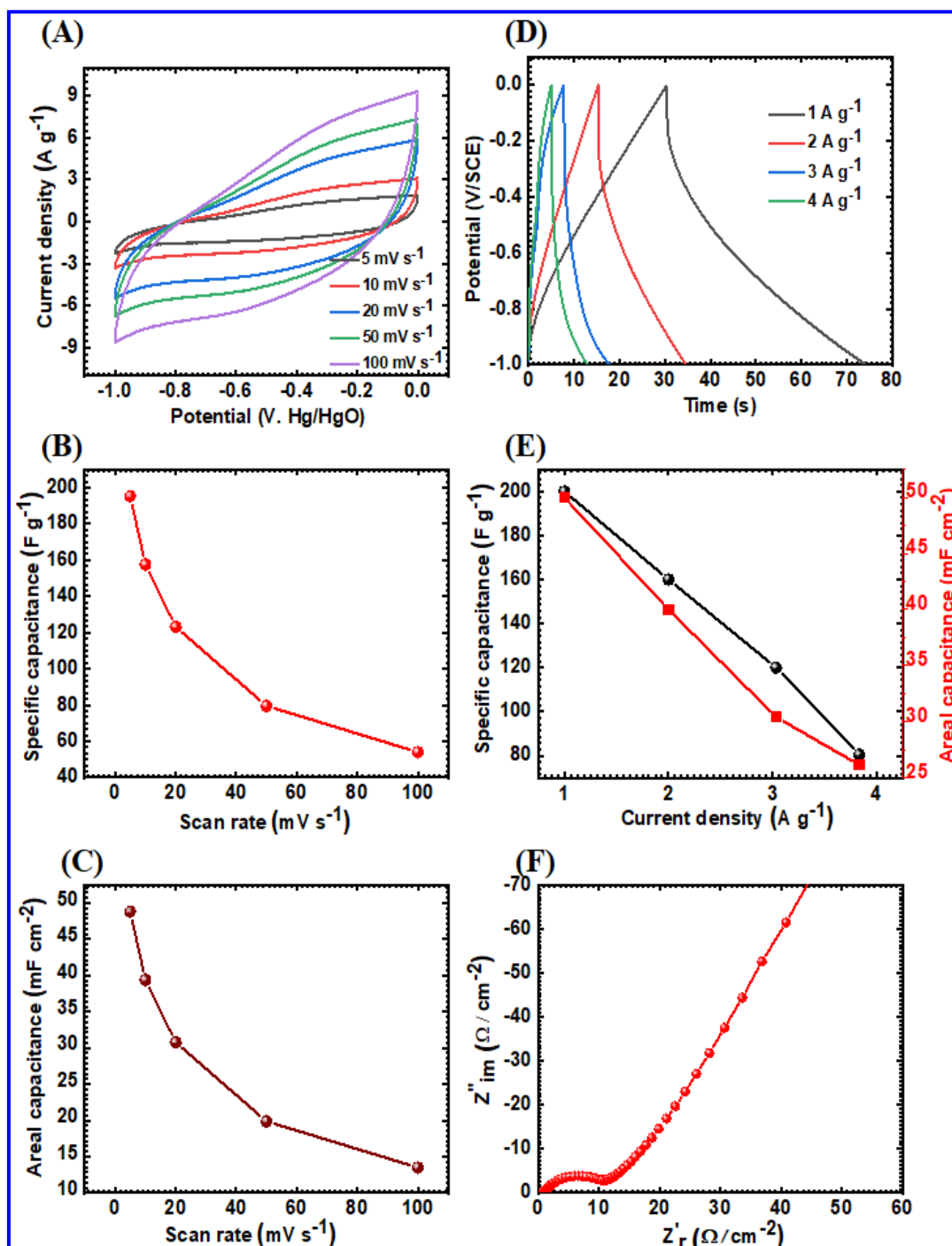


Fig. 5.16 (A) The cyclic voltammety curves of GO electrode at 5 to 100 mV s^{-1} scan rates, (B) the plot of C_s versus scan rate, (C) the areal capacitance versus scan rate, (D) the GCD curves of GO electrode at 1 to 4 A g^{-1} current densities, (E) the plots of specific capacitance and areal capacitance versus current density and (F) the Nyquist plot of GO electrode.

Table 5.2: The electrochemical properties of Mn, Mn-Ag1, Mn-Ag5, Mn-Ag3, Mn-Ag3/GO and GO electrodes.

Sr. No.	Sample	Specific capacitance (F g^{-1})	Areal capacitance (mF cm^{-2})	Capacitive retention (%)	R_{ct} (Ω/cm^{-2})	R_{s} (Ω/cm^{-2})	Rate capability (%)
1	Mn	483	135	83.72	39.2	1.7	25.57
2	Mn-Ag1	596	220	86.43	24.7	1.5	33.79
3	Mn-Ag3	786	440	91.26	13.5	1.1	54.27
4	Mn-Ag5	664	378	88.12	14.9	1.3	51.16
5	Mn-Ag3/GO	877	684	94.57	5.3	0.9	67.89
6	GO	195	48	-	12.4	1.6	21.47

Table 5.3: Comparison of supercapacitive studies of FSS-SSC device.

Sr. No	Supercapacitor Symmetric Electrode	Electrolyte	Specific Capacitance (F g^{-1})	Specific Energy (Wh kg^{-1})	Specific Power (kW kg^{-1})	Stability (%) (cycles)	Ref. No.
1.	$\text{MnO}_2/\text{MnO}_2$	CMC- Na_2SO_4	145	23	1.9	92 (2200)	[4]
2.	C- MnO_2 12h	PVA- Na_2SO_4	128	14	0.2	90 (5000)	[6]
3.	$\alpha\text{-MnO}_2$	CMC- Na_2SO_4	145	16	2.5	88 (2500)	[7]
4.	3%La- MnO_2 @GO	PVA- Na_2SO_4	142	64	1	90 (5000)	[42]
5.	Ag-GF-OMC	H_2SO_4	213	4.5	5.4	90 (10,000)	[43]
6.	$\alpha\text{-MnO}_2/\text{Ni-AAO}$	Na_2SO_4	194.2	4.2	1.4	89 (5000)	[44]
7.	Graphene@carbon cloth	PVA- H_2SO_4	11.8	1.64	0.67	-	[48]
8.	rGO@LaCe- MnO_2	Na_2SO_4	61	21.96	4	50 (3000)	[49]
9.	Ag/ MnO_2	Na_2SO_4	293	17.8	5	96 (5000)	[50]
10.	MWCNTs/ MnO_2	PVA- Na_2SO_4	204	23.3	-	80 (2500)	[51]
11.	PCNP2	$\text{H}_2\text{SO}_4/\text{PVA}$	226	7.9	0.1	92 (5000)	[52]
12.	N-G@ MnO_2 //AG	KOH	101.5	46.1	0.5	88 (2000)	[53]
13.	MnO_2 -ERGO//CNT-ERGO	PAAC/KCl	69.4	31.8	0.45	84.4 (10,000)	[54]
14.	MnO_2 -Ag3/GO	PVA- Na_2SO_4	164	57	1.6	94 (10,000)	Present Work

SECTION - C

Flexible solid state symmetric supercapacitor (FSS-SSC) device fabrication and supercapacitive evaluation of Mn-Ag₃/GO thin films.

5.2.C.1 Introduction

In this chapter, MnO₂, Ag-doped MnO₂ and MnO₂-Ag/GO thin films are prepared using SILAR method. **Table 5.2** illustrates the electrochemical parameters of MnO₂-Ag₃/GO thin films, which assists to choose the superior electrode to fabricate the symmetric device.

The present section deals with high performance symmetric FSS-SSC device fabricated using MnO₂-Ag₃/GO thin film as cathode and anode electrodes with PVA-Na₂SO₄ gel as electrolyte as well as a separator. The section 'C' deals with fabrication and electrochemical performance evaluation of symmetric FSS-SSC device.

5.2.C.2 Experimental details

5.2.C.2.1 Electrode Preparation

The SILAR method was employed to prepare the MnO₂-Ag₃/GO thin films on flexible SS substrates. The preparative parameters to prepare MnO₂-Ag₃/GO thin films are described in (Section 5.2.A.2.3).

5.2.C.2.2 Fabrication of FSS-SSC device

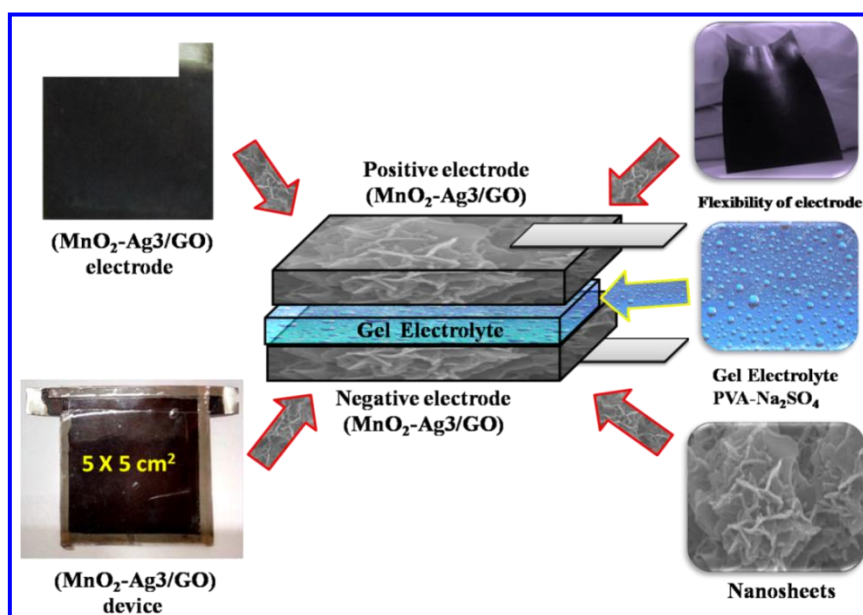


Fig. 5.17) The schematic of flexible solid state symmetric device formation.

Flexible solid-state symmetric supercapacitor (FSS-SSC) device was fabricated with $\text{MnO}_2\text{-Ag}_3/\text{GO}$ electrodes of an area of $5 \times 5 \text{ cm}^2$, wherein, $\text{MnO}_2\text{-Ag}_3/\text{GO}$ thin films were utilized as the cathode and anode with a gel electrolyte of $\text{PVA-Na}_2\text{SO}_4$. The FSS-SSC device was assembled by painting electrodes using $\text{PVA-Na}_2\text{SO}_4$ electrolyte. The device was kept under hydraulic press at a pressure of 0.5 ton for 1 hour. In symmetric supercapacitor device charge balance occurs due to same electrode material. The total mass loading on both the electrodes was 4 mg. The schematic of the FSS-SSC device formation is depicted in supporting information **Fig. (5.17)**.

5.2.C.3 Electrochemical properties of flexible solid state symmetric supercapacitor (FSS-SSC) device

The electrochemical performance of an FSSSC device is measured by two electrode system using $\text{MnO}_2\text{-Ag}_3/\text{GO}$ thin film as cathode and anode electrodes with polymer gel as electrolyte as well as separator.

5.2.C.3.1 The CV studies

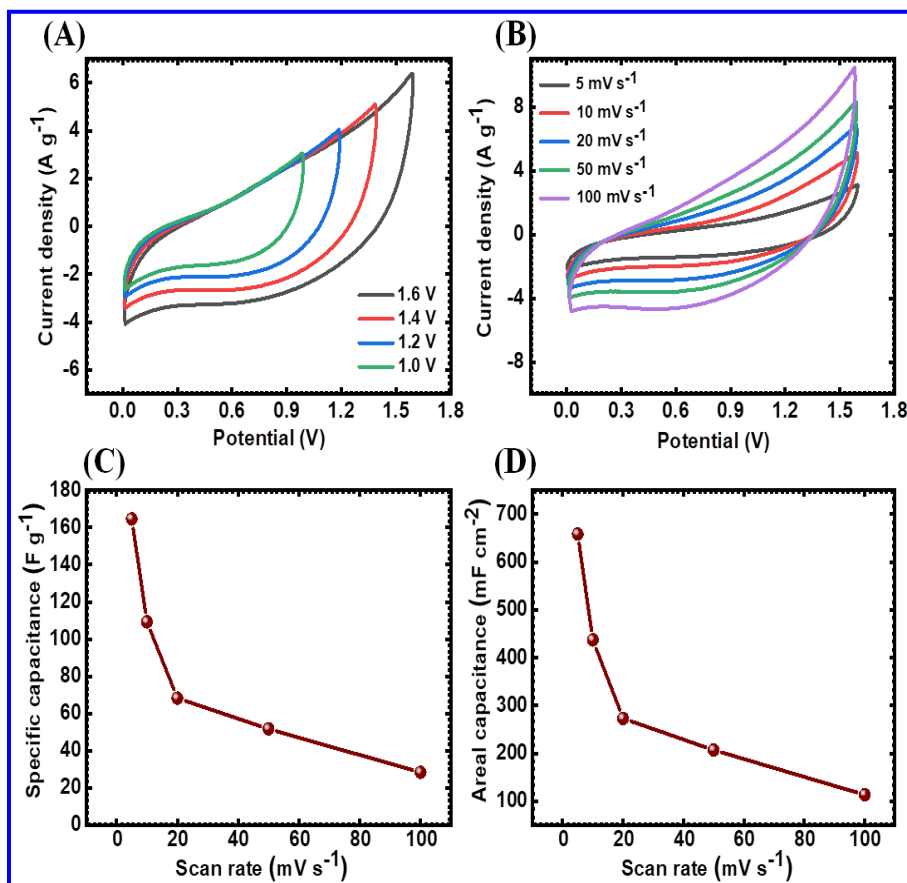


Fig. 5.18 (A) The CV plots of (FSS-SSc) device at various potential windows 0-1.6 V, (B) the CV plots of symmetric device at various scan rates 5-100 mV s^{-1} , (C) the plot of variation C_s with scan rates and (D) the plots of areal capacitance versus scan rates of symmetric device.

The flexible solid state symmetric supercapacitor (FSS-SSC) device assembled with $\text{MnO}_2\text{-Ag}_3/\text{GO}/\text{PVA-Na}_2\text{SO}_4/\text{MnO}_2\text{-Ag}_3/\text{GO}$ is tested for electrochemical activities. The CV graphs of device in working potential windows between 0 to +1.6 V at 100 mV s^{-1} scan rates are illustrated in **Fig. 5.18 (A)**. At an applied potential window of +1.6 V, maximum area covered with the CV graph results in a feasible improvement in specific energy and specific power. The CV plots in operating potential windows between 0 to +1.6 V at varied 5 to 100 mV s^{-1} scan rates are revealed in **Fig. 5.18 (B)**. The device shows the maximum C_s of 164 F g^{-1} at 5 mV s^{-1} scan rate. The variation of C_s versus scan rate is plotted in **Fig. 5.18 (C)**. The nature of CV plots of symmetric device does not change at high scan rates. The device showed a maximum areal capacitance of 658 mF cm^{-2} at a 5 mV s^{-1} scan rate. The variation of areal capacitance versus scan rate is shown in **Fig. 5.18 (D)**. The shape of the CV curves maintained analogous beside the increment of the scan rate insinuating a fabricated device owned an outstanding rate capability.

5.2.C.3.2 The GCD studies

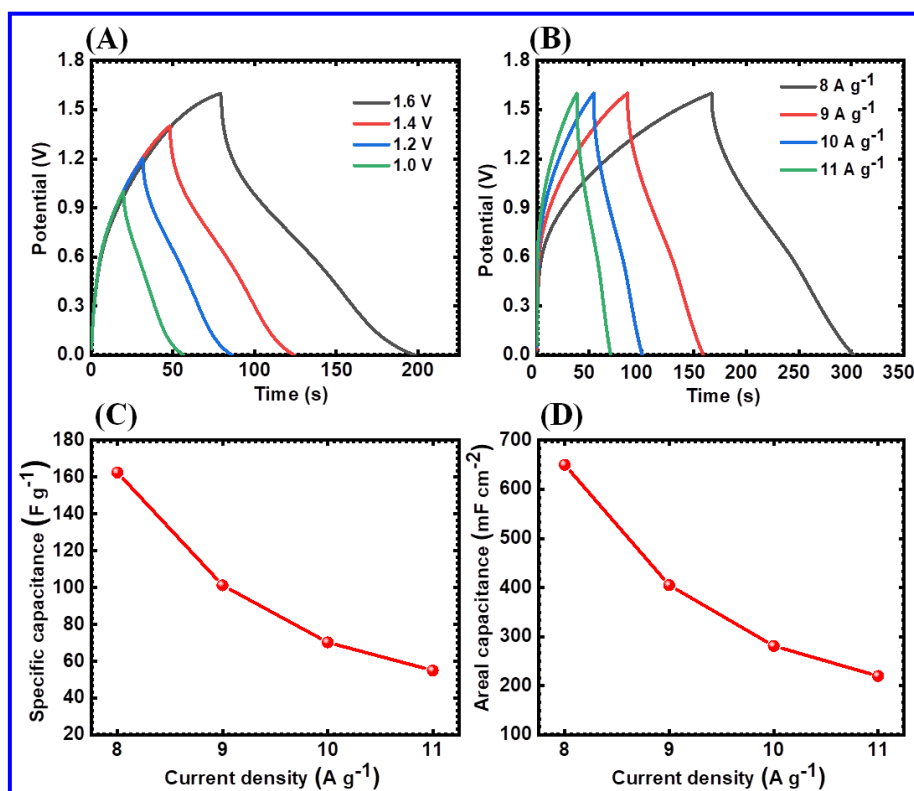


Fig. 5.19) (A) The GCD plots at 8 A g^{-1} with various potential windows, (B) GCD curves at various current density of $8\text{-}11 \text{ A g}^{-1}$, (C) the variation of C_s with applied current densities and (D) the plots of areal capacitance versus current density of symmetric device.

The GCD plots of device within applied potential window from 0 to +1.6 V at 8 A g^{-1} constant current density are displayed in **Fig. 5.19 (A)** and it is concluded that increasing potential window results into increasing charging-discharging time. The longer time of charge-discharge signifies more charge storage at +1.6 V. The CV and GCD studies show that for FSS-SSC device, +1.6 V is a suitable potential window. Therefore, further electrochemical performance of the device is carried out in the same potential window. The GCD plots of device at various current densities of 8, 9, 10, and 11 A g^{-1} with applied window of 0 to +1.6 V are illustrated in **Fig. 5.19 (B)**. The pseudocapacitive behavior is observed for GCD plots at various current densities. As seen in **Fig. 5.19 (B)**, discharge time decreases with rising charging current densities owing to the incapable interaction at interface between the electrode and electrolyte. The maximum C_s of 162 F g^{-1} was found for 8 A g^{-1} current density. The variation of C_s versus current density of the symmetric device is depicted in **Fig. 5.19 (C)**. The symmetric device showed a maximum areal capacitance of 650 mF cm^{-2} at 8 A g^{-1} current density as depicted in **Fig. 5.19 (D)**.

5.2.C.3.3 Ragone plot

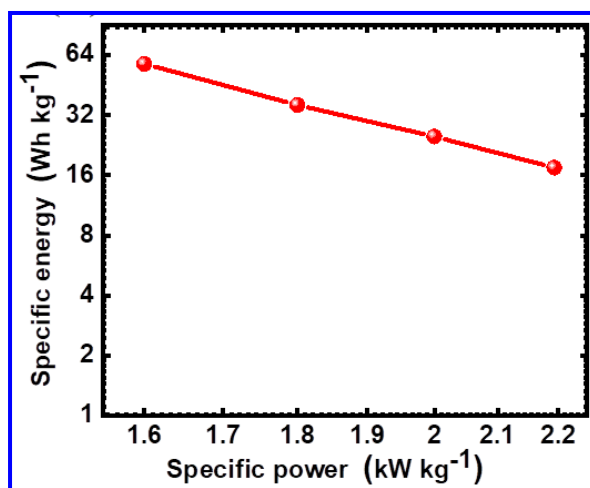


Fig. 5.20) Ragone plot of symmetric device.

The value of SP and SE calculated from GCD plot is shown in **Fig. 5.20**. The FSS-SSC device signifies the high S_E of 57 Wh kg^{-1} and S_p of 1.6 kW kg^{-1} . The value of S_E and

S_p are able to distribute different powers at specific energy and hence has versatile applications. The superior supercapacitive properties of Mn-Ag₃/GO film are accredited due to increased surface area with electrical conductivity. **Table 5.3** shows the comparing present report with literature.

5.2.C.3.4 Mechanical flexibility and stability studies

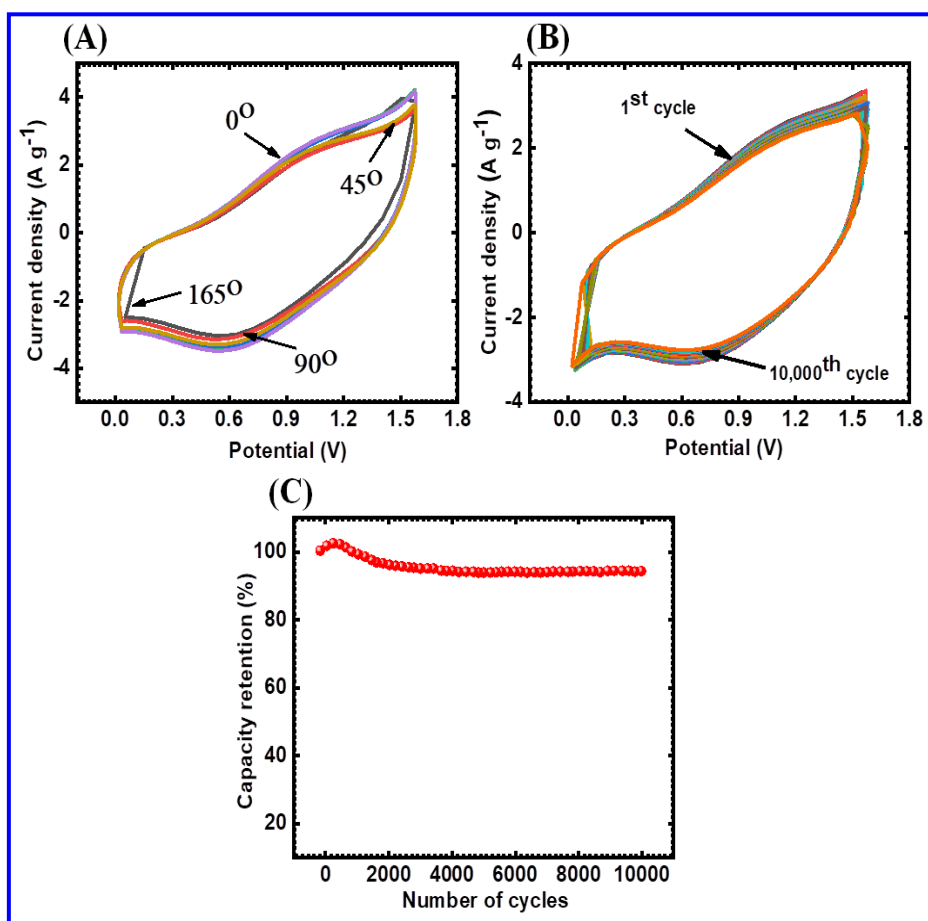


Fig. 5.21 (A) The CV curves of symmetric device at different bending angles of 0-165° at scan rate 100 mV s⁻¹, (B) the CV curves for 10,000 cycling stability and (C) the plot of capacity retention with cycle number of FSS-SSC device.

The flexibility of FSS-SSC device is necessary with no losing of its electrochemical performance and is appreciably helpful for domestic applications of various portable electronic devices [46]. The flexibility of FSS-SSC device is carried out by measuring cyclic plots at various flexible angles of device at 100 mV s⁻¹ constant scan rate. The CV plots at different flexible angles of 0, 45, 90, and 165° of device are depicted in **Fig. 5.21 (A)**. Here, fascinating to observe that when bending the device even at angle of 165°, the contour of the cyclic curve shows small

difference, signifying good adhesive of active material with superior property of the interface connecting of current collector, and electrolyte [21].

The long cycling life is a prime necessity for energy storage devices. The stability of device evaluated for 10,000 cycles at 100 mV s^{-1} scan rate is presented in **Fig. 5.21 (B)**. The capacity retention with cycle number plot of FSS-SSC device is illustrated in **Fig. 5.21 (C)**. It is observed that, Cs increases up to 450 cycles and decreases up to 94% of its initial value for the 10,000 cycles, signifying high cycling stability, and its suitability for stable energy storage applications. It indicates the good adhesive of the active material by suitable interface between electrode material, and gel electrolyte [47]. These results signify that the FSS-SSC device has excellent electrochemical performance, and life cycle.

5.2.C.3.5 The EIS studies

The EIS spectrum gives information about electrochemical performance of electrolyte and electrode interface. Nyquist graph of the FSS-SSC device is represented in the range of frequency from 0.1 kHz to 1 MHz with bias potential of 10 mV. The EIS plots of FSS-SSC device after and before 10,000th cycling stability are illustrated in **Fig. 5.22** (inset figure shows the best fitted EIS data and equivalent circuit). The Mn-Ag₃/GO thin film reveals that R_s ($1.3 \text{ } \Omega/\text{cm}^{-2}$), and R_{ct} values ($19.4 \text{ } \Omega/\text{cm}^{-2}$) before cycling are lower than $R_s = (1.7 \text{ } \Omega/\text{cm}^{-2})$, and $R_{ct} = (30.1 \text{ } \Omega/\text{cm}^{-2})$ values after the stability studies.

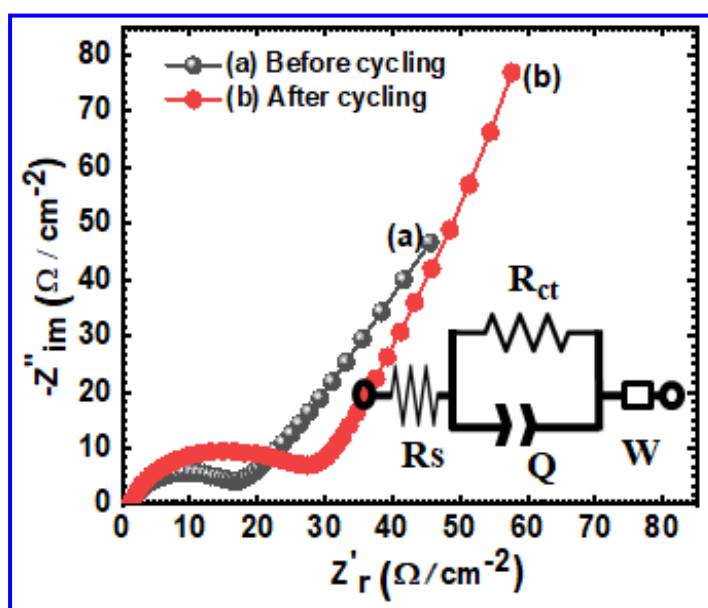


Fig. 5.22) Before and after CV cycling of Nyquist plots and (inset reveals best fitted with equivalent circuit).

5.2.C.3.6 Practical demonstration of symmetric FSS-SSC device

The practical demonstration of assembled two FSS-SSC devices with an area of 25 cm^2 each attached in series is displayed in **Fig. 5.23 (A)**. The series connected two devices contribute to fixed potential of $+3.2 \text{ V}$. The device is charged for 30 s with the voltage of $+3.2 \text{ V}$ and discharged through panel of 211 red light-emitting diodes (LEDs) for 180 seconds. **Fig. 5.23 (B)** displays photograph images after discharging of 180 seconds. The measured output power of 620 mW cm^{-2} signifies excellent storing capacity of device. The I-V characteristic of 211 red LEDs panel operated as external power source is shown in **Fig. 5.23 (C)**. At the voltage of 1.7 V , LED panel starts glowing with a current of 6 mA . The I-V characteristic of panel during on discharging of devices is illustrated in **Fig. 5.23 (D)**. The discharge current slowly decreases from 200 to 110 mA , while voltage decreases from $+3.2$ to $+1.7 \text{ V}$ in 180 seconds. Similarly, output power also decreases from 620 to 186 mW cm^{-2} .

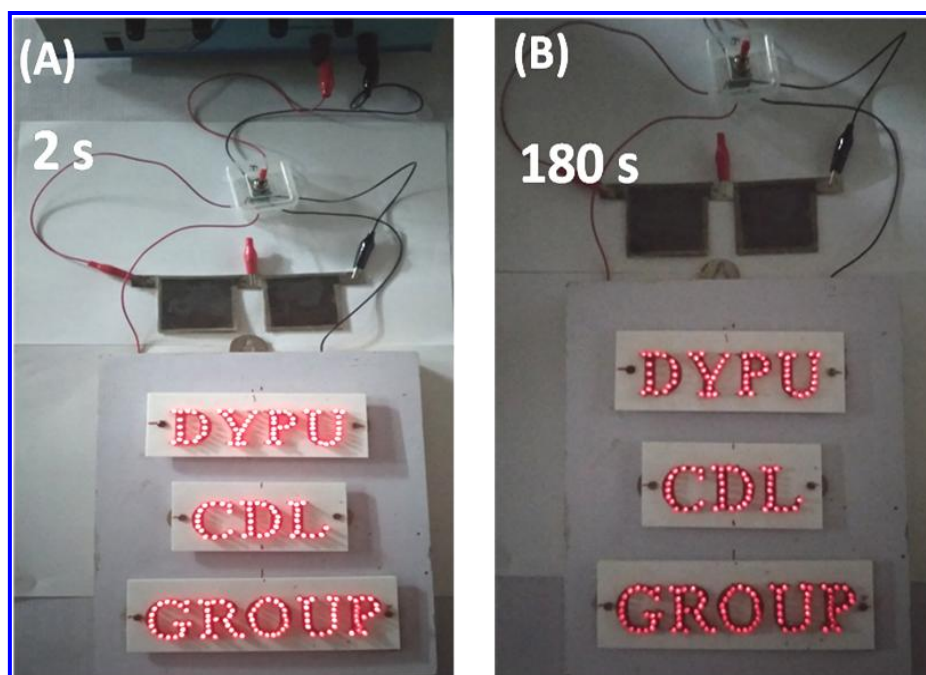


Fig. 5.23) (A, B) The photograph two (FSS-SSc) devices attached in series with charged at $+3.2 \text{ V}$ for 30 s at current density 1 A g^{-1} and discharged during a panel of 211 red LEDs (DYPU CDL GROUP) glows for 180 seconds.

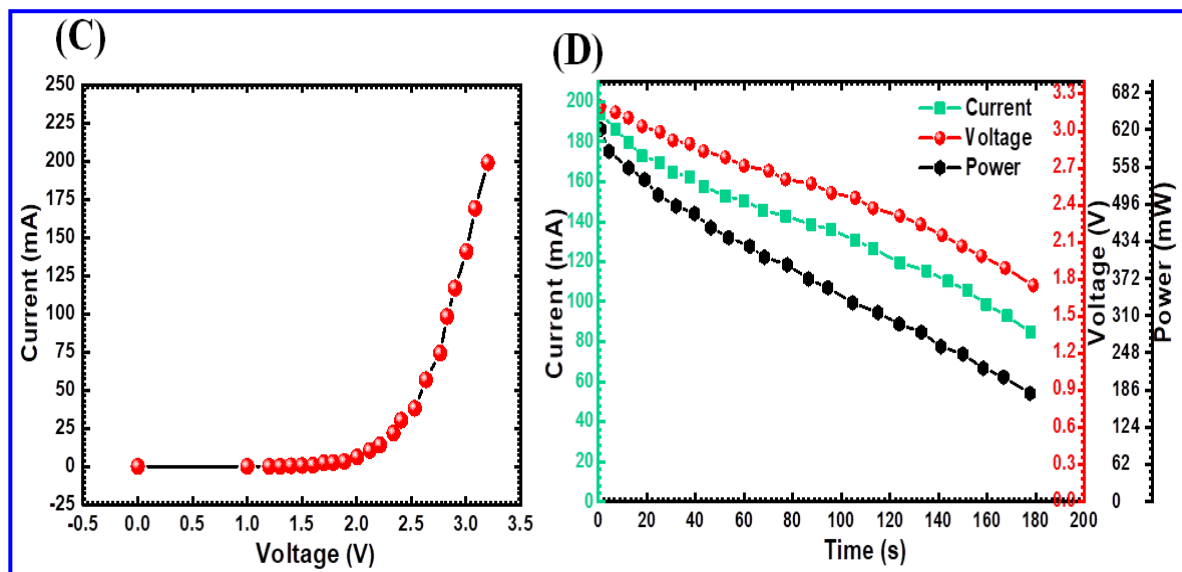


Fig. 5.23) (C) The I-V characteristic of 211 red LEDs panel operated as external power source and (D) the I-V characteristics of panel operated on discharging of devices.

5.3 Conclusions

The present work demonstrated deposition of MnO_2 and silver doped Mn-Ag3/GO thin films deposited by SILAR method on SS substrate. Here, the Mn-Ag3/GO electrode revealed high specific capacitance of 790 F g^{-1} at 5 mV s^{-1} scan rate with capacitive retention of 94.57% for 5000 CV cycles. The MnO_2 -Ag3/GO//PVA- Na_2SO_4 //MnO₂-Ag3/GO device showed the excellent flexibility and high specific energy of 57 Wh kg^{-1} with specific power of 1.6 kW kg^{-1} . In addition, FSS-SSC device showed specific capacitance retention of 94% for 10,000 CV cycles. Significantly, the two FSS-SSC devices in series stored energy of 620 mW cm^{-2} for 180 seconds when charged at +3.2 V for 30 s and discharged through a panel of 211 LEDs (DYPU CDL GROUP). The present work shows that Mn-Ag3/GO is a capable material used for charge storing appliance. The methods of fabrication of electrode and device are easy and cheap as compared to other methods. This FSS-SSC is a pragmatic approach for modern electric, electronic and hybrid vehicles.

5.4 References

- [1] N. Chodankar, D. Dubal, G. Gund, C.D. Lokhande, J. of Energy Chem., 25, (2016), 436-471.
- [2] V. Mane, D. Malavekar, S. Ubale, V. Lokhande, C. D. Lokhande, Inorg. Chem. Commun., 115, (2020), 107853-107869.
- [3] D. Dubal, O. Ayyad, V. Ruiz, P. Gomez-Romero, Chem. Soc. Rev, 44, (2015), 1777-1790.
- [4] D. Dubal, N. Chodankar, D. Kim, P. Gomez-Romero, Chem. Soc. Rev. 47, (2018), 2065-2129.
- [5] T. Xiong, T. Tan, L. Lu, W. Lee, J. Xue, Adv. Energy Mater., 8, (2018), 1-10.
- [6] W. Deng, Y. Sun, Q. Su, E. Xie, W. Lan, Mater. Lett., 137, (2014), 124-127.
- [7] N. Chodankar, D. Dubal, G. Gund, C. D. Lokhande, Electrochim Acta, 165, (2015), 338-347.
- [8] J. Zhu, W. Shi, N. Xiao, ACS Appl. Mater. Interfaces, 4, (2012), 2769-2774,
- [9] J. Shan, Y. Zhu, S. Zhang, J. Phys. Chem. C, 117, (2013), 8329-8335.
- [10] Y. Yu, B. Zhang, Y. He, J. Mater. Chem. A, 1(4), (2013), 1163-1170.
- [11] J. Kang, A. Hirata, L. Kang, X. Zhang, Y. Hou, L. Chen, Cheng Li, T. Fujita, K. Akagi, M. Chen, Angew. Chem., Int. Ed., 52, (2013), 1664-1667.
- [12] Y. Yang, T. Liu, L. Zhang, J. Mater. Sci. Mater. Electron, 27, (2016), 6202-6207.
- [13] Y. Liu, Y. Qiao, G. Wei, S. Li, Z. Lu, X. Wang, X. Lou, Energy Storage Mater., 11, (2018), 274- 281.
- [14] Z. Pei, Q. Meng, L. Wei, J. Fan, Y. Chen, C. Zhi, Energy Storage Mater., 28, (2020), 55-63.
- [15] Y. Wang, I. Zhitomirsky, Mater. Lett., 65, (2011), 1759-1761.
- [16] R. Li, X. Liu, H. Wang, Y. Wu, Z. Lu, Electrochim. Acta., 182, (2015), 224-229.
- [17] Q. Hao, Y. Yu, D. Zhao, C. Xu, J. Mater. Chem. A, 3, (2015), 15944-15950.
- [18] K. Lee, K. Lee, Y. Kang, T. Shin, Y. Sung, D. Ahn, Nanoscale, 7, (2015), 13860-13867.
- [19] S. Wang, J. Xie, T. Zhang, V. K. Varadan, J. Power Sources, 186, (2009), 532-538.
- [20] M. Jana, S. Saha, P. Samanta, N. Murmu, N. Kim, T. Kuila, J. Lee, J. Mater. Chem., A, 4, (2016), 2188-2197.

- [21] A. Patil, V. Lokhande, U. Patil, P. Shinde, C. D. Lokhande, *ACS Sustain Chem. Eng.*, 6, (2018), 787-802.
- [22] N. Chodankar, G. Gund, D. Dubal, C. D. Lokhande, *RSC Adv*, 4, (2014), 61503-61513.
- [23] Y. Hu, H. Zhu, J. Wang, Z. Chen, *J. of Alloys and Compd.* 42, (2011), 10234-10240.
- [24] M. Ocana, *Polym. Sci.* 278, (2000), 443-449.
- [25] S. Radhakrishnan, H. Kim, B. Kim, *Sens. Actuators B*, 233, (2016), 93-99.
- [26] N. Zhang, J. Sun, D. Jiang, T. Feng, Q. Li, *Carbon*, 47, (2009), 1214-1219.
- [27] T. Szabo, O. Berkesi, I. Dekany, *Carbon*, 43, (2005), 3186-3189.
- [28] A. Bourlinos, D. Gournis, D. Petridis, T. Szabo, A. Szeri, I. Dekany, *Langmuir*, 19, (2003), 6050-6055.
- [29] R. Sun, A. Nakajima, A. Fujishima, T. Watanabe, K. Hashimoto, *J. Phys. Chem. B*, 105, (2001), 1984-1990.
- [30] M. Tanveer, C. Cao, I. Aslam, Z. Ali, F. Idrees, W. Khan, M. Tahir, S. Khalid, G. Nabi, A. Mahmood, *J. Chem.*, 39, (2015), 1459-1468.
- [31] M. Pang, G. Long, S. Jiang, Y. Ji, W. Han, B. Wang, X. Liu, Y. Xi, *Electrochimica Acta.*, 161, (2015), 297-304.
- [32] M. Jana, J. Kumar, P. Khanra, P. Samanta, H. Koo, N. Murmu, T. Kuila, *J. Power Sources*, 303, (2016), 222-233.
- [33] Y. Ding, Y. Wang, L. Su, H. Zhang, Y. Lei, *J. Mater. Chem.*, 20, (2010), 9918-9926.
- [34] X. Li, Q. Li, Y. Wu, M. Rui, H. Zeng, *ACS Appl. Mater. Inter*, 7, (2015), 19316-19323.
- [35] Y. Li, Z. Li, P. K. Shen, *Adv. Mater.*, (2013), 25, 2474-2480.
- [36] S. Kong, K. Cheng, T. Ouyang, Y. Gao, K. Ye, G. Wang, D. Cao, *Electrochim. Acta.*, 226, (2017), 29-39.
- [37] Y. Zhang, Y. Liu, Z. Sun, J. Fu, S. Cheng, P. Cui, J. Zhou, Z. Zhang, X. Pan, W. Han, E. Xie, *J. Mater. Chem. A*, 7, (2019), 21290-21298.
- [38] D. Xue, D. Zhu, W. Xiong, T. Cao, Z. Wang, Y. Lv, L. Li, M. Liu, L. Gan, *ACS Sustainable Chem. Eng.*, 7, (2019), 7024-7034.
- [39] Q. Wang, Y. Zhang, H. Jiang, C. Meng, *J. Colloid Interface Sci.*, 534, (2018), 142-155.

- [40] N. Jabeen, A. Hussain, Q. Xia, S. Sun, J. Zhu, H. Xia, *Adv. Mater.*, 29, (2017), 1-9.
- [41] V. Pototskaya, O. Gichan, *Int. J. Electrochem. Sci.*, 14, (2019), 8195-8205.
- [42] J. Zhao, B. Guan, B. Hu, Z. Xu, D. Wang, H. Zhang, *Electrochim. Acta.*, 230, (2017), 428-437.
- [43] V. Mane, D. Malavekar, S. Ubale, R. Bulakhe, *Insik In, C. D. Lokhande, Electrochim. Acta*, 335, (2020), 135613-135622.
- [44] J. Zhi , W. Zhao, X. Liu , A. Chen , Z. Liu, F. Huang, *Adv. Funct. Mater.*, 24, (2014), 2013-2019.
- [45] A. Kumar, A. Sanger, A. Kumar, Y. Kumar, R. Chandra, *Electrochim Acta*, 222, (2016), 1761-1769.
- [46] S. Park, G. Wang, B. Cho, Y. Kim, S. Song, Y. Ji, M.-H. Yoon, T. Lee, *Nat. Nanotechnol.*, 7, (2012), 438-442.
- [47] H. Kim, J. Cook, H. Lin, J. Ko, S. Tolbert, V. Ozolins, B. Dunn, *Nat. Mater.*, 16, (2017), 454-460.
- [48] S. Wang, B. Pei, X. Zhao, R. Dryfe, *Nano Energy*, 2, (2013), 530-536.
- [49] R. Rajagopal, K. Ryu, *Chem Electro Chem.*, 5, (2018), 2218-2227.
- [50] H. Xia, C. Hong, X. Shi, B. Li, G. Yuan, Q. Yao, J. Xie, *J. Mater. Chem. A*, 3, (2015), 1216-1221.
- [51] N. Chodankar, S. Ji, D. Kim, *J. of the Taiwan Institute of Chemical Engineers*, 80, (2017), 503-510.
- [52] Q. Cai, J. Mao, Y. Li, J. Liu, H. Zhang, J. Huang, T. Wu, Y. Yang, C. Yuan, L. Dai, *J. Mater. Chem. A*, 8, (2020), 14254-14264.
- [53] Q. Le, M. Huang, T. Wang, X. Liu, L. Sun, X. Guo, D. Jiang, J. Wang, F. Dong, Y. Zhang, *J. Colloid Interface Sci.*, 544, (2019), 155-163.
- [54] Z. Zhang , F. Xiao, L. Qian , J. Xiao , S. Wang , Y. Liu, *Adv. Energy Mater.*, 4(10), (2014), 1-9.

CHAPTER-6

SUMMARY AND CONCLUSIONS

6.1. Introduction

The creation of efficient energies and their storage in an eco-friendly and sustainable method has become a huge global aim. From last decade, the flexible and portable electronics has been predicted for several applications like as medical bio-monitoring devices to military equipment. The electrical energy storage systems such as supercapacitors, capacitor and battery are available in recent years. The batteries have safety issue, limited service life time and small-scale power restricted applications in wearable and flexible electronic devices. The supercapacitors have capacity to store charge quickly, longer cycle life times, maintenance free, safe easy, and it has high power density than batteries battery technology. Therefore, supercapacitor technology is growing quickly to substitute batteries and capacitors.

Nowadays, the flexible and light weight energy storage devices are prominent as one of the key components. Therefore, portable and movable electronics demand a current trend of energy storage devices which is convenient for the necessity for flexibility. The FSS– SCs device is the innovative member of energy storage family, attracted considerable attention owing to their higher power density, longer lifetime, environmental friendliness and safety. The FSS– SCs devices have high mechanical reliability upon light weight, twisting, small in size, making them very reliable for flexible electronics. Though, the major key point of offered FSS– SCs device is the restricted energy density. Therefore, the improving energy density of FSS– SCs device without changing their other electrochemical features is a challenge for the scientists and researchers. To overcome these disadvantages of device, further electrode material analysis is required to increase performance of supercapacitor. The electrochemical features of FSS– SCs device are strongly depending on the active electrode material and the electrolyte. Temporarily, the combination of superior active electrode material with appropriate electrolyte effectively enhances both the power and energy capacity of the FSS– SCs device.

The earlier reports propose that the materials like metal oxides, conducting polymers and carbon based materials which increase the electrochemical performance of supercapacitor device. Among various transition metal oxides, MnO_2 is one of the most attraction electrode materials to develop the FSS– SCs device owing to its high theoretical specific capacitance (1370 F g^{-1}), low cost, environmental benignity, and

excellent electrochemical performance. Therefore, additional efforts are essential to prepare the high performance of MnO_2 electrodes by simple, binder free and inexpensive method, and also it is required to confirm the possibility of electrodes to fabricate the FSS– SCs device.

Present work deals with the synthesis of transition metal oxide MnO_2 thin films by simple, inexpensive and binder-free chemical approach. The various preparative parameters are selected to get highly porous surface morphology and their high surface area, which effectively increase the electrochemical features of MnO_2 , La doped MnO_2 and Ag doped MnO_2 thin films. Moreover, MnO_2 thin films are studied from various electrochemical techniques for supercapacitor application. Additionally, the fabrication of flexible all solid state symmetric supercapacitor devices of MnO_2 , La doped MnO_2 and Ag doped MnO_2 thin films with excellent electrochemical features using PVA- Na_2SO_4 gel electrolyte is carried out. Besides, practical demonstration of lighting of 211 red LEDs is performed by using symmetric flexible all solid state symmetric supercapacitor devices. This work has been distributed into six chapters.

Chapter-1 is introductory, in which initially, need of energy storage devices and their various types. It clarifies the most simple energy storage devices specifically capacitor, battery and supercapacitor. The evolutions of supercapacitor, recent trends of supercapacitor with its classification have been explained. The various types of supercapacitor along with examples are described, and their energy storage devices are demonstrated via Ragone plot. The different electrode materials such as carbon based materials, metal oxides/hydroxides and conducting polymers are explained. It also involves the basic requirements of supercapacitors such as the electrode material and electrolyte. Moreover, it consists of detailed explanation of MnO_2 as an active electrode material for supercapacitor. Besides, the literature survey of MnO_2 thin films, symmetric and asymmetric supercapacitive device is incorporated.

Chapter-2 covers the brief introduction of thin films, classification of thin film deposition techniques, theoretical background of chemical bath deposition and SILAR with their preparative parameters and advantages. The specifics of characterization techniques such as X– ray diffraction (XRD), Fourier transform infrared spectroscopy (FT-IR), X-ray photoelectron spectroscopy (XPS), Surface wettability, Field emission scanning electron microscopy (FE-SEM), Transmission electron microscopy (TEM),

and Brunauer-Emmett-Teller (BET) surface analysis are discussed in details. Finally, theoretical background of electrochemical supercapacitive techniques as cyclic voltammetry, galvanostatic charge-discharge and electrochemical impedance spectroscopy are studied.

Chapter-3 deals with the synthesis and characterization of MnO_2 thin films using facile inexpensive and binder free CBD and SILAR methods with their electrochemical performance evaluation. The present chapter is divided into three sections (Sections A, B and C). The Section 'A' deals with the deposition of MnO_2 thin films using CBD and SILAR methods and their characterizations. It also includes the characterization of MnO_2 thin films by different characterization techniques. The thickness of MnO_2 thin films slowly increased up to 12h in case of CBD and 60 cycles for SILAR methods. FE-SEM images demonstrated that surface morphology of C- MnO_2 12h electrode consists of fine grained particles where as S- MnO_2 60 electrode shows agglomerated and densely packed morphology. It is found that the high electrochemical performance of C- MnO_2 12h and S- MnO_2 60 electrodes are attributed due to their highest surface area than other electrodes. BET specific surface area of $250 \text{ m}^2 \text{ g}^{-1}$ for C- MnO_2 is higher than that S- MnO_2 electrode of $78 \text{ m}^2 \text{ g}^{-1}$. The section 'B' is associated with evaluation of the electrochemical performance of MnO_2 thin films in order to the effect of different times and SILAR cycles are studied. All the electrochemical properties are tested in 1 M Na_2SO_4 electrolyte using three electrode systems. The CBD α - MnO_2 films deposited for 12 hours showed maximum specific capacitance values of 757 F g^{-1} as compared to SILAR deposited \square - MnO_2 films. The CV stability showed excellent capacity retention of 95% for C- MnO_2 12h electrode after 5000 cycles. These electrochemical tests are essential to decide the superior electrode material for fabrication of supercapacitor device. Section 'C' deals with the fabrication and electrochemical properties of flexible symmetric solid state supercapacitor (FSSSC) device based on MnO_2 thin films. The comparison of C- MnO_2 12h thin film is the superior to than S- MnO_2 60 thin film, therefore C- MnO_2 12h thin film is selected to fabricate the FSSSC device.

The present chapter deals with the high performance of symmetric FSSSC devices fabricated using C- MnO_2 12h thin film as cathode and anode electrodes with PVA- Na_2SO_4 gel as electrolyte as well as a separator. The section 'C' deals with fabrication and

electrochemical performance evaluation of symmetric FSSSC supercapacitor device. Furthermore, this chapter includes the fabrication and electrochemical evaluation of C-MnO₂/12h symmetric supercapacitor device using PVA-Na₂SO₄ polymer gel electrolyte. The flexible symmetric solid state supercapacitor device with configuration of C-MnO₂/12h//PVA-Na₂SO₄//C-MnO₂/12h showed the maximum specific capacitance of 128 F g⁻¹ with ED 14 Wh kg⁻¹ at PD 0.2 kW kg⁻¹. In addition, FSSSC device exhibited capacitive retention of 90% for 5000 CV cycles. This device is feasible for practical applications as it can stored energy of 0.364 mW cm⁻² and is able to glow 211 red LEDs (DYPU CDL GROUP) for period of 160 s with two devices connected in series.

Chapter-4 emphases on the MnO₂, La-doped MnO₂ and La-MnO₂@GO composite thin film electrodes synthesized using SILAR method. This chapter is divided into three sections (Sections A, B and C). Section ‘A’ deals with preparation and characterization of MnO₂, La-doped MnO₂ and La-MnO₂@GO thin films by SILAR method. In a typical synthesis, MnO₂, 1, 3, 5 volume % La-doped MnO₂ and 3%La-doped MnO₂@GO composite thin films at room temperature (300 K). The GO was prepared via modified Hummer’s method. The XRD patterns demonstrated formation of tetragonal phase for all α -MnO₂ thin films. The scanning electron microscopic image of La-MnO₂@GO composite thin film showed that porous spongy-like nanoparticles. The Brunauer-Emmett-Teller (BET) specific surface area of 149.2 m² g⁻¹ for La-MnO₂@GO is higher than that of MnO₂ (49.7 m² g⁻¹) and La-MnO₂ (86.4 m² g⁻¹) samples. The La-MnO₂@GO composite thin film formation was confirmed subsequently from XPS study.

The Section ‘B’ is associated with the electrochemical performance of MnO₂, La-doped MnO₂ and La-MnO₂@GO thin films tested in 1 M Na₂SO₄ electrolyte. The effect of various La doping concentrations on the electrochemical performance of MnO₂ thin films was studied by CV, GCD, cycling stability and EIS analysis. The maximum electrochemical specific capacitance of 729 F g⁻¹ at scan rate of 5 mV s⁻¹ was obtained for 3%La-MnO₂@GO electrode. Section ‘C’ deals with the flexible solid state symmetric supercapacitor device configuration of SS/3%La-MnO₂@GO//PVA-Na₂SO₄//3%La-MnO₂@GO/SS was fabricated and electrochemical performance is evaluated. The flexible symmetric solid state supercapacitor device in operating potential window +1.8 V showed maximum specific capacitance of 138 F g⁻¹ with ED and PD of 60 Wh kg⁻¹ and 1.2 kW kg⁻¹, respectively. In addition, FSSSC device exhibited capacitive retention of

90% for 5000 CV cycles. Two series connected symmetric devices successfully stored output energy of 744 mW cm^{-2} for 3.5 min when charged at +3.6 V for 30 s and followed by discharge through 211 red LEDs (DYPU CDL GROUP).

Chapter-5 is also divided into three sections (Sections A, B and C). This chapter is MnO_2 , Ag-doped MnO_2 and MnO_2 -Ag/GO composite thin film were synthesized SILAR method and their characterizations in Section 'A'. In a typical synthesis, MnO_2 , 1, 3, 5 volume % Ag-doped MnO_2 and MnO_2 -Ag/GO thin films on the SS substrate. The tailored flower-like morphology and interconnected nanosheets of MnO_2 -Ag3/GO are promising electrodes materials. The XRD pattern, it is observed that the peak positions belong to the formation of β -type tetragonal structure for all MnO_2 thin films. The BET study revealed the nanosheets of MnO_2 -Ag3/GO exhibited high specific surface area of $192 \text{ m}^2 \text{ g}^{-1}$. The compositional analyses of MnO_2 -Ag3/GO are performed from XPS study. The Section 'B' is associated with the electrochemical performance of MnO_2 , Ag-doped MnO_2 and MnO_2 -Ag/GO thin films tested in three electrode system. The effect of various Ag doping concentrations on the electrochemical performance of MnO_2 thin films was studied by CV, GCD, cycling stability and EIS analysis. The maximum specific capacitance (Cs) of 877 F g^{-1} at the scan rate of 5 mV s^{-1} was obtained for MnO_2 -Ag3/GO electrode tested in Na_2SO_4 electrolyte with capacity retention of 94.57% after 5000 cycling stability.

The section 'C' deal with high performance flexible solid state symmetric supercapacitor (FSS-SSC) device have been fabricated using MnO_2 -Ag3/GO thin film as cathode and anode electrodes with PVA- Na_2SO_4 gel as electrolyte as well as a separator. In order to select the superior MnO_2 -Ag3/GO thin film to fabricate FSS-SSC device, which electrochemical performance of best MnO_2 -Ag3/GO thin films are optimized by SILAR method. **Table 5.3** illustrates the electrochemical parameters of MnO_2 -Ag3/GO thin films, which assist to choose the superior electrode to fabricate the symmetric FSSSC device. The SS/ MnO_2 -Ag/GO//PVA- Na_2SO_4 // MnO_2 -Ag/GO/SS supercapacitor device showed that excellent flexibility and high specific energy of 57 Wh kg^{-1} with specific power of 1.6 kW kg^{-1} . In additionally, FSS-SSC device showed specific capacitance retention of 94% for 10,000 cycles. Significantly, the two FSS-SSC devices in series stored output energy of 620 mW cm^{-2} for 180 seconds when charged at +3.2 V for 30 s and discharged through a panel of 211 LEDs (DYPU CDL GROUP).

Table 6.1: Supercapacitive evaluation of MnO₂, La-MnO₂@GO and MnO₂-Ag/GO electrodes in aqueous electrolytes and all symmetric FSS-SCs device in PVA-Na₂SO₄ used as polymer gel electrolyte.

Sr. No	Supercapacitor Symmetric Electrode	Methods	Electrolytes	Specific Capacitance (F g ⁻¹)	Energy Density (Wh kg ⁻¹)	Power Density (kW kg ⁻¹)	Stability (%) (cycles)
1.	α -MnO ₂	CBD	1 M Na ₂ SO ₄	757	-	-	88 (5000)
2.	Birnessite phase MnO ₂	SILAR	1 M Na ₂ SO ₄	512	-	-	95 (5000)
3.	C-MnO ₂ 12h	CBD	PVA-Na ₂ SO ₄ Polymer gel	128	14	0.2	90 (5000)
4.	3% La-MnO ₂ @GO	SILAR	PVA-Na ₂ SO ₄ Polymer gel	138	60	1.2	90 (5000)
5.	MnO ₂ -Ag3/GO	SILAR	PVA-Na ₂ SO ₄ Polymer gel	164	57	1.6	94 (10,000)

Chapter-6 summarizes and concludes all the chapters. Estimation of the supercapacitor performance of all electrode materials is the essential entity of making supercapacitor devices. The methods of material preparation, used electrolytes, specific capacitance, energy density, power density, potential windows and cycling stability are mentioned in **Table. 6.1**. The overall electrochemical performance of MnO_2 , $\text{La-MnO}_2\text{@GO}$ and $\text{MnO}_2\text{-Ag/GO}$ electrodes at optimized conditions are better than previous reports.

Finally, in comparison, the symmetric devices have better electrochemical performance in terms of higher operating potential window, specific capacitance, higher energy density and cycling stability. Fabricated flexible solid state symmetric 3% $\text{La-MnO}_2\text{@GO//PVA-Na}_2\text{SO}_4\text{/3%La-MnO}_2\text{@GO}$ device showed excellent electrochemical features as mentioned in **Table 6.1**. In conclusion, 3% $\text{La-MnO}_2\text{@GO}$ electrodes are promising electrodes for supercapacitor applications.

6.2 Future work

The current motivational work is on the preparation and electrochemical properties of La and Ag doped into the MnO_2 with GO composite thin film electrodes. The future work is proposed as following.

- Higher potential window can be tailored using the organic and redox active electrolytes.
- Enhancement of the supercapacitive properties of device by humidity and temperature studies.
- Cyclic stability and efficiency of device can be enhanced using MWCNT material.
- To explore the more polymer gel electrolytes and if necessary nanocomposite of polymer gel electrolytes with various nano-sized filler with high ionic conductivity and good mechanical properties.

CHAPTER-7

RECOMMENDATIONS

Recommendations

Today's environmental problems and reducing fossil fuels, the increasing demand for renewable energy sources has stimulated intense research on energy storage and conversion from unconventional energy sources. Recently, the SCs have huge attention since of their high charge deliver rate, excellent power density, long life span and no short circuit affect. The SCs is a promising electrochemical energy storage technology, which stores high energy density than capacitor with a high power density (PD) than the batteries. The SCs have enormous energy storage capacity, besides possessing the combined property of both conventional capacitors and batteries. According to the charge storage mechanism separates SCs into different categories as electrical double-layer capacitors (EDLCs), pseudocapacitor and hybrid capacitors. In EDLC, the electric charge is stored at the interface between the electrode and the electrolyte carbon based material (activated carbon, graphene, and carbon nanotubes etc.). The conducting polymers and metal oxides are used as pseudocapacitor and charge storage mechanism is based on quick redox reaction at the surface of electrode. One more type of SCs is a mixture of pseudocapacitors and EDLCs, known as hybrid capacitors. However, all the above-mentioned SCs (pseudocapacitors and EDLCs,) still suffer from some significant disadvantages, such as poor cyclic stability of conductive polymers, the low capacitance of carbon-based materials.

In the presented research work, thin film of MnO_2 , La doped MnO_2 and Ag doped MnO_2 thin films were prepared using CBD and SILAR methods. The electrical conductivity and charge storage capacity of these thin films were increased by means of improvement in surface area. To achieve this GO was composited with the La doped MnO_2 and Ag doped MnO_2 thin films using SILAR method. The objective of the preparation of composite electrode was to improve surface area specific capacitance and cyclic stability of the material than pristine materials. The solid state supercapacitor fabricated using these electrodes showed maximum specific energy of 57 Wh kg^{-1} and specific power of 1.6 kW kg^{-1} .

Finally, it is recommended that, at 60 SILAR cycles, Ag doped MnO_2/GO thin film show best electrochemical performance. To get best electrochemical performance optimized concentration of GO is 0.5 mg mL^{-1} .

The consequence of thin film and different nanostructure morphologies of material is explained in brief. The different electrode materials such as carbon based materials, metal oxides/hydroxides, and conducting polymers are discussed. The significance of metal oxides for SC application is described concerning a contribution from non-faradaic reactions in addition to faradaic reactions. The literature survey of carbon based materials, metal oxides/hydroxides and conducting polymers and includes preparation methods, properties, and applications. Furthermore, the literature survey of metal oxides and carbon based electrode materials for supercapacitive applications is analyzed and finally, the orientation and purpose of the thesis are described.

The thin film synthesis method and the advantages of chemical methods over physical thin film deposition methods were discussed. Out of chemical methods, the SILAR method is predictable to be more controllable large area thin film deposition process. Thickness affects the charge storage, cycling stability, resistive parameters of the film electrode material. Considering this, the optimization of thin film thickness or mass loading is necessary which can be done by varying deposition cycles in SILAR method. This method is comprised of three processes, a) adsorption, b) reaction, and c) rinsing. To evaluate the structural, morphological, and elemental compositional parameters different characterization techniques such as XRD, FE-SEM, FT-IR, XPS, contact angle measurement and BET were used. The basic principle and working mechanism of these techniques are discussed to understand obtained results. Further, fundamental aspects and applications of various electrochemical techniques for energy storage application are discussed.

The MnO_2 thin films were prepared using facile and binder-free CBD and SILAR methods and characterized for electrochemical performance evaluation. The C- MnO_2 12h electrode has slow growth rate and takes 12h to develop fine grained spherical nanoparticles on the SS substrate. The high growth rate of S- MnO_2 60 electrode results into formation of agglomerated densely packed surface morphology. Hence, the change in surface area of MnO_2 films is due to the different growth rates under different optimized conditions in both the methods. BET specific surface area of $192 \text{ m}^2 \text{ g}^{-1}$ for C- MnO_2 is higher than that S- MnO_2 electrode of $78 \text{ m}^2 \text{ g}^{-1}$.

The CBD MnO_2 films deposited for 12 hours showed maximum specific capacitance values of 757 F g^{-1} as compared to SILAR deposited MnO_2 films. The EIS measurement shows that highly porous C- MnO_2 electrode provides low charge transfer resistance, for easy access to ions for intercalation/deintercalation as compared to S MnO_2 electrodes. The cyclic stability showed excellent capacity retention of 95% for C- MnO_2 12h electrode after 5000 cycles. It is found that the high electrochemical performance of C- MnO_2 12h and S- MnO_2 60 electrodes are attributed due to their highest surface area than other electrodes. The flexible symmetric device with configuration of C- MnO_2 12h//PVA- Na_2SO_4 //C- MnO_2 12h showed the maximum specific capacitance of 128 F g^{-1} with ED 14 Wh kg^{-1} at PD 0.2 kW kg^{-1} . In addition, symmetric device exhibited capacitive retention of 90% after 5000 CV cycles. This device is feasible for practical applications as it can stored energy of 0.364 mW cm^{-2} and is able to glow 211 red LEDs (DYPU CDL GROUP) for period of 160 s with two devices connected in series.

In a typical synthesis, MnO_2 , 1, 3, 5 volume %La-doped MnO_2 and 3%La-doped MnO_2 @GO composite thin films synthesized using SILAR method at room temperature (300 K). The GO was prepared via modified Hummer's method. The XRD patterns demonstrated formation of α - MnO_2 tetragonal phase for all thin films. The BET specific surface area of $149 \text{ m}^2 \text{ g}^{-1}$ for La- MnO_2 @GO is higher than that of MnO_2 ($49 \text{ m}^2 \text{ g}^{-1}$) and La- MnO_2 ($86 \text{ m}^2 \text{ g}^{-1}$) samples. The effect of various La doping concentrations and ratio of GO in the composite film on the electrochemical performance of MnO_2 thin films was studied by CV, GCD, cycling stability and EIS analysis. Thus the composition of La doped into MnO_2 and composite with GO in proper ratio can be used to modify structural and morphological properties and able to improve specific capacitance.

The maximum electrochemical specific capacitance of 729 F g^{-1} at scan rate of 5 mV s^{-1} was obtained for 3%La- MnO_2 @GO electrode and stability of 94% over 5000 CV cycles. The flexible symmetric solid state supercapacitor device configuration of SS/3%La- MnO_2 @GO//PVA- Na_2SO_4 //3%La- MnO_2 @GO/SS was fabricated and electrochemical performance was evaluated. The flexible symmetric solid state supercapacitor device in operating potential window +1.8 V showed maximum specific capacitance of 138 F g^{-1} with ED and PD of 60 Wh kg^{-1} and 1.2 kW kg^{-1} , respectively.

In addition, symmetric device exhibited capacitive retention of 90% after 5000 CV cycles. Initially, these two symmetric devices are connected in series and charged with a potential of +3.6 V for 30 s and discharged through panel of 211 red LEDs for more than 3.5 min. The measured storing output power of symmetric device is 0.364 mW cm⁻² which signifies excellent charge storing capability.

In a typical synthesis, MnO₂, 1, 3, 5 volume %Ag-doped MnO₂ and MnO₂-Ag₃/GO thin films on the SS substrate using by SILAR method. The effect of various Ag doping concentrations on MnO₂ with composite of GO on chemical composition, crystal structure, surface morphology, and electrochemical properties was studied. The tailored flower-like morphology and interconnected nanosheets of MnO₂-Ag₃/GO are promising electrodes materials. The XRD pattern, it is observed that the peak positions belong to the formation of β -type tetragonal structure for all MnO₂ thin films. This mesoporous structure exhibited high specific surface area of 192 m² g⁻¹ for MnO₂-Ag₃/GO electrode as compared to other material. Thus, the effect of various Ag doping concentrations on MnO₂ with composite of GO in proper ratio can be used to modify structural and morphological properties and able to improve specific capacitance. This highlights superiority of MnO₂-Ag₃/GO composite thin film as compared to other thin films.

The maximum specific capacitance of 877 F g⁻¹ at the scan rate of 5 mV s⁻¹ was obtained for MnO₂-Ag₃/GO electrode with capacity retention of 94.57% after 5000 cycling stability. The electrochemical parameters of MnO₂-Ag₃/GO thin films, which assist to choose the superior electrode to fabricate the symmetric device. In conclusion, the highest specific surface area offered by MnO₂-Ag₃/GO material helps to reduce ion diffusion resistance and maximum active sites exposed to the electrolyte improves the infiltration of electrolyte ions in the electrode. The SS/MnO₂-Ag₃/GO//PVA-Na₂SO₄//MnO₂-Ag₃/GO/SS supercapacitor device showed that excellent flexibility and high specific energy of 57 Wh kg⁻¹ with specific power of 1.6 kW kg⁻¹. In addition, symmetric device showed specific capacitance retention of 94% for 10,000 cycles. Significantly, the two symmetric devices connected in series stored output energy of 620 mW cm⁻² for 180 seconds when charged at +3.2 V for 30 s and discharged through a panel of 211 LEDs (DYPU CDLGROUP).

Conclusions

The conclusions from the present research work are listed as follows:

1. The MnO_2 , 3%La- MnO_2 @GO and MnO_2 -Ag3/GO composite electrodes were successfully synthesized via facile and binder free CBD and SILAR methods, deposited on SS substrates, and used for supercapacitor applications.
2. The mass loading per unit area of electrode is controlled through variation of time period and deposition cycles. Optimum mass loading of electrode was essential for highest electrochemical performance.
3. At the optimum mass loading charge transfer resistance per unit mass is minimum and there after it increased. For C- MnO_2 , thin film deposited at 12 hours CBD method shows best electrochemical performance. And, for S- MnO_2 , thin film deposited at 60 SILAR cycles shows best electrochemical performance.
4. The La doped MnO_2 with GO composition to improve specific surface area. As the bare MnO_2 has very low specific capacitance, optimization of volume concentration doping of La with GO of this material is essential. For, bare MnO_2 doping of La with 0.5 mg mL^{-1} concentrations of GO suspension provides better effect on electrochemical properties.
5. The electrode of the 3%Ag- MnO_2 /GO makes a good stoichiometric thin film with enhanced electrochemical properties.
6. Symmetric solid-state supercapacitor fabricated using MnO_2 -Ag3/GO showed maximum specific energy of 57 Wh kg^{-1} at the power density of 1.6 kW kg^{-1} .

Finally, it is recommended that the fabrication of flexible symmetric solid state device (MnO_2 -Ag3/GO// MnO_2 -Ag3/GO) showed excellent electrochemical performance in PVA- Na_2SO_4 gel electrolyte as compared to the other flexible symmetric devices. Therefore, the use of SILAR is an effective chemical method for enhancing the supercapacitor performance of MnO_2 -Ag3/GO composite electrode. SILAR offers an expedient method for the grounding of mixed metal salts that participates in a noteworthy degree of mixing, resulting in nanosheets with a large surface area, which have been useful for monitoring the surface morphology.

The present work deals with the synthesis of MnO_2 thin films by facile and binder-free chemical approach. The numbers of preparative parameters were optimized to get highly porous surface morphology with high specific surface area, which successfully enhance the electrochemical performance of MnO_2 thin films. The doping with composite thin films showed better SC performance than MnO_2 thin films. Therefore, the doping with composite thin films showed superior electrochemical performance was used as one electrode for fabrication of symmetric devices.

Finally, in comparison, the symmetric devices have better electrochemical performance in terms of higher operating potential window, specific capacitance, higher energy density and cycling stability. Fabricated flexible solid state symmetric 3%La- MnO_2 @GO and MnO_2 -Ag3/GO devices showed excellent electrochemical features as mentioned. In conclusion, MnO_2 -Ag3/GO electrodes are promising electrodes for supercapacitor applications.

Future plan

In this study, the doping MnO_2 thin films and their composites with rGO were synthesized using SILAR method. The introduction of rGO improves electrical conductivity, specific surface area, and overall electrochemical performance of bare material. Instead of rGO, other carbon based materials like as, MWCNTs, carbon foam and carbon aerogel for the composition will be used. Along with this, the doping of other transition metals (Ni, Co, VO_2) to form a bimetallic compound will also enhance the electrochemical energy storage properties of the electrode material. To understand the process of energy storage in MnO_2 electrode, physical characterization of these materials should be carried out to examine changes in the crystal structure, surface morphology, and chemical composition using techniques such as XRD, SEM, TEM, and XPS. Further, the fabricated of flexible symmetric and asymmetric solid-state supercapacitor devices through and electrochemical performance evaluation could give a better understanding of actual processes involved in charge storage.